



Terms and Conditions of Use of Digitised Theses from Trinity College Library Dublin

Copyright statement

All material supplied by Trinity College Library is protected by copyright (under the Copyright and Related Rights Act, 2000 as amended) and other relevant Intellectual Property Rights. By accessing and using a Digitised Thesis from Trinity College Library you acknowledge that all Intellectual Property Rights in any Works supplied are the sole and exclusive property of the copyright and/or other IPR holder. Specific copyright holders may not be explicitly identified. Use of materials from other sources within a thesis should not be construed as a claim over them.

A non-exclusive, non-transferable licence is hereby granted to those using or reproducing, in whole or in part, the material for valid purposes, providing the copyright owners are acknowledged using the normal conventions. Where specific permission to use material is required, this is identified and such permission must be sought from the copyright holder or agency cited.

Liability statement

By using a Digitised Thesis, I accept that Trinity College Dublin bears no legal responsibility for the accuracy, legality or comprehensiveness of materials contained within the thesis, and that Trinity College Dublin accepts no liability for indirect, consequential, or incidental, damages or losses arising from use of the thesis for whatever reason. Information located in a thesis may be subject to specific use constraints, details of which may not be explicitly described. It is the responsibility of potential and actual users to be aware of such constraints and to abide by them. By making use of material from a digitised thesis, you accept these copyright and disclaimer provisions. Where it is brought to the attention of Trinity College Library that there may be a breach of copyright or other restraint, it is the policy to withdraw or take down access to a thesis while the issue is being resolved.

Access Agreement

By using a Digitised Thesis from Trinity College Library you are bound by the following Terms & Conditions. Please read them carefully.

I have read and I understand the following statement: All material supplied via a Digitised Thesis from Trinity College Library is protected by copyright and other intellectual property rights, and duplication or sale of all or part of any of a thesis is not permitted, except that material may be duplicated by you for your research use or for educational purposes in electronic or print form providing the copyright owners are acknowledged using the normal conventions. You must obtain permission for any other use. Electronic or print copies may not be offered, whether for sale or otherwise to anyone. This copy has been supplied on the understanding that it is copyright material and that no quotation from the thesis may be published without proper acknowledgement.

Investigating The Load, Friction And Sealability Characteristics Of Graphite Valve Packings

Máire Ní Ruaidhe, B.A., B.A.I.

A thesis submitted to the University of Dublin in partial fulfilment of the
requirements for the degree of

Doctor in Philosophy

Trinity College Dublin

Supervisor

Prof. A.A. Torrance

External examiner

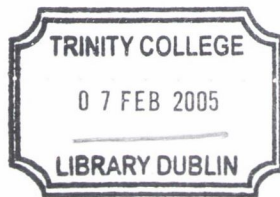
Prof. R.S. Sayles

Imperial College London

Internal examiner

Prof. John Monaghan

Trinity College Dublin

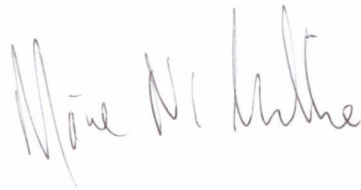


TH6815
7476

Declaration

I declare that I am the sole author of this thesis and that all the work presented in it, unless otherwise referenced, is my own. I also declare that the present work has not previously been submitted, in whole or in part, to any other university or college for any degree or qualification.

I authorise the library of the University of Dublin to lend this thesis.

A handwritten signature in cursive script, appearing to read 'Máire Ní Ruaidhe', written in dark ink.

Máire Ní Ruaidhe

December, 2004

DECLARATION

- This thesis has not been submitted as an exercise for a degree at any other university.
- Except where stated, the work described therein was carried out by me alone.
- I give permission for the Library to lend or copy this thesis upon request.

Signed:

Maureen M. Martin

Acknowledgments

This project began many years ago in the minds of the members of the European Sealing Association (ESA) would wished to commemorate the memory of one of their founder members, the late Mr. Denis Gilley, who I never had the honour of meeting. It is through their desire to honour Denis' memory and promote excellence in sealing technology that this project was initiated.

There is a vast number of people who have helped me in the completion of this project and I am indebted to each and every one of them. It has been a truly amazing experience.

I would like to start by thanking my supervisor Prof. A.A. Torrance for all his help and guidance over the course of this thesis.

I would like to thank the entire ESA for their enthusiasm, encouragement and help over the course of this project. I would especially like to thank Dr. Brian S Ellis from the ESA, who so warmly welcomed me into their association and who has given me amazing support, advice and more than the odd pint of Guinness over the course of the last 6 years.

To Ralf Vogel from Burgmann Packings who was my industrial supervisor, for his caring support and help over the course of this project I would like to extend my thanks. To David Edwin Scott and Andrew Goulding from James Walker for supplying me with test samples and advise at the drop of a hat.

To Dr. Thomas Klenk and Dr. Hans Kocklemann from the MPA, at the University of Stuttgart for the use of their test equipment, expert advice and warm welcome into their research group on my visits to Stuttgart.

To John Dennis and Dr. John Harrison from Imperial College London

for the use of their high pressure triaxial test rig without which this project could not have been completed.

To all the staff in the Department of Mechanical Engineering, especially Prof. John Fitzpatrick who developed the relationship between the ESA and the Department in the projects initial years.

To the many great friends I have made among the postgraduate students who have passed through this department in the last 4 years. It has made those dark days of research seem not so bad, especially since The Pav is so close. To Triona (for all the tea breaks and chat), Kevin, Richard, Linda, James, John B, John G, John T, Paul, John V, Alex, Luca, Zep, Danny B, Tadgh, Mary W, Leandro, Bruce, Adriele, Susanne, Toman, Conor B, Conor MacC, Ray, George and Laura to name but a few.

Finally to my family and Dallas for all their support and patience over the years.

Abstract

It is widely accepted that valve stem leakage accounts for the majority of fugitive emissions from petrochemical and chemical sites often accounting for over 50% of fugitive emissions from these sites. The most common valve sealing device is the compression packing and even though compression packings have been used for over 150 years, there is still a considerable lack of knowledge into how they effect a seal in a valve. This project hopes to bridge this gap by gaining a greater scientific understanding of their behaviour in order to implement improvements in compression packing installation and operation.

In the present study an non-linear elastoplastic finite element (FE) model of 1.5 g/cm^3 exfoliated graphite was implemented in ABAQUS/Standard using the modified Cam clay material model. Recent experimental testing has proven that packing rings demonstrate non-linear elastoplastic behaviour. Previous compression packing research has lead to the development analytical models to predict valve packing behaviour. They assume that packing ring behaviour is linear elastic over the loading range. In order to obtain a greater scientific understanding of compression ring behaviour realistic FE modelling was carried out.

The FE model was used to investigate the influence of loading, valve stem cycling, valve stem friction and wear on the behaviour of an exfoliated graphite packing ring set. It was found that FE analysis was vastly superior to analytical models in predicting the behaviour of exfoliated graphite packing rings in a valve under operational conditions.

Experimental tests to determine the coefficient of friction based on asperity slope and atmosphere found that the coefficient of friction of exfoliated graphite increases with distance slid. FE analysis using the modified Cam clay material model showed that the increase in coefficient of friction resulted from a failure of the surface layer of the compression packing. The accuracy of these methods indicate that this concept should be applied to analysis other packing ring types.

Contents

1	Introduction	1
1.1	General introduction	1
1.2	Objectives and scope of thesis	4
1.3	Chapter content summary	6
2	Literature review	9
2.1	Valves	9
2.2	Valve packing materials	10
2.3	Packing behaviour	11
2.4	Packing test methods	15
2.5	Analytical models	16
2.6	Friction and wear based on surface roughness	19
2.6.1	Boundary lubrication	19
2.6.2	Real surfaces	25
2.6.3	Wear analysis	26
2.7	Exfoliated graphite packing rings	27
2.7.1	Exfoliated graphite foil	28
2.7.2	Manufacturing exfoliated graphite packing rings	29
2.7.3	Previous graphite testing	32
2.7.4	Frictional properties of graphite	33
2.8	Summary	35
2.8.1	Project plan	36

3	Constitutive material model	38
3.1	Selection of a commercial FE package	38
3.2	Elasto-plastic modelling	41
3.2.1	Extension to general stress and strain space	41
3.2.2	Stress invariants	41
3.2.3	Basic concepts	42
3.2.4	Coincidence of axes	42
3.2.5	Yield function	42
3.2.6	Plastic potential	44
3.2.7	Hardening/softening rules	46
3.3	Modified Mohr Coulomb material model	47
3.3.1	Basic assumptions	47
3.3.2	Exponential elastic behaviour	48
3.3.3	Flow rules	49
3.3.4	Hardening rules	49
3.3.5	Mohr-Coulomb failure criterion	50
3.4	Modified Cam clay Model	52
3.4.1	Elastic model	53
3.4.2	Yield locus	55
3.4.3	Hardening rule	55
3.4.4	Plastic potential	57
3.4.5	Critical state	58
3.5	Input parameters for FE material model	58
3.5.1	Loading and unloading parameters	59
3.5.2	Poisson's ratio	62
3.5.3	Pre-consolidation stress	62
3.5.4	Strength in tension	63
3.5.5	Critical state parameters	64
3.5.6	Friction angle	64
3.6	Summary	65

4	Experimental and FE methods for compression packing analysis	66
4.1	Material Testing	66
4.1.1	Compression test rig	66
4.1.2	Triaxial test rig	68
4.2	FE methods	71
4.2.1	Compression test simulation	73
4.2.2	Valve cycling model	75
4.3	Summary	80
5	Material model validation and valve packing FE results	81
5.1	Material testing	81
5.1.1	Compression test results	81
5.1.2	Triaxial test results	82
5.2	FE material model input parameters	86
5.2.1	Loading and unloading parameters	86
5.2.2	Poisson's Ratio	91
5.2.3	Friction angle	92
5.2.4	Critical state line, M	92
5.2.5	Predetermined input parameters	95
5.2.6	Material model input parameter summary	98
5.3	FE material model validation	98
5.4	Valve packing behaviour	103
5.4.1	Axial stress	103
5.4.2	Stress against the stem	105
5.4.3	Force required to cycle stem	108
5.4.4	Wear analysis	108
5.5	Conclusion	118
6	Friction and wear analysis	119
6.1	Introduction	119
6.2	Wedge test rig	120

6.3	Friction results	123
6.3.1	1.5 g/cm^3 exfoliated graphite	123
6.3.2	Special 1.5 g/cm^3 exfoliated graphite	124
6.3.3	Average coefficient of friction	126
6.3.4	Experimental data analysis	130
6.3.5	Modified Oxley model	131
6.3.6	Intrinsic coefficient of friction	135
6.3.7	Wedge test FE model	137
6.3.8	FE wedge test results	147
6.4	Wear results	149
6.4.1	1.5 g/cm^3 exfoliated graphite	149
6.4.2	Special 1.5 g/cm^3 exfoliated graphite	149
6.4.3	Wear coefficient, K for exfoliated graphite	156
6.5	Summary	159
7	Discussion	161
7.1	Introduction	161
7.2	Limitations of the present study	163
7.2.1	Range of materials tested	163
7.2.2	Constitutive FE material model	164
7.2.3	Valve cycling model	165
7.2.4	Wedge test	165
7.3	FE analysis of a valve packing set	165
7.3.1	Applied axial stress	166
7.3.2	Radial sealing stress	167
7.3.3	Force to cycle stem	169
7.4	Comparison with analytical solutions	169
7.4.1	Decay in radial stress against the stem	169
7.4.2	Force required to cycle stem	171
7.5	Compression packing friction	174
7.5.1	Intrinsic coefficient of friction	175
7.5.2	FE analysis of wedge test	176

7.6	Packing ring wear	181
7.7	Valve design rules	183
7.7.1	Optimum initial radial stress	186
7.8	Achievements of this study	187
8	Conclusion	188
8.1	Main conclusions	188
8.2	Future work	190
A	Compression test results	199
A.1	1.3 g/cm^3 exfoliated graphite	199
A.2	1.8 g/cm^3 exfoliated graphite	199
B	Triaxial test results	206
C	Exfoliated graphite friction and wear results	214
C.1	Friction results	214
C.1.1	1.4 g/cm^3 exfoliated graphite	214
C.1.2	1.6 g/cm^3 exfoliated graphite	216
C.2	Wear results	216
C.2.1	1.4 g/cm^3 exfoliated graphite	216
C.2.2	1.6 g/cm^3 exfoliated graphite	218
D	Teadit friction and wear results	222
D.1	Friction data	223
D.1.1	Teadit 2001	223
D.1.2	Teadit 2200	223
D.1.3	Teadit 2202	232
D.1.4	Correlation data	236
D.2	Wear data	236
D.2.1	Teadit 2001	238
D.2.2	Teadit 2200	240
D.2.3	Teadit 2202	240

D.2.4 Wear coefficient, K for braided graphite packing rings . 241

List of Figures

1.1	Valve stuffing box	3
2.1	A gate valve	10
2.2	An example of a live loaded ball valve	12
2.3	Initial axial and radial stress distribution in a compression packing set	13
2.4	The effect of gland pressure on leakage	14
2.5	Surface texture	21
2.6	Slip line field model of asperity interaction	23
2.7	Forces on a wedge which experiences no elastic recovery behind the wedge	25
2.8	(a) Graphite flake, (b) Graphite intercalations, (c) Graphite foil	29
2.9	Die formed graphite ring after compression	31
2.10	Experimental test data obtained by Bouvard et al. on the testing of graphite powder	33
2.11	Atomic structure of graphite	34
3.1	Yield function presentation	43
3.2	Plastic potential presentation	45
3.3	Mohr Coulomb plastic potential in p-q space	50
3.4	Stress conditions at failure	51
3.5	Behaviour under isotropic compression	54
3.6	The modified Cam clay model	56
3.7	Associated flow rule	57

3.8	Details of a typical oedometer consolidation cell (reproduced from Fig. 1(a) of BS 1377:Part5:1990)	60
3.9	Calculation of compression index and swelling index	61
3.10	Calculation of preconsolidation stress	63
3.11	The influence of β on the Cam clay yield surface	65
4.1	Compression test rig	67
4.2	Triaxial test rig	69
4.3	Exfoliated graphite discs used during triaxial testing	70
4.4	Triaxial cell	72
4.5	Exterior of triaxial cell, Imperial College, London	72
4.6	Compression test FE simulation	75
4.7	Compression test FE simulation	76
4.8	FE model used to simulate valve stem cycling	77
4.9	FE mesh used to simulate valve stem cycling	78
5.1	Compression of one 1.5 g/cm^3 exfoliated graphite packing ring	82
5.2	K_{rad} for the initial compression of one 1.5 g/cm^3 exfoliated graphite packing ring	83
5.3	K_{rad} for the second loading cycle of one 1.5 g/cm^3 exfoliated graphite packing ring	84
5.4	Triaxial test results for 1.5 g/cm^3 exfoliated graphite at a confining pressure of 1 MPa	85
5.5	Plot of $\log \sigma_v$ vs. void ratio for 1.5 g/cm^3 exfoliated graphite .	87
5.6	Plot of $\ln p$ vs. void ratio for 1.5 g/cm^3 exfoliated graphite . .	88
5.7	Comparison of loading and unloading behaviour of exfoliated graphite with that of powder graphite	90
5.8	Graph of $-\epsilon_1$ vs. ϵ_v for 1.5 g/cm^3 exfoliated graphite	91
5.9	Mohr Coulomb failure envelope for 1.5 g/cm^3 exfoliated graphite	93
5.10	Evolution of axial stress and axial strain versus time at critical state	96
5.11	Determining M, the critical state line	97

5.12	Comparison of FE and experimental results for the compression of one 1.5 g/cm^3 exfoliated graphite packing ring	100
5.13	Comparison of FE results with experimental results for K[ID] for the compression of one 1.5 g/cm^3 exfoliated graphite ring .	101
5.14	Comparison of experimental results and FE analysis using ABAQUS/Standard for K[ID] and K[OD] for one 1.5 g/cm^3 exfoliated graphite ring	102
5.15	Axial stress at the top of seal 1 for $\mu_{stem} = 0.05$ to $\mu_{stem} = 0.20$, under load control conditions	103
5.16	Axial stress at the top of seal 1 for $\mu_{stem} = 0.25$ to $\mu_{stem} = 0.35$, under load control conditions	104
5.17	Axial stress at the top of seal 1 for $\mu_{stem} = 0.05$ to $\mu_{stem} = 0.20$, under displacement control conditions	105
5.18	Axial stress at the top of seal 1 for $\mu_{stem} = 0.25$ to $\mu_{stem} = 0.40$, under displacement control conditions	106
5.19	Axial stress at the top of seal 1 for $\mu_{stem} = 0.45$, under displacement control conditions	106
5.20	Radial stress against stem after initial compression under displacement control conditions	107
5.21	Radial stress against stem after initial compression under load control conditions	107
5.22	Comparison of radial stress against the stem on initial compression and after 5 cycles for $\mu_{stem} = 0.05$ to $\mu_{stem} = 0.20$, under load control conditions	109
5.23	Comparison of radial stress against the stem on initial compression and after 5 cycles for $\mu_{stem} = 0.25$ to $\mu_{stem} = 0.35$, under load control conditions	110
5.24	Comparison of radial stress against the stem on initial compression and after 5 cycles for $\mu_{stem} = 0.05$ to $\mu_{stem} = 0.20$, under displacement control conditions	111

5.25	Comparison of radial stress against the stem on initial compression and after 5 cycles for $\mu_{stem} = 0.25$ to $\mu_{stem} = 0.40$, under displacement control conditions	112
5.26	Comparison of radial stress against the stem on initial compression and after 5 cycles for $\mu_{stem} = 0.45$, under displacement control conditions	113
5.27	Force required to cycle the stem under load control conditions for $\mu_{stem} = 0.05$ to $\mu_{stem} = 0.20$	114
5.28	Force required to cycle the stem under load control conditions for $\mu_{stem} = 0.25$ to $\mu_{stem} = 0.35$	115
5.29	Force required to cycle the stem under displacement control conditions for $\mu_{stem} = 0.05$ to $\mu_{stem} = 0.20$	116
5.30	Force required to cycle the stem under displacement control conditions for $\mu_{stem} = 0.25$ to $\mu_{stem} = 0.40$	117
5.31	Force required to cycle the stem under displacement control conditions for $\mu_{stem} = 0.45$	117
5.32	Plot of W_c versus S_c	118
6.1	Cross section of test head	121
6.2	Friction test rig	122
6.3	Stroke number versus coefficient of friction for 1.5 g/cm^3 exfoliated graphite in air	124
6.4	Stroke number versus coefficient of friction for 1.5 g/cm^3 exfoliated graphite in argon	125
6.5	Stroke number versus coefficient of friction for Special 1.5 g/cm^3 exfoliated graphite in air	126
6.6	Stroke number versus coefficient of friction for Special 1.5 g/cm^3 exfoliated graphite in argon	127
6.7	Wedge angle vs. average coefficient of friction for exfoliated graphite packings in air	128
6.8	Wedge angle vs. average coefficient of friction for exfoliated graphite packings in argon	129

6.9	Forces on a hard rigid wedge sliding over a softer material . .	132
6.10	Elastic recovery	133
6.11	Consolidation and swelling behaviour of exfoliated graphite . .	134
6.12	Correlation of measured initial coefficient of friction with pre- dicted initial coefficient of friction	136
6.13	2D plane strain model of wedge test	138
6.14	The evolution of the deviatoric stress towards failure based on the initial intrinsic coefficient of friction	139
6.15	8.12° wedge partitioned to produce a spring loaded wedge . . .	140
6.16	Failure of the material behind a wedge	141
6.17	The yield and failure surfaces of the standard and extended modified Cam clay material models	142
6.18	FE mesh of wedge test rig	144
6.19	Zoomed section of wedge test FE mesh	144
6.20	Zoomed section of wedge test FE mesh detailing the element density at the wedge block interface	145
6.21	Element distortion in surface layer of block after 6 cycles . . .	146
6.22	Zoomed section of element distortion in surface layer of block after 6 cycles	146
6.23	Pressure under a 8.12° wedge	148
6.24	Zoomed section of the pressure under a 8.12° wedge	149
6.25	Stress, S11 under a 8.12° wedge	150
6.26	Zoomed section of the stress, S11 under a 8.12° wedge	150
6.27	Stress, S22 under a 8.12° wedge	151
6.28	Zoomed section of the stress, S22 under a 8.12° wedge	151
6.29	Stress, S33 under a 8.12° wedge	152
6.30	Zoomed section of the stress, S33 under a 8.12° wedge	152
6.31	Stroke number vs. η for a interfacial friction of $\mu = 0.15$ at the wedge block interface	153
6.32	Stroke number versus wear for 1.5 g/cm^3 exfoliated graphite in argon	154

6.33	Stroke number versus wear for 1.5 g/cm^3 exfoliated graphite in argon	155
6.34	Stroke number versus wear for special 1.5 g/cm^3 exfoliated graphite in air	156
6.35	Stroke number versus wear for special 1.5 g/cm^3 exfoliated graphite in argon	157
6.36	Wear coefficient, K for exfoliated graphite: in air	158
6.37	Wear coefficient, K for exfoliated graphite: in argon	159
7.1	Stress at the top of seal 1 for $\mu_{stem} = 0.15$ under displacement load control conditions	167
7.2	Comparison of radial stress against the stem on initial com- pression and after 5 stem strokes under conditions of displace- ment and load control	168
7.3	Comparison of the force required to cycle the stem under dis- placement and load control conditions	170
7.4	Stress against the stem on initial compression, comparing FE data with analytical models	171
7.5	Stress against the stem after 5 cycles, comparing FE data with analytical models	172
7.6	Comparison of FE data with the empirical formula for the force required to cycle the stem	173
7.7	Stroke number at which dramatic increase in coefficient of fric- tion for 1.5 g/cm^3 exfoliated graphite is seen	178
7.8	Change in average asperity slope with bandwidth	180
7.9	Correlation between predicted friction coefficient, μ and the wear coefficient, K	182
A.1	Compression of one 1.3 g/cm^3 exfoliated graphite packing ring	200
A.2	K[-] for the initial compression of one 1.3 g/cm^3 exfoliated graphite packing ring	201

A.3	K[-] for the second loading cycle of one 1.3 g/cm^3 exfoliated graphite packing ring	202
A.4	Compression of one 1.8 g/cm^3 exfoliated graphite packing ring	203
A.5	K[-] for the initial compression of one 1.8 g/cm^3 exfoliated graphite packing ring	204
A.6	K[-] for the second loading cycle of one 1.8 g/cm^3 exfoliated graphite packing ring	205
B.1	Triaxial test results for triaxial test 1 (See Table B)	208
B.2	Triaxial test results for triaxial test 2 (See Table B)	209
B.3	Triaxial test results for triaxial test 3 (See Table B)	210
B.4	Triaxial test results for triaxial test 4 (See Table B)	211
B.5	Triaxial test results for triaxial test 5 (See Table B)	212
B.6	Triaxial test results for triaxial test 6 (See Table B)	213
C.1	Test data for 1.4 g/cm^3 exfoliated graphite in air	215
C.2	Test data for 1.4 g/cm^3 exfoliated graphite in argon	215
C.3	Test data for 1.6 g/cm^3 exfoliated graphite in air	216
C.4	Test data for 1.6 g/cm^3 exfoliated graphite in argon	217
C.5	Time versus wear for 1.4 g/cm^3 exfoliated graphite in air . . .	217
C.6	Time versus wear for 1.4 g/cm^3 exfoliated graphite in argon .	218
C.7	Time versus wear for special 1.6 g/cm^3 exfoliated graphite in argon	219
C.8	Time versus wear for special 1.6 g/cm^3 exfoliated graphite in argon	220
D.1	(a) Teadit 2001 (b) Teadit 2200 (c) Teadit 2202	222
D.2	Teadit 2001, wedge test results for tests carried out on PTFE sections of packing rings in air	224
D.3	Teadit 2001, wedge test results for tests carried out on PTFE sections of packing rings in argon	225
D.4	Teadit 2001, wedge test results for tests carried out on non-PTFE sections of packing rings in air	226

D.5	Teadit 2001, wedge test results for tests carried out on non-PTFE sections of packing rings in argon	227
D.6	Teadit 2200, wedge test results for tests carried out on PTFE sections of packing rings in air	228
D.7	Teadit 2200, wedge test results for tests carried out on PTFE sections of packing rings in argon	229
D.8	Teadit 2200, wedge test results for tests carried out on Non-PTFE sections of packing rings in air	230
D.9	Teadit 2200, wedge test results for tests carried out on Non-PTFE sections of packing rings in argon	231
D.10	Teadit 2202, wedge test results for tests carried out on PTFE sections of packing rings in air	232
D.11	Teadit 2202, wedge test results for tests carried out on PTFE sections of packing rings in argon	233
D.12	Teadit 2202, wedge test results for tests carried out on Non-PTFE sections of packing rings	234
D.13	Teadit 2202, wedge test results for tests carried out on Non-PTFE sections of packing rings	235
D.14	Wedge angle vs. average coefficient of friction for Teadit 2001	236
D.15	Wedge angle vs. average coefficient of friction for Teadit 2200	237
D.16	Wedge angle vs. average coefficient of friction for Teadit 2202	237
D.17	Wear coefficient, K for Teadit 2001 on non PTFE sections: in air	238
D.18	Wear coefficient, K for Teadit 2001 on non PTFE sections: in argon	239
D.19	Wear coefficient, K for Teadit 2001 on PTFE sections: in air	239
D.20	Wear coefficient, K for Teadit 2001 on PTFE sections: in argon	240
D.21	Wear coefficient, K for Teadit 2200 on non PTFE sections: in air	241
D.22	Wear coefficient, K for Teadit 2200 on non PTFE sections: in argon	242

D.23 Wear coefficient, K for Teadit 2200 on PTFE sections: in air .	242
D.24 Wear coefficient, K for Teadit 2200 on PTFE sections: in argon	243
D.25 Wear coefficient, K for Teadit 2202 on non PTFE sections: in air	243
D.26 Wear coefficient, K for Teadit 2202 on non PTFE sections: in argon	244
D.27 Wear coefficient, K for Teadit 2202 on PTFE sections: in air .	244
D.28 Wear coefficient, K for Teadit 2202 on PTFE sections: in argon	245
D.29 Wear coefficient, K for Teadit 2001	245
D.30 Wear coefficient, K for Teadit 2200	246
D.31 Wear coefficient, K for Teadit 2202	246

List of Tables

3.1	FE material model input parameters	59
5.1	Calculated values of λ and κ from experimental tests	89
5.2	FE material model input parameters and their associated error	99
5.3	FE material model input parameters	99
6.1	Intrinsic coefficient of friction at the beginning of the test . . .	136
7.1	Strokes until η reaches 0.75 for 1.5 g/cm^3 exfoliated graphite with an intrinsic coefficient of friction of $\mu = 0.15$	179
B.1	Triaxial test initial parameters	207

Nomenclature

Latin symbols

B	Coefficient
c	Cohesion
d_i	Inner diameter
d_o	Outer diameter
d_s	Diameter of the stem
e	Void ratio
f	Lubrication parameter
F	Yield function
F_G	Gland force
F_n	Normal force
F_S	Frictional stem force
F_t	Tangential force
h	Wear depth
h_e	Elastic recovery height
h_t	indentation depth
ID	Inner Diameter
k	State parameter
k_s	Shear strength of the softer material
K_0	$\frac{\sigma_h}{\sigma_v}$
K_{rad}	Radial stress transfer coefficient

K_t	Tangent bulk modulus
K	Wear Coefficient
l	Length of packing in its compressed state
L	Stroke number
m	Vector of state variables
M	Shape factor for Cam Clay ellipse/ slope of the critical state line
n	Number of strokes
N	Constant
OD	Outer Diameter
p	$\frac{1}{3}(\sigma_{xx} + \sigma_{yy} + \sigma_{zz})$ isotropic stress, axial symmetry: $p = \frac{1}{3}(\sigma_{ax} + 2\sigma_{rad})$
p_c	Isotropic preconsolidation stress
p_t	Tensile strength
p_0	Initial pressure
P	Plastic potential
P_{AX}	Axial stress in a packing ring set at a distance l from the top of the packing ring set
P_I	Initial radial stress against the stem
P_G	Applied gland load
P_S	System pressure
q	Deviatoric stress
r_i	Inner radius
r_o	Outer radius
s	Distance slid
S_i	Average radial stress against the stem

S_t	Average radial stress against the stem which produces the maximum allowable leakage
t	Ring thickness
v	Specific volume
V	Wear volume
w	Width of the wedge
Z	Distance slid

Greek symbols

α	Wedge angle
α^*	Effective wedge angle
β	Cap curvature
γ	Deviatoric strain
Γ	Constant
ϵ_1	Axial strain
ϵ_a	Axial strain
ϵ_{el}	Elastic strain
ϵ_p^p	Plastic volume strain
ϵ_q^e	Elastic deviatoric strain
ϵ_q^p	Plastic deviatoric strain
ϵ_r	Radial strain
ϵ_v	Volume strain, $\epsilon_v = \epsilon_1 + \epsilon_2 + \epsilon_3$
$\Delta\epsilon_i^p$	six components of incremental plastic strain
$\delta\epsilon_p$	$\delta\epsilon_{xx} + \delta\epsilon_{yy} + \delta\epsilon_{zz}$, volumetric strain, axial symmetry: $\delta\epsilon_p = \epsilon_a + 2\epsilon_r$
$\delta\epsilon_q$	Deviatoric strain : axial symmetry: $\delta\epsilon_q = \frac{2}{3}(\epsilon_a - \epsilon_r)$
$\delta\sigma_i$	Represents the six components of accumulated stress
η	$\frac{q}{p}$

κ	swelling index (defines the slope of the swelling line)
λ	compression index (defines the slope of the virgin consolidation line)
Λ	Scalar multiplier
μ	Coefficient of friction
μ_0	Initial intrinsic coefficient of friction
μ_1	Coefficient of friction between the stem and the packing inner diameter
μ_2	Coefficient of friction between the housing and the packing outer diameter
$\sigma_1, \sigma_2, \sigma_3$	Stress components in principle stress space
$\sigma_x, \sigma_y, \sigma_z, \tau_{xy}, \tau_{xz}, \tau_{yz}$	Stress components in (x,y,z)
σ_{ax}	Axial stress
σ_B	Axial stress applied to follower
σ_f	Normal failure strength
σ_h	Horizontal stress
σ_{rad}	Radial stress
σ_v	Vertical stress
σ_y	Yield stress
τ_f	Shear failure strength
ν	Poisson's ratio
ϕ	Internal friction angle
ψ	Dilatancy angle

Chapter 1

Introduction

1.1 General introduction

Manufacturing industry is responsible for a wide range of environmental pollution emission to air (acidifying substances, greenhouse gases, persistent organic pollutants, heavy metals and other types of pollutants), emissions to water, contamination of soil and the generation of waste. Environmental pollution has severe consequences for our planet. Global warming, flooding severe storms, droughts, acid rain, fish kills and the dramatic increase in the instances of asthma are all as a result of global industrialisation [1].

As industry consists of large and easily identifiable point sources of pollution it has always been a prime target of environmental policy [2], the target of which are fugitive emissions. A fugitive emission is defined as ‘Any chemical or mixture of chemicals, in any physical form, which represents an unanticipated or spurious leak from anywhere on an industrial site’ [3]. Fugitive emissions are emissions that cannot reasonably be collected and pass through a stack, vent or similar opening. Examples include particulate matter from coal piles, roads and quarries, and VOC emissions from valves, flanges and pumps at refineries and organic chemical plants [4].

Worldwide fugitive emission legislation is becoming increasingly rigorous. The European Commission (EC) is putting in place a series of directives and

legislation which will lead to much closer control, and reduction of fugitive emissions across the entire European Union (EU). The Directive on the Control of Volatile Organic Compounds (VOCs) Council Directive 1999/13/EC from Solvent Using Industries was formally adopted in March 1999 by the European Commission and is now law. The Directive requires a reduction in VOC emissions of between 57% and 67% using 1990 levels as a baseline. EU Member States have until 2007 to integrate the Directive into national law, but all new installations will have to comply immediately.

The Solvents Directive is part of a much bigger EU strategy which aims to eliminate low-level ozone pollution. This strategy includes initiatives such as the Auto Oil Programme and the EC Framework Directive on Ambient Air Quality. However, it is the Integrated Pollution Prevention and Control (IPPC) Directive that will have the biggest impact of all, together with the Solvents Directive, on reducing industrial VOC and fugitive emissions [5].

It is widely expected that valve stem leakage account for the majority of fugitive emissions from chemical and petrochemical plants [3]. In investigating the source of fugitive emissions from industrial sites it was found that the major proportion of fugitive emissions come from only a small fraction of the sources (e.g. less than 1% of valves in gas/vapour can account from more than 70% of the fugitive emissions in a refinery) [3]. An American review carried out by Reyes and Reddington [6] in the early 1980's found that valves were responsible for approximately 19% of all light water reactor power plant shut-downs (more than any other type of component) and that valve stem leakage was one of the main causes. A survey undertaken by the Electrical Power Research Institute (EPRI) [7] indicated that approximately 80% of problems contributing to boiling water reactor plant non availability were due to valve stem seal leakage or seal related problems. Valve problems are found also to result in a significant amount of utility expenditure in terms of maintenance and manpower and cost.

By definition, a valve is a mechanical device that controls the flow of a fluid. The valve is one of the most basic and indispensable components

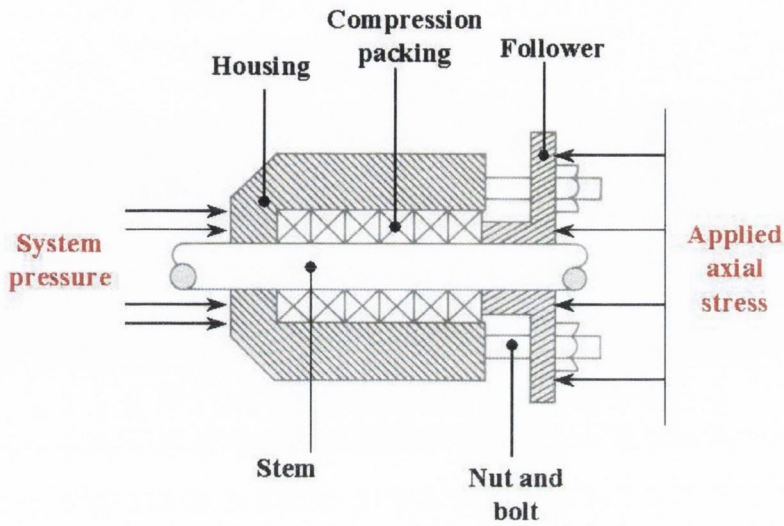


Figure 1.1: Valve stuffing box (Source: [8])

of our modern technological society. The original and still most common of these valve sealing device is the compression packing, so called because of the manner in which it performs the sealing function. Made from relatively soft, pliant materials, compression packings consists of a number of rings inserted into the annular space (stuffing box) between the rotating and/or reciprocating part of the valve. By tightening a follower against the top or outboard ring, pressure is transmitted to the packing set, expanding the rings radially against the side of the stuffing box and the reciprocating and/or rotating member, effecting a seal, as seen in Figure 1.1. Even though valve packings have been used for over 150 years there is still a vast lack of knowledge into how they effect a seal in a valve due to the lack of material data and scientific analysis of their behaviour. Improvements in valve sealing cannot be made without an improved fundamental understanding of their behaviour in a valve. It was in light of environmental concerns, legislative demands and the lack of detailed data on the behaviour of compression packing rings that this research was initiated.

1.2 Objectives and scope of thesis

Previous research [9, 10, 11] into the behaviour of compression packing rings has led to purely analytical solutions. These analytical solutions presume that packing ring behaviour is elastic in nature. Recent experimental testing has proven that compression packing ring behaviour shows non linear elastoplastic behaviour [12].

Many practical problems in engineering are either extremely difficult or impossible to solve using conventional analytical methods. Such methods involve finding mathematical equations, which define the required variables. In the past it was common practice to simplify such problems to the point where an analytical solution could be obtained which, it was hoped bore some resemblance to the solution of the real problem. The advent of high speed computers has given tremendous impetus to all numerical methods for solving engineering problems. The finite element method forms one of the most versatile classes of such methods [13, 14]. In order to gain a greater scientific understanding of the complex behaviour of a compression packing ring set in a valve the FE method is to be used in conjunction with experimental testing and analytical analysis to determine the in-situ behaviour of a packing ring set in a valve.

The first objective of this thesis was to develop a non-linear elastoplastic [15] FE material model of exfoliated graphite packing rings. Exfoliated graphite packing rings were chosen because their mechanical properties do not differ significantly from one manufacturer to another. They are also one of the more homogeneous packing ring types and represent a good starting point for developing experimental and FE methods to describe general compression packing behaviour. The input parameters of the FE material model were determined experimentally and the FE material model was then validated.

The second objective of this project was to use the FE material model of exfoliated graphite developed in the first part of this thesis to investigate the influence of loading, stuffing box friction, valve stem cycling and wear

on the behaviour of an exfoliated graphite packing ring set. Results from FE analysis are compared with previously developed analytical models to establish how the two methods compared.

The third objective of the thesis was to investigate the influence of surface roughness and environment on the friction and wear behaviour of compression packing rings. The influence of valve stem surface roughness on the friction and wear behaviour of exfoliated graphite packing rings was investigated using experimental, analytical and FE methods. Practical engineering experience shows that the texture of the rubbing surfaces plays an important role in the forces that develop in a contact under conditions of boundary lubrication.

There is a significant lack of knowledge into the friction and wear mechanisms that occur at the valve packing interface. Standard valve stem friction testing has to date involved large scale conventional testing. Tests are carried out with components of relatively large mass under heavy loads. Results are dependant on factors which cannot be controlled or measured. In recent years, several workers have published models of asperity contacts which allow the effects of surface roughness on friction to be predicted [16, 17, 18, 19]. These models are based on theoretical, experimental and FE analysis. To date a model capable of predicting the friction and wear behaviour of exfoliated graphite has not been developed.

There is very little data available on the friction and wear behaviour of exfoliated graphite. In order to investigate the influence of surface roughness on the friction and wear behaviour of exfoliated graphite a test rig of a single asperity sliding against the series of packing rings was designed and built. This test rig allowed for the influence of valve stem surface roughness on the frictional and wear behaviour of compression packing rings to be investigated. The test rig measured the frictional forces on a single asperity and the resultant wear that occurred. An analytical model developed by Oxley et al. [20] was used to determine the intrinsic coefficient of friction of the interface at the asperity and the packing rings at the beginning of the

test. The FE material model of exfoliated graphite packing rings developed in the first part of this thesis was used to set up a model of the wedge test rig. The FE model of the wedge test rig was used to determine the evolution of stresses in the compression packing rings during a test. The results of this analysis was used to explain the experimental results.

1.3 Chapter content summary

This thesis is composed of eight chapters:

1. In chapter(1), the reasons for carrying out this body of work are discussed in light of the required improvement in the scientific understanding of valve compression packing behaviour due to environmental concerns and legislative demands regarding reductions in fugitive emissions.
2. In chapter(2), previous compression packing ring research is discussed. Recent experimental testing has proven that packing ring behaviour has non-linear elastoplastic behaviour. Previously developed analytical methods presume that the compression packing ring behaviour is linear elastic over the loading range. These methods are not capable of accurately modelling the behaviour of compression packing rings in a valve. Therefore a non-linear elastoplastic FE analysis of compression packing rings is to be carried out in order to gain a greater scientific understanding of compression packing rings in a valve.

This thesis looks at only one compression packing ring type, this being exfoliated graphite. Exfoliated graphite is relatively homogeneous compared with other packing ring types and represents a good starting point for developing experimental and FE methods for describing general compression packing ring behaviour.

An analytical model developed by Oxley et al. [20] is proposed as a viable model with which to predict the influence of surface roughness on

the friction behaviour of exfoliated graphite packing rings. This model has been adapted to model elastoplastic material but it is not known if this model can be applied to exfoliated graphite. There is very little data available on the friction and wear behaviour of exfoliated graphite therefore an experimental test will have to be designed and built to investigate the influence of surface roughness on the friction and wear behaviour of exfoliated graphite packing rings.

3. In chapter(3), the selection of the FE material model and commercial FE package with which to model exfoliated graphite is discussed. The modified Cam clay material model in ABAQUS/Standard was chosen as the best available FE material model and FE package with which to model exfoliated graphite packing rings.
4. In chapter(4), the experimental test and the data manipulation methods required to determine the input parameters of the FE material model are discussed. The FE model used to validate the FE material model is described as well as the FE model used to investigate the influence of loading, valve stem cycling, valve stem friction and wear on the behaviour of an exfoliated graphite packing.
5. In chapter(5), the results of the experimental tests used to determine the input parameters for the FE material model are detailed. The input parameters for the FE material model are determined through the manipulation of the experimental data. The FE model is validated by comparing experimental results from the compression test rig with FE results from a model of the same test rig. Results of FE analysis carried out on a FE model of an exfoliated graphite packing rings set to investigate the influence of loading, valve stem cycling, valve stem friction and wear are detailed.
6. In chapter(6), the design of the test rig to investigate the influence of surface roughness and environment on the friction and wear behaviour

of compression packing rings is detailed. The experimental results show that the coefficient of friction increases with stroke number. This meant that the Oxley model can only be used to determine the initial intrinsic coefficient of friction at the asperity packing ring interface. It is not possible to determine the stresses and strains in the packing ring set during a wedge test, therefore a FE model of the wedge test rig is set up to determine these variables in order to investigate the increase in coefficient of friction with stroke number. The coefficient of friction at the asperity packing ring interface in the FE model is determined from the Oxley model.

7. In chapter(7), the main results from this thesis are discussed.
8. In chapter(8), the main conclusions of the study are listed and the perspectives for future work are proposed.

Chapter 2

Literature review

2.1 Valves

The valve is essential to virtually all manufacturing processes and every energy production and supply system. Yet it is one of the oldest known to man with a history of thousands of years. As new industries developed, they become major users of valves. Industries such as textiles, wood pulp, chemicals, food processing, pharmaceuticals, and power generation. Later the petroleum industry was born, and with it a demand for higher performance valves that could withstand the great pressures of oil and gas flowing from wells to the surface [21].

Although many different types of valves are used to control the flow of fluids, the basic valve types can be divided into two general groups: stop valves and check valves. Stop valves are used to shut off or, in some cases partially shut off the flow of a fluid. Stop valve are controlled by movement of the valve stem. A check valve normally only allows fluid to flow through it in one direction. This thesis looks at the particular case of the gate valve, which is a type of stop valve in particular the sealing of this type of valve using exfoliated graphite packing rings. An example of a gate valve and the relevant sealing arrangement can be seen in Figure 2.1.

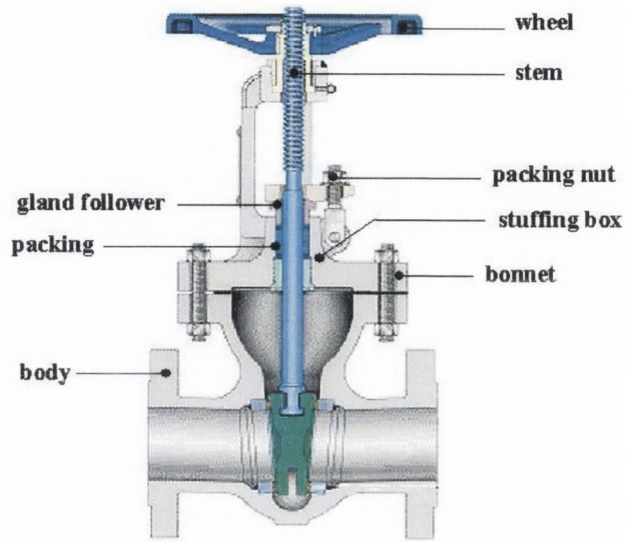


Figure 2.1: A gate valve (Source: [22])

2.2 Valve packing materials

The oldest and still most common method of sealing a stop valve is through the use of a compression packing set. Compression packings are made from various materials in a variety of shapes, sizes and constructions, dependent upon the service requirements. The temperature, pressure, pH and chemical compatibility of the application in which the valve is in service will determine the type of compression packing ring used. The main types of packing materials are natural cellulosic fibres (i.e cotton, jute, flax, ramie, hemp), man made fibres (i.e. acrylic, aramid, PTFE), metals (i.e. foils, wires) and exfoliated graphite [23].

Despite the introduction of more modern sealing technologies, packings continue to be a major choice for users because they are high pressure and temperature resistant, extremely cost-effective, relatively easy to install and maintain.

2.3 Packing behaviour

Packing performance, or the likelihood of packing system leakage, can be affected by many factors including

- Frequency of stem movement
- System pressure and temperature
- Stem and stuffing box finish
- Stuffing box depth and diameter
- Accuracy of stem guidance
- Fluid medium
- Vibration
- Quality of installation
- Packing composition
- Gland pressure

Previous research [24] has shown that packing composition and gland pressure have the greatest impact on packing leakage. These tend to mask all other factors. Many other factors (e.g. fluid medium, system temperature and pressure) are established by system design and are therefore fixed.

Gland pressure, or the loading of a packing ring set, can be applied in two separate ways. The most common method of loading a valve packing set involves compressing a follower against the top of the packing ring set using a series of bolts, thus displacing the packing ring set by a fixed amount.

Packing manufactures recommend the use of live loaded valve packing sets in critical applications. A live loaded system maintains a near constant applied axial stress on the packing ring set. Live-loading provides excellent benefits, especially in systems with frequent pressure or temperature

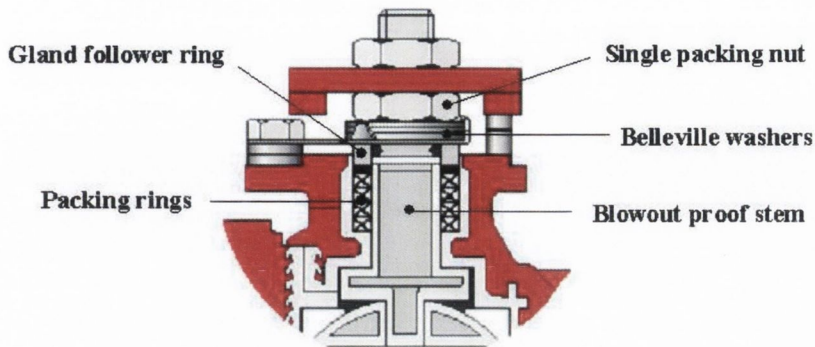


Figure 2.2: An example of a live loaded ball valve (Source: [25])

changes or high-cycle applications. It compensates for pressure and temperature changes and wear. An example of a live loaded ball valve is seen in Figure 2.2. The entire packing system is loaded by a set of Belleville washers to provide a stem seal that is under a near constant applied axial stress. When wear occurs in the packing ring set the spring set elongates resulting in a slight reduction in applied axial stress.

The minimum gland load on the packing to achieve sealing depends upon,

- Packing style and density
- Packing area
- Packing height
- System pressure.

The performance of a packing depends strongly on its fit in the stuffing box. Packing sets that have an interference fit will be difficult to install. However, if the rings are too loose, a high proportion of the gland load will go into deforming the rings rather than being transferred into radial sealing stress.

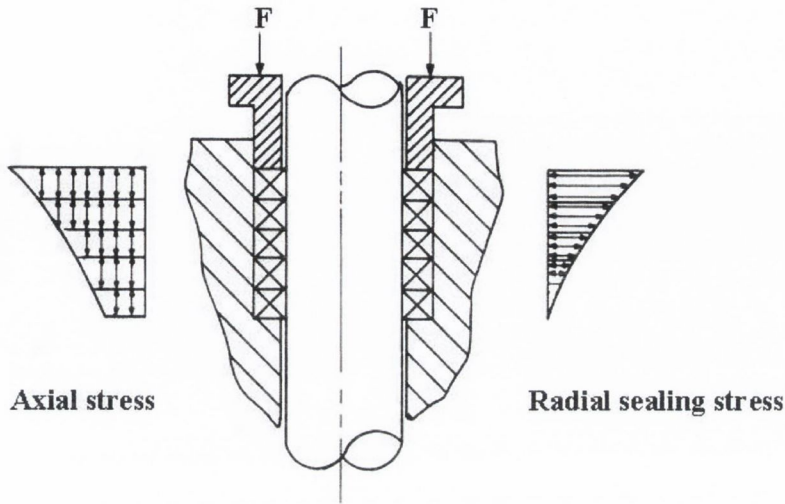


Figure 2.3: Initial axial and radial stress distribution in a compression packing set (Source: [26])

Minimising the gland load will also minimise stem friction and subsequent packing wear. When a load is initially applied to the packing by the gland follower, it creates a compressive stress in the packing height as shown in Figure 2.3. The packing in the stuffing box is subject to two axial forces, the thrust due to the gland follower on one end and to the media pressure from the other. Opposing the free transmission of force along the packing is the frictional drag on both the housing and the shaft due to radial expansion of the packing under axial loading and internal friction between fibres of the packing ring as it is compressed. This in turn causes a non-uniform distribution of axial stress in the packing ring set, and in the radial stress along the length of the packing ring set. Much of the load therefore, is transmitted only to the upper packing rings.

Only a portion of the applied axial stress is transferred into radial sealing stress. The radial sealing stress also decays exponentially through the packing set as shown in Figure 2.3. Threshold sealing occurs at the point where the radial pressure against the stem and the stuffing box exceeds the fluid

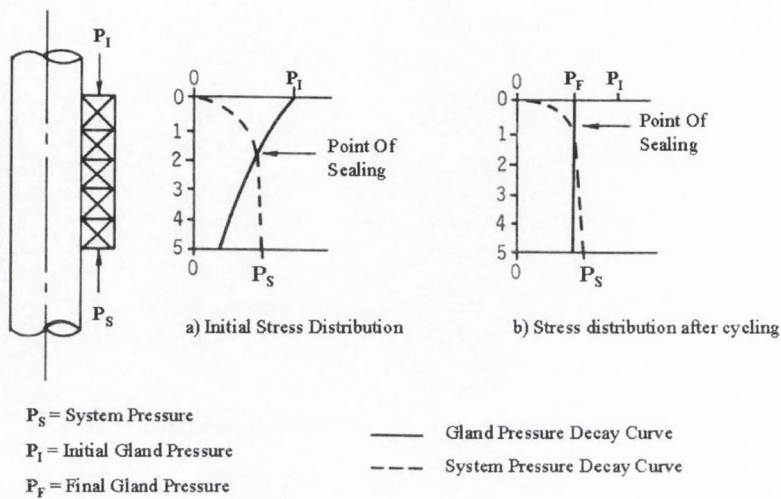


Figure 2.4: The effect of gland pressure on leakage (Source: [26])

pressure in the flow channel [26]. The transmission of axial compressive stress and the subsequent conversion to radial sealing stress depends strongly on packing material and density.

A five ring packing set is illustrated in Figure 2.4. The initial radial packing pressure, P_I , decreases exponentially from the top to the bottom rings. The system pressure, P_S , acts on the bottom rings and decreases upward through the packing. At the point where the initial radial packing pressure, P_I , exceeds the system pressure P_S , threshold sealing occurs. The initial radial stress distribution against the stem develops into a more uniform distribution after a series of valve stem cycles as seen in Figure 2.4b, this phenomenon is called stress shakedown.

2.4 Packing test methods

To date there has been a significant lack of detailed repeatable testing of compression packing rings. Due to the complex behaviour of compression packing rings in a valve and the vast number of variables that influence their behaviour it is highly important that compression packing ring behaviour be investigated experimentally. Test results and data given by packing manufacturers for the behaviour of their compression packings are often questionable and not comparable, because the test methods are unknown or different or not standardised.

In 1958 Turnbull [27] stated there had been no detailed study into the physical properties of packing materials and that the development of any analytical theory into the behaviour of gland packings would rely on the proper characterisation of packing materials. Characterisation of packing material involves detailed material testing, analysis and mathematical modelling to date there has been a serious lack of such analysis.

Harwanko (1980) [28] stated that there was in particular a need for recommendations as to required level of gland follower load which needs to be attained on a valve to be packed with a given gland packing material, to ensure a specified valve packing performance. One such study that was carried out involved a simulated life cycle test programme which was carried out by EPRI (1988) [26]. Testing conducted during this program determined that the maximum initial gland load for die formed graphite packings should be $1.75 \times \text{system pressure} \times \text{packing area}$. This is a very general formula however, which does not take into account the effect of different densities of graphite rings on the required gland load.

One of the most significant developments in valve packing testing occurred at the State Materials Testing Institute (MPA), in the University of Stuttgart [12]. Four state of the art packing test rigs have been developed to determine the deformation, relaxation, friction and tightness behaviour of the compression packing rings.

2.5 Analytical models

Various analytical models have been developed since the middle of the 20th century to predict the decay in axial and radial stress through a packing ring set of length, l and the force required to cycle the valve stem under operational conditions. In 1958 Thomson [29] published a paper which attempted to analyse the fundamentals of gland packing behaviour. The problem he was attempting to solve is a complex one, but in the absence of any existing analysis even an approximate theory was going to represent a useful step forward. At a discussion into Professor Thomson's paper at the Institution of Mechanical Engineers, London in the same year, D.F. Denny [30] remarked that "Professor's Thomson's paper was of a different character and contained opinions that many people might find controversial but one thing was clear that it underlined the fact that packed glands had been used for at least 100 years, but no one understood fully how they worked".

The approximate theory developed by Thomson [29] was a useful basis for design, for the correlation of service data and as a means along which further research might proceed. Due to the complexity of the problem of valve sealing, certain simplifying assumptions were made. Discrepancies between calculated and observed values were evident.

Denny and Turnbull [9] presented many experimental data mainly obtained from special tests, and it is a measure of the complexity of the problem that they were unable to proceed logically step by step from the data to final conclusion. They analysed the behaviour of packing rings in a stuffing box before any shaft movement had taken place and before fluid pressure is applied. They found that when the gland force is applied to the top of the packing ring set the friction of the packing against the walls prevents the transmission of the full force to the bottom of the box. Thus the axial stress in the packing decays along the length of the packing ring set. They showed theoretically that the decay is exponential in form under certain conditions and can be described by Equation 2.1.

$$\frac{P_{AX}}{P_G} = e^{-(\mu_1 + \mu_2)K_{rad} \cdot \frac{l}{t}} \quad (2.1)$$

where P_{AX} is the axial stress in the packing ring set at a distance l from the top of the packing ring set, P_G is the applied gland pressure, K_{rad} the ratio of radial stress to axial stress, μ_1 is the coefficient of friction between the packing and housing, μ_2 is the coefficient of friction between the packing and the stem and t is the thickness of the packing. It can be seen that the relation between P and l is exponential only so long as $(\mu_1 + \mu_2)K$ is constant.

This relatively simple exponential law for the distribution of axial pressure along a soft packing was found to be valid provided the pressure in the packing does not fall below a certain critical value. Denny and Turnbull found that if the axial pressure does fall below this critical value a more complex analysis must be used.

In 1989 Salter [11] developed Equation 2.2 which predicts the radial sealing stress along a packing ring set of length l .

$$\sigma_2 = K_{rad}P_G[-4K_{rad}[\frac{\mu_1 + \mu_2(d_O/d_i)}{(d_O/d_i)^2 - 1}(\frac{l}{d_i})]] \quad (2.2)$$

where σ_2 is the radial stress against the stem, P_G is the applied gland pressure, K_{rad} the ratio of axial stress to radial stress, μ_1 is the coefficient of friction between the packing and housing, μ_2 is the coefficient of friction between the packing and the stem. The parameters d_i and d_0 represent the inner and outer diameters of the packing ring respectively.

Equations 2.1 and 2.2 presume that the material properties are linear elastic in nature and that K_{rad} is constant over the loading range. Klenk [12] proved experimentally that these two assumptions can not be made for a wide variety of packing materials. He found that packing ring material behaviour was elastoplastic and that K_{rad} varied over the loading range.

Several researchers have also tried to develop analytical models to predict the force required to cycle a valve stem under operational conditions. The importance of this variable cannot be over estimated. If the force required to cycle the valve stem exceeds the manual capabilities of the operator or the

power of the actuator, it will become impossible to open and close the valve successfully. This problem could have potentially dangerous and costly consequences for an industrial site. An analytical model to predict the frictional stem force F_s is given by the following analytical relation [9, 29, 31, 32].

$$F_S = F_G \frac{r_i}{r_o + r_i} [1 - \exp(\frac{-2\mu_1 K_{rad} l}{r_o - r_i})] \quad (2.3)$$

To be able to determine the friction stem force, the following variables must be known: the geometrical dimensions of the packing (outer and inner radius, r_o and r_i and the length l of the packing ring set in the compressed state), the packing characteristics (friction coefficient, μ_1 between the packing ring set inner diameter and the stem; radial stress conversion factor, K_{rad}); the axial stress on the upper packing ring (σ_{ax}), and the gland load F_G , which is given by

$$F_G = \pi(r_o^2 - r_i^2)\sigma_{ax} \quad (2.4)$$

Equation 2.3 was developed by Thomson by means of an integration of the axial force over the packing length, resulting in an exponential decrease in the axial stress from the gland follower to the stuffing box bottom due to friction. A second integration leads to the frictional stem force. During both integrations it is assumed that the coefficient of friction does depend on axial stress. Klenk [12] proved experimentally that this is incorrect. He demonstrated that Thomson's formula underestimates the frictional stem force.

Klenk devised a new formula, seen in Equation 2.5 to predict the frictional stem force and verified the formula by means of extensive experimental investigation on a variety of different packing ring types of different lengths.

$$F_s = \mu_1 \cdot \pi \cdot d_s \cdot l \cdot K_{rad} \cdot \sigma_B \quad (2.5)$$

where F_s is the frictional stem force, d_s is the diameter of the stem, l is the length of the packing in its compressed state, K_{rad} is the ratio of radial stress to axial stress and σ_B is the applied axial stress at the follower.

2.6 Friction and wear based on surface roughness

The purpose of research in tribology is understandingly the minimisation and elimination of losses resulting from friction and wear at all levels of technology where rubbing surfaces are involved. Solid surfaces, irrespective of the method of formation, are rough on a microscale [33]. A solid surface, or more exactly a solid-gas or solid-liquid interface, has a complex structure and complex properties dependent upon the nature of solids, the method of surface preparation and the interaction between the surface and the environment.

This is particularly the case for valve stem friction and wear. Friction and wear at the valve stem packing interface is a complex phenomenon which is not fully understood. The nature of the valve stem finish, the material properties of the packing rings and the atmosphere all play an important role in determining the resultant frictional forces and wear when the valve stem is cycled.

Standard valve stem friction testing involves investigating the valve stem friction on a conventional/macroscopic scale. In macrotribology, tests are carried out on components with relatively large mass under heavily loaded conditions. It is impossible to measure the radial stress, so the friction coefficient must be inferred from the stem force. In these tests wear is inevitable and the bulk properties of mating surfaces dominate the tribological performance. Microtribological studies are needed to develop a fundamental understanding of friction and wear mechanisms that occur at the valve packing interface. A tangential force equal to the friction force, is required to initiate and maintain repeated sliding which will result in the formation of wear particles and eventual interface failure [34, 35, 33].

2.6.1 Boundary lubrication

The friction behaviour at the stem packing interface is one of either dry or boundary lubrication, the least understood of the lubrications regimes.

Loads and speeds are such that there is no conventional hydrodynamic or elastohydrodynamic film separating the rubbing surfaces. No generally accepted model of boundary lubrication has been developed to date and the analysis of boundary lubrication regimes is still based on practical experience and observation.

Practical engineering experience shows that the texture of rubbing surfaces plays an important role in the forces that develop between the rubbing surface. Surface texture is the repetitive or random deviation from the nominal surface that forms the three dimensional topography of the surface. Surface texture includes (1) roughness, (2) waviness, (3) lay and (4) flaws. Figure 2.5 shows an example of surface texture with unidirectional lay [36].

Different manufacturing processes produce differences in surface texture. Turning produces surfaces which have a lay: the asperities are long and aligned in the direction of tool travel. Ground and polished surfaces have roughness which is uniform in circumference and transverse direction [38]. There are the processes commonly used to finish valve stems. Turning and grinding will give a lay roughly perpendicular to the motion of the stem. Polishing will give an isotropic surface, but due to its expense it is seldom used.

Surface roughness most commonly refers to the variations in the height of the surface relative to a reference plane. It is usually defined by one of the statistical height descriptor advocated by ISO (International Standards Organisation). These are R_a (center line average) and R_q (rms). For the complete characterisation of a surface profile the parameters R_a and R_q are not sufficient. These parameters are seen to be primarily concerned with the relative departure in the vertical direction only. They do not provide any information about the slopes, shapes and sizes of the asperities or frequency or regularity of their occurrences. It is possible for surfaces of widely differing profiles with different frequencies and different shapes to give the same R_a or R_q values [36]. Another problem with most real surfaces is that the broad based asperities which tend to possess low slopes, tend to dominate the numerical height characteristics and consequently dominate the numeri-

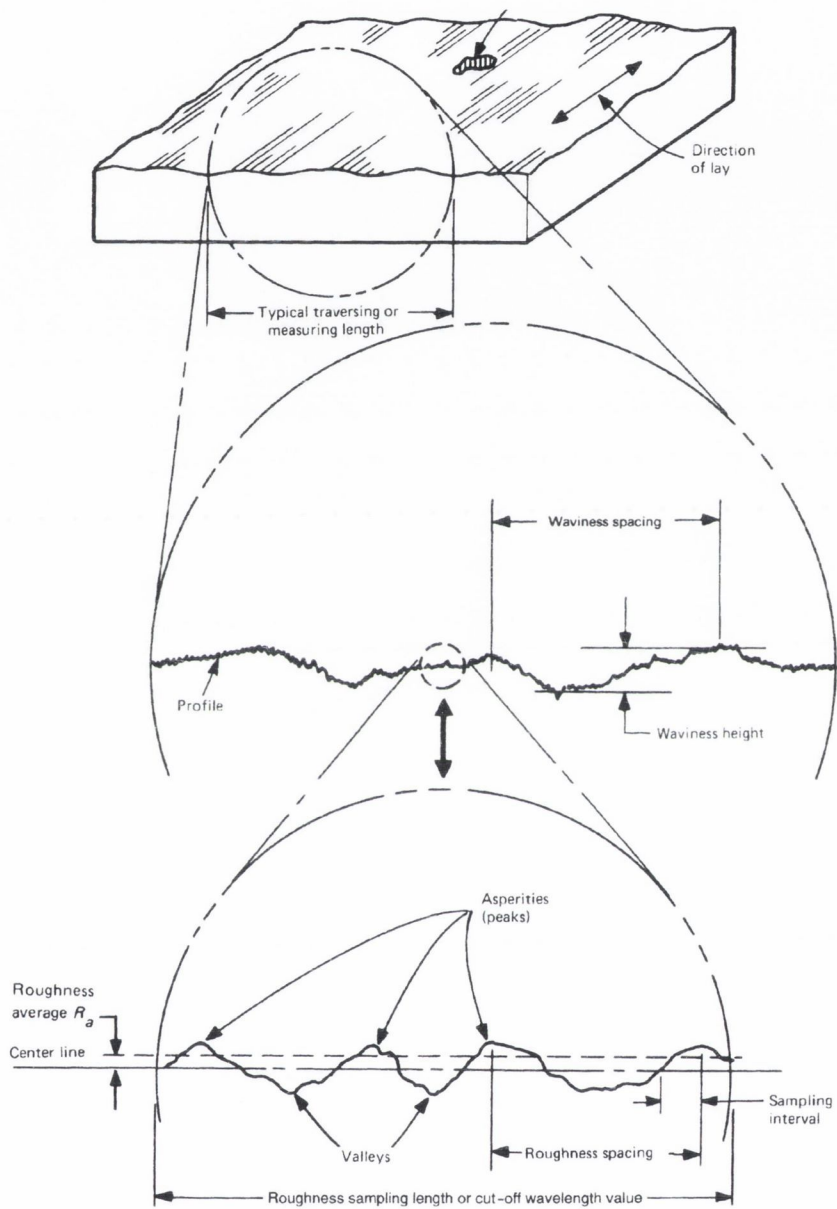


Figure 2.5: Surface texture (Source: [37])

cal values of R_a and R_q [39].

Early theories of boundary friction developed by Bowden and Tabor [34, 35] explained Amonton's law (see Equation 2.8) in terms of plastically yielding asperity contacts, and related the coefficient of friction, μ to the interfacial shear strength f of the real contact area. This gives a good explanation of the magnitude of μ in many contacts, but takes no account of the texture of the rubbing surfaces, which practical engineering experience shows to be important.

Work by Kapoor and Johnson [38] on conformal contacts has shown that even at low loads surface roughness plays an important role in subjecting a thin layer to severe contact stresses. Contact pressure at asperity (roughness peaks) were found to be much higher than the nominal (average) pressure. Although there are few such contacts, repeated sliding ensures that ultimately these high contact pressures transverse the entire surface, subjecting it to severe contact stresses and plastic flow [40]. It is these asperity contacts which cause the plastic flow, and the depth of the plastically deformed layer relates to their dimension rather than the dimension of the nominal contact area.

There is very little literature available on the frictional behaviour of graphite. There is however a significant amount of literature available on the frictional behaviour of a harder surface sliding against a softer surface. The influence of asperity slope on the friction behaviour of a material can be investigated using single asperity models. In recent years, several workers have published single asperity models which can predict friction based on surface roughness [16, 17, 18, 19]. These models assume that an asperity contact can be represented as a hard wedge which slides over a soft perfectly plastic surface, pushing a plastic wave ahead of it. Slip line fields can then be developed to predict the stress and strain in the softer material due to the passage of the hard asperity. An example is shown in Figure 2.6.

The stress and strain depends on the interfacial shear strength ratio (f), used in Bowden and Tabor's theory and the angle that the hard wedge makes

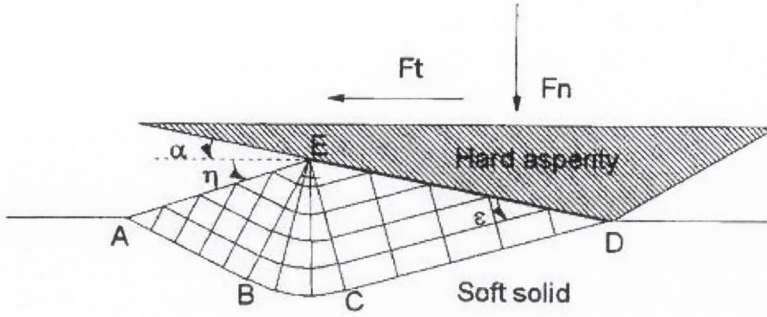


Figure 2.6: Slip line field model of asperity interaction (Source: [16])

with the soft surface. If a real hard surface can be represented as an array of such asperities, then its friction can be calculated successfully from its slope distribution, a surface texture parameter, and f a lubrication parameter [41, 42, 43].

When the soft solid material shows rigid plastic behaviour, the force per unit width of the wedge can be determined and used to find μ , the coefficient of friction.

$$F_t = [A \sin \alpha + \cos(2\epsilon - \alpha)] EDk_s \quad (2.6)$$

$$F_n = [A \cos \alpha + \sin(2\epsilon - \alpha)] EDk_s \quad (2.7)$$

$$\mu = \frac{F_t}{F_n} \quad (2.8)$$

where $A = 1 + \pi/2 + 2\epsilon - 2\eta - 2\alpha$, k_s = shear strength of the soft material, $2\epsilon = \arccos(f)$, $f = \tau/k$, τ being the shear strength of ED.

Provided the asperity contacts are mainly plastic, the above model gives a reasonable account of the effects of changing surface texture on μ in single asperity tests [17] and for real surfaces [41, 42, 43, 44]. The main conclusions are that μ should fall with surface slope, and interfacial shear strength.

Bowden and Tabor [34, 35] considered that the shear strength of the interface arose from the defects in the boundary film covering the contacting surfaces, leading to local micro-welds at the gaps in the film. The value of f was taken to be the fraction of the contact not covered by the boundary film. This implies that the shear strength of the boundary film itself can be ignored. However, Briscoe and Evans [45] showed that boundary films do have a measurable shear strength, τ_f , given by

$$\tau_f = p\mu_0 + \tau_0 \quad (2.9)$$

where p is the pressure of the film. The intrinsic shear strength of the interface, τ_0 can generally be ignored, in which case, as shown by Black et al. [20], the model of Figure 2.6 leads to a simple expression for μ :

$$\mu = \tan(\tan^{-1}\mu_0 + \alpha) \quad (2.10)$$

Again, friction falls to zero as asperity slope and film strength fall. Equation 2.10 is found by resolving the forces on the front face of the wedge if no elastic recovery occurs behind the wedge. The forces on the wedge assuming no elastic recovery behind the wedge are shown in Figure 2.7.

There is experimental evidence that friction coefficients may actually rise if boundary lubricated surfaces becomes too smooth. For instance, Hirst and his co-workers[46, 47] showed how steel surfaces lubricated with stearic acid and rubbed in a Bowden-Leden machine could give extremely high values of friction when both surfaces were prepared so as to have very low asperity slopes. Whilst all this work has proved useful in understanding the friction of metals, caution will be needed in applying it to graphite whose mechanical properties are much more complex.

Exfoliated graphite does not exhibit perfect plastic behaviour. For elastic-plastic contact analysis, the analytical equations are very complex and most numerical techniques are laborious. These problems can potentially be overcome by using finite element analysis [33].

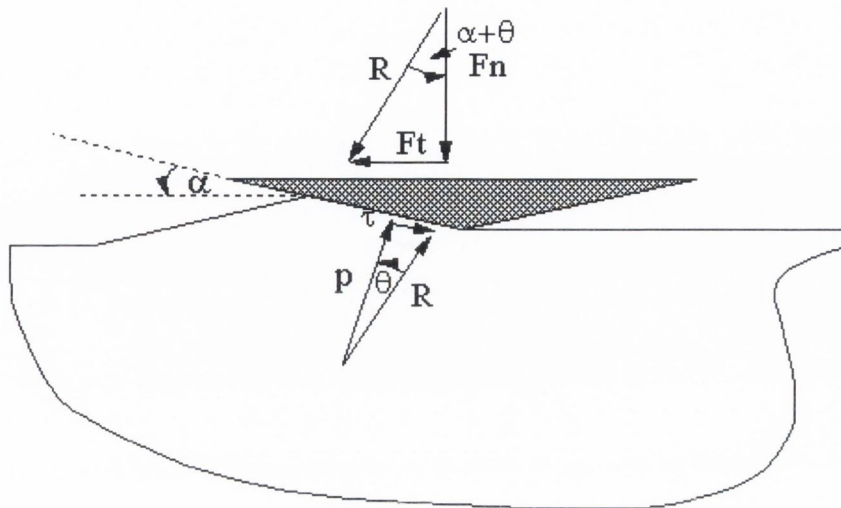


Figure 2.7: Forces on a wedge which experiences no elastic recovery behind the wedge

2.6.2 Real surfaces

The data obtained from single asperity analysis maybe used to model real surfaces. Multiple asperity contact, or real surfaces, have been modelled using mainly statistical methods [48]. This is due to the complex nature of most real surface profiles. Greenwood and Williamson [49] were perhaps the first to develop a comprehensive model which could theoretically examine interfacial conditions based on multiple asperity contacts. Their model is based on a density of asperities of constant slope whose height distribution has a Gaussian distribution. In recent years, research has been carried out using finite difference numerical methods to analysis contact analysis of real surfaces [50]. This techniques allows for a digital numerical record of a real surface to be subjected to contact. The principle advantage of this model is that results do not depend upon asperity models or statistical models of the surface. This model, however, assumes that the materials are elastic/perfectly plastic with conservation of volume [39].

2.6.3 Wear analysis

Wear is the surface damage or removal of material from one or both surfaces in sliding, rolling or impact motion relative to one another. Wear occurs as a result of the material, geometrical and topographical characteristics of the surfaces, and the overall conditions under which the surfaces are made to slide against each other e.g. loading, temperature, atmosphere, type of contact etc. In most cases wear occurs through surface interactions at asperities. Wear is not a material parameter but a unique characteristic of the system being measured. It is a characteristic feature of the wear process that the amount of material removed is small. Wear in sliding is usually a very slow process that is very steady and continuous [33].

Wear occurs by mechanical and/or chemical means. These include the following six principals; each show quite distinct phenomena that only have one thing in common: the removal of solid material from rubbing surfaces. These are : (1) adhesive, (2) abrasive, (3) fatigue, (4) impact by erosion and percussion, (5) chemical and (6) electric arc induced [51, 33]. Over long sliding distances either one mechanism or a series of mechanisms cause the continuous removal of material from the mating surfaces.

Wear occurs at the valve stem interface as a result of valve stem cycling. The majority of the wear occurs on the packing ring set inner diameter. Excessive wear has severe consequences for valve stem sealing. As wear occurs at the packing ring set inner diameter the radial sealing stress against the stem decreases. If the radial sealing stress falls below a critical value leakage will occur unless the valve packing set is live loaded. The vast majority of valve packing sets are not live loaded therefore if a significant amount of wear occurs in the packing ring set an unacceptable amount of leakage will occur. It is invaluable to be able to calculate the wear rate of packing sets and to determine the allowable wear before leakage.

Wear in general is evaluated by the amount of volume lost and the state of the wear surface. The degree of wear is described by the wear rate, specific wear rate or wear coefficient [52]. The wear coefficient may be determined

by using Archard's law [53]. Archard's law is detailed in Equation 2.11.

$$V = KF_s \quad (2.11)$$

where V is the wear volume, K is the wear coefficient, F is the normal force and s is the distance slid.

The wear volume V , depends on the forces at the wear surface interface. In the case of valve packing wear this is the radial stress against the stem. This variable is hard to determine using standard valve test methods. To determine the wear that occurs in a given system it is necessary to carry out a series of tests to determine the influence of the material, geometrical and topographical characteristics of the surfaces, and the overall conditions under which the surfaces are made to slide against each other e.g. loading, temperature, atmosphere, type of contact etc.

Wear tests can be carried out in an endless number of ways as the outcome of the test strongly depend not only on the characteristics of the rubbing materials, but also on the whole mechanical system and its environment. In order to determine the influence of surface roughness on the wear behaviour of valve packing rings it is necessary to carry out fundamental testing of the wear behaviour of valve packing rings.

2.7 Exfoliated graphite packing rings

The packing ring type under investigation in this thesis is exfoliated graphite, so chosen because their material properties do not vary considerably from one manufacturer to another. They are also one of the more homogeneous packing ring types and represent a good starting point for developing experimental and analytical methods to describe general packing ring behaviour.

Exfoliated graphite packing rings are in use in critical applications, such as nuclear power plants and oil refineries, where leakage poses serious environmental, safety and health risks. Field experience with graphite packings has generally been very encouraging. However less than complete understand-

ing of their characteristics and incorrect application has at times created problems.

Since the 1980's nuclear power plants (and other critical applications) have been selectively replacing asbestos packing rings with graphite packing rings. They have reported significant reductions in valve stem leakage. Test results and experience of the last few years with stuffing boxes packed with exfoliated graphite have shown that this material gave a tighter sealing and longer periods of leak free operation than were obtained with asbestos based packings [26].

The decline in the use of asbestos was aided by reductions in the cost of graphite and by the major packing manufactures ceasing the production of asbestos due to health and safety concerns. Liability associated with the use of asbestos based products persuaded many manufacturers of asbestos packing to withdraw their products in the 1980's. On January 23, 1986 the US Environmental Protection Agency (EPA) proposed a plan involving immediate prohibition of the use of asbestos in certain products and the phasing out of domestic mining and importation of asbestos over a ten year period. In 1991 the EU banned five of the six forms of asbestos. All forms of asbestos will be banned in the EU by 2005.

2.7.1 Exfoliated graphite foil

Exfoliated graphite packing rings are manufactured from exfoliated graphite foil. The raw material used in the production of exfoliated graphite foil is natural graphite flake with a well orientated crystalline structures shown in Figure 2.8a. Graphite intercalation compounds as seen in Figure 2.8b are produced from the natural graphite flakes [54]. The thermal deposition of these compounds leads to the formation of expanded flakes (worms), which are compressed into foils without binder or filler shown in Figure 2.8c.

The resulting alignment of the graphite particles and their planar structures produces a high degree of directional dependency (anisotropy) in the properties. The high purity of exfoliated graphite is derived from the raw

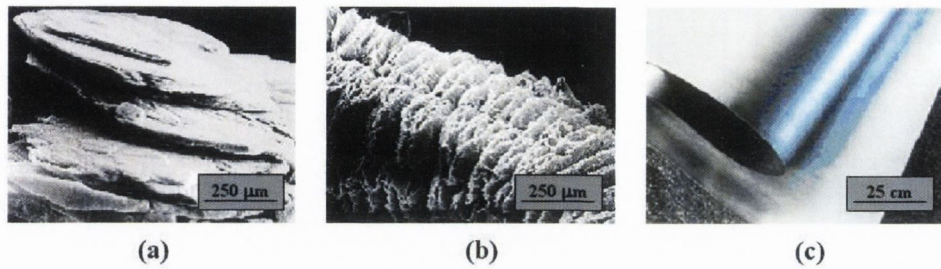


Figure 2.8: (a) Graphite flake, (b) Graphite intercalations, (c) Graphite foil (Source: [55])

materials used, as well as from the quality of the mechanical, chemical and thermal purification processes [55].

Exfoliated graphite has many inherent properties that make it a very effective material in sealing applications [26].

- It exhibits a high resistance to inorganic and organic acids, alkalis, solvents, hot waxes and oils in addition to being compatible with main services such as steam, air and water. It is particularly suitable for heat transfer media, demineralised water, all petroleum products and steam at high pressures and temperatures
- It can be used up to $2500^{\circ}C$ in non-oxidising environments
- Minimum corrosion on metallic flanges due to low chloride content

2.7.2 Manufacturing exfoliated graphite packing rings

Exfoliated graphite products for valve stem packings can be supplied in three different forms. They include:

- Ribbon tape
- Laminated rings

- Die formed rings

The advantages and disadvantages of each product are discussed below. Ribbon tape was one of the early exfoliated graphite products offered for valve stem and pump packing applications [56]. With the flexible ribbon tape, each packing ring is formed in place in the stuffing box. The ribbon is first cut to a specific length determined by a formula for the stuffing box in question. It is then wrapped around the stem, compressed by the gland follower and pushed into the stuffing box to form a solid endless ring. This process is repeated until the required number of rings have been formed.

The main advantage of the ribbon tape is versatility. Plants need only stock a small range of ribbon widths to satisfy most of their valve and pump applications. The time required for installation and the difficulty of producing consistent quality rings are significant disadvantages. High quality rings require the correct number of wraps and uniform forming pressure. Differences in the skill level of the installer and the constraints of field conditions frequently result in installations of inconsistent quality and reliability. The time required to form each individual ring in the stuffing box makes it an expensive approach.

Laminated rings were the original exfoliated graphite product used for valve stem packings [7]. The manufacturing process involved cutting rings out of cured laminated sheet that has been predensified to $1.1g/cm^3$. The rings are cut to exact dimensions, which provide a slight interference fit with both the stem and stuffing box. It is recommended that laminated rings should not be split for installation but rather installed over the top of the valve stem. The claimed advantages of laminated rings is that they are diametrically stable and tend to experience less wear due to the lateral orientation of the graphite planes. The most common applications of laminated rings are on control valves.

The disadvantage of laminated packing rings is the extremely accurate fit required to provide good sealing. Although the rings are manufactured to a relatively low density, they do not readily expand to form a seal since



Figure 2.9: Die formed graphite ring after compression (Source: [26])

the orientation of the lateral planes of the graphite tends to prevent radial expansion. The packing has to be compliant so that it overcomes any relatively small imperfections (pits) in the valve. Very accurate stem and stuffing box dimensions are required for ring fabrication making installation difficult. The lack of versatility coupled with installation difficulty has limited the use of laminated rings.

Packing rings die-formed from flexible graphite tape have become the preferred graphite packing product. They are manufactured to precise size and density producing a consistent quality and reliable sealing performance. Die formed rings are manufactured by wrapping exact lengths of flexible graphite tape around a mandrel. The ring is formed with a die and press, collapsing the graphite tape into a tightly locked chevron configuration as shown in Figure 2.9.

The chevron pattern

- Improves the transfer of axial gland load into radial sealing forces
- Provides a tortuous path for leakage
- Improves bonding of the ribbon laminations, producing good ring integrity

The final product is a solid ring. It can be bias cut (at 45°) to allow it to be twisted around the valve stem for installation in the stuffing box.

Exfoliated graphite packing rings are manufactured in a variety of different densities. The choice of packing ring density of a die-formed graphite ring for a particular application is a compromise. It must have a certain amount of flexibility while being sufficiently dense to produce good integrity and minimum consolidation. Low density rings will undergo high initial consolidation but will achieve sealing at fairly low gland pressures. They will, however, undergo large amounts of in-service consolidation leading to poor long term reliability. Higher density rings will exhibit less consolidation. There is a limit, however. If the amount of pressure required by the die forming process exceeds the expected gland pressure, the ring will not deform sufficiently to seal against the valve stem.

A series of compression packings are installed in a valve as a set. An exfoliated graphite packing ring set can be used by itself, but at higher pressures or bigger clearances in the stuffing box braided end rings must be used. Three die formed rings and two braided end rings is the standard packing set arrangement recommended for square sectioned packings [26].

2.7.3 Previous graphite testing

There has been relatively little documented testing of the bulk material properties of exfoliated graphite. Bouvard et al. [57] presented results on the mechanical properties of graphite powder under conditions of large deformation, utilising both isotropic and triaxial states of stress.

The initial density of the poured graphite powder tested was 0.5 g/cm^3 . The variation in axial stress σ_z for the direct shear box and the mean stress $p = (\sigma_x + \sigma_y + \sigma_z)/3$ for the true triaxial test rig is in the range of 0-5 MPa. The initial density of the graphite powder and the stress range used by Bouvard et al. to carry out experimental testing is much lower than that used when testing exfoliated graphite in this thesis.

The compression behaviour of the graphite powder from triaxial and die compression testing can be seen in Figure 2.10. The compression behaviour of graphite powder shows non-linear elasto-plastic behaviour. Before failure

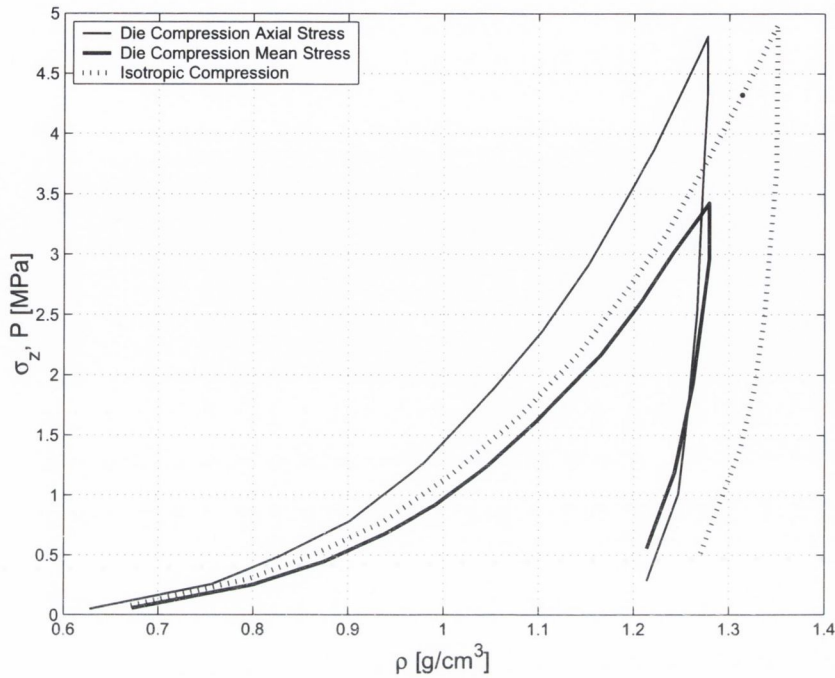


Figure 2.10: Experimental test data obtained by Bouvard et al. [57] on the testing of graphite powder

the graphite powder was seen to dilate. They also found that the failure strength of graphite powder can be correctly represented using the Mohr Coulomb failure criterion, a geotechnical failure criterion which is detailed in Section 3.3.5.

2.7.4 Frictional properties of graphite

Several materials with lamellar structures exhibit low values of friction under certain conditions, and are therefore of interest as solid lubricants. Foremost among these materials is graphite (an allotrope of carbon); its structure is shown in Figure 2.11 [51].

Bonding between the atoms within the layers of the structure is covalent and strong, while the bonding between the layers is considerably weaker.

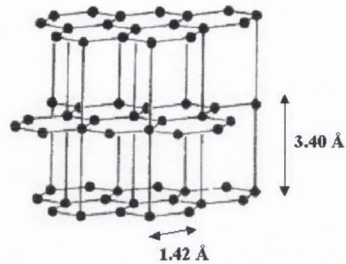


Figure 2.11: Atomic structure of graphite (Source: [51])

In the graphite the interplanar bonding is from Van Der Waals forces, with a weak covalent bond contribution resulting from the interaction between the p-electron orbitals of the carbon atoms. The interplanar bond energy is about one tenth to one hundredth of that between atoms within the layers. A graphite crystal is strongly anisotropic in its mechanical behaviour and physical properties: in particular it is much less resistant to shear deformation in the basal plane (i.e. parallel to the atomic planes) than in other directions.

The low friction characteristic of graphite is associated with its lamellar structure and weak interplanar bonding, but by no means do all compounds with similar structures show low friction, and the low friction values cannot therefore be ascribed to these factors alone. Indeed, even with graphite, only when there are chemical species present which adsorb on exposed surfaces does a low friction condition result.

The sliding friction of graphite against itself or other materials in air is low; typically, $\mu \approx 0.1$. If the surface of graphite is examined by electron diffraction after sliding, it is found that the basal planes have become orientated nearly parallel to the plane of the interface, with a misalignment of order of 5° . The friction of the graphite depends strongly on the nature of the ambient atmosphere. In vacuum or in dry nitrogen, μ is typically ten times greater than in air, and graphite under these conditions wears very rapidly. Controlled addition of gases and vapours reveals that the low friction and

wear of graphite depends on the presence of oxygen, water vapour, or other condensable vapours [51].

2.8 Summary

Compression packing rings are made from various materials in a variety of shapes, sizes and constructions. Their behaviour in the valve depends on the applied axial stress, the system pressure, the material properties of the packing ring material and the friction between the packing ring set and the stuffing box walls.

Various analytical models have been developed since the 1950's to predict the decay in axial and radial stress through a packing ring set of length, l and the force required to cycle the valve stem under operational conditions. These analytical models have assumed that the packing ring material properties are linear elastic, and that K_{rad} is constant over the loading range. Klenk [12] proved experimentally that a wide range of packing ring materials display highly non-linear elastoplastic behaviour and that K_{rad} is not constant over the loading range.

It is extremely difficult if not impossible to describe the behaviour of compression packing rings in a valve using analytical models. This is due to the non-linear elastoplastic material behaviour of the packing rings and complex boundary conditions that the packings rings are subjected to in a valve. Due to the complexity of the problem, the FE method is to be used to investigate the behaviour of compression packing rings in a valve.

The packing ring material under investigation in this thesis is exfoliated graphite. Exfoliated graphite packing rings are porous and show non-linear elastoplastic compression behaviour [12]. Due to the lack of material data available for exfoliated graphite, a complete series of tests must be carried out to characterise its behaviour. This test data will allow for a more informed decision to be made as to the best available constitutive material model to describe exfoliated graphite. The FE model will be used to determine the

influence of applied axial stress, stuffing box friction, valve stem cycling and packing ring wear on the behaviour of exfoliated graphite packing ring set.

Friction and wear at the valve stem packing interface is a complex phenomenon which is not fully understood. The friction behaviour at the stem packing interface is one of either dry or boundary lubrication. Practical engineering experience has shown that surface texture plays an important role in the frictional forces that develop between two rubbing surfaces. A single asperity test rig was developed and built to investigate the influence of asperity slope on the friction and wear behaviour of compression packing rings. The FE material model developed in the first part of this thesis was used to investigate the evolution of stresses in the packing ring set during a test. This will improve the fundamental understanding of the mechanisms that occur at the asperity packing interface.

2.8.1 Project plan

- Carry out material testing to determine the compression and failure behaviour of exfoliated graphite
- Determine the best available FE package with which to model exfoliated graphite packing rings
- Develop a constitutive material model which will accurately model the behaviour exfoliated graphite
- Investigate the influence of loading, stuffing box friction and valve stem cycling on an exfoliated graphite packing ring set using FE analysis
- Design and build a single asperity tribotest to investigate the influence of asperity slope on the friction and wear behaviour of compression packing rings
- Complete a series of tests to investigate the influence of asperity slope on the friction and wear behaviour of compression packing rings

- Implement a FE model of the tribotest to investigate the evolution of stresses, and the subsequent failure of the packing asperity interface

Chapter 3

Constitutive material model

3.1 Selection of a commercial FE package

Constitutive material modelling is implemented in this thesis for exfoliated graphite packing rings. Exfoliated graphite packing rings were chosen because their mechanical properties do not differ significantly from one manufacturer to another. They are also one of the more homogeneous packing ring types and represent a good starting point for developing experimental and Finite Element (FE) methods to describe general compression packing behaviour. A wide range of exfoliated graphite packing rings are used in practice. The most widely used density is 1.5 g/cm^3 exfoliated graphite. Constitutive material modelling is implemented in this thesis exclusively for 1.5 g/cm^3 exfoliated graphite purely due to time constraints.

There is a limited amount of experimental data available on the behaviour of exfoliated graphite. This meant that detailed experimental testing had to be carried out to determine the compression, yield and failure behaviour of 1.5 g/cm^3 exfoliated graphite. Details of the test methods used to characterise the behaviour of exfoliated graphite packing rings are presented in Chapter 4. Tests were carried out in a simulated valve and in a high pressure triaxial test rig. The results of this analysis are presented in Chapter 5. Exfoliated graphite packing rings are porous in nature and exhibit non-linear

elastoplastic compression behaviour [12]. The test results show that the compression behaviour can be approximated by the idealised clay compression model, shown in Figure 3.5. Exfoliated graphite is seen to yield according to pressure dependent yield criterion, i.e. the material becomes stronger as it yields. This behaviour is seen in soils, i.e. clayey and sandy type materials. The failure of exfoliated graphite was found to be slightly more complex, five of the 6 high pressure triaxial tests were found to fail according to the linear Mohr Coulomb failure criterion. A sixth sample was seen to fail in critical state. These are two separate failure criteria which describe the failure of geotechnical materials. These two failure criteria are detailed later in this chapter.

Experimental testing established that exfoliated graphite would be best modelled using a geotechnical material model, i.e. a soil material model. While the finite element method has been used in many fields of engineering practice for over 30 years, it is only relatively recently that it has begun to be widely used for analysing geotechnical problems [58, 59]. This is because there are many complex issues which are specific to geotechnical engineering which have only been resolved in recent years [60].

Due to the complexity of real soil behaviour, a single constitutive model that describes all facets of behaviour, with a reasonable number of input parameters that can readily be determined from simple laboratory tests does not exist. An ideal soil model describes the soil behaviour correctly and uses only a few parameters. Between these two demands, which are in fact conflicting, an optimum has to be found [58].

The decision was made at the beginning of this body of research to use a commercially available FE package. This would mean that the techniques developed in this thesis could be used by any valve packing manufacturer to investigate the behaviour of their compression rings. Only certain FE packages have geotechnical FE material models available in their code. The chosen FE package must have the following basic requirements,

- A geotechnical material model that will model the compression, yield

and failure behaviour of exfoliated graphite

- The ability to model friction at the packing stuffing box interface
- The ability to model valve stem cycling

Initially a decision was made as to the best available commercial FE package and constitutive material model. This was the modified Mohr Coulomb material model in DIANA [61]. DIANA is a commercial FE package developed by TNO Building and Construction Research, in Delft, Netherlands. DIANA has very advanced geotechnical constitutive models implemented in its code. The modified Mohr Coulomb material model allows for the modelling of non-linear elastoplastic compression, strength in tension and Mohr Coulomb failure. However convergence problems were encountered while trying to model contact friction. Following discussions with the developers of DIANA it was concluded that at the time of writing it was not possible to include contact friction at the packing set stuffing box interface using DIANA. Contact friction plays a significant role in influencing the compression and valve stem cycling behaviour of packing rings in a valve and therefore cannot be omitted.

The modified Cam clay material model in ABAQUS/Standard was chosen as the best available alternative. ABAQUS/Standard [62] is a commercial FE package developed by ABAQUS Inc. in Rhode Island. ABAQUS/Standard has geotechnical constitutive material models available in its code. They are not as advanced as the material models available in DIANA but its contact modelling capabilities are vastly superior to those of DIANA. The modified Cam clay material model has the ability to model non-linear elastoplastic compression behaviour, it has no strength in tension and its failure is governed by critical state theory.

This chapter details the theoretical background to the modified Mohr Coulomb material model and the modified Cam clay material model. This is followed by a detailed description of the data manipulation required to

obtain the input parameters for the two material models from the tests data already obtained for this thesis.

3.2 Elasto-plastic modelling

The behaviour of most geological materials have been found to depend on the applied hydrostatic stress [63]. Geotechnical materials are stress path dependent and their behaviour is known to depend on the stress history which the material has undergone. The constitutive elasto-plastic relationships are incremental in nature so that they account for the stress path dependance of the material. The essential features of this plasticity theory are detailed below.

3.2.1 Extension to general stress and strain space

If the concepts of elasto-plastic materials are to be of general use, their behaviour must be formulated in general multi-axial stress and strain space, this general multi axial stress and strain space gives six independent components of stress and six of strain, this makes the formulation of a theory of elasto-plasticity quite difficult. If the material can be approximated as isotropic (i.e. properties independent of orientation) and if yield is essentially dependent on stress magnitude, simplifications can be made in the theory by using invariants of stress and strain [58].

3.2.2 Stress invariants

The concept of stress invariant is based on the following principle, the magnitudes of the components of the stress vector ($\sigma_x, \sigma_y, \sigma_z, \tau_{xy}, \tau_{xz}, \tau_{yz}$) are known to depend on the direction of the chosen coordinate axes. On the other hand principle stresses (σ_x, σ_y and σ_z) always act on the same plane and have the same magnitude. The direction of the chosen coordinate axes has no influence on the plane on which they act or the magnitude of the

stresses. Therefore they can be described as invariant to the choice of axes [64, 65].

The concept of principle stresses can be used to reduce the complexity of the elasto-plastic theory. The state of stress can be fully defined by either specifying the six component values in a fixed direction of a specific coordinate axis, or by defining the magnitude of the principle stresses and the direction of the three planes on which the principle stresses act. In either case six independent pieces of information are required.

By working in terms of stress invariants provides considerable reduction in the complexity of the task of formulating elasto-plastic behaviour, because the number of stress and strain parameters reduces from six to three. In order to use this concept it is necessary to define material as isotropic which may be a simplification of the model. To model anisotropic behaviour the formulation must be in terms of six independent stresses and strains [66, 67].

3.2.3 Basic concepts

To formulate an elasto-plastic constitutive model requires the following essential ingredients [63, 58].

3.2.4 Coincidence of axes

The principle directions of accumulated stress and incremental plastic strain are assumed to coincide. This differs from elastic behaviour where the principle directions of incremental stress and incremental strain coincide [58].

3.2.5 Yield function

Under uniaxial stress conditions the onset of plastic yielding is defined by σ_y , the yield stress. Under multi-axial stress conditions it is not realistic to define a yield stress, as several components of stress are non-zero. Instead it is more prudent to define a yield function F . This function, F separates purely elastic from elasto-plastic behaviour [67].

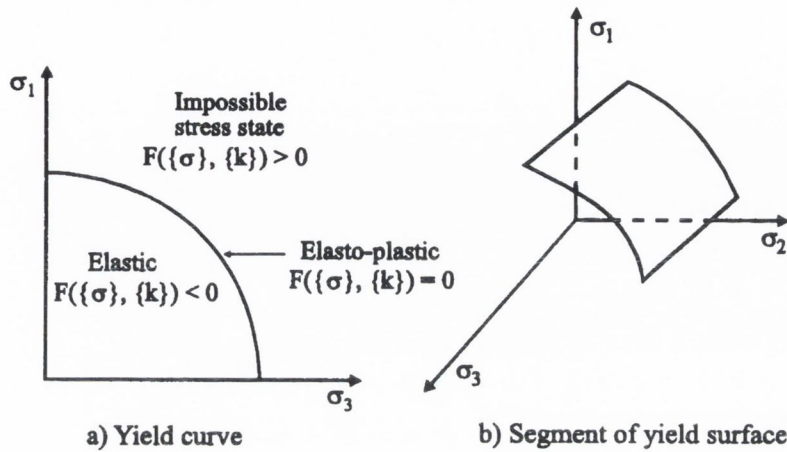


Figure 3.1: Yield function presentation (Source: [58])

F is a scalar function of stress expressed in terms of either the stress components or stress invariants and state parameters $\{k\}$:

$$F = (\{\sigma\}, \{k\}) = 0 \quad (3.1)$$

In general, the surface is a function of the stress state $\{\sigma\}$ and its size is also seen to change as a function of the state parameter $\{k\}$. $\{k\}$ is related to the softening/hardening parameter.

Elastic behaviour can occur if $F(\{\sigma\}, \{k\}) < 0$, and plastic (or elasto-plastic) behaviour can occur if $F(\{\sigma\}, \{k\}) = 0$. $F(\{\sigma\}, \{k\}) > 0$ is an impossible stress state.

Equation 3.1 defines the surface in a stress space. If Equation 3.1 is expressed in terms of the principal stresses and $\sigma_2 = 0$, the yield function can be represented by the curve in Figure 3.1a. The surface which defines the yield function is called the yield curve. If σ_2 is not equal to zero, the yield function has to be shown in three dimensional $\sigma_1 - \sigma_2 - \sigma_3$ space where it forms a yield surface, see Figure 3.1b [58].

The elastic domain is the space under the curve or the surface which defines the yield function. The advantage of assuming that the material

conforms to isotropic behaviour and of expressing the yield function in terms of stress invariants should now be more apparent. If we did not make such an assumption, the yield function would have to be expressed in terms of six stress components and the surface it would form would have to be described in six dimensional space. Clearly, it is not possible to draw such a space and therefore visualisation of such a space is difficult [66, 58].

3.2.6 Plastic potential

Under uniaxial stress conditions it is assumed that the direction of plastic strains is the same as that of the imposed stress. Under uniaxial stress conditions this concept follows logically. However, in the multi-axial case the situation is not as straightforward as there are potentially six non-zero components of stress and strain.

Therefore a method of specifying the direction of plastic straining at every stress state has to be found. This can be accomplished by including a flow rule in the elasto-plastic material model. The flow rule defines the direction of the plastic strains and can be expressed as follows:

$$\Delta\epsilon_i^p = \Lambda \frac{\partial P(\{\sigma\}, \{m\})}{\partial \sigma_i} \quad (3.2)$$

where $\Delta\epsilon_i^p$ represents the six components of incremental plastic strain, P is the plastic potential function and Λ is a scalar multiplier. A plastic potential is of the form:

$$P(\{\sigma\}, \{m\}) = 0 \quad (3.3)$$

where $\{m\}$ is essentially a vector of state parameters the values of which are irrelevant to this problem, because only the differentials of P with respect to the stress components are needed in the flow rule, see Equation 3.2.

The plastic potential defined by Equation 3.2 is shown in Figure 3.2. Figure 3.2 shows a portion of a plastic potential surface plotted in principal stress space. Due to the assumption that the principal directions of accu-

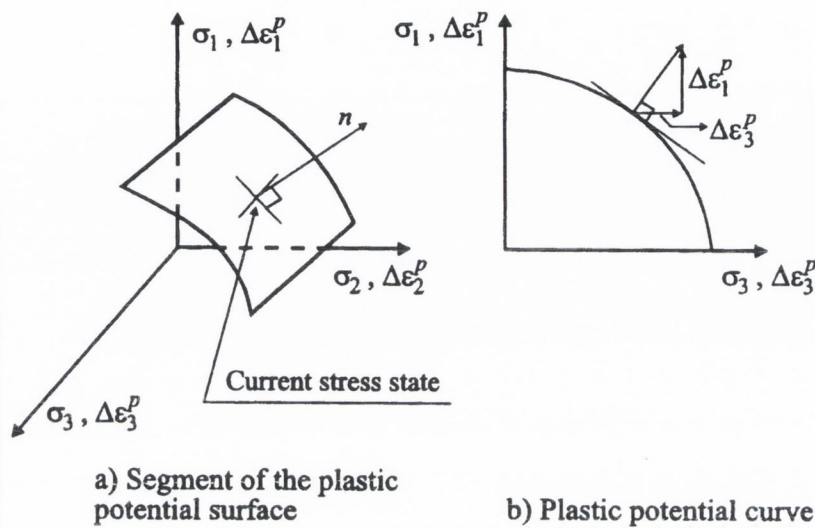


Figure 3.2: Plastic potential presentation (Source: [58])

culated stress and incremental plastic strain coincide, it is possible to plot incremental principal strains and accumulated principal stresses on the same axes. The components of the outward vector normal to the plastic potential surface at the current stress state provide the relative magnitudes of the plastic strain increment components.

Figure 3.2b presents the plastic potential when $\sigma_2 = 0$. This allows one to plot the plastic potential function in two-dimensional space $\sigma_1 - \sigma_3$. The normal vector only provides an indication of the relative sizes of the strain components. Λ , the scalar parameter defined in Equation 3.2 controls the magnitude of the vector. Λ is a function of the hardening/softening rule. The plastic potential can be a function of the six independent stress components. The corresponding surface is in six dimensional stress space and the components of a vector normal to the surface at the current stress state represent the relative magnitudes of the incremental stress components [66, 63].

A further simplification may be introduced which involves assuming the plastic potential function is the same as the yield function (*i.e.* $P(\{\sigma\}, \{m\}) = F(\{\sigma\}, \{k\})$). In this case the flow rule is said to be associative. An associated flow rule produces an incremental plastic vector normal to the yield surface and the normality condition is said to apply. If the yield function and the plastic potential function are different (*i.e.* $P(\{\sigma\}, \{m\}) \neq F(\{\sigma\}, \{k\})$) the flow rule is said to be non-associative [66, 58].

Flow rules are very important part of geotechnical constitutive modelling because the flow rule governs the dilatancy effects of the material. Dilatancy effects can have a significant influence on volume changes and on strength. If the flow rule is non-associative the finite element analysis can take a significantly longer time to solve. Therefore there are significant cost effects if a non-associated flow rule is implemented in a FE analysis. If the flow rule is associative, the constitutive matrix is symmetric and so is the global stiffness matrix. If the flow rule is non-associative both the constitutive matrix and the global stiffness matrix become non-symmetric. The inversion of non-symmetric matrices is much more costly, in terms of storage and computer time.

3.2.7 Hardening/softening rules

The hardening and softening rules specify how the state parameters $\{k\}$ vary with plastic straining. This enables the scalar function, Λ , in Equation 3.2 to be calculated. If the material's behaviour is perfectly plastic, no hardening or softening will occur and the state parameters $\{k\}$ are constant. Therefore it is not necessary to define a hardening or softening rule. This follows from the fact that once the stress state reaches and is maintained at yield, the material strains indefinitely [58, 68], *i.e.* the material is perfectly plastic. For materials that are not perfectly plastic hardening and/or softening will occur during plastic straining. Under these circumstances rules are required to specify how the yield function changes.

3.3 Modified Mohr Coulomb material model

The modified Mohr-coulomb material model is useful in simulating the behaviour of sandy type materials. The failure surface of the modified Mohr-Coulomb model is the so-called double-hardening model in which the shear failure and the compressive failure are uncoupled [61]. The elastic behaviour is assumed to be non-linear and the plastic behaviour is a combination of shear failure and irrecoverable compaction [69]. The modified Mohr-Coulomb has both an associated and a non-associated flow rule, either can be chosen by the user.

The model is integrated numerically using fully implicit Euler backward integration on a local (integration point) level [61].

3.3.1 Basic assumptions

The stress tensor σ and the strain tensor ε can be introduced in vector format as

$$\sigma = [\sigma_{xx}, \sigma_{yy}, \sigma_{zz}, \sigma_{xy}, \sigma_{yz}, \sigma_{zx}]^T \quad (3.4)$$

$$\varepsilon = [\varepsilon_{xx}, \varepsilon_{yy}, \varepsilon_{zz}, 2\varepsilon_{xy}, 2\varepsilon_{yz}, 2\varepsilon_{zx}]^T \quad (3.5)$$

the hydrostatic pressure is defined as

$$p = -\frac{1}{3}(\sigma_{xx} + \sigma_{yy} + \sigma_{zz}) \quad (3.6)$$

and the deviatoric-like stress as

$$\xi = \mathbf{P}\sigma \quad (3.7)$$

in which

$$\mathbf{P} = \begin{bmatrix} \frac{2}{3} & -\frac{1}{3} & -\frac{1}{3} & 0 & 0 & 0 \\ -\frac{1}{3} & \frac{2}{3} & -\frac{1}{3} & 0 & 0 & 0 \\ -\frac{1}{3} & -\frac{1}{3} & \frac{2}{3} & 0 & 0 & 0 \\ 0 & 0 & 0 & 2 & 0 & 0 \\ 0 & 0 & 0 & 0 & 2 & 0 \\ 0 & 0 & 0 & 0 & 0 & 2 \end{bmatrix} \quad (3.8)$$

the effective deviatoric stress is then defined according to

$$q = \sqrt{\frac{3}{2} \xi^T \mathbf{R} \xi} \quad (3.9)$$

$$\mathbf{R} = \text{diag}[1, 1, 1, \frac{1}{2}, \frac{1}{2}, \frac{1}{2}] \quad (3.10)$$

and the third invariant of the deviatoric stress tensor is defined as

$$J_3 = \xi_1 \xi_2 \xi_3 + \frac{1}{4} \xi_4 \xi_5 \xi_6 - \frac{1}{4} \xi_2 \xi_6^2 - \frac{1}{4} \xi_3 \xi_4^2 \quad (3.11)$$

the strains are defined in a slightly different fashion. the volumetric strain is defined as

$$\varepsilon_v = \varepsilon_{xx} + \varepsilon_{yy} + \varepsilon_{zz} \quad (3.12)$$

and for the deviatoric strains we adopt

$$\gamma = \mathbf{Q} \varepsilon \quad (3.13)$$

in which $\mathbf{Q} = \mathbf{R} \mathbf{P} = \mathbf{P} \mathbf{R}$.

3.3.2 Exponential elastic behaviour

Terzagi (1925) [70] observed experimentally that clays followed the following elastic law

$$K_t = \frac{1+e}{\kappa} p \quad (3.14)$$

in which K_t is the bulk tangent modulus, e is the void ratio, κ is a material parameter and p is the current hydrostatic pressure. In this form the soil has no tensile strength. Therefore Equation 3.14 is modified to

$$K_t = \frac{1+e}{\kappa}(p + p_t) \quad (3.15)$$

in which p_t is the so-called tensile pressure. This tensile pressure p_t is simply an numerical artifice to take tensile stress into account when the initial pressure is equal to zero.

3.3.3 Flow rules

The plastic flow in shear failure is assumed to be non-associated and is determined by the plastic potential

$$g_1 = q - \frac{6 \sin \phi_i}{3 - \sin \phi} (p + p_{shift}) \quad (3.16)$$

in which ψ is the so-called dilatancy angle and p_{shift} is illustrated graphically in Figure 3.3.

The plastic flow of the compression cap is determined by the plastic potential

$$g_2 = (p + p_{shift})^2 + \alpha q^2 - p_c^2 = 0 \quad (3.17)$$

α determines the shape of the elliptical cap and is shown graphically in Figure 3.3. The plastic potential laws assume associative flow in the p-q space and non-associative flow in the deviatoric plane [69].

3.3.4 Hardening rules

A hardening rule assumes a law analogous to the elastic compressive laws seen in Section 3.3.2 which adheres to the critical state concept:

$$p_c = p_{c0} \exp\left[\frac{1+e}{\lambda - \kappa} \epsilon_v^p\right] \quad (3.18)$$

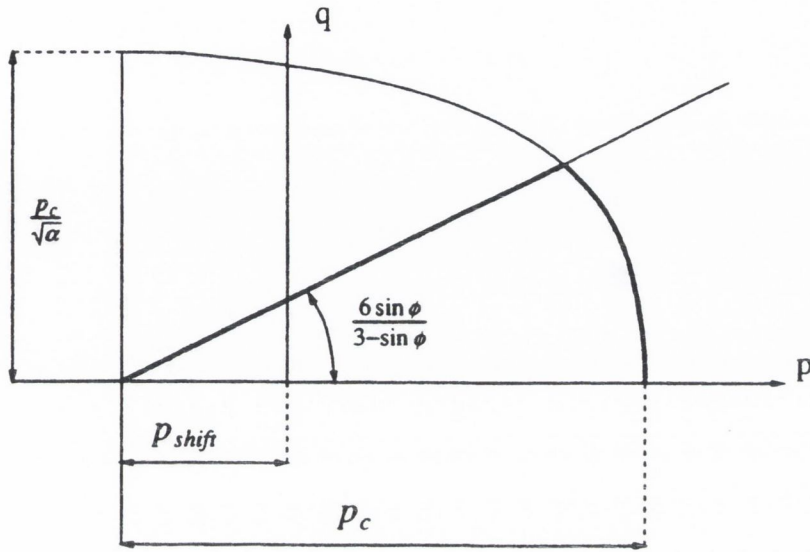


Figure 3.3: Mohr Coulomb plastic potential in p-q space (Source: [61])

where p_c is the preconsolidation pressure (preconsolidation stress is the maximum stress that the material has been subjected to), p_{c0} is the initial preconsolidation pressure, e is the void ratio, λ and κ are the loading and unloading defined by critical state theory. ϵ_v^p is the plastic volumetric strain.

3.3.5 Mohr-Coulomb failure criterion

A knowledge of shear strength is required in the solution of problems concerning the stability of soil masses. If at any point on any plane within a soil mass the shear stress becomes equal to the shear strength of the soil, failure will occur at that point. The shear strength (τ_f) of a soil at a point on a particular plane was originally expressed by Coulomb [71] as a linear function of the normal stress (σ_f) on the plane at the same point:

$$\tau_f = c + \sigma_f \tan \phi \quad (3.19)$$

where c and ϕ are the shear strength parameters, now described as the

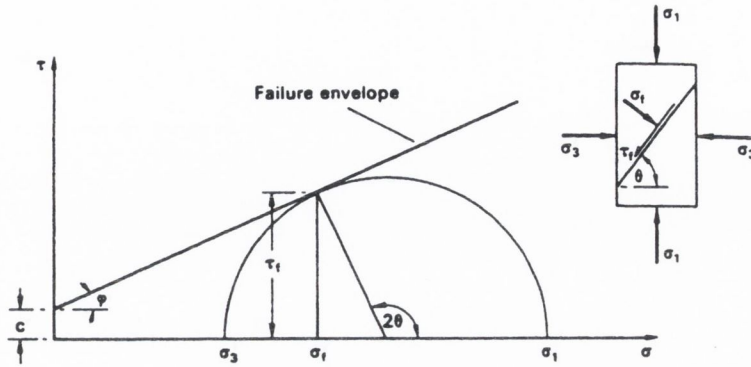


Figure 3.4: Stress conditions at failure (Source: [72])

cohesion intercept (or the apparent cohesion) and the angle of shearing resistance, respectively. Failure will thus occur at any point where a critical combination of shear stress and normal stress develops.

The shear strength can be expressed in terms of the major and minor principal stresses σ_1 and σ_3 at failure. At failure Equation 3.19 will be tangential to the Mohr circle representing the state of stress, as shown in Figure 3.4. Compressive stresses are taken as positive. The coordinates of the tangent point are τ_f and σ_f where:

$$\tau_f = \frac{1}{2}(\sigma_1 - \sigma_3)\sin 2\theta \quad (3.20)$$

$$\sigma_f = \frac{1}{2}(\sigma_1 + \sigma_3) + \frac{1}{2}(\sigma_1 - \sigma_3)\cos 2\theta \quad (3.21)$$

and θ is the theoretical angle between the major principal plane and the plane of failure. It is apparent that

$$\theta = 45^\circ + \frac{\phi}{2} \quad (3.22)$$

From Figure 3.4 the relationship between the effective principal stresses at failure and the shear strength parameters can also be obtained. Now:

$$\sin\phi = \frac{\frac{1}{2}(\sigma_1 - \sigma_3)}{c\cot\phi + (\sigma_1 + \sigma_3)} \quad (3.23)$$

Therefore

$$(\sigma_1 - \sigma_3) = (\sigma_1 + \sigma_3)\sin\phi + 2c\cos\phi \quad (3.24)$$

or

$$\sigma_1 = \sigma_3 \tan^2\left(45^\circ + \frac{\phi}{2}\right) + 2c \tan\left(45^\circ + \frac{\phi}{2}\right) \quad (3.25)$$

Equations 3.24 and 3.25 are referred to as the Mohr-Coulomb failure criterion. If a number of states of stress are known, each producing shear failure in the soil, the criterion assumes that a common tangent, can be drawn to the Mohr circles representing the states of stress: the common tangent is called the failure envelope of the soil. A state of stress plotting above the failure envelope is impossible. The criterion does not involve consideration of strains at or prior to failure and implies that the effective intermediate principal stress σ_2 has no influence on the shear strength of the soil.

3.4 Modified Cam clay Model

The Cam-clay model based on the critical state concept is perhaps the most widely used model today for geotechnical analysis [60].

The first critical state models were a series of Cam-clay formulations developed at the University of Cambridge by Roscoe and his co-workers. The formulation of the original Cam-clay model as an elasto-plastic constitutive model is presented by [73] and [74]. [75] proposed the modified Cam-clay model and in recent years the egg Cam-clay model has been developed at Delft University [76].

The modified Cam-clay model has five basic ingredients

- the elastic model

- the yield locus
- the hardening rule
- the plastic potential
- the critical state

The modified Cam-clay model gives good predictions of deformations, not only under compression but also under shear. However the stresses are not always described properly.

3.4.1 Elastic model

Both the Cam clay and the modified Cam clay models were originally developed for triaxial loading conditions. These models are essentially based on the following assumptions:

A piece of clay, which is subjected to slow, perfectly drained isotropic ($\sigma_1 = \sigma_2 = \sigma_3$) compression, moves along a trajectory in the $v - \ln p$ plane ($v = \text{specific volume} = 1 + e$ where e is the void ratio) , which consists of a virgin consolidation line and a set of swelling lines, see Figure 3.5 [58].

On initial loading, the soil moves down the virgin consolidation line. If the soil is unloaded from point 'b', it moves up the swelling line 'bc' . When the soil is reloaded, it moves back down the same swelling line until point 'b' is reached, at which point it begins to move along the virgin consolidation line again. If unloaded from point 'd', it moves up the swelling line 'de'. The virgin consolidation line and the swelling lines are assumed to be straight in $v - \ln p'$ space and are given by the following equations:

$$v + \lambda(\ln p) = v_1 \quad (3.26)$$

$$v + \kappa(\ln p) = v_s \quad (3.27)$$

Equation 3.26 represents the virgin consolidation line and Equation 3.27 the swelling line. The values of κ , λ and v_1 are characteristics of the particular

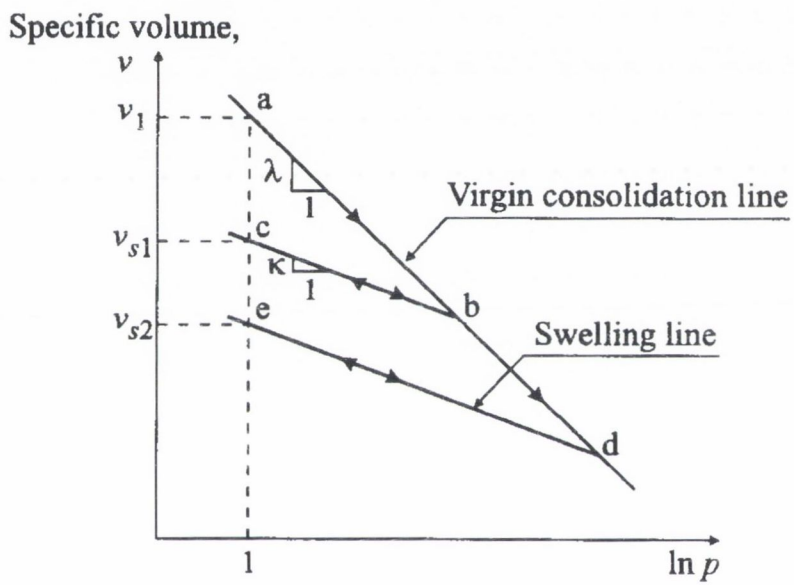


Figure 3.5: Behaviour under isotropic compression (Source: [58])

type of clay, whereas the value of v_s is different for each swelling line. Volume change along the virgin consolidation line is mainly irreversible or plastic, while volume change along a swelling line is reversible or elastic.

The Modified Cam clay model does not define the elastic shear strain, so it is necessary to define the elastic shear strain separately. The hypothesis of Muir Wood is assumed [15], and the elastic shear strain is defined by Equation 3.28, with a constant value for Poisson's ratio ν :

$$\delta\epsilon_q^e = \frac{2(1+\nu)}{9(1-2\nu)} \frac{\delta q}{\nu p} \quad (3.28)$$

where q is the deviatoric stress and ϵ_q^e is the elastic component of the deviatoric strain.

3.4.2 Yield locus

Consider a drained triaxial test. At first the clay will behave elastically. At some point the clay will yield, irrecoverable deformations will occur. At that specific moment the stress point of the clay sample has reached the yield locus. The yield locus of the Modified Cam clay model is an ellipse in the $p - q$ triaxial plane (see part a of Figure 3.6):

$$f = q^2 - M^2[p(p_c - p)] \quad (3.29)$$

The shape of the ellipse is defined by the shape parameter M , and its initial size or major axis is determined by the preconsolidation stress, p_c (the maximum historical stress). The higher the preconsolidation stress the larger the initial ellipse. In addition, the yield surface only changes its size but not its shape and location in $q - p$ space. This assumption is called isotropic hardening.

3.4.3 Hardening rule

When the sample is loaded, in for example a drained triaxial test, the stress path follows the line AB, as seen in Figure 3.6a and reaches the yield locus.

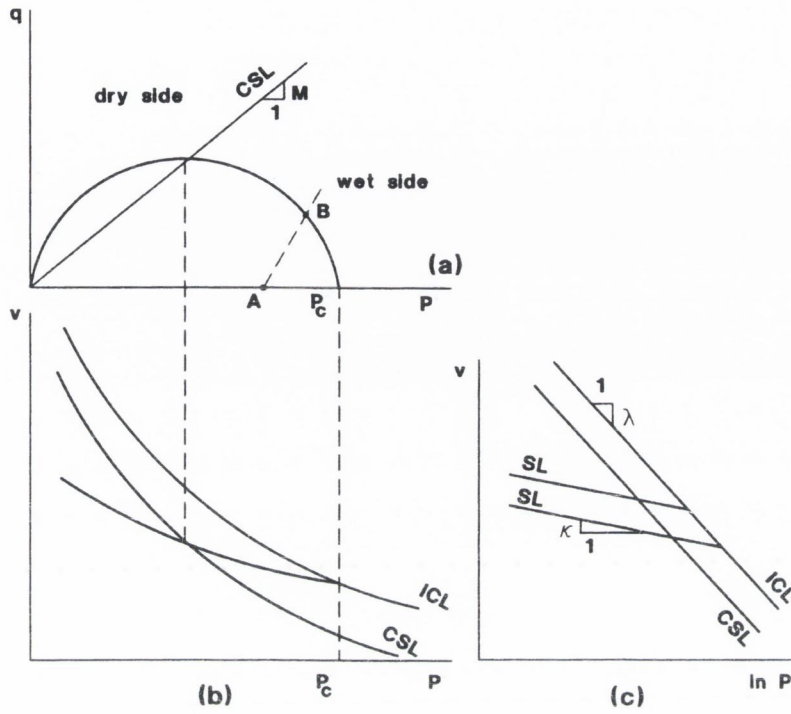


Figure 3.6: The modified Cam clay model (Source: [76])

From this moment, as the load increases hardening occurs. The yield locus will grow while the load is increased and the clay will harden. Hardening is defined by an increase in preconsolidation stress p_c . From Equation 3.28 follows:

$$\delta \varepsilon_p^p = (\lambda - \kappa) \frac{\delta p_c}{\nu p_c} \quad (3.30)$$

Hardening is seen to depend only on the volumetric strain. A sample which is highly overconsolidated will soften when it is loaded beyond the yield surface. This will cause the yield locus to decrease. Softening is described by the same formula as hardening, Equation 3.30 [76].

The volumetric response of soil to applied stress depends on its stress history. If a soil yields on a point to the right of critical state line (CSL),

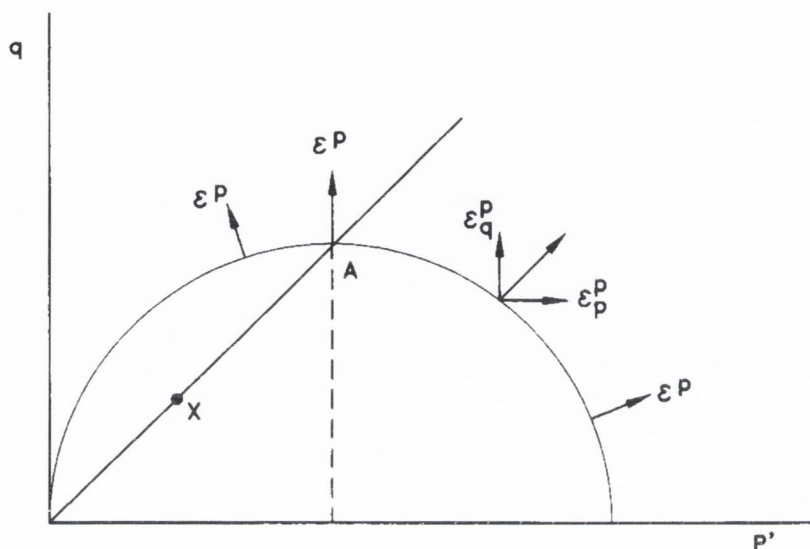


Figure 3.7: Associated flow rule (Source: [58])

incremental plastic strains are positive (compressive), and hardening behaviour occurs (see Figure 3.6a). This side of the yield surface is called wet or subcritical. If yielding occurs to the left of the CSL (dry or supercritical) the incremental plastic volume strain are negative (dilatant) and softening behaviour results.

3.4.4 Plastic potential

The plastic strain vector is assumed to be normal to the yield locus $f = 0$ in the $p - q$ stress plane (associated flow rule, see Figure 3.7), so

$$\frac{\delta \varepsilon_p^p}{\delta \varepsilon_q^p} = \frac{\delta f / \delta p}{\delta f / \delta q} = \frac{M^2 - \eta^2}{2\eta} \quad (3.31)$$

where $\eta = q/p$, ε_p is the volumetric strain and ε_q is the deviatoric strain.

3.4.5 Critical state

When a clay sample is loaded sufficiently, in most cases the clay will reach a stage at which shear can occur infinitely, while volume changes or stress changes no longer occur. This state is called the critical state, and occurs when the stress point in the $p - q$ plane lies exactly on the top of the ellipse [68].

The critical state line in the $p - q$ plane is the line which connects the top of the ellipses of different sizes:

$$\eta = M \quad (3.32)$$

where $\eta = q/p$. When the stress point lies on the line, it is not necessarily in the critical state. It is possible that the stress point lies on the critical state line and also inside the current yield locus (point X in Figure 3.7). That point doesn't lie at the top of the ellipse and is therefore not in the critical state [76].

Each critical state combination of p_{cs} and q_{cs} is associated with a critical state combination of p_{cs} and v_{cs} . The critical state line, which lies in the $p - v$ plane, connects the values of p_{cs} and v_{cs} can be written as:

$$v = \Gamma - \lambda \ln p_{cs} \quad (3.33)$$

$$\Gamma = N - (\lambda - \kappa) \ln 2 \quad (3.34)$$

where Γ and N are constants.

Combinations of p , q and v that simultaneously satisfy Equations 3.32 and 3.33, are critical states.

3.5 Input parameters for FE material model

The two FE material models to be used in this thesis are detailed in this chapter. Table 3.5 summarises the required input parameters for the mod-

ified Mohr Coulomb material model in DIANA and the modified Cam clay material model in ABAQUS/Standard and their physical meanings. The experimental methods required to determine these input parameters will now be described.

Table 3.1: FE material model input parameters

ABAQUS	Physical meaning	DIANA	Physical meaning
λ	Loading parameter	λ	Loading parameter
κ	Unloading parameter	κ	Unloading parameter
ν	Poisson's ratio	ν	Poisson's ratio
e_0	Initial void ratio	e_0	Initial void ratio
M	Failure criterion	$\sin\phi$	Failure criterion
β	Yield surface shape	p_c	Preconsolidation stress
K	Dependance of yield on σ_2	p_t	Strength in tension

3.5.1 Loading and unloading parameters

λ and κ the loading and unloading parameters used in both the FE material models can be calculated using two separate experimental methods. These methods have been developed to characterise the behaviour of soil type materials. The first method involves carrying out an oedometer test. In an oedometer test a cylindrical specimen of soil enclosed in a metal ring is subjected to a series of increasing static loads, while changes in thickness are recorded against time. The soil specimen is confined laterally, thereby allowing only one-dimensional strain, i.e. strain in the direction of load application. The test is described in BS Standard 1377:Part 5:1990. An example of an oedometer test rig is show in Figure 3.8.

The principles of the oedometer test are the same as that of the compression test rig detailed in Section 4.1.1. The compression test rig allows for the one-dimensional compression of compression packing rings. Therefore the methods used to determine λ and κ using a oedometer test can be applied

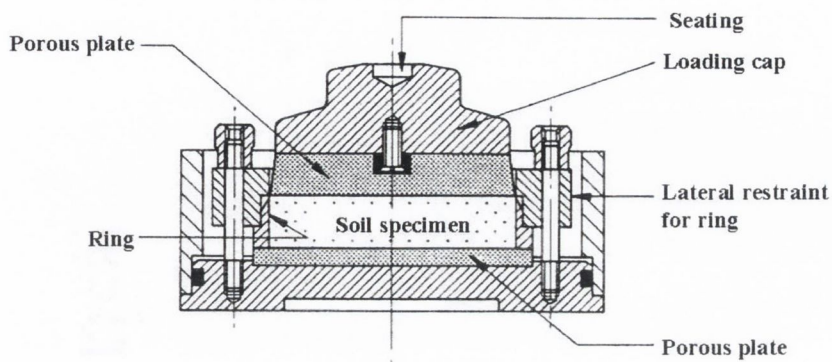


Figure 3.8: Details of a typical oedometer consolidation cell (reproduced from Fig. 1(a) of BS 1377:Part5:1990)

to results from the compression test rig. The applied axial stress is plotted against void ratio. Initially the preconsolidation stress for the test must be calculated; this is carried out using the method described in Section 3.5.3. The data is then approximated by a bi-linear curve as seen in Figure 3.9. The straight portion before the preconsolidation stress is called the overconsolidation (OC) line, while the straight line after the preconsolidation stress point is called the normally consolidated or virgin consolidation line. The slope of the OC line in the e vs. $\log(\sigma_v)$ axis is designated as C_s or the swelling index and is also assumed to be the same as the slope of any subsequent unloading curve. The slope of the NC/VCL line is designated as C_c or the compression index.

From the calculated values of C_c and C_s the values of λ and κ can be determined using Equations 3.35 and 3.36 respectively.

$$\lambda = \frac{C_c}{\ln 10} = 0.434C_c \quad (3.35)$$

$$\kappa = \frac{C_s}{\ln 10} = 0.434C_s \quad (3.36)$$

The second method involves the manipulation of test data from a triaxial

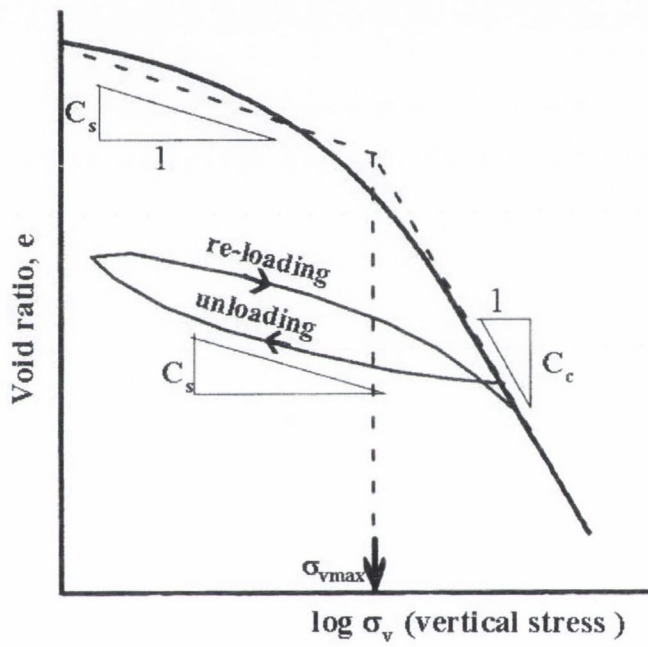


Figure 3.9: Calculation of compression index and swelling index

test. The principle of the triaxial test are described in Section 4.1.2. The natural log of applied pressure, $\ln p$ is plotted against the specific volume, $v (1+e)$. The data is approximated by linear lines, these being the virgin consolidation line and the swelling lines as seen in Figure 3.5. The slope of the virgin consolidation line corresponds to the value of λ and the slope of the swelling line is equal to κ .

3.5.2 Poisson's ratio

Poisson's ratio is calculated using experimental data from triaxial tests. On initial compression the negative normal strain ε_1 is plotted against volumetric strain ε_v . The slope of this line is determined and Poisson's ratio ν is calculated from the formula $1 - 2\nu = \tan(\text{initial slope})$, detailed in [77].

3.5.3 Pre-consolidation stress

The preconsolidation stress of soil can be determined by loading a sample of a soil in an oedometer or compression test rig where the sample is loaded under one-dimensional strain. The results are plotted in a semi-logarithmic void ratio, e vs. \log of effective vertical stress, $\log(\sigma_v)$ plot, see Figure 3.10.

Using this plot the preconsolidation stress is determined following Casagrande's procedure [78]:

1. By eye locate the sharpest point of the consolidation curve (point A)
2. Draw a horizontal line from point A (line A-B)
3. Draw a tangent to consolidation curve at point A (line A-C)
4. Bisect the angle between the tangent to the straight line from point A (line A-D)
5. Draw a tangent to the straight line portion of the consolidation line (line E-F)

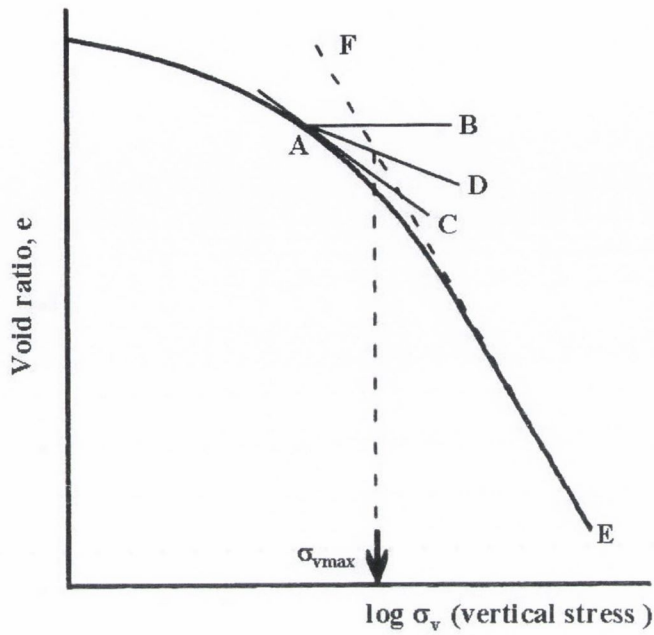


Figure 3.10: Calculation of preconsolidation stress

6. The intersection of the lines A-D and E-F projected to the horizontal axis gives the preconsolidation stress σ'_{vmax}

3.5.4 Strength in tension

Since soil type materials are rarely tested in tension, it is usually necessary to guess the magnitude of the strength of the soil in hydrostatic tension. The choice of tensile strength should not have a strong effect on the numerical results unless the soil is stressed in hydrostatic tension. A common approximation is to set p_t equal to 5% to 10% of the initial yield stress in hydrostatic compression.

3.5.5 Critical state parameters

Triaxial compression tests allow for the calibration of the yield parameters M and β . M is the ratio of the deviatoric stress, q , to the hydrostatic stress, p , at critical state and can be obtained from the stress values when the material has become perfectly plastic (critical state). At critical state p is plotted against q and M is determined from the slope of the p - q line at that point. Under axisymmetric triaxial test conditions the following equations are the definitions of p and q

$$p = \frac{1}{3}(\sigma_a + 2\sigma_r) \quad (3.37)$$

$$q = \sigma_a - \sigma_r \quad (3.38)$$

where σ_a is the applied axial stress and σ_r is the confining pressure.

β represents the curvature of the cap part of the yield surface and can be calibrated from a number of triaxial tests at high confining pressures (on the "wet" side of critical state). β must be between 0.0 and 1.0, this effect can be seen in Figure 3.11.

To calibrate the parameter K , which controls the yield dependence on the third stress invariant, experimental results obtained from a true triaxial (cubical) test are necessary. These results are generally not available, and the user may have to guess (the value of K is generally between 0.8 and 1.0) or ignore this effect [62].

3.5.6 Friction angle

The friction angle $\sin\phi$ is determined from triaxial test data. Three or more triaxial compression tests are carried out at different confining pressures. At failure the values of σ_1 and σ_3 are recorded and plotted on a graph of σ_1 vs. σ_3 . The slope of the line that joins these points is equal to ϕ the friction angle. The sin of the friction angle is inputted into the modified Mohr Coulomb material model in DIANA to describe the failure of the material.

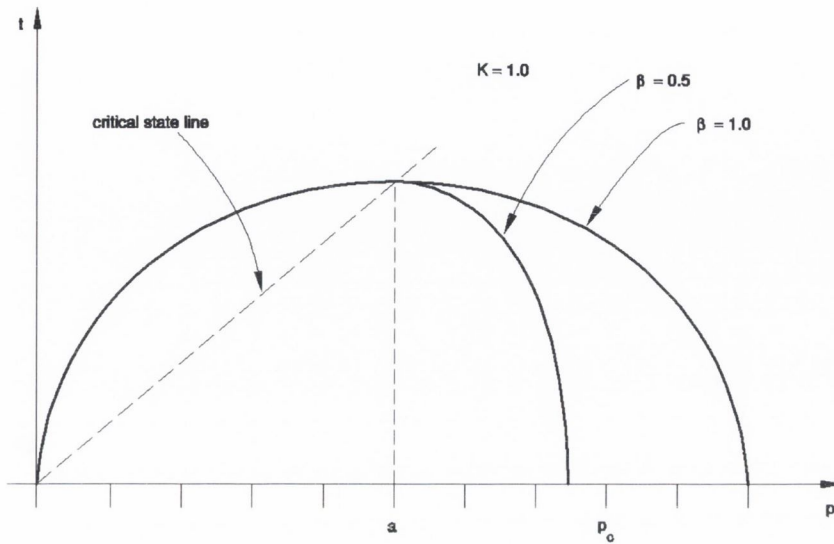


Figure 3.11: The influence of β on the Cam clay yield surface (Source: [62])

3.6 Summary

The use of geotechnical material models to describe the behaviour of exfoliated graphite packing rings were discussed in this chapter. Chapter 5 details the material testing carried out on exfoliated graphite. This material testing established that the compression, yield and failure behaviour of exfoliated graphite mimics that of a soil. The modified Mohr Coulomb material model was initially chosen as the best available material model with which to model exfoliated graphite. Convergence problems were encountered during FE analysis resulting from problems with contact friction. Therefore an alternative FE material model and FE package had to be chosen. This was the modified Cam clay material model in ABAQUS/Standard. Both material models are described in detail in this chapter. The methods required to determine the input parameters for the two material models are also described in this chapter.

Chapter 4

Experimental and FE methods for compression packing analysis

4.1 Material Testing

Material testing is carried out with two separate aims in mind. The first aim is to determine detailed information on the behaviour of individual packing rings in a valve, secondly testing has to be carried out to determine the input parameters for the FE constitutive material models which are detailed in Chapter 3.

4.1.1 Compression test rig

The compression test rig is a simulated valve stuffing box. It was designed and built by Klenk [12] and is located in the MPA at the University of Stuttgart. It allows for the controlled compression of individual or multiple compression packing rings. The test rig is shown in Figure 4.1.

The test rig is instrumented to measure the following variables

- Applied axial stress at the follower

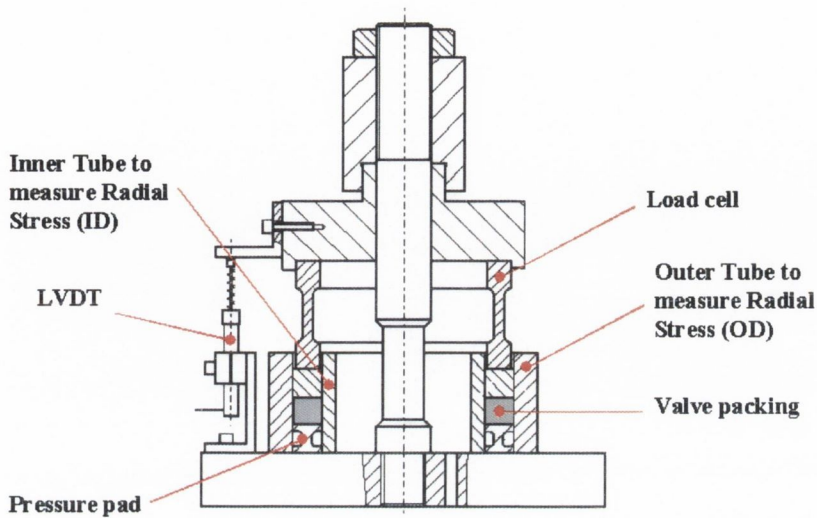


Figure 4.1: Compression test rig (Source [12])

- Axial stress under the final packing ring
- Deformation of an individual packing ring or a set of packings rings
- Radial stress at the OD of a single packing ring
- Radial stress at the ID of a single packing ring

Axial deformation is measured using 3 LVDT's mounted in a 120° arrangement. The radial stress measurements are carried out using special measuring tubes, which represent the stem (inner tube) and the housing (outer tube). Both the measuring tubes are instrumented with strain gauges in 5 vertical positions over the tube length and 4 positions in the circumferential direction [12]. Data from the strain gauges are used to determine the radial stresses in the inner and outer tubes.

It is only possible to make accurate measurements of radial stress when single packing rings are being tested. By measuring the resultant radial stress in the inner and outer measuring tubes under a given applied axial stress the

radial stress coefficient K_{rad} , can be calculated. K_{rad} is the ratio of radial stress to axial stress (see Equation 4.1).

$$K_{rad} = \frac{\sigma_r}{\sigma_a} \quad (4.1)$$

where σ_r is the radial stress and σ_a is the applied axial stress. The applied axial stress is measured using a load cell. A pressure pad positioned at the bottom of the test rig allows for the measurement of the axial stress under the final packing ring. The decay of axial stress through a series of packing rings can be measured using this feature.

Experimental data from this test is used to determine the loading and unloading parameters λ and κ for the FE constitutive material models. FE analysis of the compression test rig is also carried out to validate the FE constitutive material models.

4.1.2 Triaxial test rig

Triaxial testing was carried out to determine various input parameters for the FE material models. The triaxial apparatus is the most widely used piece of laboratory equipment for soil and rock testing. There are many different types of triaxial test devices, including hollow cylinder and true triaxial test rigs. The most common type of triaxial test apparatus is the conventional cylindrical triaxial test rig. The convention triaxial test rig consists of three parts, a triaxial cell, a loading device and a device for generating confining pressure illustrated in Figure 4.2.

The triaxial cell itself consists of a cell body into which the specimen is placed. The specimen is cylindrical in shape and encased in a flexible rubber jacket to prevent the cell fluid from entering the specimen [72]. The principle of a conventional triaxial test is as follows, a cylindrical specimen is subjected to steadily increasing hydrostatic pressure (i.e. equal amounts of confining pressure and axial stress are applied to the sample) until the required confining pressure is reached. The confining pressure is held constant at this value while the axial stress is increased until failure occurs [80].

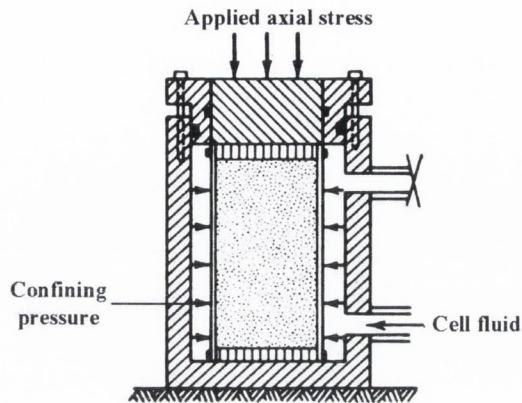


Figure 4.2: Triaxial test rig (Source:[79])

The engineer should specify cell confining pressures that relate to the in-situ conditions [81].

Standard soil mechanics triaxial cells are designed for pressures up to 1000 kN/m^2 . The cells are made from corrosion resistant metal, with an acrylic plastic transparent cylindrical body. Steel cells are also manufactured for tests at higher pressures of up to 7 MN/m^2 . Tests on rock specimens are carried out in steel cells with loading devices which are capable of applying pressure up to 70 MN/m^2 . In order to simulate the stress conditions experienced by standard valve packings in situ in a valve, it is necessary to use a rock triaxial test rig. Recommended procedures for rock triaxial testing are described by Vogler and Kovari [82].

Triaxial cells are available in several different sizes, each of which can accommodate several different specimen diameters by means of an interchangeable base and top cap fittings. Most tests are performed on samples with a diameter of 38mm and a height of 76mm [58]. Friction between the steel platens and the ends of the test sample can interfere with results obtained from triaxial tests. Research has shown that if a height to diameter ratio of 2:1 is used these effects can be ignored [80]. Manufacturing a continuous



Figure 4.3: Exfoliated graphite discs used during triaxial testing

cylinder of exfoliated graphite of height 76 mm and diameter 38 mm proved unfeasible, as it was not possible to achieve the same density through the entire cylinder. Therefore the author had to determine a new method to test exfoliated graphite. As a compromise 38.1 mm diameter by 6 mm high discs of exfoliated graphite were designed and manufactured to for triaxial testing, an example of such a disc can be seen in Figure 4.3. These discs were stacked one on top of another inside the rubber jacket.

In order to determine the input parameters for the FE material models, the following variables must be recorded during a triaxial test, applied axial stress, confining pressure, axial strain and radial strain. Triaxial test rigs are instrumented to measure the applied axial stress and confining pressure applied to the triaxial sample. Axial and radial strains in a triaxial cell are normally measured using strain gauges. In the case of soil testing, strain gauges are attached to the rubber membrane. When testing rocks the strain gauges are glued to the rock samples themselves during testing. Strain gauges are capable of measuring strains up to 20%. Exfoliated graphite is a highly compressible material, strains in one-dimensional compression were seen to exceed 20% (See Figure 5.1). In light of this fact another method had to be found to measure the radial and axial strains seen in exfoliated graphite during triaxial testing.

Both internal and external mechanical devices have been developed to measure the strains in axisymmetric triaxial test rigs. These devices were

originally conceived to detect strain localisations, they have a good resolution and a large strain range [83]. A review of the latest measuring devices used in triaxial testing by Scholey et al. [84] stated that internal devices directly attached to the test specimen also gives the most accurate strain measurements. Due to the stresses experienced by the packing ring set in a valve triaxial testing had to be carried out in a high pressure triaxial test rig. The triaxial test rig also had to be instrumented to measure large strains. This type of machine is a very specialised piece of equipment and extremely expensive. Therefore testing had to be carried out in a third party location.

Tests were carried out using a rock mechanics triaxial test rig in the Department of Earth Science and Engineering, Imperial College, London. In this cell, radial strains are made on two perpendicular diameters by a prestrained cantilever transducer, which contacts the core sample via metal inserts bonding to the retaining jacket. Axial strains were measured using vertically mounted LVDT's, which follow the ram travel. The set-up is shown in Figure 4.4. The exterior of the actual triaxial cell is shown in Figure 4.5.

The following parameters were data logged during each test: axial applied load, radial confining pressure, axial strain and radial strain. These outputs are used to calibrate the elastic and plastic compressive behaviour and the failure surface [69] of the FE material models. The data manipulation methods required to determine the input parameters from triaxial test data can be seen in Section 3.5.

4.2 FE methods

Two FE models are detailed in this section. The first FE model is a simulation of the compression test rig described in Section 4.1.1. Experimental data from the compression test rig is compared with results from the FE model of the same test rig in order to validate the FE model. This FE model is used to validate the FE constitutive material models for 1.5 g/cm^3 exfoliated graphite. The second FE model uses the FE material model validated

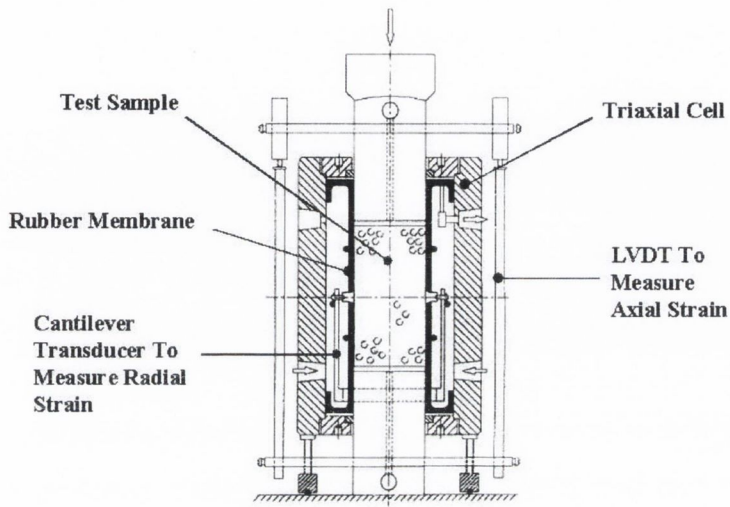


Figure 4.4: Triaxial cell

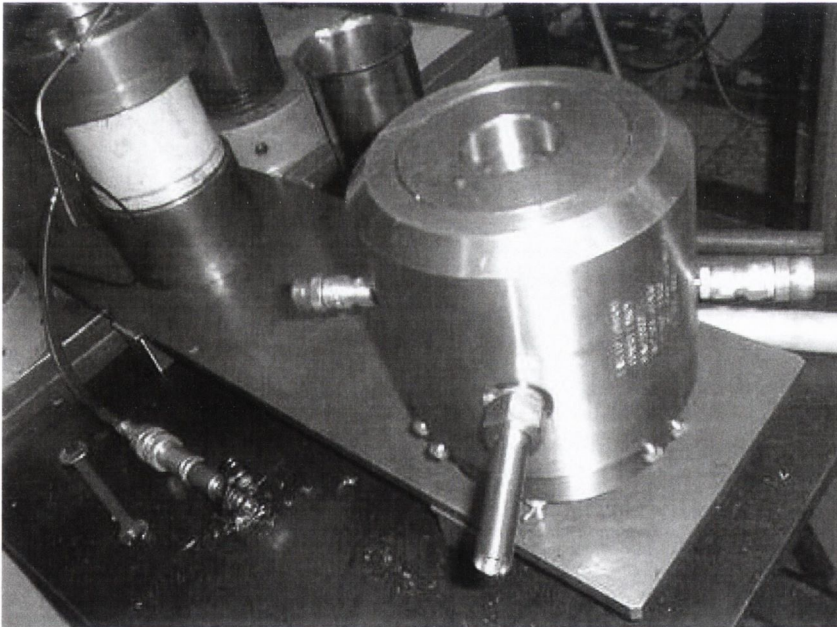


Figure 4.5: Exterior of triaxial cell, Imperial College, London

using the FE model of the compression test rig to investigate the influence of loading, valve stem friction, valve stem cycling and wear on the behaviour of an exfoliated graphite packing ring set.

4.2.1 Compression test simulation

The FE model of the compression test rig can be seen in Figure 4.6. The FE model is an axisymmetric half model of one 1.5 g/cm^3 exfoliated graphite packing ring in the compression test rig. FE analysis is carried out to validate the input parameters of the modified Cam clay material model in ABAQUS/Standard and the modified Mohr Coulomb material model in DIANA. The model is constrained in the 2 direction along the bottom of the stem, housing and seal. The model is constrained in the 1 direction along the left hand side of the stem and along the right hand side of the housing. A linearly increasing pressure of 40 MPa is applied to the top of the seal and then unloaded in the same manner.

Coulomb friction is defined at the packing ring ID stem interface and at the packing ring OD housing interface, with $\mu_{stem} = 0.1$ and $\mu_{housing} = 0.2$. These values were chosen based on the measured R_z values from the compression test rig at the MPA in the University of Stuttgart. The R_z for the stem was calculated to be $2.3 \text{ }\mu\text{m}$ and the R_z value of the inner diameter of the housing was calculated as $6.3 \text{ }\mu\text{m}$. There is no direction correlation between R_z and μ the coefficient of friction between the steel valve components and exfoliated graphite packing rings. Therefore these values can only be said to represent a possible value of coefficient of friction at the interface of the packing rings inner and outer diameters and the stem and the housing. The influence of coefficient of friction on the compression behaviour of a single compression packing ring was investigated using FE analysis. Variations in the coefficient of friction between 0.05 and 0.25 do not have a significant influence on the compression behaviour of a single packing ring. This however is not the case when it comes to the analysis multiple packing rings where the coefficient of friction of the interface of the

compression packing rings and the stuffing box has significant influence on the behaviour of the compression packing rings.

The FE mesh of the compression test simulation can be seen in Figure 4.7. The FE mesh was chosen as a compromise between time to convergence of the model and solution accuracy. This compromise had to be made as the model had to be run in excess of 100 times. The input parameters for the FE model were determined experimentally as seen in Section 5.2, there is significant variability in some of the calculated values and the influence of this variability had to be studied to investigate the influence of input parameters variability on the FE solution, which had to match the experimental results as closely as possible.

In ABAQUS the stem, housing and compression packing ring was composed of CAX4R elements. CAX4R elements are axisymmetric, 4 noded reduced integration elements which have hourglass control. ABAQUS recommends the use of reduced integration elements with the Cam clay material model. It improves the convergence rate of the FE model. Hourglassing can be a problem with first-order, reduced-integration elements in stress/displacement analyses. Since the elements have only one integration point, it is possible for them to distort in such a way that the strains calculated at the integration point are all zero, which, in turn, leads to uncontrolled distortion of the mesh. CAX4R elements allow for the control of this hourglassing phenomenon. Contact was defined by contact surfaces in ABAQUS. The steel contact surfaces, i.e. the inner diameter of the stem and the housing were defined as the master contact surfaces and the inner and out diameters of the valve packing ring were defined as the slave contact surfaces.

The same mesh was used in DIANA with different elements. CQ16A elements were used to model the stem, housing and compression packing ring. CQ16A elements are eight-nodes isoparametric axisymmetric solid ring elements. CONT2 elements were used to define the contact elements. CONT2 are 2 dimensional contact elements. Contact and target surfaces had to be

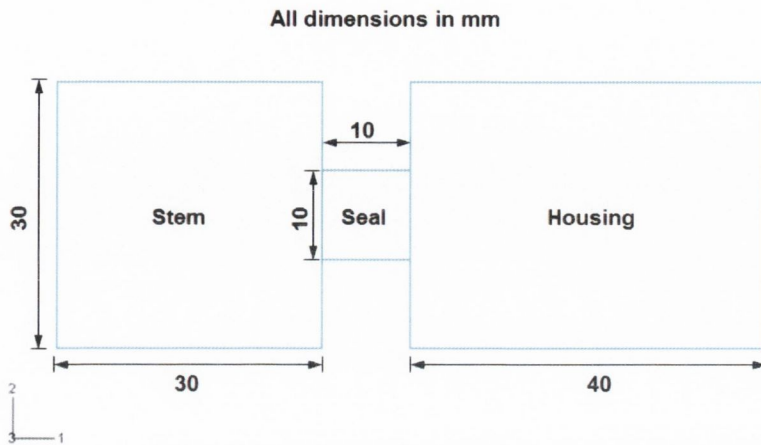


Figure 4.6: Compression test FE simulation

defined for contact analysis to be carried out in DIANA. The inner and outer diameters of the compression packing ring were defined as contact surfaces and the stem and inner diameter of the housing were defined as the target surfaces. A condition of zero Coulomb friction was defined at the interface of the target and contact surfaces in DIANA because the FE model could not converge unless this condition was assumed. DIANA does not presently have the capability to model contact friction.

4.2.2 Valve cycling model

Valve stem friction has a significant influence on the stresses that occur in the valve packing set both on initial compression and when the valve stem is cycled. The valve cycling model was then used to investigate the influence of loading, valve stem friction, valve stem cycling and wear on behaviour of an exfoliated graphite packing ring set. The FE model is a simulation of a test rig developed by AMTEC [85] to measure the force on a valve stem when it is cycled. The model is an axi-symmetric half model of three 1.5 g/cm^3 exfoliated graphite packing rings in a valve. A schematic of the FE model can

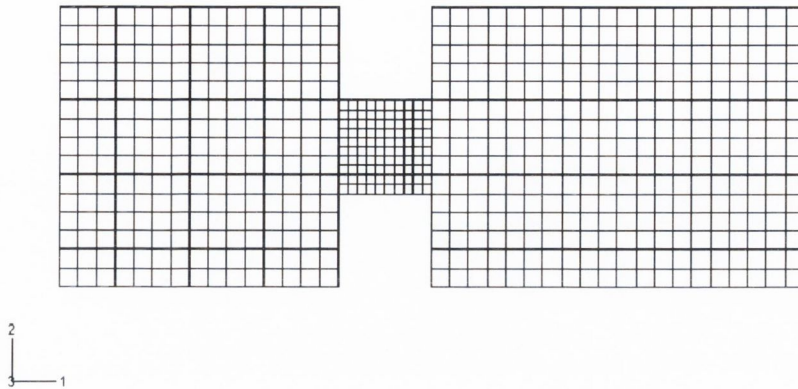


Figure 4.7: Compression test FE simulation

be seen shown in Figure 4.8. The dimensions of the individual packings rings are $56 \times 40 \times 8 \text{ mm}$. A 0.1 mm gap was included at the interface of the packing ring OD and the housing. this is standard practice in industry as it allows for ease of installation of the packing rings into the valve. The base of the stem, seal 3 and the housing are confined in the 2 direction. The left hand side of the stem and the right hand side of the housing are confined in the 1 direction. The FE mesh used can be seen in Figure 4.9. The stem, housing, follower and compression packing rings was composed of CAX4R elements which are described in Section 4.2.1. Contact was defined by master and slave surfaces. The steel component, i.e. the follower, stem, and housing were defined as the master surfaces and the packing ring surfaces were define as the slave surfaces. The FE mesh was chosen so that it produced an accurate solution, within a moderate time frame. The FE mesh also had to have a significant number of data points with which to analysis the stresses along the stem.

Two separate loading conditions were investigated. The packing rings are subjected to load control conditions and displacement control conditions. Displacement control conditions mimic the behaviour of a packing ring subjected to simple bolt loading whereas load control conditions simulate the behaviour of a live loaded valve which maintains a near constant force ap-

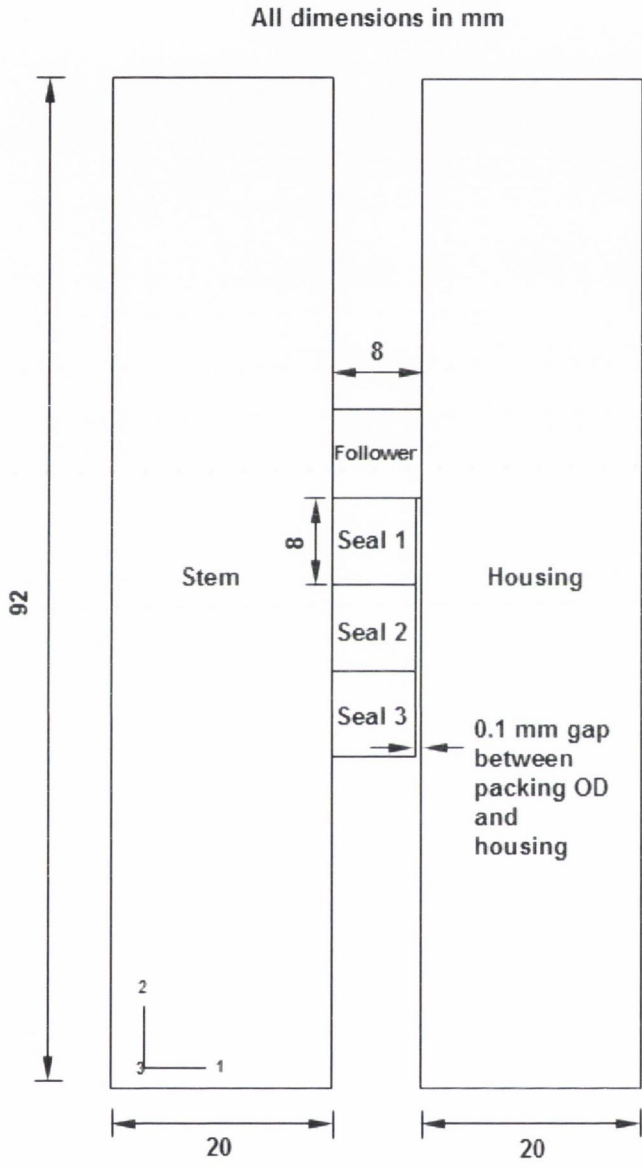


Figure 4.8: FE model used to simulate valve stem cycling

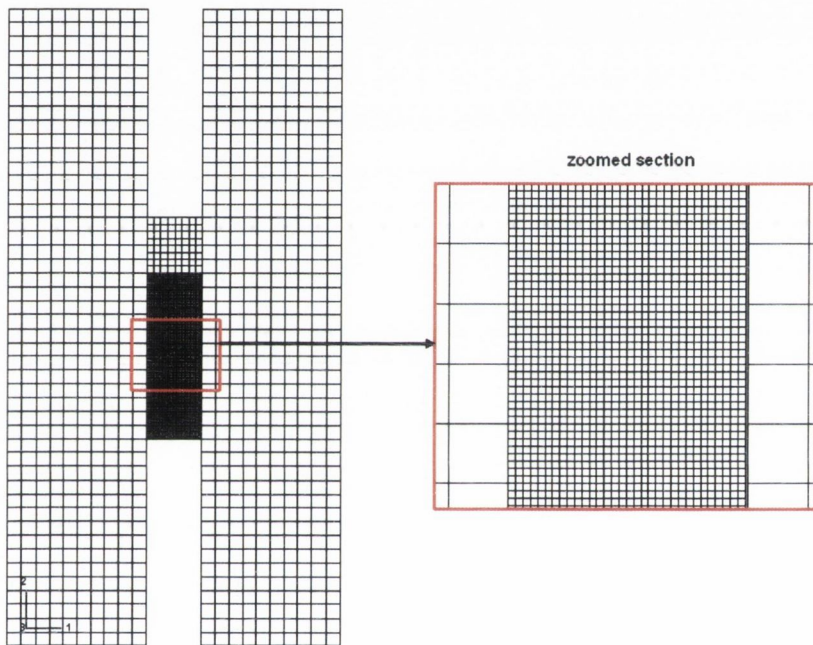


Figure 4.9: FE mesh used to simulate valve stem cycling

plied to the top of the packing ring set.

Under load control conditions a pressure of 40 MPa is applied to the top of the follower. Under displacement control conditions a displacement of 2.99 mm was applied to the top of seal 1. This displacement develops an average stress of 40 MPa at the top of seal 1 when the friction at the valve packing ID stem interface is $\mu_{stem} = 0.20$. Under displacement control conditions convergence problems were encountered when the displacement was applied to the top of the follower. The follower was omitted from the displacement control model and the model was found to converge under these conditions. Omitting the follower from the displacement control model does not affect the results as it has minimal effect on the stresses applied to the top of seal 1.

The model was subjected to six separate loading steps. Initially the 3 seals are loaded axially either by a constant applied axial stress or by a fixed displacement at the top of seal 1 as described above. This stress/displacement is held constant and the valve stem is then cycled 5 times. Each load step occurs over a time period of 400 seconds. The initial loading is linearly ramped over the course of 400 seconds. The valve stem is then closed over the course of 200 seconds and opened over the remaining 200 seconds of the load step. Opening and closing the valve stem involves displacing the valve stem in the + and - 2 direction by 10 mm. The influence of stem friction on the forces developed against the stem were investigated. The friction between the packing ring set OD and the housing was held constant at $\mu_{housing} = 0.20$. The friction between the packing ring set ID and the stem was varied between 0.05 and 0.5 in steps of 0.05. It was not possible to carry out the full spectrum of analysis under both load control and displacement controlled conditions as convergence problems were encountered. Under load control conditions convergence occurred up to and including $\mu_{stem} = 0.35$, under displacement control conditions the model converged up to and including $\mu_{stem} = 0.45$.

The influence of wear on the radial stress distribution against the stem was investigated using this model. After the valve stem was cycled 5 times

the valve stem was moved away from the packing ring set inner diameter by 0.05 mm. This allows for the simulation of wear of the packing ring inner diameter. This method of analysing wear is much easier to implement in FE analysis code as opposed to the removal of elements from the packing ring set to simulate wear. The relaxation in radial stress against the stem was investigated as the valve stem was moved away from the packing ring set ID. The coefficient of friction between the packing ring set ID and the stem was defined as $\mu_{stem} = 0.15$ and the coefficient of friction between the packing ring set OD and the housing was defined as $\mu_{housing} = 0.20$.

4.3 Summary

This chapter details the material testing required to determine the input parameters for the FE constitutive material models and the validation of FE material model input parameters. Two FE models are detailed in this chapter. The first FE model is a simulation of the compression test rig. The FE model is used to validate the input parameters for the FE material model. The input parameters of the FE material models can be validated by comparing the FE results from the compression test rig model with the experimental test from the same test rig. The second FE model is a model of a packing ring set in a valve. This model uses the FE material model developed in this thesis is to investigate the influence of loading, valve stem friction, valve stem cycling and wear on the behaviour of a 1.5 g/cm^3 exfoliated graphite packing ring set.

Chapter 5

Material model validation and valve packing FE results

5.1 Material testing

5.1.1 Compression test results

The compression test rig, detailed in Section 4.1.1 was used to carry out a series of experiments to characterise the static behaviour of individual exfoliated graphite packing rings in a valve. During a test the packing ring is subjected to 2 loading cycles. The test results for 1.5 g/cm^3 exfoliated graphite packings are detailed in this chapter. Results for 1.3 g/cm^3 and 1.8 g/cm^3 exfoliated graphite packing rings can be seen in Appendix A.

Figure 5.1 describes the compression behaviour of one 1.5 g/cm^3 exfoliated graphite packing ring was subjected to 2 loading/unloading cycles. A 1.5 g/cm^3 exfoliated graphite packing ring is seen to have a non-linear elastoplastic response to applied axial stress. K_{rad} , the ratio of radial stress to applied axial stress on initial compression is seen in Figure 5.2. K_{rad} is seen to have a non linear relationship with applied axial stress over the loading range. Figure 5.3 details K_{rad} on second compression. On second compression, K_{rad} is seen to have a more uniform response to applied axial

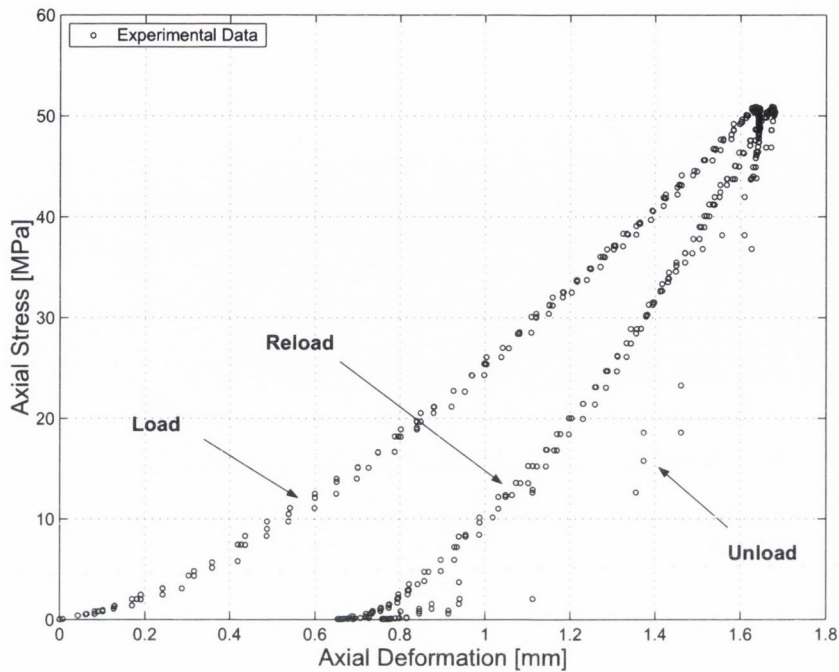


Figure 5.1: Compression of one 1.5 g/cm^3 exfoliated graphite packing ring

stress over the loading range.

5.1.2 Triaxial test results

A series of triaxial tests were carried out using a high pressure rock mechanics triaxial test rig located in the Department of Earth Science and Engineering, Imperial College, London detailed in Section 4.1.2. These tests were carried out in order to determine the input parameters for the modified Mohr Coulomb material model in DIANA and the modified Cam clay material model in ABAQUS/Standard. Details of the input parameters and the methods required to determine these parameters can be seen in Section 3.5.

The raw data from a triaxial test for 1.5 g/cm^3 exfoliated graphite using a confining pressure of 1 MPa is shown in Figure 5.4. The test specimen was subjected to two unloading cycles during the course of the test. Exfoliated

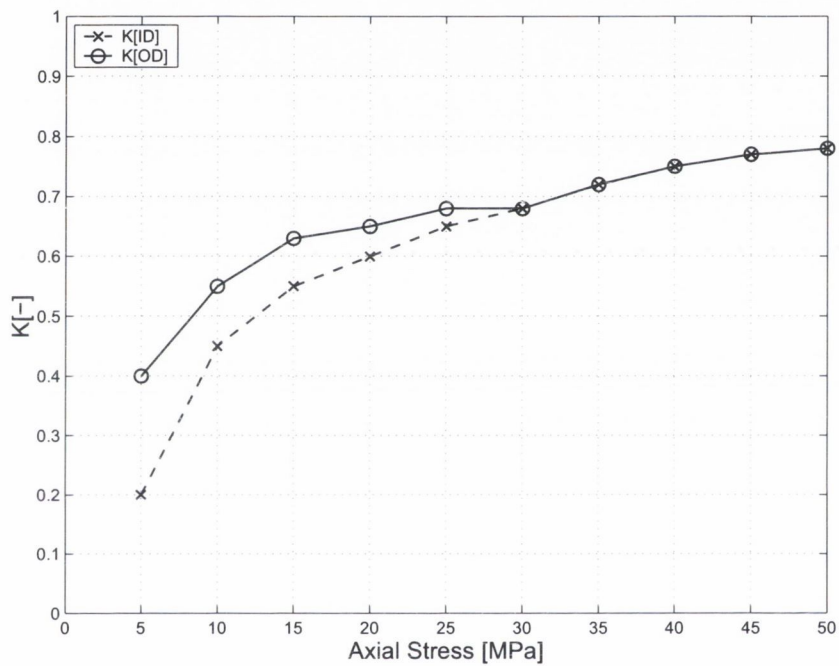


Figure 5.2: K_{rad} for the initial compression of one 1.5 g/cm^3 exfoliated graphite packing ring

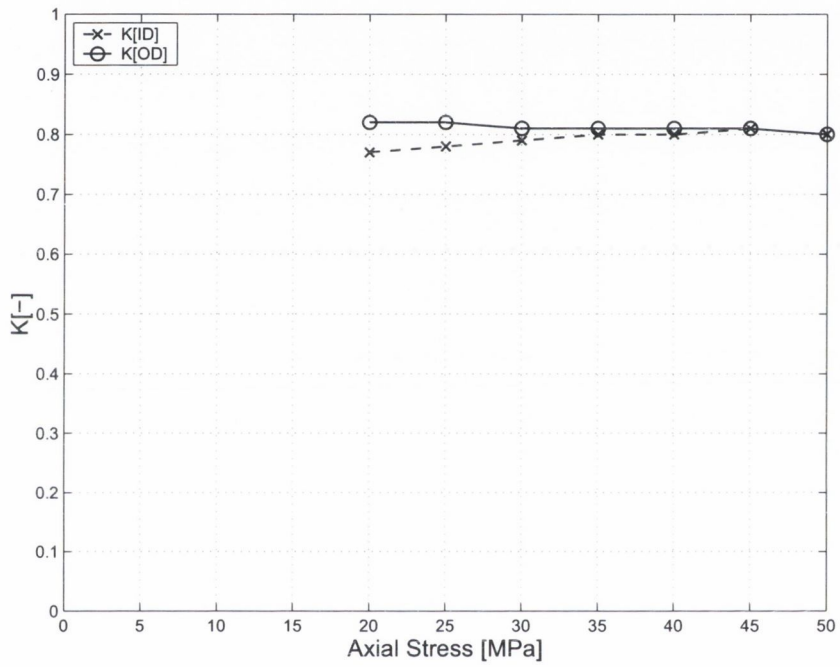


Figure 5.3: K_{rad} for the second loading cycle of one 1.5 g/cm^3 exfoliated graphite packing ring

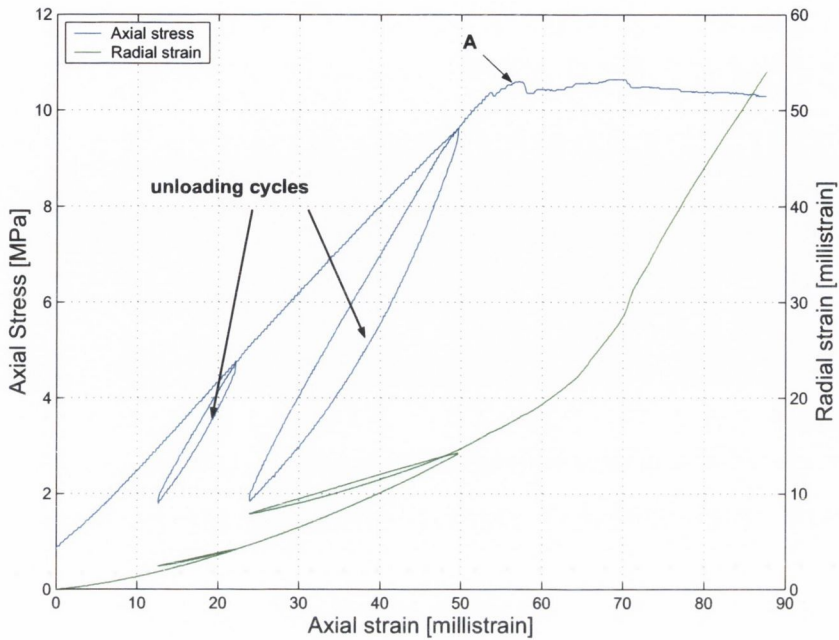


Figure 5.4: Triaxial test results for 1.5 g/cm^3 exfoliated graphite at a confining pressure of 1 MPa

graphite is seen to display non-linear elastoplastic behaviour. Point A on the graph corresponds to the peak stress of exfoliated graphite during this test. At point A failure is said to have occurred in the test specimen. At point A a bang is heard and the cylindrical test specimen shears on a failure plane. The test specimen is then seen to slip and crack further after this point. The cracking and slipping of the sample causes erratic axial stress, axial strain and radial strain responses in the specimen. In total six triaxial tests were carried out, details of the test results for these triaxial tests can be seen in Appendix B.

5.2 FE material model input parameters

5.2.1 Loading and unloading parameters

The loading and unloading parameters λ and κ can be calculated through the use of data from either the compression test rig detailed in Section 4.1.1 or the triaxial test rig detailed in Section 4.1.2.

The first method involves manipulating data obtained from the compression test rig. A single compression packing ring is placed in the compression test rig and subjected to two loading/unloading cycles. The log of applied axial stress $\log \sigma_v$ is plotted against the change in void ratio, e . Figure 5.5 shows the plot of $\log \sigma_v$ vs. void ratio for 1.5 g/cm^3 exfoliated graphite. The experimental data is seen to be highly non-linear and has to be approximated using the swelling and compression lines as described in Section 3.5.1. This method has the potential to produce inaccuracies in the calculated data as the method is quite subjective. There is no distinct point on the graph at which the behaviour of the material changes from elastic to plastic, but rather a knee in the data at which time the evolution of strains change from elastic to plastic. The swelling line, C_s describes the elastic behaviour of the material and the compression line, C_c describes the plastic irrecoverable behaviour of exfoliated graphite. Although there is some ambiguity as to the values of C_c and C_s the final chosen values are only chosen after rigorous analysis. FE variability studies were carried out determine the optimum values of C_c and C_s . The slopes of these lines are used to determine λ and κ the loading and unloading indices for the modified Cam-clay and modified Mohr Coulomb material models.

$$\lambda = \frac{C_c}{\ln 10} = \frac{-0.258}{\ln 10} = -0.11 \quad (5.1)$$

$$\kappa = \frac{C_s}{\ln 10} = \frac{-0.035}{\ln 10} = -0.015 \quad (5.2)$$

The positive values of λ and κ are inputted into the FE material model. It is vitally important that the calculated values of λ and κ are validated

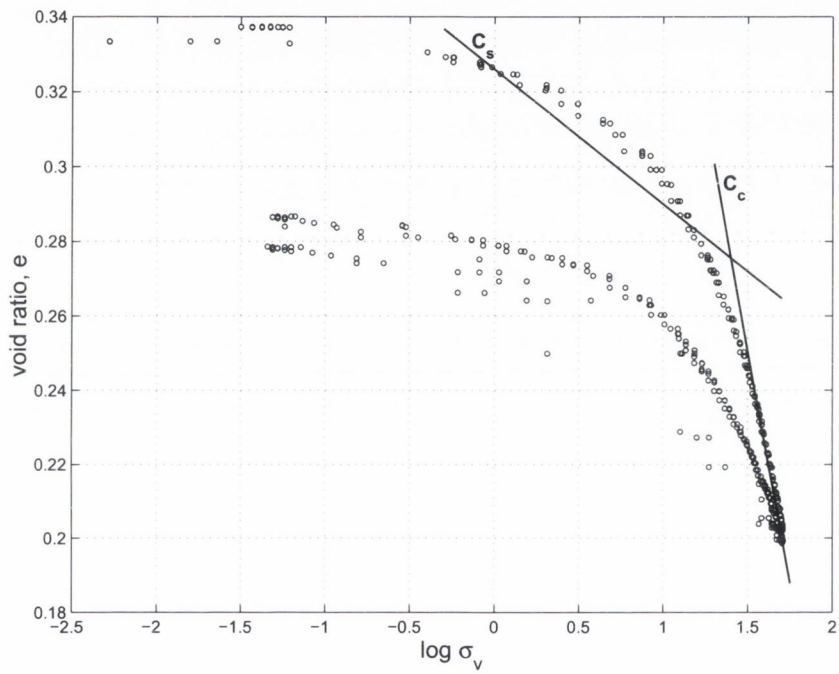


Figure 5.5: Plot of $\log \sigma_v$ vs. void ratio for 1.5 g/cm^3 exfoliated graphite

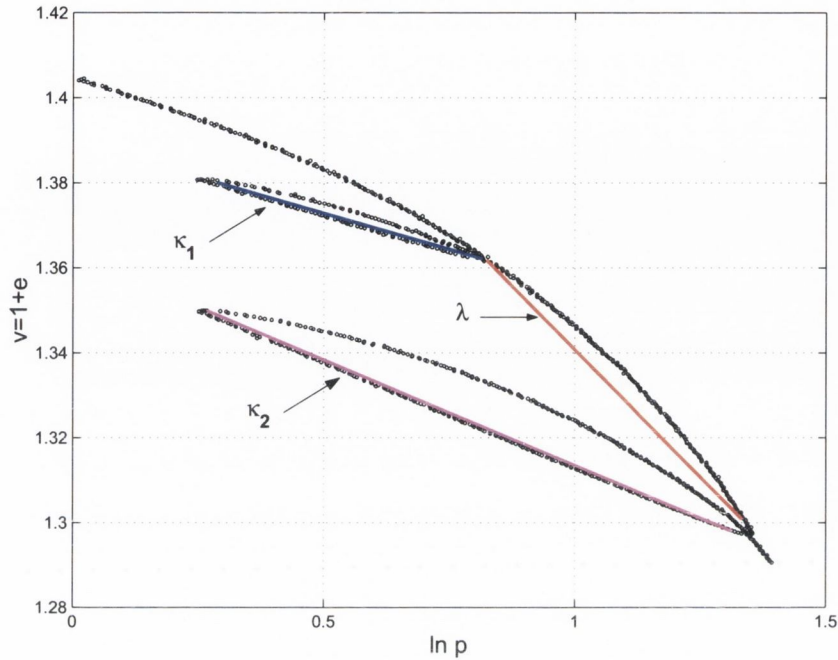


Figure 5.6: Plot of $\ln p$ vs. void ratio for 1.5 g/cm^3 exfoliated graphite

using FE analysis to determine if the calculated values produce the same response in the FE model as seen in the experimental tests. Validation of the input parameters are presented in Section 5.3. The loading and unloading parameters λ and κ can also be calculated from triaxial test data. In a triaxial test a material specimen is hydrostatically loaded up to a predefined value of confining pressure, the axial stress is then varied to determine the loading and unloading behaviour and final failure of the material. In order to determine the loading and unloading parameters λ and κ from triaxial test data the natural log of the pressure, $\ln p$ is plotted against the specific volume, v as shown earlier in Figure 3.5. The slope of the virgin consolidation line corresponds to the value of λ and the slope of the swelling line corresponds to that of κ .

The plot of $\ln p$ vs. v for 1.5 g/cm^3 exfoliated graphite can be seen in Figure 5.6. The triaxial test sample of exfoliated graphite was subjected to

two unloading cycles, therefore κ can be calculated twice to determine the variability in κ on second unloading. The calculated values of λ and κ are shown in Table 5.1.

The value of λ is the same under triaxial and one dimensional compression test conditions, the same is not true for κ . The values of κ are much greater under triaxial test conditions compared with compression test conditions. Under triaxial test conditions κ is seen to vary on second unloading producing a greater elastic response than seen on first unloading. On first unloading κ was calculated as 0.034, on second unloading the value of κ was seen to increase to 0.050. This could be due to variations in the density of the graphite discs used during triaxial testing. Triaxial testing was carried out using exfoliated graphite discs, which were stacked one on top of another in the triaxial cell. An example of one such disc can be seen in Figure 4.3.

Careful attention was paid to the manufacture of these discs, but variations in density were seen across the diameter of the discs with a minimum at the centre. The manufacturing process has been optimised for hollow rings. It is significantly more difficult to manufacture uniform density discs. It is possible that the larger values of κ seen in triaxial testing resulted from the less dense section at the centre of the exfoliated graphite discs. As the triaxial specimen is compressed the center section will collapse in on itself as a uniform density is developed through the disc set. This could result in a greater elastic response in the specimen.

Table 5.1: Calculated values of λ and κ from experimental tests

Material	Test Method	κ	λ
Graphite Powder	Die Compression	0.06	0.95
Graphite Powder	Triaxial Compression	0.108	0.96
Exfoliated Graphite	Die Compression	0.015	0.11
Exfoliated Graphite	Triaxial Compression	0.042	0.11

The values of λ and κ for exfoliated graphite are compared with the

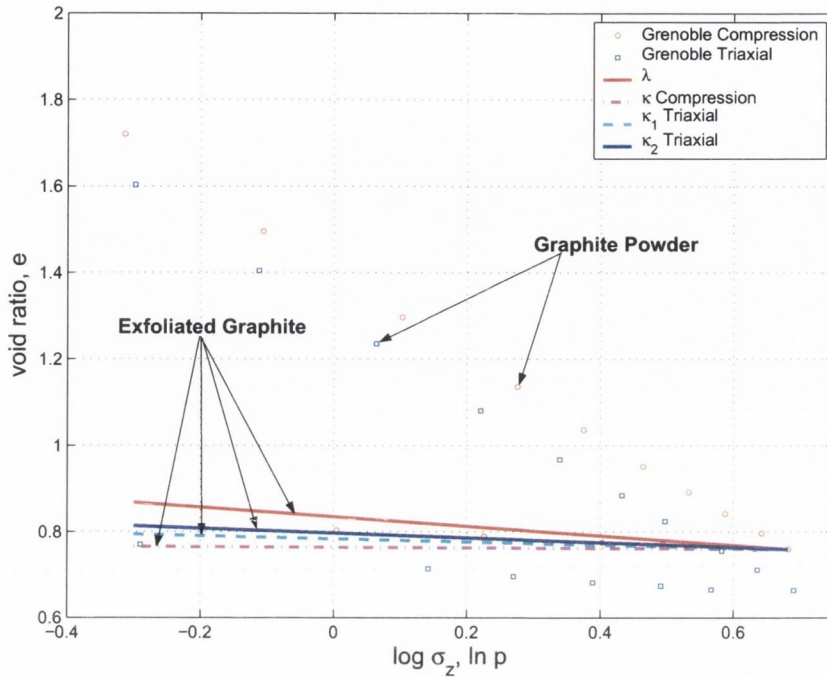


Figure 5.7: Comparison of loading and unloading behaviour of exfoliated graphite with that of powder graphite

values of λ and κ found by Bouvard et al. [57] for graphite powder. The comparison of this data can be seen in Figure 5.7. Exfoliated graphite is seen to have a much stiffer response on initial loading than graphite powder. This results from the fact that the initial density of the graphite powder used by Bouvard et al. was much lower than that of the exfoliated graphite specimens. Exfoliated graphite has a stiffer response to applied axial stress (as it has a greater density), it will not compress as much under the same loading as the looser (less dense) graphite powder. Bouvard et al. also observed variations in κ under die compression and triaxial test conditions. κ was calculated as a greater value under triaxial test conditions, the same response was seen in exfoliated graphite samples.

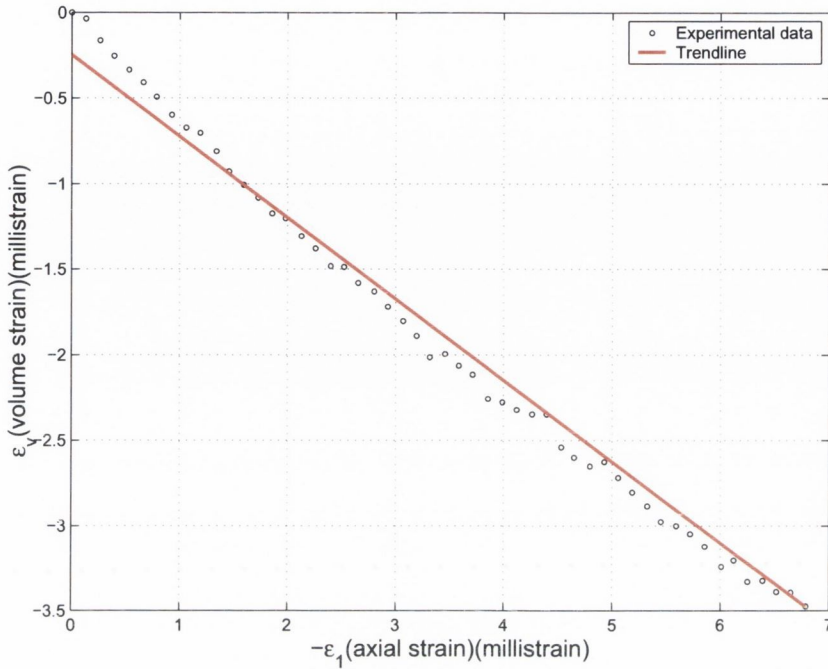


Figure 5.8: Graph of $-\epsilon_1$ vs. ϵ_v for 1.5 g/cm^3 exfoliated graphite

5.2.2 Poisson's Ratio

Poisson's ratio was calculated using a method described in Section 3.5.2, which involves plotting the negative axial strain $-\epsilon_1$ vs. the volume strain ϵ_v for a triaxial test. The slope of the curve is inputted into Equation 5.3 to determine Poisson's Ratio. The plot of $-\epsilon_1$ vs. ϵ_v for 1.5 g/cm^3 exfoliated graphite is shown in Figure 5.8. Poisson's ratio is calculated using the following method:

$$1 - 2\nu = \tan(\text{initial slope}) \quad (5.3)$$

$$1 - 2\nu = \tan(0.47) \quad (5.4)$$

$$v = 0.25 \quad (5.5)$$

5.2.3 Friction angle

The friction angle, ϕ defines the failure of the modified Mohr Coulomb material model and is determined using the method described in Section 3.3.5. In order to determine the friction angle a minimum of three triaxial test have to be carried out. The triaxial test involves applying a gradually increasing hydrostatic pressure to the sample until the chosen confining pressure is reached, at this point the confining pressure is held constant and the axial stress is increased until failure occurs. Failure corresponds to point A in Figure 5.4. The axial stress and the confining pressure at failure are recorded and plotted on a graph. Figure 5.9 shows results for 1.5 g/cm^3 exfoliated graphite. Three tests were carried out at different confining pressures and a subsequent best fit line was fitted through the test data to obtain the linear Mohr Coulomb relationship. The slope of this line corresponds to the value of the friction angle ϕ .

5.2.4 Critical state line, M

The modified Cam clay material model fails according to critical state failure criterion. Failure occurs when the material reaches an ultimate condition in which plastic shearing could continue indefinitely without changes in volume or stress [68]. This phenomenon of perfect plasticity has become known as a critical state and is defined by the constant M, which is described fully in Section 3.4.5. M is determined by plotting the mean stress, p against the deviatoric stress, q at critical state.

In the case of exfoliated graphite, failure was investigated using the triaxial test method as described in Section 4.1.2. Six triaxial tests were carried out, the details of these tests can be seen in Table Appendix B. Five of the six tests were carried out using conventional triaxial test methods. A con-

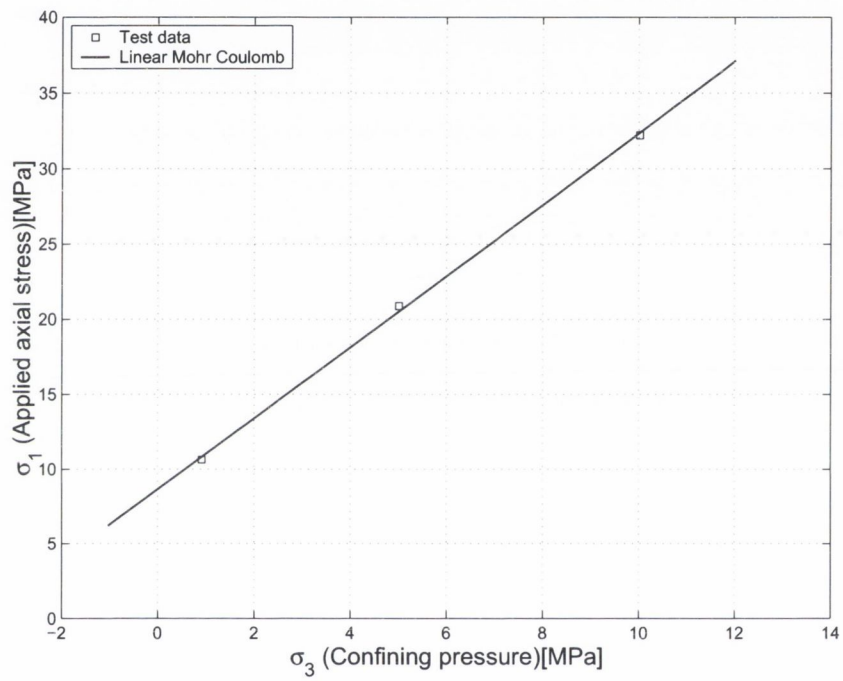


Figure 5.9: Mohr Coulomb failure envelope for 1.5 g/cm^3 exfoliated graphite

ventional triaxial test involves loading the test sample under hydrostatic test conditions until the required confining pressure has been achieved, the axial stress is then increased until the sample fails. All five conventional triaxial tests failed according to the modified Mohr Coulomb material model failure criterion.

The sixth triaxial test was a multistage test, multistage testing is used mainly in rock testing where there is can be a lack of available samples. Multistage testing involves changing the plane of failure of the material by increasing the hydrostatic pressure when the peak stress of the material has been reached, thus giving data on multiple failure planes from the one triaxial sample. The multistage test carried out on exfoliated graphite involved applying confining pressures of 1, 5, 10, 20, 30 MPa to the sample. At a confining pressure of 10 MPa constant straining was observed in the sample with only a slight increase in applied axial stress compared to other tests. A condition of near perfectly plasticity or critical state failure was observed. The material was not seen to be reaching a peak stress which would define Mohr Coulomb failure. This was the only point during triaxial testing where this phenomenon was observed. This may result from the fact that the friction angle at critical state ϕ_{cs} and λ of a material may be assumed to be material constants but M , which defines the failure in critical state is known to depend on the loading conditions [86]. The change in axial stress and axial strain with time for this portion of the test can be seen in Figure 5.10.

In order to determine M for this portion of the test p , the pressure is plotted against the deviatoric stress q . The actual experimental data shows significant scatter therefore the choice of best fit line with which to model the data was somewhat difficult to determine. The graph of p vs. q for exfoliated graphite at a confining pressure of 10MPa can be seen in Figure 5.11.

During testing it was expected that exfoliated graphite would reach a peak stress under triaxial test conditions. However in the case of the multistage test at 10MPa the test displayed constant shearing with a small increase in axial stress. A near critical state had been reached, due to time constraints

it was decided that the next stage for this test should be carried out. It is likely that after a given amount of time the stress would reach a constant value while the material would undergo constant shearing (perfect plasticity). This point was not reached during experimental testing before the confining pressure on the test sample had to be changed so that multistage testing could be continued. For this reason the 8 of the 17 data points was used to calculate the value of M for the modified Cam clay material model. The data points from Figure 5.11 were sorted according to increasing values of q , the deviatoric stress. The 4 data points with the minimum value of q and the 4 data points with the maximum value of q were discarded. The 9 remaining data points were used to calculate M . The trendline through the data points was validated using FE analysis as seen in Section 5.3 to determine if this value of M gave a best fit to the experimental data for the compression of one 1.5 g/cm^3 exfoliated graphite packing ring.

5.2.5 Predetermined input parameters

Four input parameters did not need to be calculated experimentally, these being the preconsolidation stress p_c , the strength in tension, p_t , K the dependance of yield on σ_2 for the modified Cam clay material model and β the yield surface shape of the modified Cam clay material model.

The preconsolidation pressure p_c , is the pressure that the compression packing was subjected to when it was manufactured, in the case of 1.5 g/cm^3 this is 11 MPa [Burgmann Packings, personal communication, 2001].

The choice of tensile strength should not have a strong effect on the numerical results unless the soil is stressed in hydrostatic tension. A common approximation is to set p_t equal to 5% to 10% of the initial yield stress in hydrostatic compression [62]. Exfoliated graphite is known to be capable of supporting tensile stresses of up to 8 MPa. The properties of exfoliated graphite especially tensile strength, can vary greatly depending on production methods [Carbon Lorraine, personal communication, May 2004].

β represents the curvature of the cap part of the yield surface and can

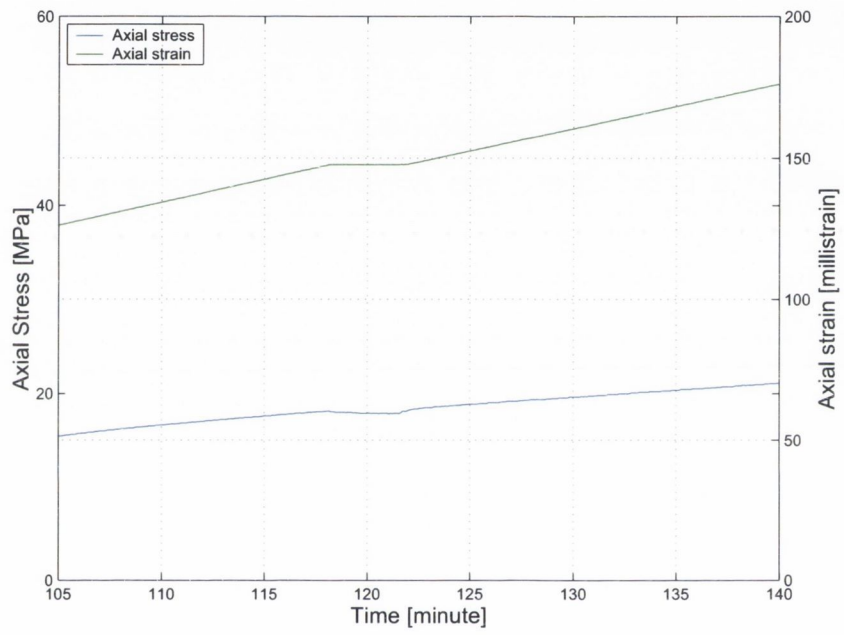


Figure 5.10: Evolution of axial stress and axial strain versus time at critical state

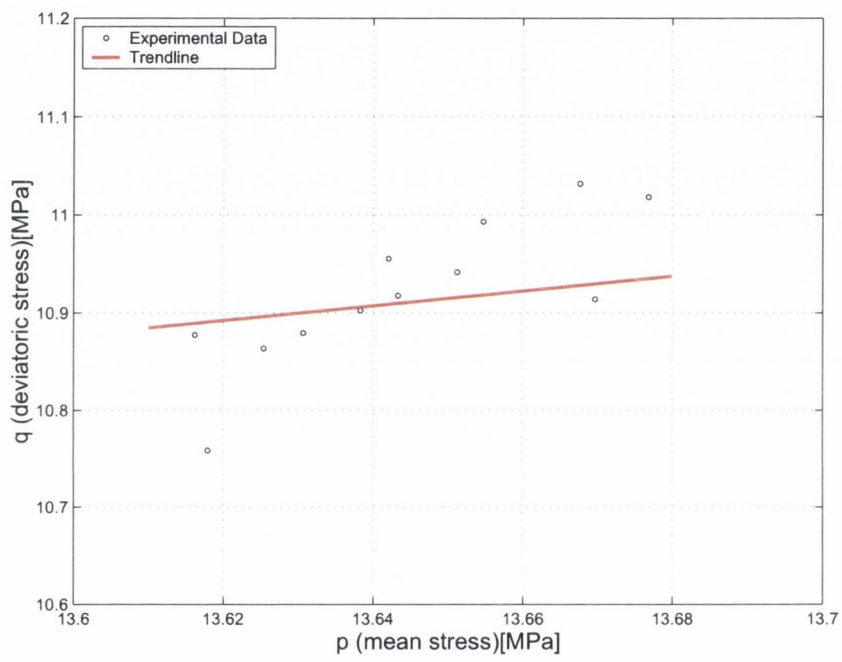


Figure 5.11: Determining M , the critical state line

be calibrated from a number of triaxial tests at high confining pressures (on the "wet" side of critical state). β must be between 0.0 and 1.0, this effect can be seen in Figure 3.11. To calibrate the parameter K , which controls the yield dependence on the third stress invariant, experimental results obtained from a true triaxial (cubical) test are necessary. These results are generally not available, and the user may have to guess (the value of K is generally between 0.8 and 1.0) or ignore this effect [62].

5.2.6 Material model input parameter summary

Table 5.2 details the input parameters for the FE material models and the respective experimental errors associated with these values. Two separate values of κ are included in the table because the value of κ under triaxial test conditions was significantly higher than that obtained under confined compression conditions. Experimental tests carried out by Bouvard et al. It is not possible to compare the errors for κ since the results from compression tests are so significantly different than those from triaxial tests. [57] found that κ varied depending on the loading conditions whereas λ didn't. They are not strictly comparable therefore it was deemed necessary to include the value of κ under both triaxial and confined compression conditions and their respective errors.

5.3 FE material model validation

Table 5.3 details the input parameters for the modified Mohr Coulomb material model in DIANA and the modified Cam clay material model in ABAQUS/Standard respectively. Different values of κ are used in DIANA and ABAQUS/Standard. The values of κ under triaxial test conditions is seen to give the best result in DIANA whereas the value of κ under one dimensional compression is seen to give the a best match to the experimental test results in ABAQUS/Standard. Contact friction has a significant influence on the loading and unloading behaviour of compression packing rings in a valve, but it is not known if the

Table 5.2: FE material model input parameters and their associated error

Input parameters		Error
λ	0.11	$\pm 10\%$
$\kappa_{compression}$	0.015	$\pm 10\%$
$\kappa_{triaxial}$	0.042	$\pm 35\%$
ν	0.25	$\pm 20\%$
e_0	0.5	-
p_c	11 MPa	-
p_t	1.1 MPa	-
$\sin\phi$	0.406	$\pm 5\%$
M	0.75	$\pm 20\%$
β	1	-
K	1	-

inclusion of contact friction in DIANA would allow for the use of κ under one dimensional compression. The loading and unloading behaviour of the modified Cam Clay material model and the modified Mohr Coulomb material models are formulated for triaxial test conditions and should therefore give the same results given the same values of λ and κ .

ABAQUS		DIANA	
λ	0.11	λ	0.11
κ	0.015	κ	0.042
ν	0.25	ν	0.25
e_0	0.5	e_0	0.5
M	0.75	p_c	11 MPa
β	1	p_t	1.1 MPa
K	1	$\sin\phi$	0.406

Table 5.3: FE material model input parameters

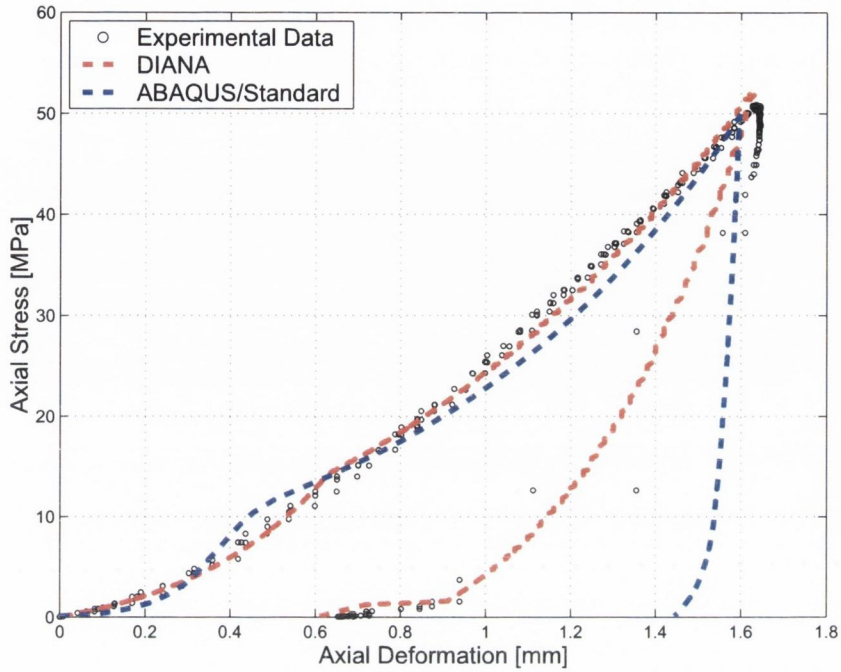


Figure 5.12: Comparison of FE and experimental results for the compression of one 1.5 g/cm^3 exfoliated graphite packing ring

Figure 5.12 compares the FE results for the axial compression of one 1.5 g/cm^3 exfoliated graphite packing ring with experimental results obtained for tests carried out using the compression test rig detailed in Section 4.1.1. The FE model is detailed in Section 4.2.1. On initial loading both DIANA and ABAQUS/Standard show very good correlation with the experimental data. On unloading DIANA is seen to match the experimental data slightly better than ABAQUS/Standard.

Figure 5.13 details $K[\text{ID}]$, the ratio of radial stress to axial stress on initial compression for both DIANA and ABAQUS/Standard. FE results for $K[\text{OD}]$ are omitted as they are very similar to that of $K[\text{ID}]$. The FE results from ABAQUS/Standard are compared with the experimental data for $K[\text{ID}]$ and $K[\text{OD}]$. The results for ABAQUS/Standard are seen to match

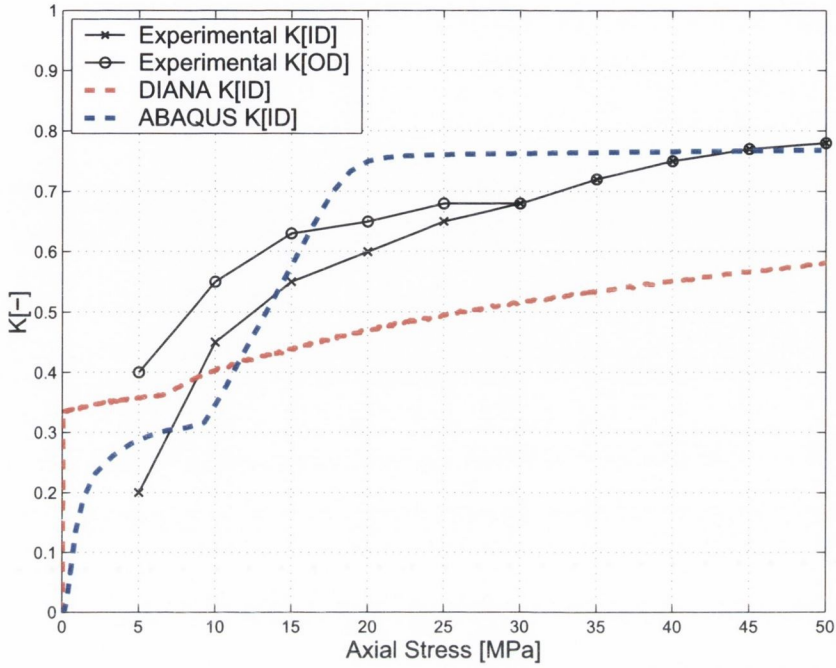


Figure 5.13: Comparison of FE results with experimental results for $K[ID]$ for the compression of one 1.5 g/cm^3 exfoliated graphite ring

the experimental data more closely than DIANA. The lower values of $K[-]$ seen in DIANA probably result from the lack of friction at the contact interfaces. At the time of writing it was not possible to include contact friction in DIANA as convergence problems occurred. Friction is known to aid the transfer in applied axial stress into radial sealing stress. For completeness Figure 5.14 is included to show both $K[ID]$ and $K[OD]$ for ABAQUS/Standard as compared with experimental data.

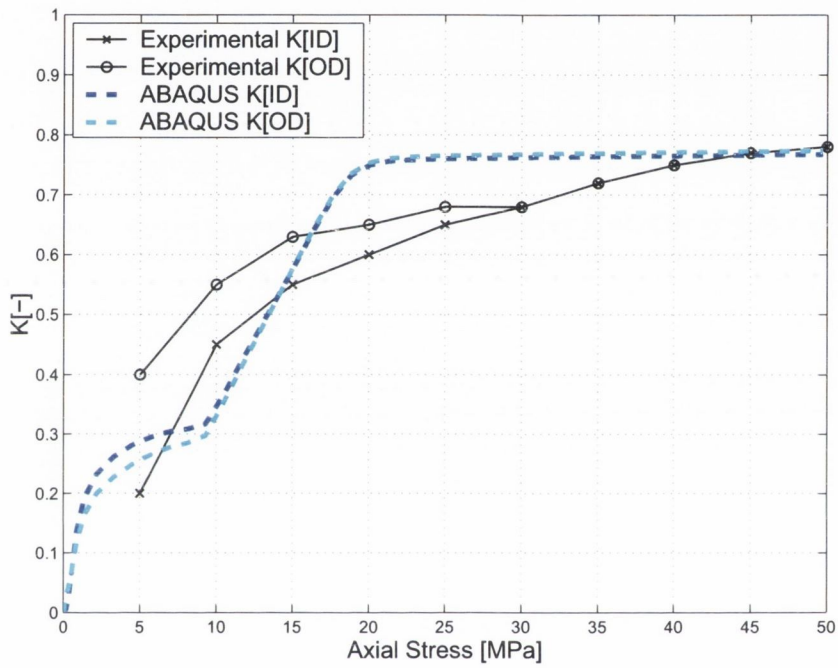


Figure 5.14: Comparison of experimental results and FE analysis using ABAQUS/Standard for K[ID] and K[OD] for one 1.5 g/cm^3 exfoliated graphite ring

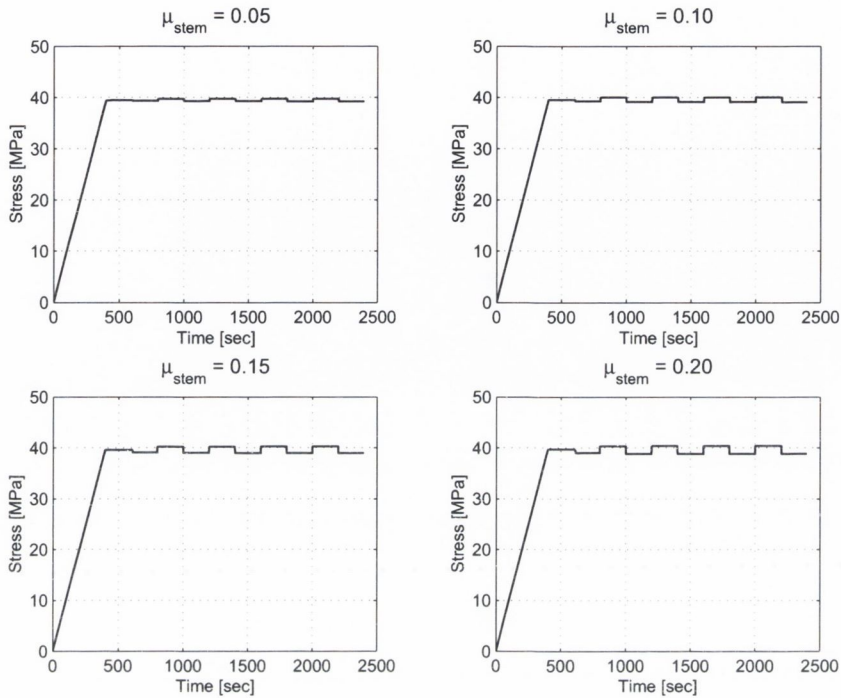


Figure 5.15: Axial stress at the top of seal 1 for $\mu_{stem} = 0.05$ to $\mu_{stem} = 0.20$, under load control conditions

5.4 Valve packing behaviour

5.4.1 Axial stress

Figures 5.15 and 5.16 detail the average stress at the top of seal 1 under load control conditions. The coefficient of friction between the stem and packing ring set inner diameter μ_{stem} is varied and the resultant influence of stem friction on the applied axial stress is investigated. As the valve stem is cycled increasing fluctuations in applied axial stress can be seen with increasing stem friction.

Figures 5.17, 5.18 and 5.19 details the applied axial stress at the top of seal 1 under displacement control conditions. The force is not constant, after the valve has been cycled once a significant decay in applied axial stress can

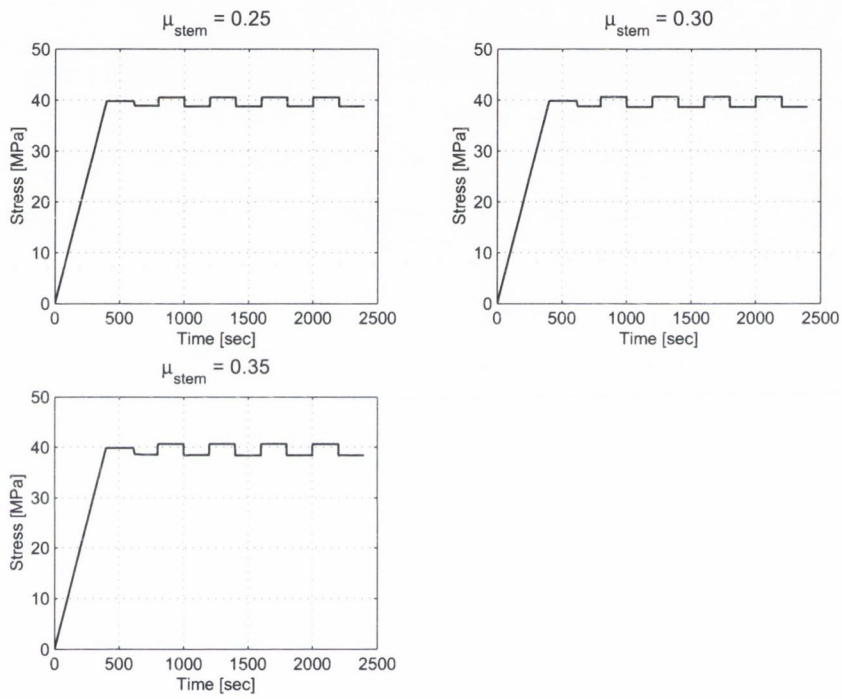


Figure 5.16: Axial stress at the top of seal 1 for $\mu_{stem} = 0.25$ to $\mu_{stem} = 0.35$, under load control conditions

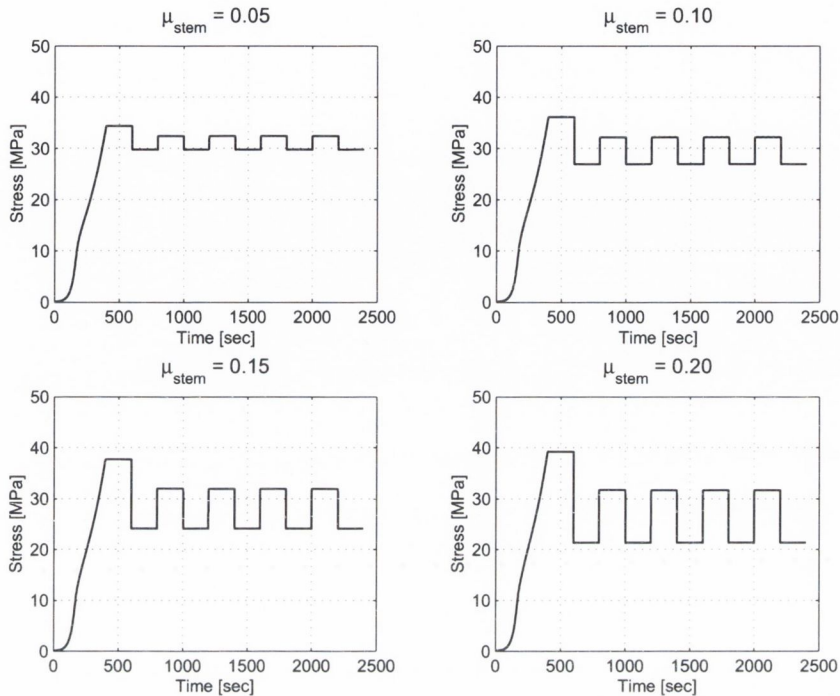


Figure 5.17: Axial stress at the top of seal 1 for $\mu_{stem} = 0.05$ to $\mu_{stem} = 0.20$, under displacement control conditions

be seen at the top of seal 1. This phenomenon becomes more pronounced as the coefficient of friction between the stem and the packing rings set is increased. On cycling the stress at the top of seal 1 fluctuates depending in whether or not the valve is being opened or closed.

5.4.2 Stress against the stem

The stress distribution against the stem after initial compression under displacement control conditions is seen in Figure 5.20. The stress distribution against the stem under displacement control conditions shows less scatter than results under load control conditions, which can be seen in Figure 5.21.

After the initial compression stage the valve is cycled 5 times. The radial

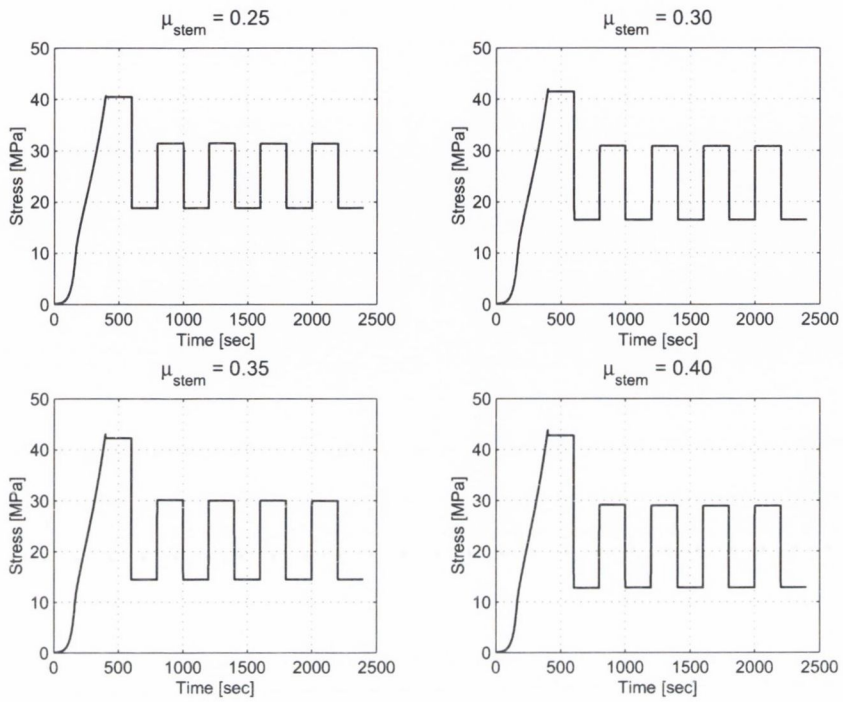


Figure 5.18: Axial stress at the top of seal 1 for $\mu_{stem} = 0.25$ to $\mu_{stem} = 0.40$, under displacement control conditions

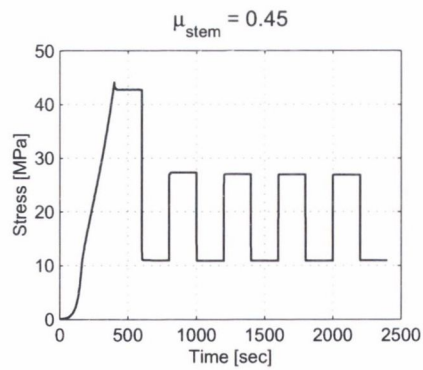


Figure 5.19: Axial stress at the top of seal 1 for $\mu_{stem} = 0.45$, under displacement control conditions

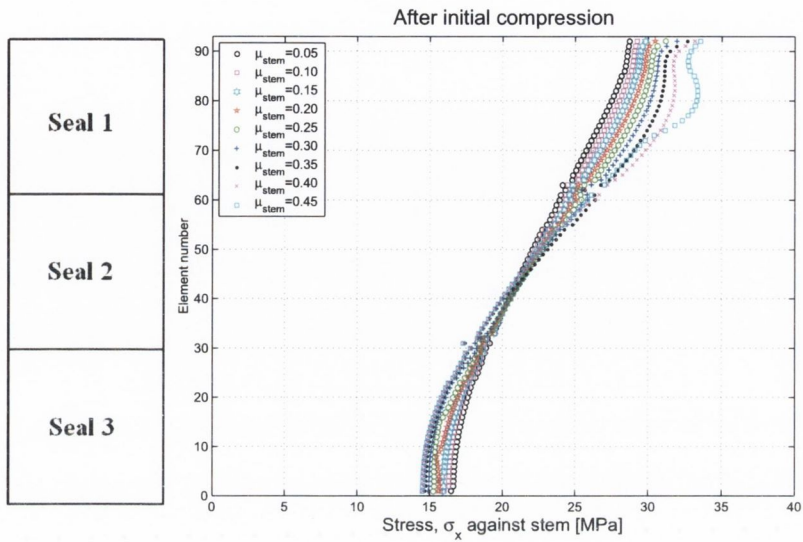


Figure 5.20: Radial stress against stem after initial compression under displacement control conditions

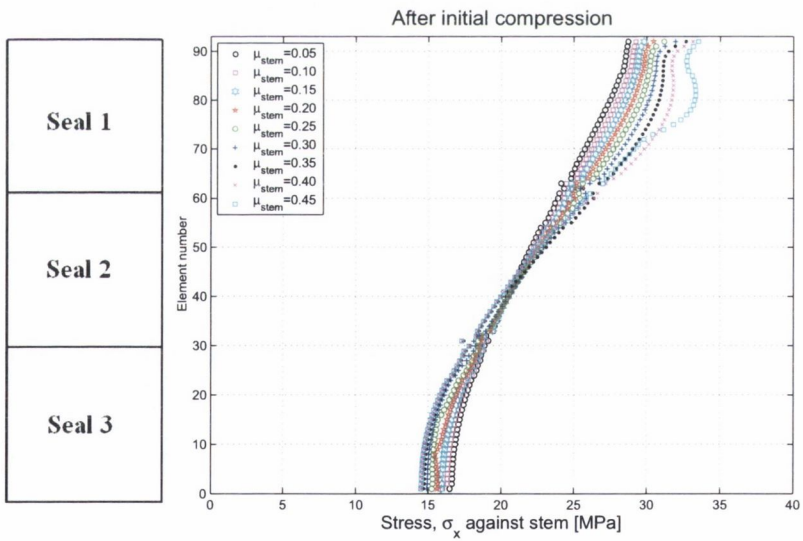


Figure 5.21: Radial stress against stem after initial compression under load control conditions

stress distribution against the stem on initial compression and after 5 valve cycles is compared to determine the influence of valve stem cycling on the radial stress distribution against the stem. Figures 5.22 and 5.23 show the influence of valve stem cycling on the stress distribution against the stem under load control conditions. After the valve stem is cycled 5 times the radial sealing stress against the stem is seen to increase.

Under displacement control conditions the stress against the stem on initial compression and after 5 cycles is very similar for values of $\mu_{stem} = 0.05$ to $\mu_{stem} = 0.20$ as seen in Figure 5.24. For values of $\mu_{stem} = 0.25$ to $\mu_{stem} = 0.45$ the stress against the stem deviates after initial compression, this result can be seen in Figures 5.25 and 5.26. The stress distribution against the stem is seen to deteriorate after cycling, leading to a reduction in sealing stress against the stem, and hence an increase in the likelihood of leakage.

5.4.3 Force required to cycle stem

Figures 5.27 and 5.28 show the force required to cycle the stem under load control conditions as the friction between the stem and the packing ring inner diameter is increased from $\mu = 0.05$ to $\mu = 0.35$. As expected the force required to move the stem increases as the coefficient of friction between the stem and the packing ring set inner diameter is increased.

The force required to cycle the stem under displacement control conditions can be seen in Figures 5.29, 5.30 and 5.31. The force required to cycle the stem under displacement control conditions is not as large as under load control conditions because the radial stress against the stem is lower under displacement control conditions than for load control conditions.

5.4.4 Wear analysis

FE analysis is carried out using a FE model described in Section 4.2.2. The model is loaded under displacement control conditions, the valve stem is then

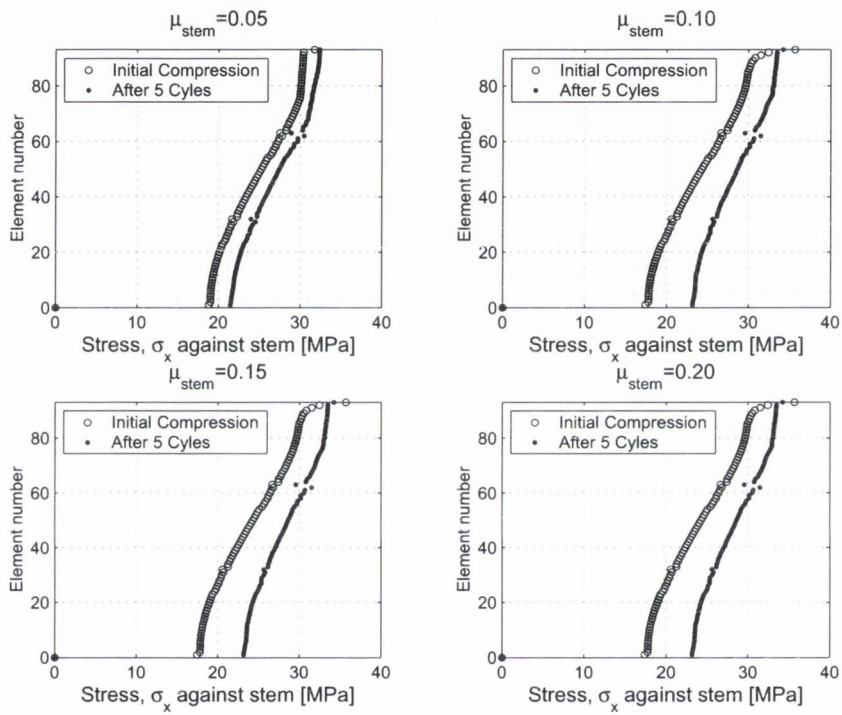


Figure 5.22: Comparison of radial stress against the stem on initial compression and after 5 cycles for $\mu_{stem} = 0.05$ to $\mu_{stem} = 0.20$, under load control conditions

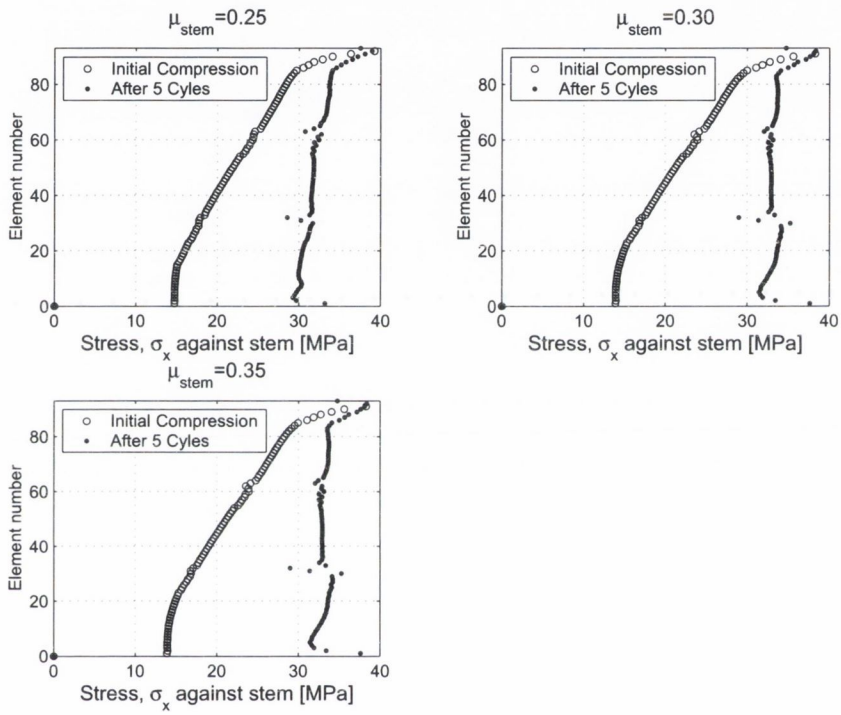


Figure 5.23: Comparison of radial stress against the stem on initial compression and after 5 cycles for $\mu_{stem} = 0.25$ to $\mu_{stem} = 0.35$, under load control conditions

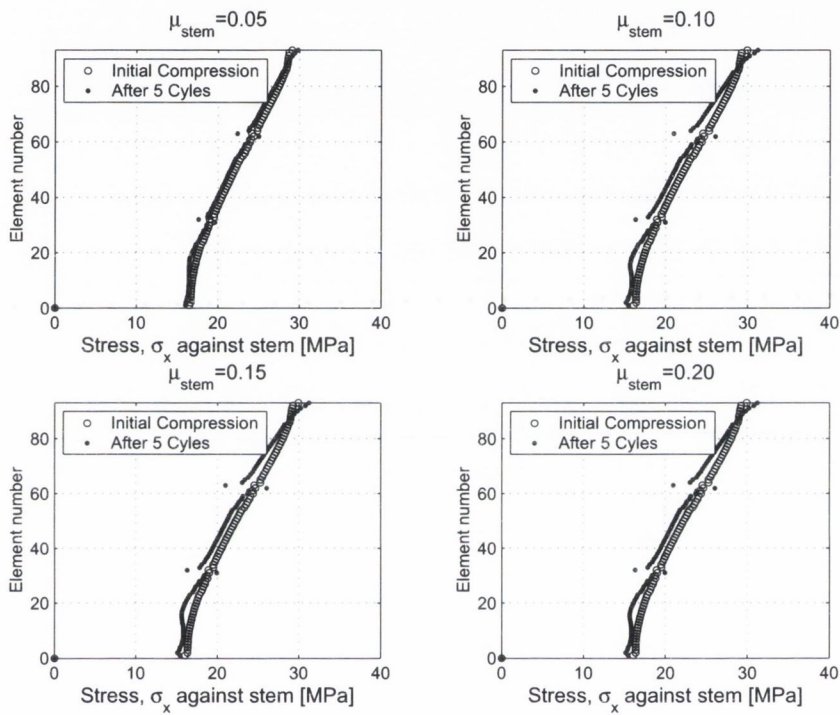


Figure 5.24: Comparison of radial stress against the stem on initial compression and after 5 cycles for $\mu_{stem} = 0.05$ to $\mu_{stem} = 0.20$, under displacement control conditions

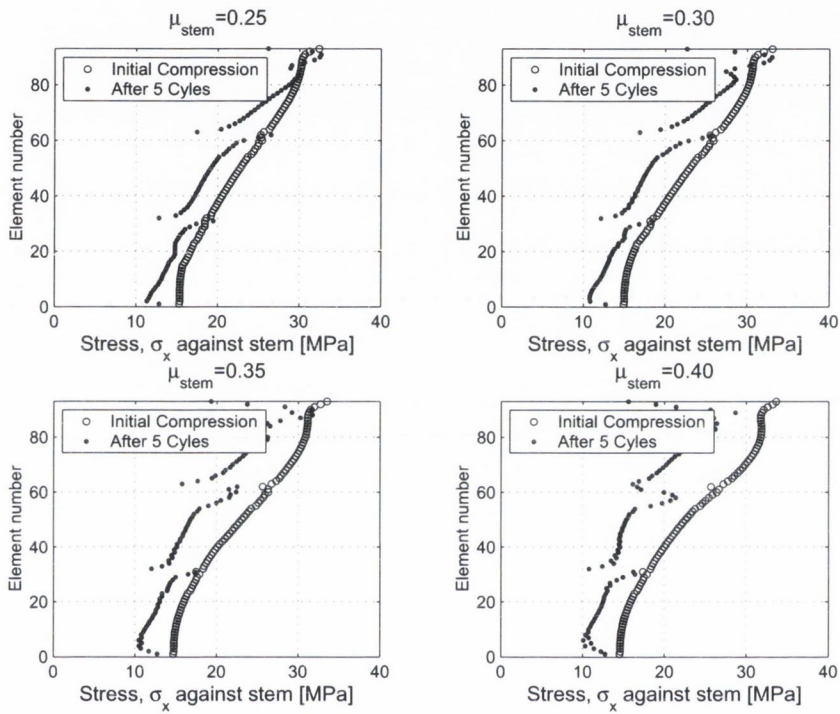


Figure 5.25: Comparison of radial stress against the stem on initial compression and after 5 cycles for $\mu_{stem} = 0.25$ to $\mu_{stem} = 0.40$, under displacement control conditions

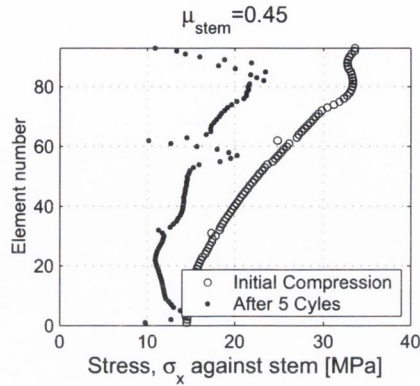


Figure 5.26: Comparison of radial stress against the stem on initial compression and after 5 cycles for $\mu_{stem} = 0.45$, under displacement control conditions

cycled 5 times. Following this initial analysis the stem is then moved away from the ID of the packing rings set. The relaxation in radial stress against the stem is recorded. The FE data is used to generate a law to predict the stress relaxation that occurs due to wear of the packing ring set ID. The stress against the stem is taken as an average along the length of the packing ring set. W_c , the wear depth divided by the packing ring thickness is plotted against S_c , the current stress divided by the initial stress before any wear occurred.

The results of this analysis can be seen in Figure 5.32. The trend line of this data can be used to predict the reduction in radial sealing stress that will occur if wear occurs at the packing ring set ID.

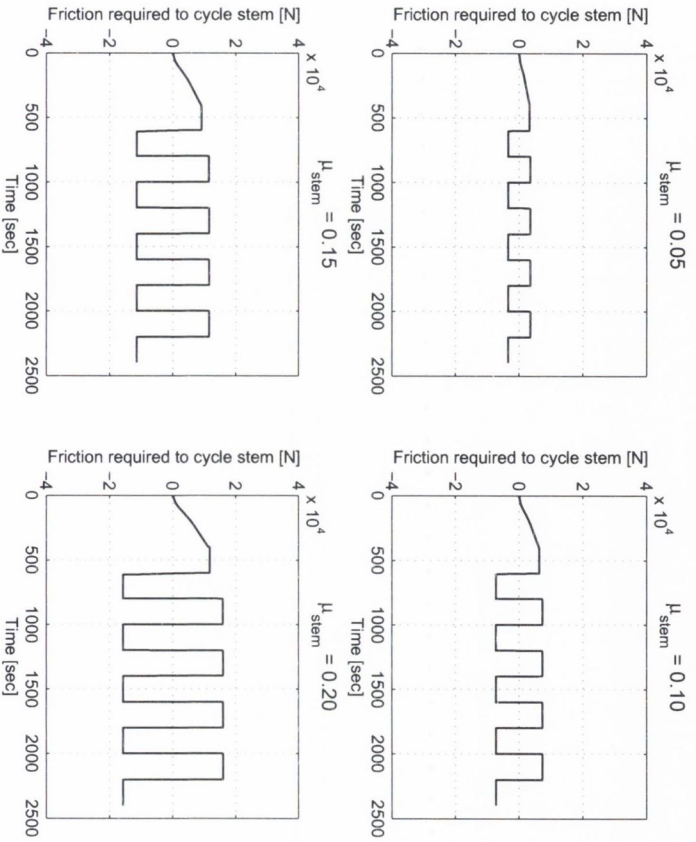


Figure 5.27: Force required to cycle the stem under load control conditions for $\mu_{stem} = 0.05$ to $\mu_{stem} = 0.20$

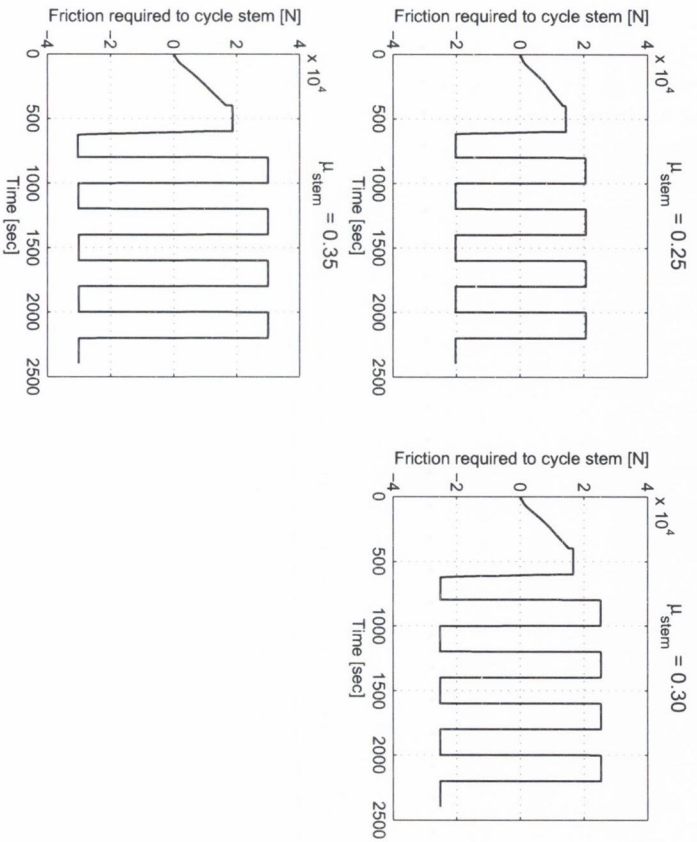


Figure 5.28: Force required to cycle the stem under load control conditions for $\mu_{stem} = 0.25$ to $\mu_{stem} = 0.35$

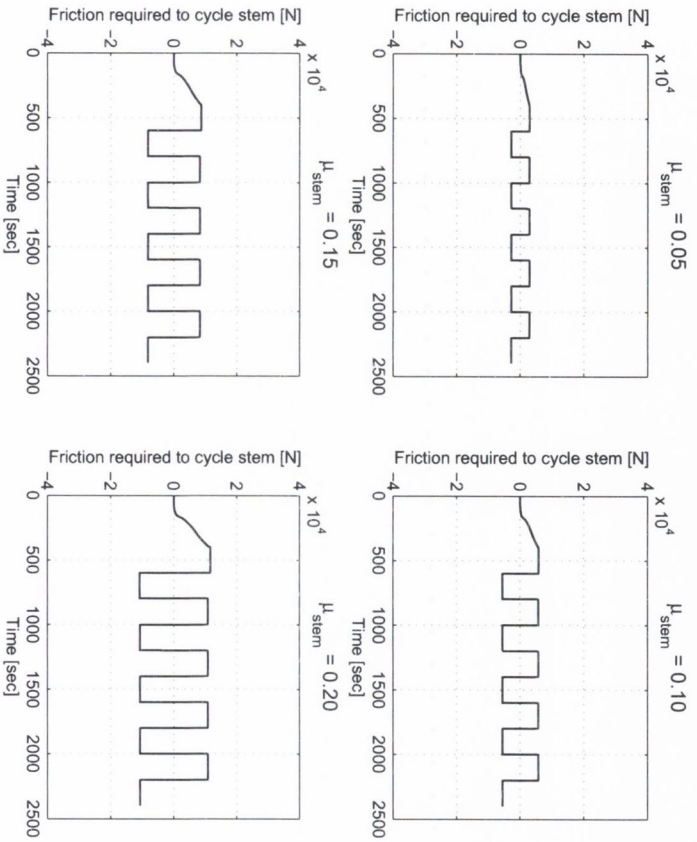


Figure 5.29: Force required to cycle the stem under displacement control conditions for $\mu_{stem} = 0.05$ to $\mu_{stem} = 0.20$

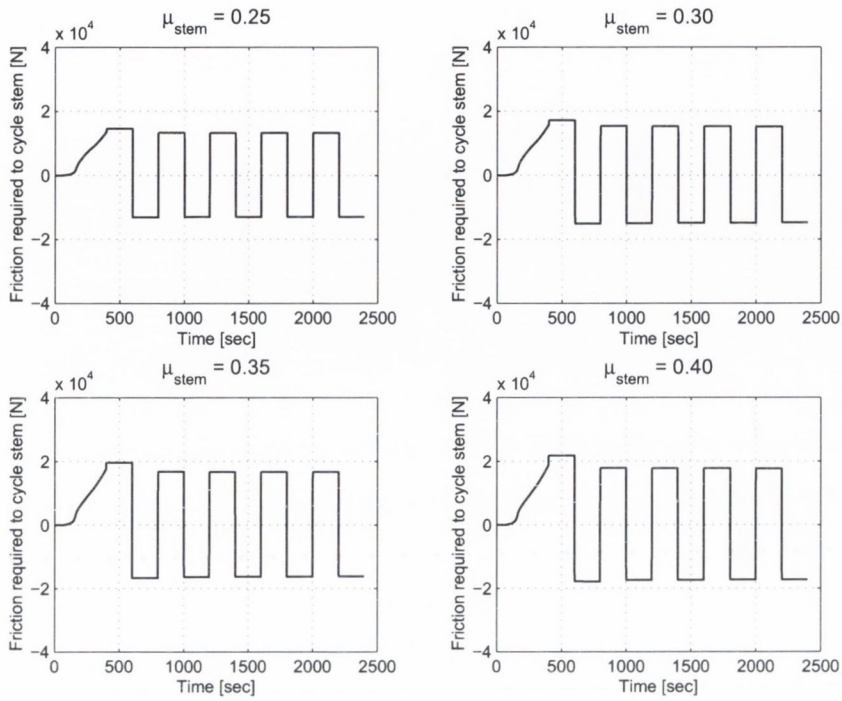


Figure 5.30: Force required to cycle the stem under displacement control conditions for $\mu_{stem} = 0.25$ to $\mu_{stem} = 0.40$

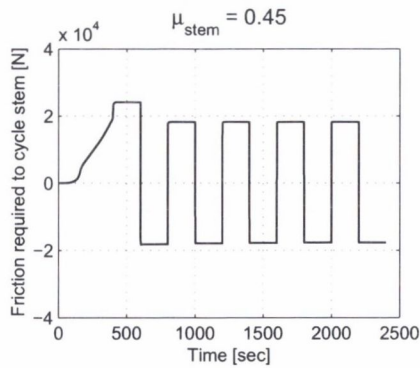


Figure 5.31: Force required to cycle the stem under displacement control conditions for $\mu_{stem} = 0.45$

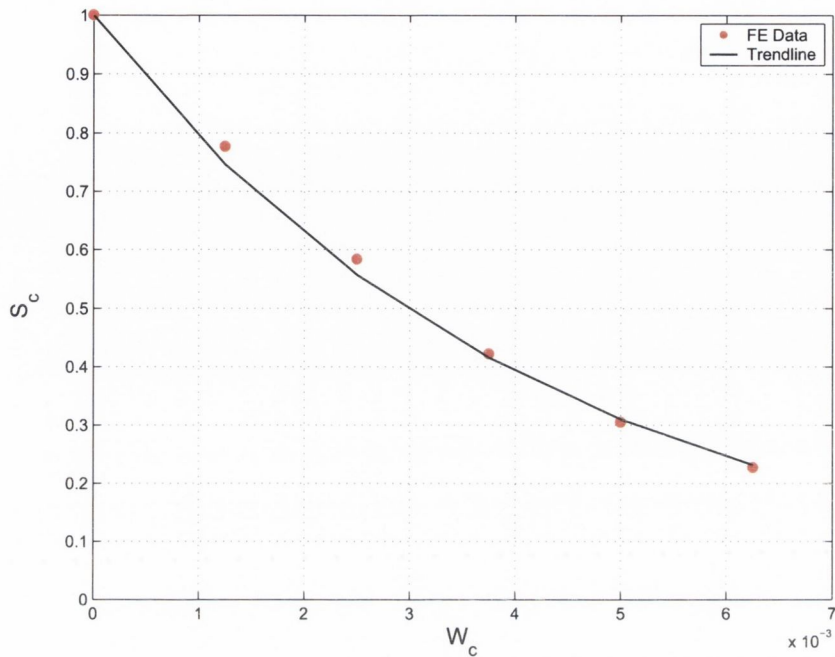


Figure 5.32: Plot of W_c versus S_c

5.5 Conclusion

This chapter presents results from the compression test rig and from tri-axial testing for 1.5 g/cm^3 exfoliated graphite. Results from these experimental tests are used to determine the input parameters for the FE material models. The Cam clay material model in ABAQUS/Standard for 1.5 g/cm^3 is then validated using FE analysis. The Cam clay material model in ABAQUS/Standard is then used to investigate the influence of loading, valve stem friction, valve stem cycling and wear on the behaviour of an exfoliated graphite packing ring set.

Chapter 6

Friction and wear analysis

6.1 Introduction

Practical engineering experience shows that the texture of rubbing surfaces plays an important role in the forces that develop between these surfaces, this phenomenon is described in detailed in Section 2.6. In this thesis the influence of valve stem surface roughness on the friction and wear behaviour of the packing-stem interface is investigated. The valve stem is made up of a series of asperities (microscale hills and valleys), these asperities have an average slope of a given angle depending on the method of manufacture of the valve stem, i.e. turning or grinding. The effect of asperity slope on the friction and wear behaviour of exfoliated graphite is investigated in this chapter using experimental, analytical and FE methods.

There is very little literature available on the frictional behaviour of exfoliated graphite. There is however, a significant amount of published literature available on the behaviour of a harder surface sliding over a softer surface. This literature details analytical models which can be used to model the behaviour of a single hard asperity sliding on a softer surface. One such model is the Oxley model detailed in Section 2.6.1, which has been previously adapted for elastoplastic materials. It is proposed that this model could be used to model the influence of asperity slope on the friction behaviour of exfoliated

graphite packing rings. The wedge asperity model developed by Oxley et al [20] is quite well suited to modelling such surfaces, since their lay, perpendicular to the direction of motion, tends to produce counterface, thus conforming to the model's basic assumption.

However, it is not known if the Oxley model will realistically model the influence of asperity slope on the friction behaviour of exfoliated graphite packing rings. Therefore an experimental test had to be devised that could investigate the influence of asperity slope on the friction and wear behaviour of compression packing rings.

6.2 Wedge test rig

In designing a tribological test to investigate the influence of asperity slope on the friction and wear behaviour of compression packing rings the following issues had to be considered and their demands be brought to bear on the design of the experimental test rig.

Previous friction testing has been based on large scale macro analysis of complete packing ring sets in real or simulated valve. This type of analysis does not allow for the measurement of radial stress at the packing stem interface. This leads to some uncertainty in the interpretation of the experimental results. The tribological test rig should allow for the controlled application and measurement of radial stress against the packing ring set.

The friction of graphite depends strongly on the nature of the ambient atmosphere. In vacuum or in dry nitrogen, μ is typically ten times greater than in air, and graphite under these conditions wears very rapidly. Controlled addition of gases and vapours reveals that the low friction and wear of graphite depends on the presence of oxygen, water vapour, or other condensable vapours [51]. The influence of oxygen on the friction and wear behaviour of graphite packing rings is significant and as a result the tribological test needs to allow for the control of the atmosphere in the test rig.

The test rig is a microtribological test rig which was designed and built

to investigate the influence of asperity surface slope and environment on the friction and wear behaviour of compression packing rings. The test rig is designed so that it mimics the interaction of a single asperity on an on/off valve as it is opened and closed. Valve stems are normally manufactured by either turning or grinding the valve stem a section of bar stock. This produces asperities at 90° to the direction of sliding of the on off valve.

A single asperity is modelled by a large scale steel wedge. The test rig consists of a wedge of a selected angle mounted on an arm. The arm and wedge are loaded with a given force, the wedge test rig accurately controls and records the radial force applied to the packing ring set by the steel wedge. The wedge is rubbed back and forth in a reciprocating motion against the ID of the 3 packing rings mounted inside the test head shown in Figure 6.1. The test head has an outer diameter of 50mm. The size of the test rig was kept at a minimum to avoid bending of the tool and to allow for control of the atmosphere in the test head. Problems with controlling the atmosphere within the test head are reduced if space is kept to a minimum. The test rig allows for tests to be carried out using different media, i.e. air or argon.

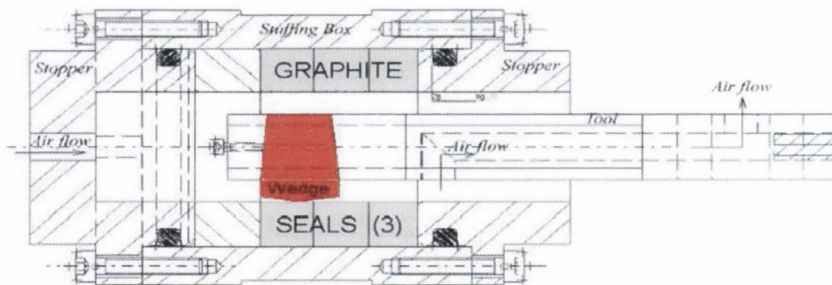


Figure 6.1: Cross section of test head

The stuffing box is fixed and the arm and wedge is connected to the existing part of the rig (dynamometer). On the right hand side the system is closed, with a piece of flexible rubber membrane for air tightness. The rubber membrane is soft enough not to affect the test data. Two connectors, one on the tool and one on the left stopper are attached to plug tubes to

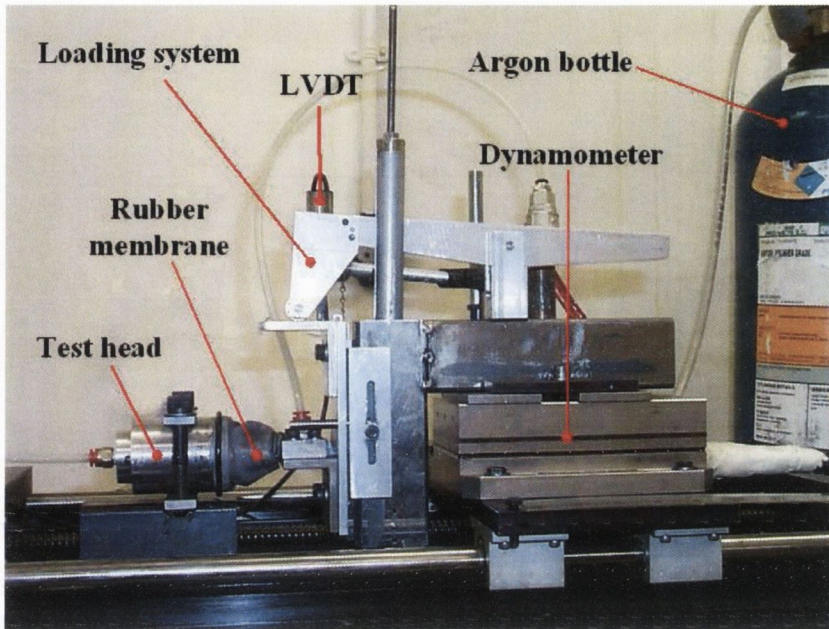


Figure 6.2: Friction test rig

facilitate air/gas flow. The friction test rig system is shown in Figure 6.2.

The test is controlled by a PC and in house software. This software allows the users to input the speed of sliding, the acceleration, the number of samples and the length of the test. The computer controls the stepper motor through the stepper interface.

The dynamometer transmits two signals in volts to the amplifiers, one for normal force and the other for tangential force. From this data the computer is able to calculate the coefficient of friction using Amonton's law, see Equation 2.8. The wedge test rig is also instrumented with an LVDT to measure the vertical displacement of the wedge during cycling. From this data the wear that occurs during testing can be recorded. All wedge tests in this thesis were carried out using the following test conditions, the wedge was loaded with a force of 20 N. The wedge was then stroked against the inner diameter of 3 packing rings with an average speed of 6.316 mm/s for

201 strokes, with a stroke length of 30 mm. Four different wedge angles were used during the programme of experimental testing, these being 4.00° , 5.88° , 8.12° and 8.93° wedge angles. These wedge angles represent the spectrum of asperity angles seen on standard valve stems. A ground and polished valve stem will have an average asperity angle of approximately 4° while a turned valve stem will have an approximate average asperity slope of approximately 8° .

6.3 Friction results

Tests were carried out using four different densities of exfoliated graphite and 3 different braided graphite packing rings types. Results for 1.5 g/cm^3 exfoliated graphite and a special 1.5 g/cm^3 exfoliated graphite packing ring type are detailed in this chapter. The special 1.5 g/cm^3 exfoliated graphite packing ring has a secondary substance included in the packing ring that cannot be detailed in this thesis due to a company confidentially agreement. This secondary substance is an additive which is known to aid lubrication at the packing stem interface. Results for 1.4 g/cm^3 exfoliated graphite and 1.6 g/cm^3 exfoliated graphite are detailed in Appendix B. Results for the 3 braided graphite packing ring types Teadit 2001, Teadit 2200 and Teadit 2202 can be seen in Appendix D.

6.3.1 1.5 g/cm^3 exfoliated graphite

Results for the coefficient of friction of 1.5 g/cm^3 exfoliated graphite are displayed in Figures 6.3 and 6.4 for air and argon respectively. Tests were carried out using 5.88° , 8.12° and 8.93° wedge angles. The results for 1.5 g/cm^3 exfoliated graphite in air shows that the wedge angle has a distinct influence on the coefficient of friction. The greater the wedge angle the higher the coefficient of friction. There is also a definite increase in coefficient of friction with increasing stroke number. The increase is between 9% and 13% in air depending on the angle of the wedge. In argon these effects are greatly

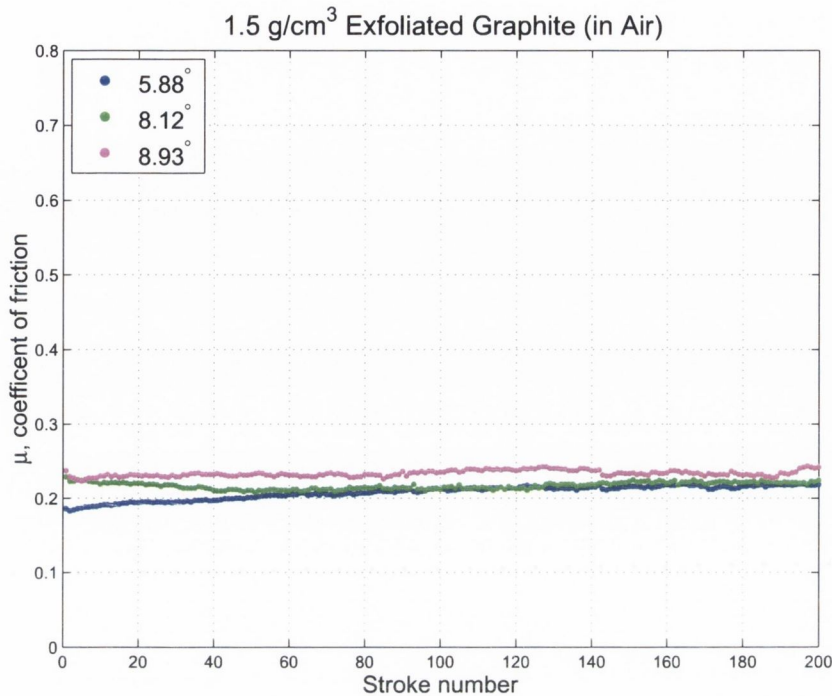


Figure 6.3: Stroke number versus coefficient of friction for 1.5 g/cm^3 exfoliated graphite in air

magnified. An increase of between 42% to 50% in the coefficient of friction is seen over the course of 201 strokes.

6.3.2 Special 1.5 g/cm^3 exfoliated graphite

Figures 6.5 and 6.6 detail the friction test results for 1.5 g/cm^3 special exfoliated graphite packing rings in both air and argon respectively. The initial coefficient of friction is significantly lower for special exfoliated graphite ring compared with standard 1.5 g/cm^3 exfoliated graphite packing rings. An increase in coefficient of friction with increasing stroke number is seen for special exfoliated graphite packing rings. In air this increase is between 15% and 38% depending on wedge angle. The dramatic increases seen in standard

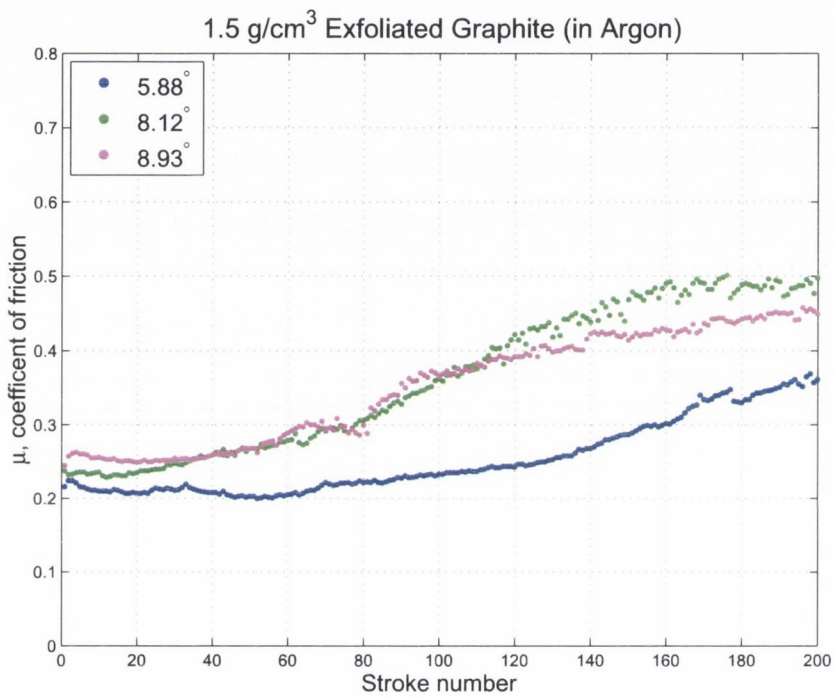


Figure 6.4: Stroke number versus coefficient of friction for 1.5 g/cm³ exfoliated graphite in argon

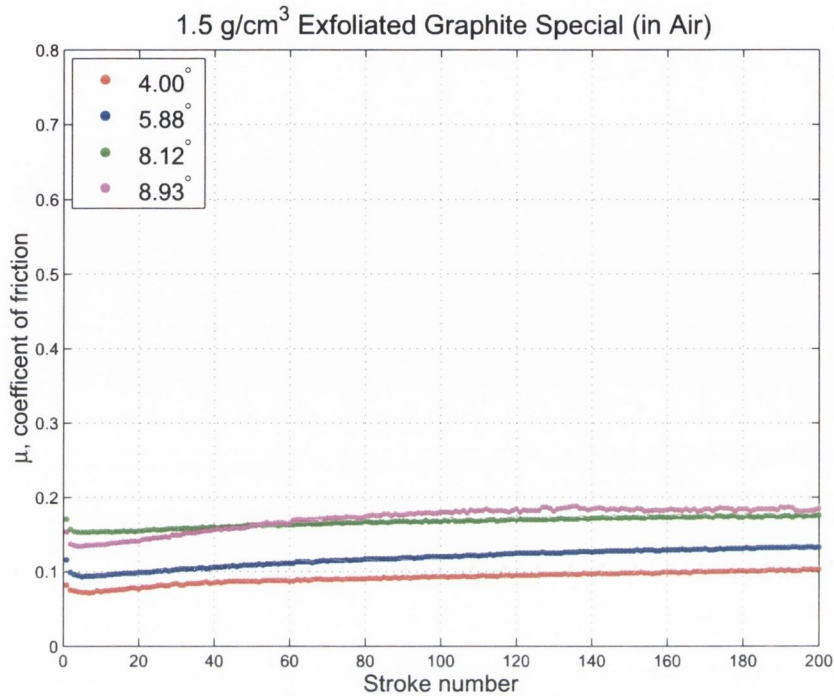


Figure 6.5: Stroke number versus coefficient of friction for Special 1.5 g/cm^3 exfoliated graphite in air

exfoliated graphite packing rings tested in argon are not seen with special 1.5 g/cm^3 exfoliated graphite tested. In argon a gradual increase of between 27% and 63% is seen over the course of 201 strokes.

6.3.3 Average coefficient of friction

The average coefficient of friction, μ is calculated for each test and plotted against the corresponding wedge angle. The data includes the average coefficient of friction results for 1.4 g/cm^3 , 1.5 g/cm^3 , 1.5 g/cm^3 special and 1.6 g/cm^3 exfoliated graphite. This data does not account for the increases seen in the coefficient over the course of a test. It is simply a result which gives a general picture of the magnitude of the average coefficient of friction

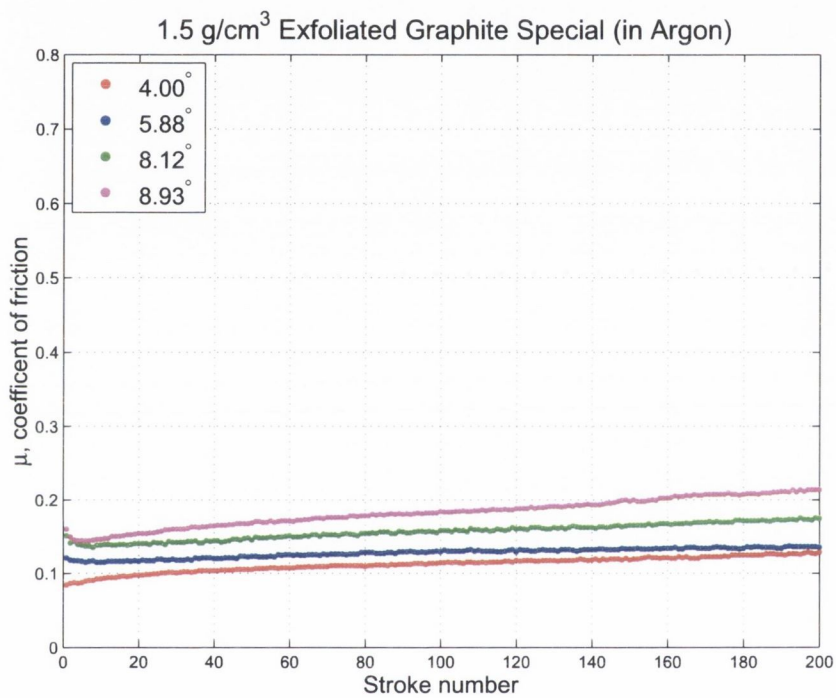


Figure 6.6: Stroke number versus coefficient of friction for Special 1.5 g/cm³ exfoliated graphite in argon

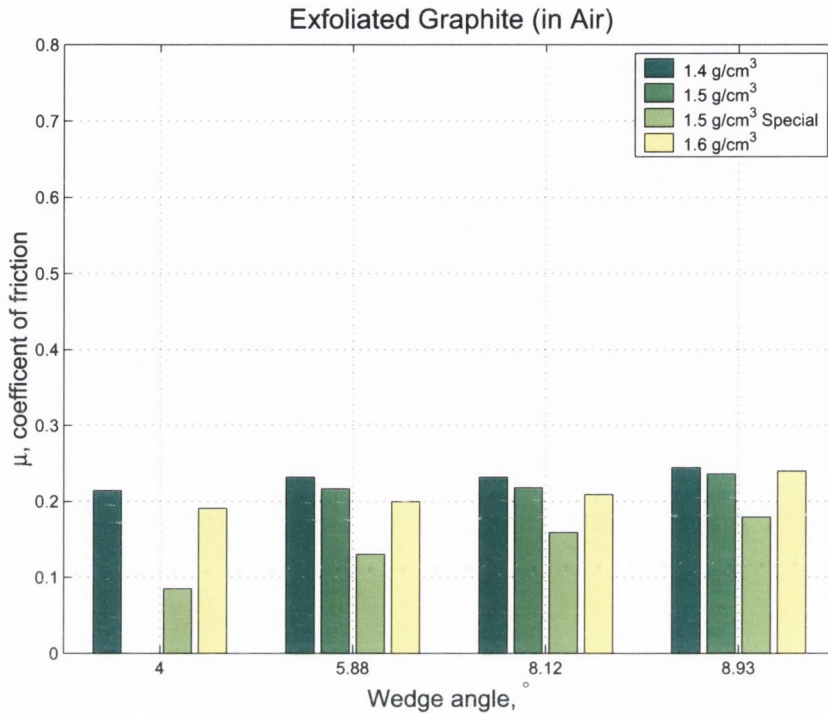


Figure 6.7: Wedge angle vs. average coefficient of friction for exfoliated graphite packings in air

under differing operational conditions. The results shown in Figures 6.7 and 6.8 are for exfoliated graphite packing rings in air and argon respectively.

In air the average coefficient of friction is seen to increase with wedge angle. An decrease in μ is seen with increasing density of standard exfoliated graphite packing rings. Special 1.5 g/cm^3 have a much lower average coefficient of friction compared with standard 1.5 g/cm^3 exfoliated graphite packing rings. The average coefficient of friction for tests carried out in argon is generally seen to be higher than the corresponding value in air. Denser packing rings are not seen to demonstrate the same trend in argon as in air.

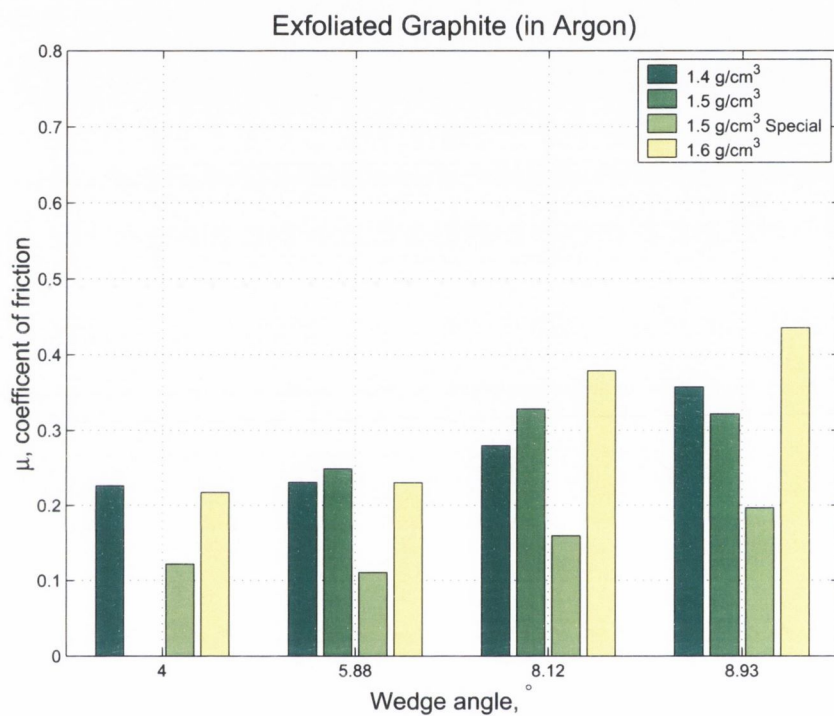


Figure 6.8: Wedge angle vs. average coefficient of friction for exfoliated graphite packings in argon

6.3.4 Experimental data analysis

It is evident from the friction test results that the Oxley model is not capable of predicting the frictional behaviour of exfoliated graphite packing rings. The Oxley model is a rigid plastic model which is not capable of modelling the increase in coefficient of friction with stroke number. It can however be used to determine the initial intrinsic coefficient of friction at the interface of the steel wedge and exfoliated graphite based on density and atmosphere.

The experimental results show that there is a dependence of coefficient of friction on wedge angle. This dependence is not however, as pronounced as that found in metals. This occurs because exfoliated graphite experiences significant elastic recovery around the wedge when it is indented into the packing rings. This elastic recovery seen in exfoliated graphite reduces the actual effective angle of the wedge. The original Oxley model detailed in Section 2.6.1 is modified to account for the elastic recovery of exfoliated graphite. This modification improves the accuracy of the calculated values of initial intrinsic coefficient of friction. The modification of the Oxley model to allow for elastic recovery is detailed in Section 6.3.5.

The results for 1.5 g/cm^3 exfoliated graphite and special 1.5 g/cm^3 exfoliated graphite show that the coefficient of friction increases with stroke number. In argon the increase in coefficient of friction with stroke number for 1.5 g/cm^3 is much more dramatic than in air. A significant increase in coefficient of friction is seen in 8.12° and 8.93° degree wedge angles compared with the 5.88° degree wedge angle. This increase in coefficient of friction in argon is seen to depend on wedge angle and cannot be explained by a reduction in oxygen in the system as the test progresses. It was initially hypothesised that the increase in coefficient of friction seen over the course of a test could be attributed to a reduction in oxygen within the test head as the test progressed. This cannot however explain the increases in coefficient of friction seen in tests carried out in air or the dependence of increase in coefficient of friction on wedge angle in argon. Other processes had to be occurring in the packing rings during the wedge test.

The surface layer of the inner diameter of the packing ring set was thought to be failing under the pressure of the wedge and thus causing the increase in coefficient of friction. It is not possible to measure and record the stresses and strains in the packing ring set during a wedge test. The only variables recorded in a wedge test are the normal and tangential forces on the wedge and the wear of the packing ring set during a test. FE analysis is the only method available with which to determine the stresses and strains within the packing ring set during a test. The modified Cam Clay material model developed in this thesis to model 1.5 g/cm^3 exfoliated graphite is used to investigate the stresses and strains in a 1.5 g/cm^3 exfoliated graphite packing ring set during a wedge test. Before FE analysis of the wedge test rig can be carried out the intrinsic coefficient of friction has to be determined. The next two sections detail the modification of the original Oxley model to account for elastic recovery and the subsequent calculation of the initial intrinsic coefficient of friction of the wedge packing interface from the experimental data. The coefficient of friction at the interface of the wedge and the packing ring set in the FE model is calculated using the modified Oxley model.

6.3.5 Modified Oxley model

The Oxley model described in Section 2.6.1 is altered to allow for the elastic recovery of exfoliated graphite. Elastic recovery results in a reduction of the actual wedge angle, developing a new reduced wedge angle which depends on the level of elastic recovery of the material. The original Oxley model is modified to allow for the elastic recovery found in exfoliated packing rings. The modified Cam clay material model developed in this thesis to model 1.5 g/cm^3 exfoliated graphite is used to determine the effective wedge angle which occurs due to elastic recovery.

The forces on a hard wedge sliding over a softer material is described graphically in Figure 6.9. If there is no elastic recovery behind the wedge, the overall friction can be found by resolving the forces on the front face of the wedge:

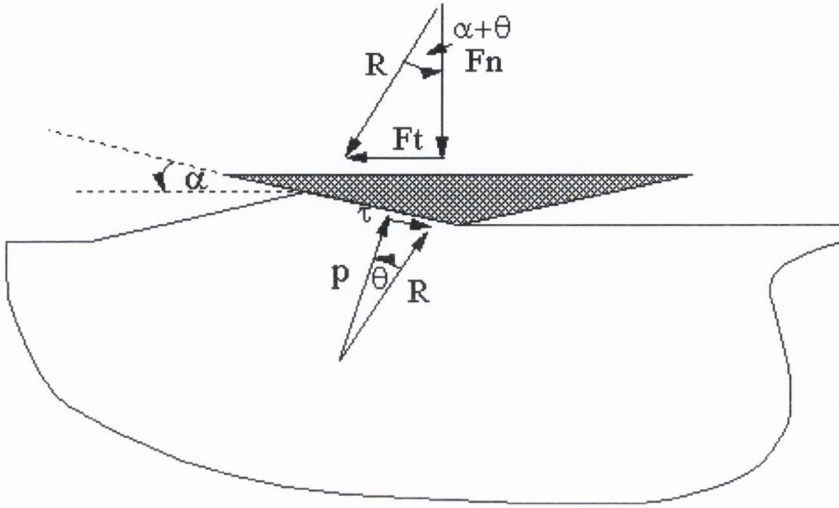


Figure 6.9: Forces on a hard rigid wedge sliding over a softer material

$$\mu_0 = \frac{\tau}{p} \quad (6.1)$$

where μ_0 is the intrinsic coefficient of friction of the interface, τ is the shear stress and p , is the pressure.

$$\mu = \frac{F_t}{F_n} = \tan(\alpha + \theta) \quad (6.2)$$

$$\mu = \tan(\alpha + \text{atan}[\mu_0]) \quad (6.3)$$

where μ is the coefficient of friction, F_t is the tangential friction force and F_n is the normal friction force.

Exfoliated graphite displays elastoplastic behaviour. The elastic recovery of exfoliated graphite causes a reduction in the actual effective angle of the wedge. The effective wedge angle α^* can be seen in Figure 6.10 and is determined as follows:

$$\alpha^* = \text{atan}\left[\left(\frac{h_t - h_e}{h_t + h_e}\right)\tan\alpha\right] \quad (6.4)$$

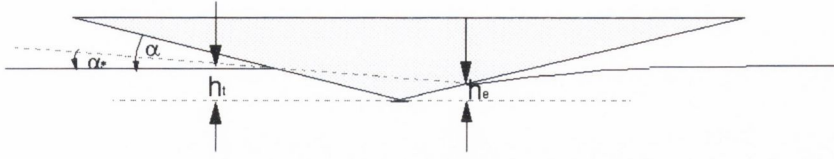


Figure 6.10: Elastic recovery

First $\frac{h_e}{h_t}$ has to be calculated. If the elastic range of exfoliated graphite was big enough to allow for complete recovery behind the wedge ($h_e = h_t$), the elastic strain would be given by [87]:

$$\varepsilon_{el}^* \approx \frac{1}{2} \tan[\alpha] \quad (6.5)$$

We assume that the actual recovery will be proportional to the actual elastic range so that:

$$\frac{h_t}{h_e} \approx \frac{\varepsilon_{el}^*}{\varepsilon_{el}} \approx \frac{\tan \alpha}{2\varepsilon_{el}} \quad (6.6)$$

Figure 6.11 details the idealised consolidation and swelling behaviour of exfoliated graphite that is implemented in the modified Cam clay material. The elastic range of exfoliated graphite is determined from information in Figure 6.11. Suppose, we consolidate the graphite to a void ratio e under pressure p . When we release the pressure, it will swell by an amount Δe . This gives:

$$\Delta e = -\kappa \ln\left(\frac{p}{p_0}\right) \quad (6.7)$$

We also have:

$$(1 + e_0) - (1 + e) = -\lambda \ln\left(\frac{p}{p_0}\right) \quad (6.8)$$

Dividing Equation 6.7 by Equation 6.8 gives:

$$\frac{\Delta e}{(1 + e_0) - (1 + e)} = \frac{\kappa}{\lambda} \quad (6.9)$$

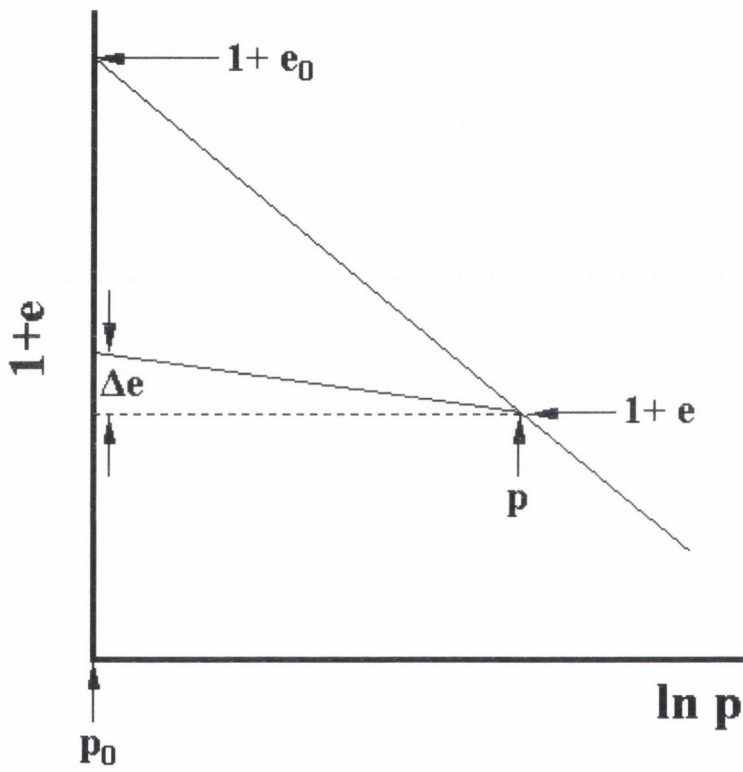


Figure 6.11: Consolidation and swelling behaviour of exfoliated graphite

Multiply both sides by $(1 + e_0) - (1 + e)$, then divide both sides by $(1 + e)$:

$$\varepsilon_v = \frac{\Delta e}{(1 + e)} = \frac{\kappa}{\lambda} \left[\left(\frac{1 + e_0}{1 + e} \right) - 1 \right] \quad (6.10)$$

Therefore

$$\varepsilon_v \approx \frac{\kappa}{\lambda} \left[\left(\frac{1 + e_0}{1 + e} \right) - 1 \right] \approx \frac{\kappa}{\lambda} \left[\left(\frac{1.773}{1 + e} \right) - 1 \right] \quad (6.11)$$

The value of $1 + e_0 = 1.773$ is calculated from Figure 5.5, the pressure is set to atmospheric pressure and the resultant value of specific volume, $(1+e)$ is calculated, which corresponds to a value of 1.773. The elastic recovery ε_{el} is then determined from Equation 6.12.

$$\varepsilon_{el} = \frac{\varepsilon_v}{3} \quad (6.12)$$

6.3.6 Intrinsic coefficient of friction

The modified Oxley model is used to determine the initial intrinsic coefficient of friction μ_0 at the wedge exfoliated graphite packing interface. The wedge angle α used in the equation is replaced by the effective wedge angle α^* determined in Section 6.3.5. The intrinsic coefficient of friction for exfoliated graphite in air and argon is determined by inverting Equation 6.3. The calculated values for the intrinsic coefficient of friction for exfoliated graphite are shown in Table 6.1.

The predicted initial intrinsic coefficient of friction is plotted against the measured initial intrinsic coefficient of friction for each individual test, this gives a measure of the scatter within the friction test results.

The plot of predicted intrinsic coefficient of friction vs. measured coefficient of friction can be seen in Figure 6.12. The initial intrinsic coefficient of friction is seen to predict the results from the experimental data very closely. The data obtained from this analysis is to be used as the input parameter for the coefficient of friction at the wedge packing interface in the FE model of the wedge test rig.

Table 6.1: Intrinsic coefficient of friction at the beginning of the test

Ring Density (g/cm^3)	Gas	μ_0 [Mean]	μ_0 [Std. dev]
1.4	Air	0.103835	0.024211
1.5	Air	0.101932	0.007564
1.5 Special	Air	0.029577	0.015057
1.6	Air	0.107324	0.02475
1.4	Argon	0.124303	0.020089
1.5	Argon	0.153286	0.042702
1.5 Special	Argon	0.024032	0.12565

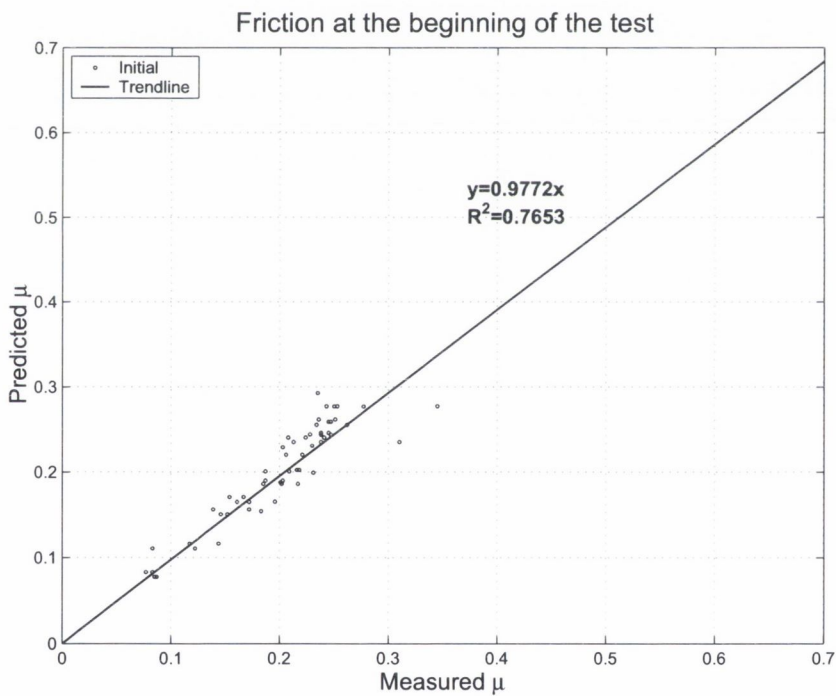


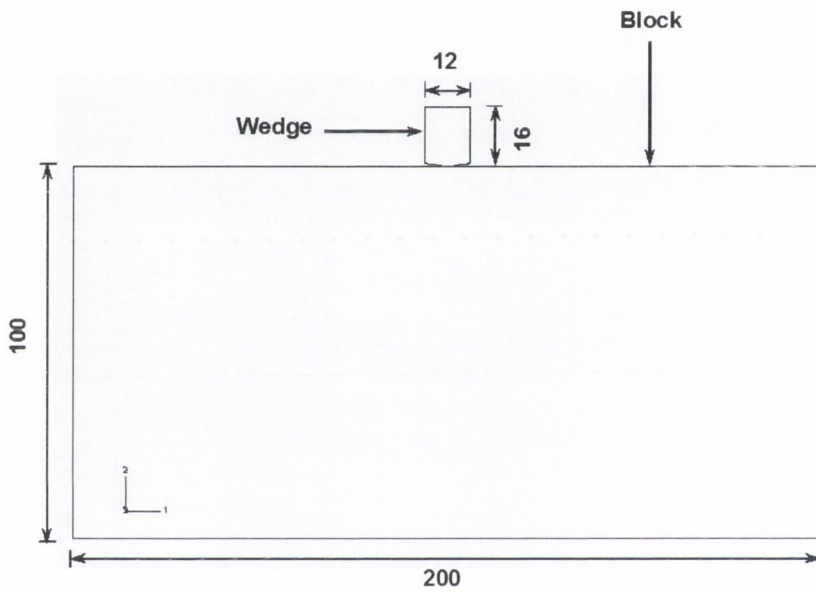
Figure 6.12: Correlation of measured initial coefficient of friction with predicted initial coefficient of friction

6.3.7 Wedge test FE model

The increase in coefficient of friction seen in exfoliated graphite packing rings during the course of a test cannot be attributed to the presence of argon (lack of oxygen) in the test head as the increase in coefficient of friction is seen to depend on wedge angle. It is hypothesised that the increase in coefficient of friction seen in exfoliated graphite packing rings during a wedge test results from the failure of the surface layer of the packing ring set inner diameter as it undergoes interaction with the steel wedge. It is not possible to determine the stresses and strains in the packing rings under the wedge using experimental analysis. Therefore FE analysis of the wedge test rig was undertaken in order to investigate this hypothesis.

The FE model of the wedge test rig is a 2D plane strain model of a wedge sliding against a block of material, the block represents the 3 packing rings in the wedge test. A schematic of the FE model can be seen in Figure 6.13. The block is confined in the 1 direction along its left and right hand sides. The block is confined along its base in the 2 direction. When the wedge is being indented into the block it is confined along its right hand side in the 1 direction. FE analysis is carried out for all 4 wedge angles, these being 4° , 5.88° , 8.12° and 8.93° wedge angles. Coulomb friction is defined at the interface of the wedge and the block. A coefficient of friction $\mu = 0.15$ is chosen, this corresponds to the initial intrinsic coefficient of friction for 1.5 g/cm^3 exfoliated graphite in argon.

FE analysis of the wedge test was carried out for the particular case of 1.5 g/cm^3 exfoliated graphite exfoliated graphite packing rings in argon. FE analysis of the wedge test rig is carried out using the modified Cam clay material model in ABAQUS/Standard developed in this thesis for 1.5 g/cm^3 exfoliated graphite. FE analysis can only be carried out for 1.5 g/cm^3 exfoliated graphite as it is the only density of exfoliated graphite that has been fully defined mathematically. The reason for carrying out FE analysis for the particular case of the wedge test in an argon rich environment is as follows, the experimental results for 1.5 g/cm^3 exfoliated graphite in argon



All dimensions in mm

Figure 6.13: 2D plane strain model of wedge test

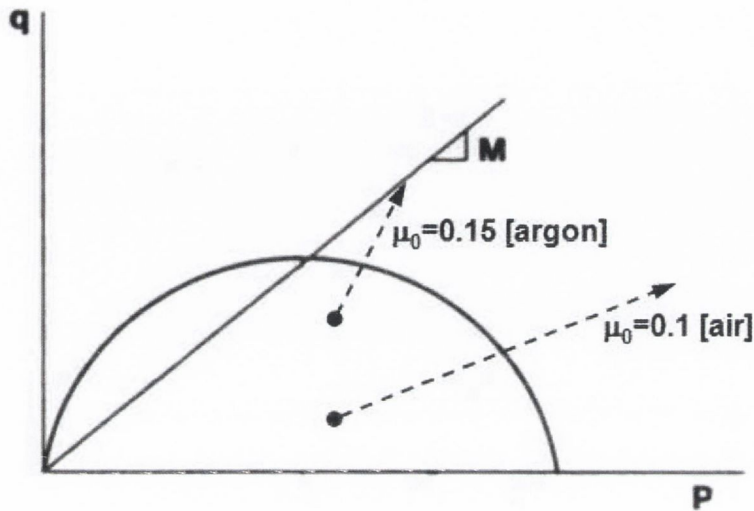


Figure 6.14: The evolution of the deviatoric stress towards failure based on the initial intrinsic coefficient of friction

show dramatic increases in coefficient of friction over the course of a test, whereas the increases in coefficient of friction in air are more gradual. FE analysis of exfoliated graphite packing rings in argon should produce the same distinct dramatic increases in coefficient which should allow for the validation of the hypothesis that the increase in coefficient of friction can be related to failure of the surface layer of the packing ring inner diameter. It was not possible to carry out the same analysis in air due to time constraints and is proposed as future work.

From theory it is known that a greater initial intrinsic coefficient of friction should cause failure in the material faster according to the following reasoning. The initial intrinsic coefficient of friction in argon is greater than that in air. A higher initial coefficient of friction will result in a greater initial deviatoric stress. This behaviour is shown graphically in Figure 6.14.

Experimental tests carried on the wedge test rig were executed according to the following protocol, a constant force of 20 N was applied to the top of

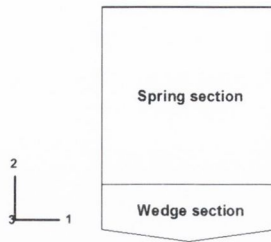


Figure 6.15: 8.12° wedge partitioned to produce a spring loaded wedge

the wedge, the wedge was then stroked against the inner diameter of the 3 packing rings for 201 strokes. The wedge is spring loaded so that a constant force is maintained on the wedge even if a build up (a wave) of material occurs ahead of the wedge. In order to simulate the spring part of the wedge in the FE model the wedge was partitioned into two sections. Separate linear elastic material properties were given to the two sections. The soft section of the wedge is a simulated spring which has a much lower modulus than the steel wedge. The partitioning of a 8.12° degree wedge can be seen in Figure 6.15.

Convergence problems occurred when the wedge was indented into the block under load control conditions, therefore the model had to be run under displacement control conditions. Further convergence problems were encountered in regards to the modified Cam clay material model itself. It was found that the FE model would not converge unless a pressure was applied to the top of the block. The top of the block is a free surface, i.e. there were no boundary conditions constraining this surface. If no pressure is applied to the top of the block plastic collapse was found occur on this free surface [86]. If the material has no strength in tension it also has no cohesion so as the wedge is stroked against the block the material behind the wedge will collapse. The principle of plastic collapse can be seen in Figure 6.16, once the slope (material behind the wedge) has failed the model will no longer converge. This occurs because the modified Cam clay material model has no strength in tension and hence no cohesive strength. Whereas, in fact exfoli-

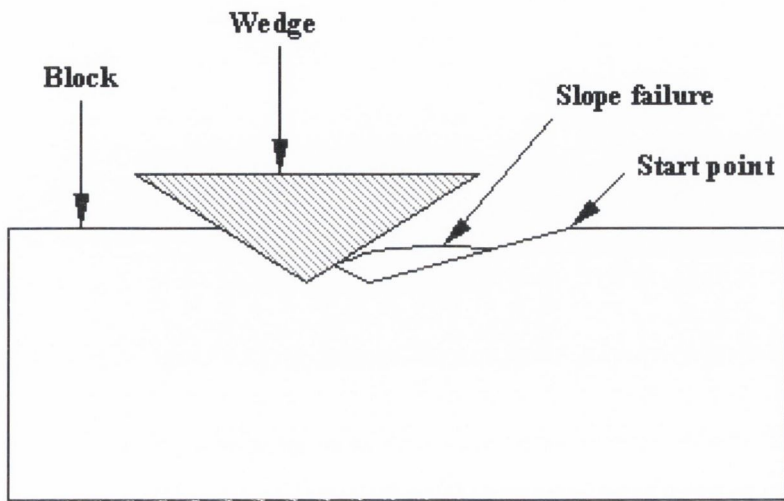


Figure 6.16: Failure of the material behind a wedge

ated graphite can have a tensile strength of up to 8 MPa [Carbon Lorraine, personal communication May 2004].

A pressure of 20 MPa is applied to the top of the block during FE analysis to overcome this problem. This pressure value of 20 MPa applied to the top of the block gives an artificial tension strength to the exfoliated graphite block of 6.7 MPa. The artificial tensile stress allows for convergence of the FE model to occur.

The modified Cam clay material model has been extended by Groen et al. [88] to allow the model to support tensile stresses. A comparison of the yield and failures surfaces of the modified Cam clay material model and the extended modified Cam clay material model which can support tensile stresses can be seen in Figure 6.17.

The yield surface of the modified Cam clay material model is changed to allow for strength in tension. The yield surface, f of the extended version of the modified Cam clay material model is defined as follows:

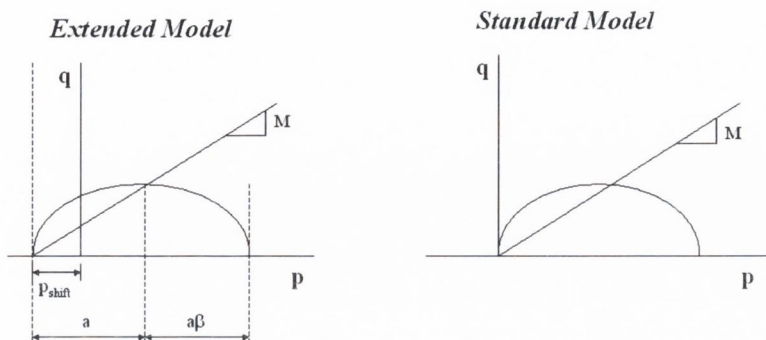


Figure 6.17: The yield and failure surfaces of the standard and extended modified Cam clay material models

$$f = q^2 + \frac{M^2}{\beta^2} [(p + p_{shift} - 2a) + a^2(1 - \beta^2)] \quad (6.13)$$

where p_{shift} is a reference pressure to model cohesive behaviour and a is a measure of the current degree of overconsolidation. This extension of the modified Cam clay material model has been implemented in DIANA but not in ABAQUS/Standard. If the FE model of the wedge test rig were to be implemented properly the yield surface of the modified Cam clay material model in ABAQUS/Standard would need to be altered to the form shown in Equation 6.13.

The wedge has the same dimensions in the FE model as in the experimental test the block however is significantly larger than the three packing rings in the wedge test rig. The block was setup in this manner so that the reactions forces that occur at the boundaries of the block would not effect the stresses and strains at the wedge block interface as they are far field boundary conditions. This means that the 20 MPa applied to the top of the block in the FE model can be subtracted from the final results when determining the stresses at the wedge block interface.

The modified Cam clay material model is a non-linear elastoplastic ma-

terial model and is therefore a computationally intensive material model to solve; when used in conjunction with contact friction the computational time required to solve the model increases significantly. The FE mesh comprises of CPE4R plane strain, reduced integration elements with hourglass control. ABAQUS recommends the use of reduced integration elements with the Cam clay material model. It improves the convergence rate of the FE model. Hourglassing can be a problem with first-order, reduced-integration elements in stress/displacement analyses. Since the elements have only one integration point, it is possible for them to distort in such a way that the strains calculated at the integration point are all zero, which, in turn, leads to uncontrolled distortion of the mesh. CAX4R elements allow for the control of hourglassing. Contact was defined by contact surfaces in ABAQUS. The steel wedge was defined as the master surface and the top of the block was defined as the slave surface.

The FE mesh was chosen as a compromise between accuracy and time to solution convergence. The mesh can be seen in Figure 6.18, with further detailed views of the mesh around and under the wedge in Figures 6.19 and 6.20. The area of interest under the wedge, this has the much denser mesh than the rest of the block. In total there were 16,621 elements in the block with represents the 3 packing rings.

The FE model of the wedge test rig is implemented using the following load steps, initially a pressure of 20 MPa was applied to the top of the block, the wedge was then indented into the top of the block by 0.5 mm, after indentation the wedge was cycled back and forward against the top of the block 6 times. After 6 cycles the mesh under the wedge is seen to have undergone excessive distortion: a converged solution cannot be found after this point. The element distortion for a 8.12° wedge after $5\frac{1}{2}$ cycles can be seen in Figures 6.21 and 6.22.

The failure of the modified Cam clay material is related to the changes in deviatoric stress, q and pressure stress, p . The modified Cam clay material model is said to have failed when the parameter $\eta = \frac{q}{p}$ reaches a set value.

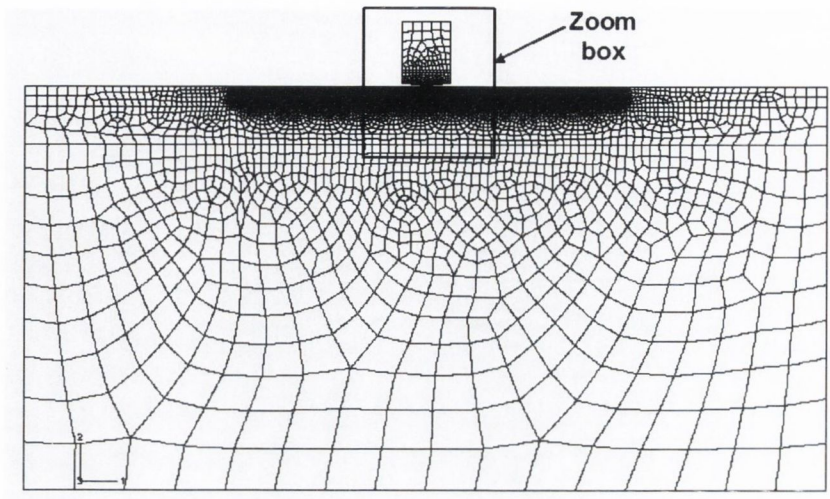


Figure 6.18: FE mesh of wedge test rig

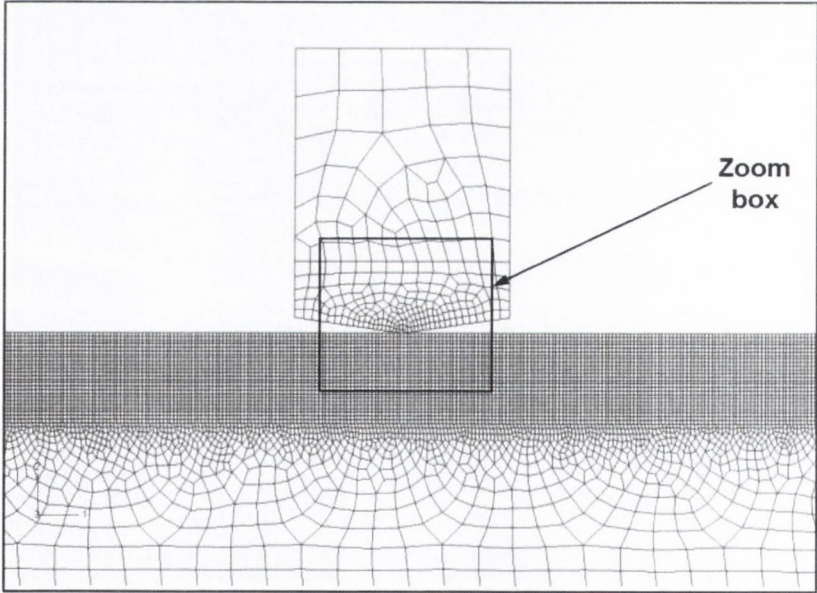


Figure 6.19: Zoomed section of wedge test FE mesh

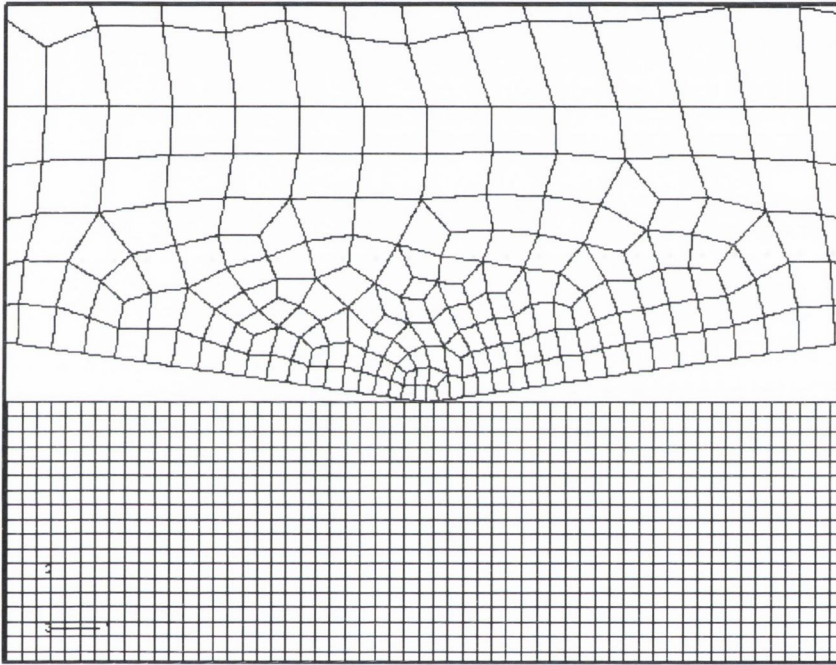


Figure 6.20: Zoomed section of wedge test FE mesh detailing the element density at the wedge block interface

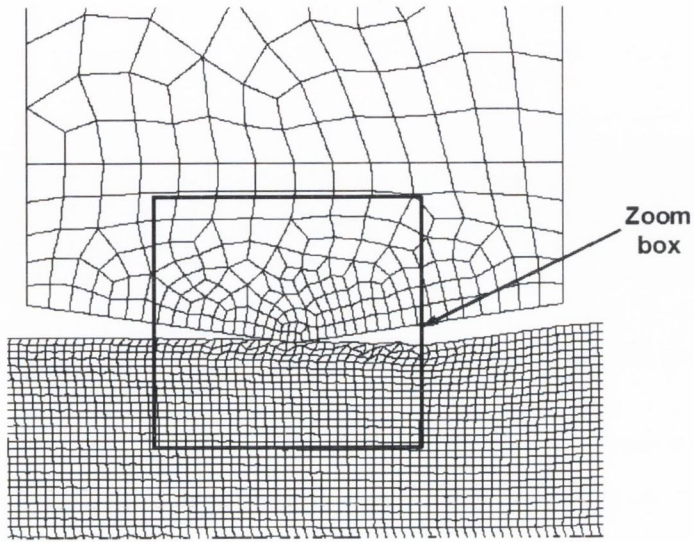


Figure 6.21: Element distortion in surface layer of block after 6 cycles

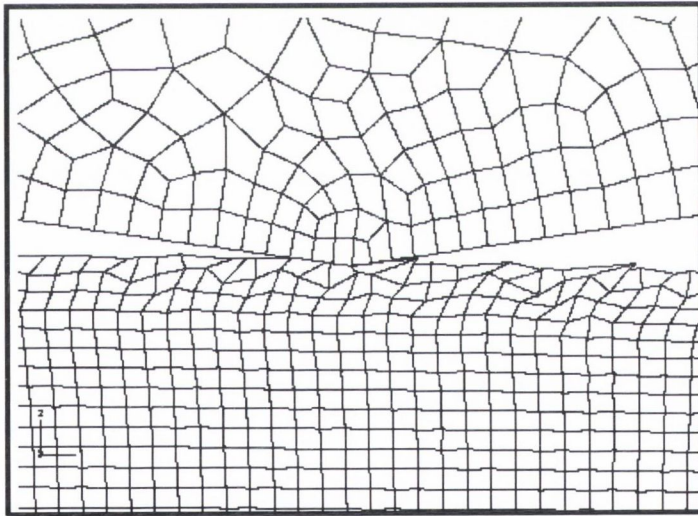


Figure 6.22: Zoomed section of element distortion in surface layer of block after 6 cycles

If the stress in the material reaches this value of η the material is expected to disintegrate/fail. The deviatoric stress and pressure stress is determined at the mid point of each half stroke in the FE model of the wedge test. A single stroke includes a backward and forward movement of the wedge across the top of the block. The pressure stress is outputted directly from the FE model and the deviatoric stress is calculated using Equation 6.14, from the S11, S22 and S33 stress outputs from the FE model.

$$q = \sqrt{\frac{1}{2}(\sigma_2 - \sigma_3)^2 + \frac{1}{2}(\sigma_3 - \sigma_1)^2 + \frac{1}{2}(\sigma_1 - \sigma_2)^2} \quad (6.14)$$

6.3.8 FE wedge test results

Example results from FE analysis carried out on a 8.12° wedge are detailed below. Figures 6.23 and 6.24 show the pressure stress under the wedge after 1½ strokes. Figures 6.25 and 6.26 shows the S11 stresses under the wedge after 1½ strokes of the wedge. Figures 6.27, 6.28, 6.29 and 6.30 show the corresponding results for S22 and S33 stress under the wedge after 1½ wedge strokes.

As detailed in Section 6.3.7 an artificial pressure of 20 MPa had to be applied to the top of the block to give the exfoliated graphite block a tensile strength which is needed to obtain a converged solution. This pressure is subtracted from the FE results for pressure and S22 when calculating η . This can be done since the block is significantly large compared with the interaction area between the wedge and the block. The reaction forces at the boundaries of the block are far field, i.e. they have little to no effect on the pressure and stress that develop in the block under the wedge. The result of stroke number versus η is plotted to determine how η evolves with stroke number. The trendlines for the evolution of η with stroke number are shown in Figure 6.31. The actual FE data shows some scatter, the results are approximated by trendlines. As expected the slope of the stroke versus η curve increases with increasing wedge angle.

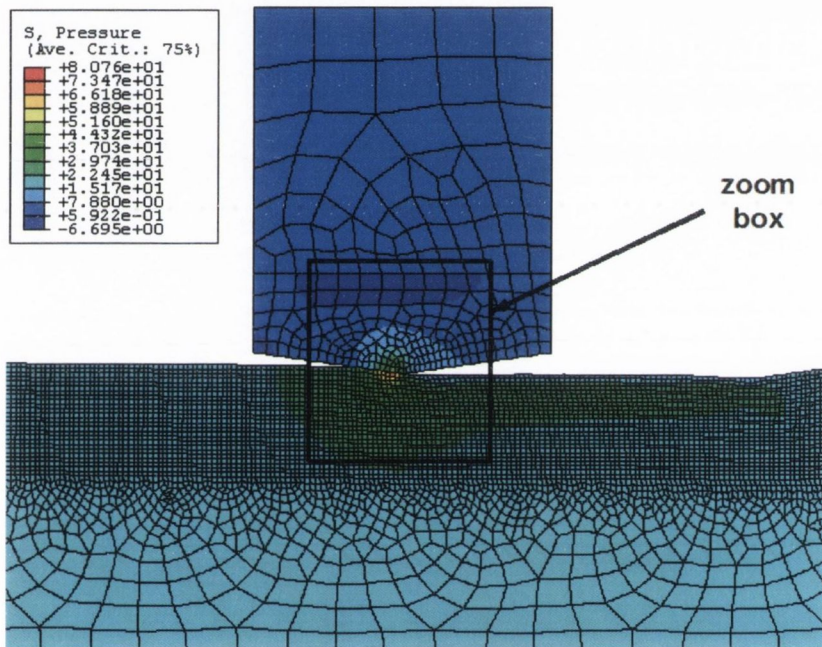


Figure 6.23: Pressure under a 8.12° wedge

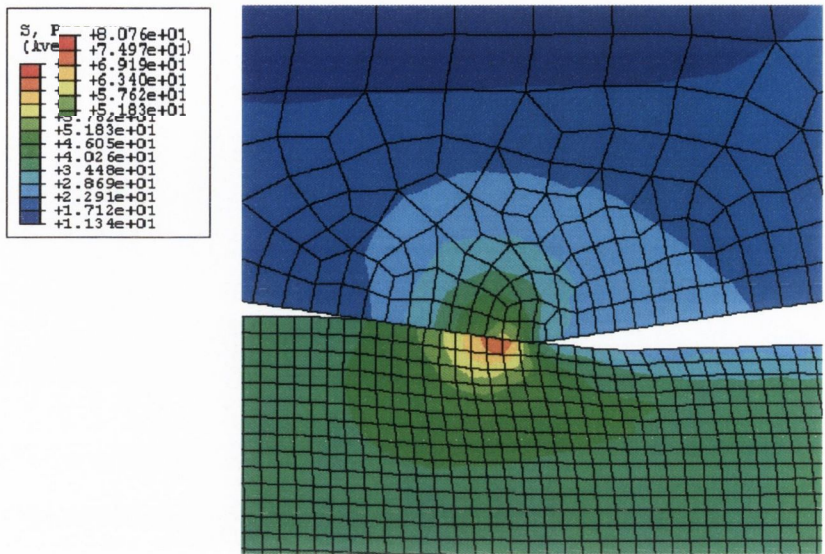


Figure 6.24: Zoomed section of the pressure under a 8.12° wedge

6.4 Wear results

6.4.1 1.5 g/cm³ exfoliated graphite

Wear tests on 1.5 g/cm³ exfoliated graphite were carried out using 5.88°, 8.12° and 8.93° degree wedge angles. Results in air and argon can be seen in Figures 6.32 and 6.33 respectively. A definite dependence of wear on wedge angle can be seen in this data. The slope of the wear curves are used to determine the wear coefficient using Equation 6.15 of a particular packing material, given a specific wedge angle and environment.

6.4.2 Special 1.5 g/cm³ exfoliated graphite

Tests on Special 1.5 g/cm³ exfoliated graphite were carried out using all four wedge angles. Sample test results for stroke number versus wear in microns can be seen in Figures 6.34 and 6.35. Tests were carried out in both air and argon. Wear results for special 1.5 g/cm³ exfoliated graphite packing rings

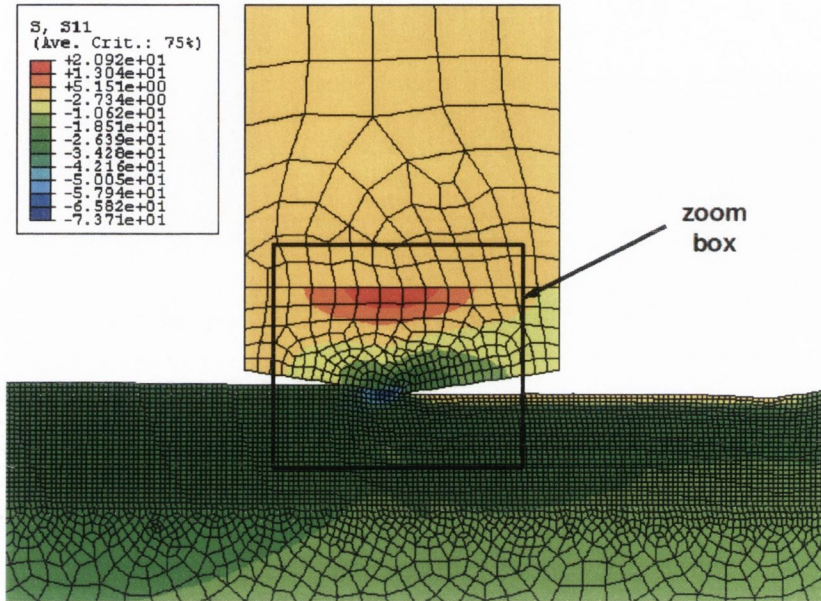


Figure 6.25: Stress, S11 under a 8.12° wedge

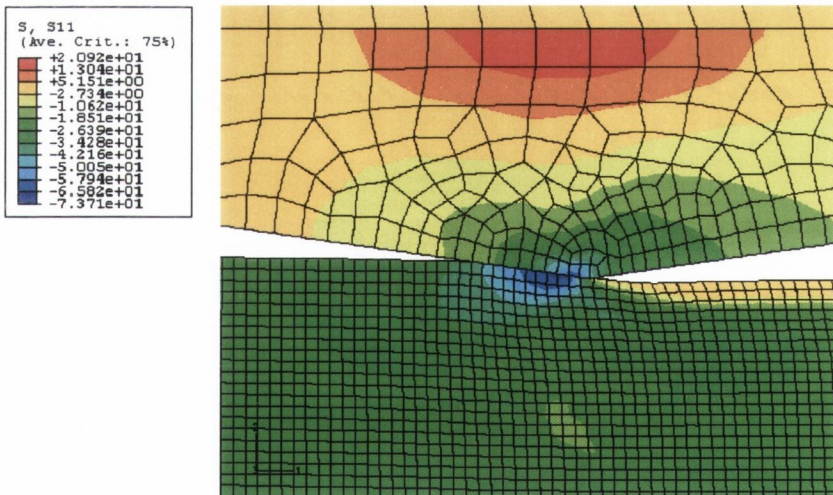


Figure 6.26: Zoomed section of the stress, S11 under a 8.12° wedge

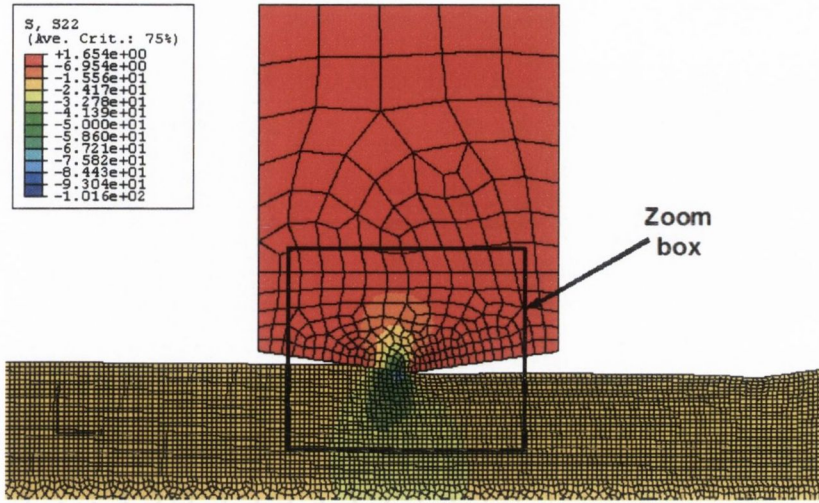


Figure 6.27: Stress, S_{22} under a 8.12° wedge

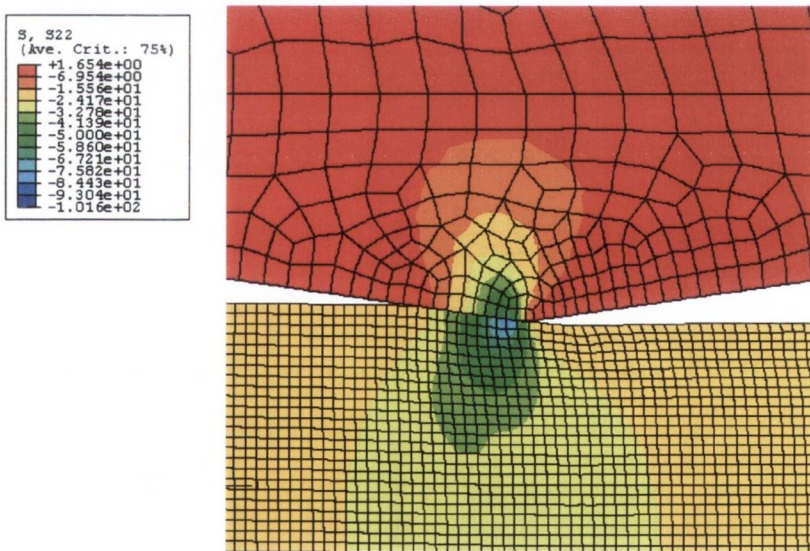


Figure 6.28: Zoomed section of the stress, S_{22} under a 8.12° wedge

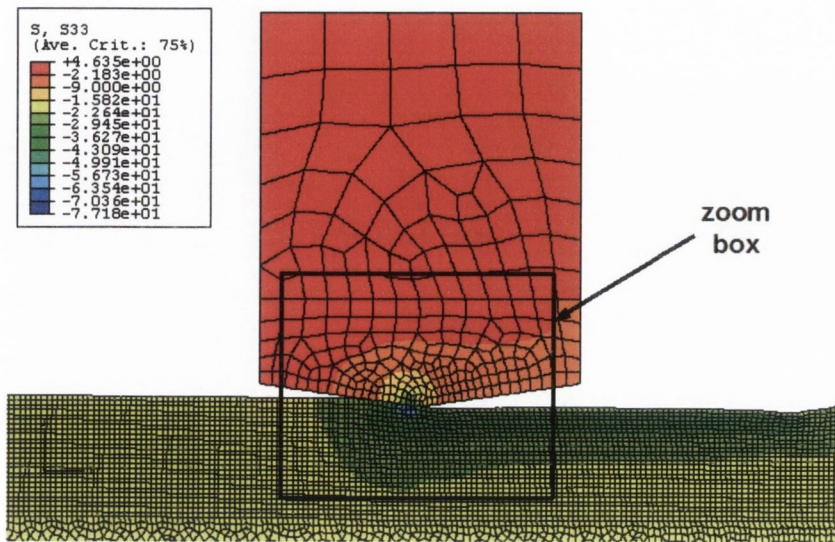


Figure 6.29: Stress, S_{33} under a 8.12° wedge

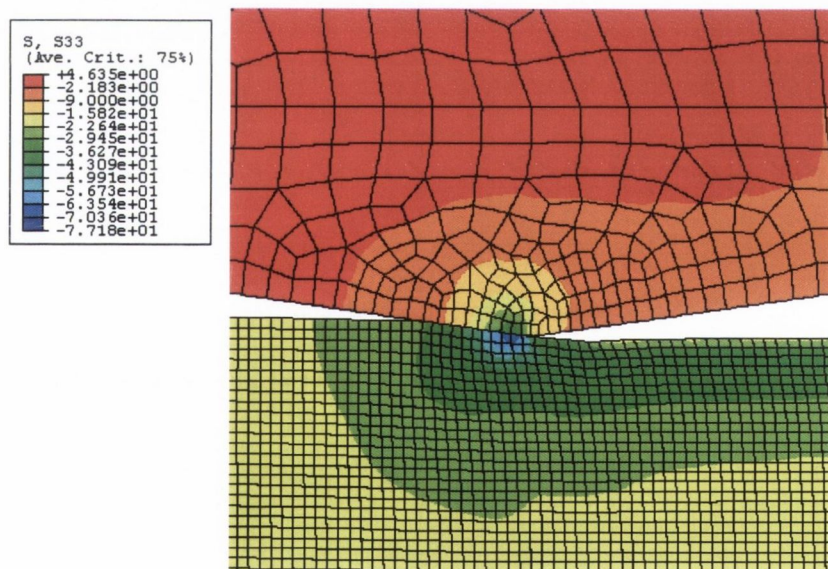


Figure 6.30: Zoomed section of the stress, S_{33} under a 8.12° wedge

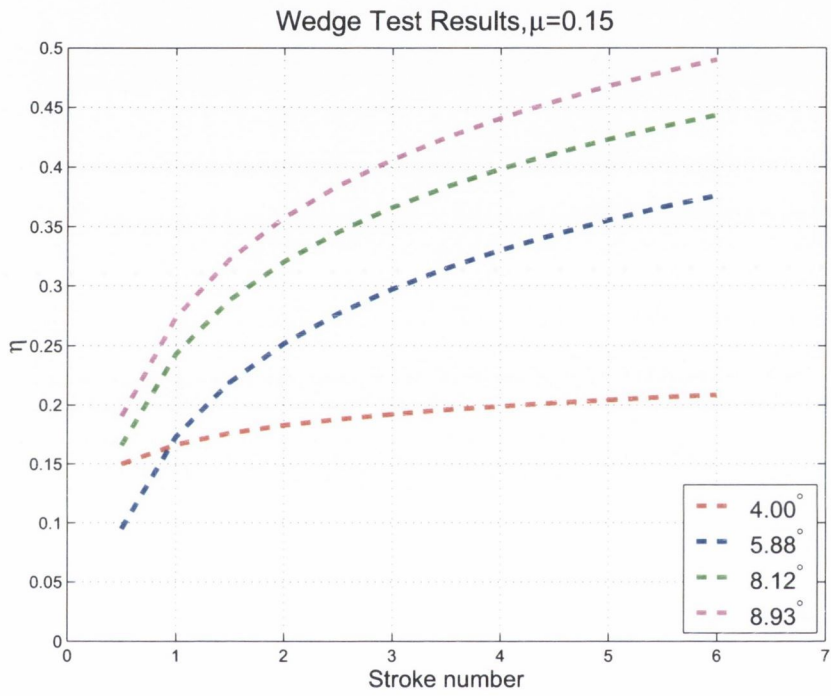


Figure 6.31: Stroke number vs. η for a interfacial friction of $\mu = 0.15$ at the wedge block interface

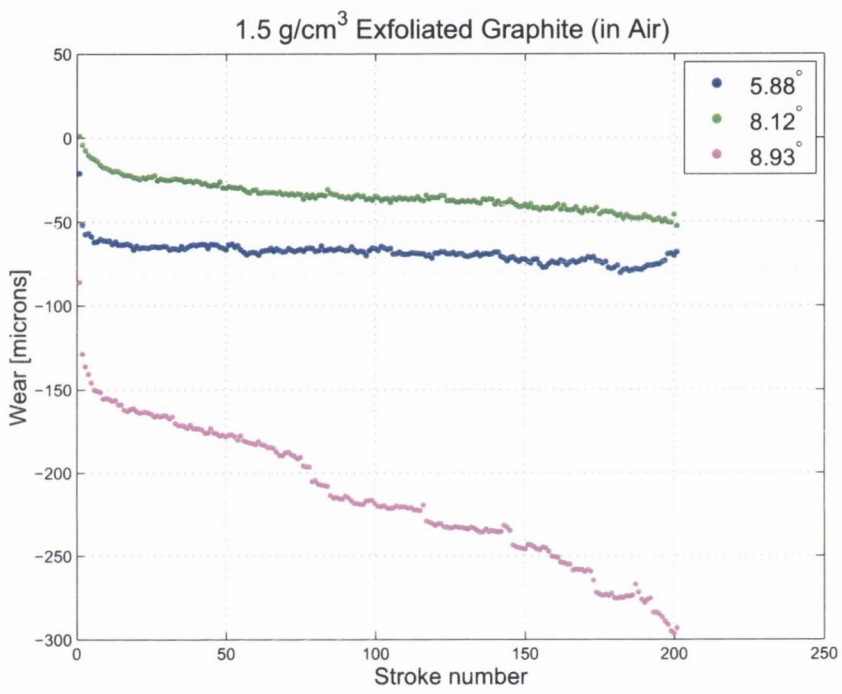


Figure 6.32: Stroke number versus wear for 1.5 g/cm³ exfoliated graphite in argon

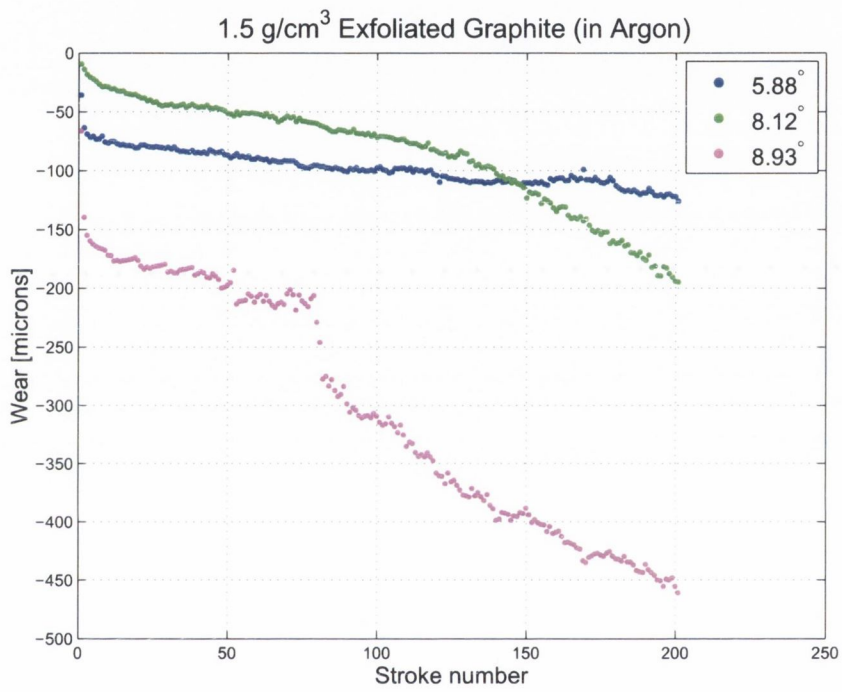


Figure 6.33: Stroke number versus wear for 1.5 g/cm³ exfoliated graphite in argon

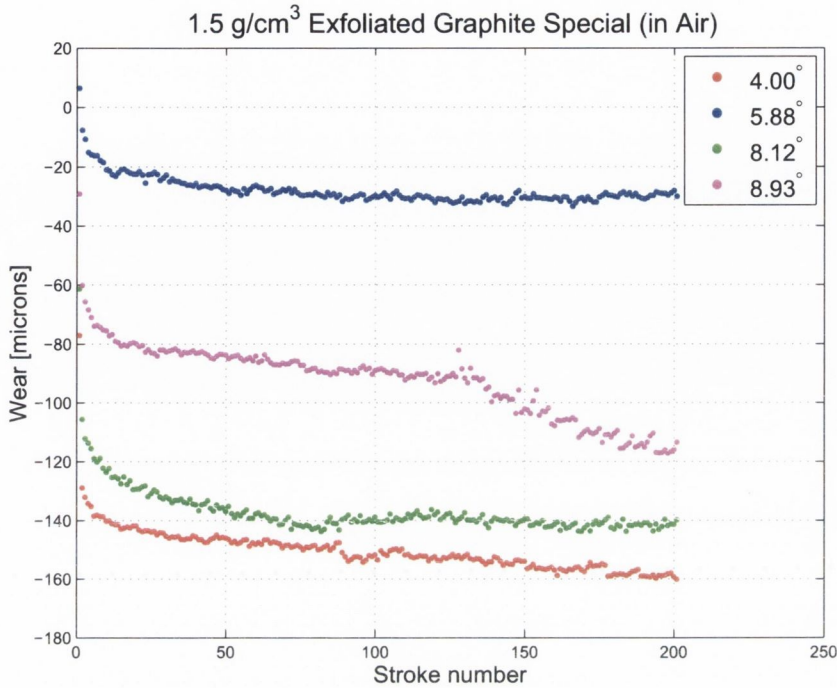


Figure 6.34: Stroke number versus wear for special 1.5 g/cm^3 exfoliated graphite in air

exhibit significantly less wear than standard 1.5 g/cm^3 exfoliated graphite packing rings. The dependence of wear on wedge angle is not as marked in special 1.5 g/cm^3 exfoliated graphite packing rings compared with standard 1.5 g/cm^3 exfoliated graphite packing rings.

6.4.3 Wear coefficient, K for exfoliated graphite

Data for the wear coefficient is calculated from individual wear test data. In the initial part of the test, most of the downward displacement of the wedge is due to densification of the exfoliated graphite packing rings, so only the final third of the test data is used to calculate the wear coefficient for each material type and atmosphere under investigation. Equation 2.11, detailed

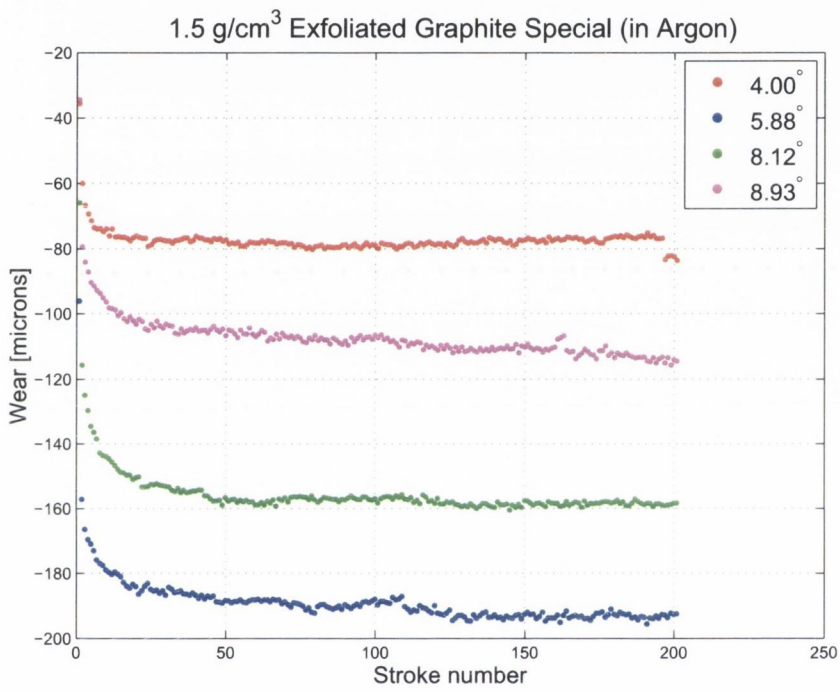


Figure 6.35: Stroke number versus wear for special 1.5 g/cm³ exfoliated graphite in argon

in Section 2.6.3 is modified into a form which is applicable to our particular application. The volume, V is replaced by $V = wd$ where w is the width of the wedge and d is the wear depth. The sliding distance, s can be replaced by $s = 2ln$, where $2l$ is the distance slid during one stroke (each stroke consists of 2 lengths) and n is the number of strokes.

This gives a modified version of Archard's law as seen in Equation 6.15 which will be used to determine the wear coefficient of valve packing rings.

$$K = \frac{wdl}{2Fln} = \frac{w}{2} \times \frac{\text{gradient}}{\text{force}} \tag{6.15}$$

where $\frac{\text{gradient}}{\text{force}}$ is the slope of the stroke v 's wear curve obtained from the wedge test.

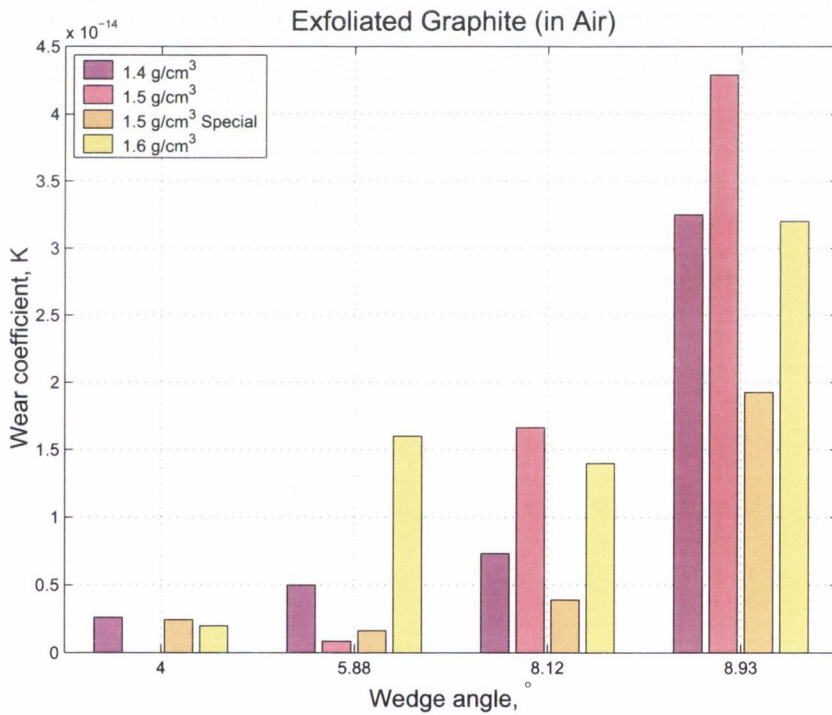


Figure 6.36: Wear coefficient, K for exfoliated graphite: in air

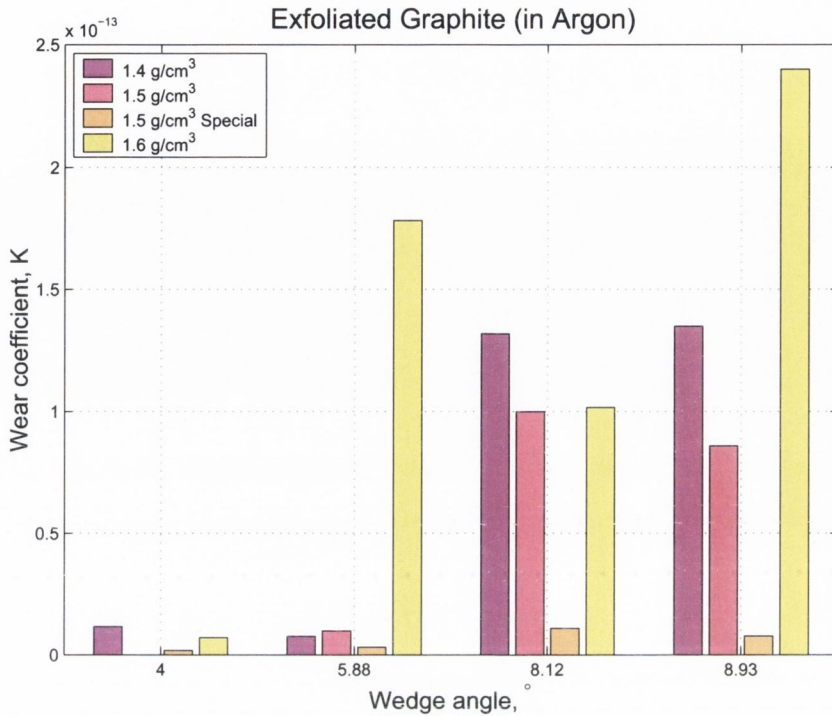


Figure 6.37: Wear coefficient, K for exfoliated graphite: in argon

The wear coefficient, K for each of the densities of exfoliated graphite against the corresponding wedge angle is shown in Figure 6.36 for air and Figure 6.37 for argon. The values of K are shown to be dependent not only on wedge angle but also on the atmosphere within the test head. K values in argon are much larger than those in air. The special 1.5 g/cm³ displays much lower values of K in air and argon than any of the other exfoliated graphite packing ring types.

6.5 Summary

The experimental methods and analysis techniques required to determine the influence of asperity slope on the friction and wear behaviour of exfoliated

graphite packing rings are detailed in this chapter. Results from the wedge test rig are presented, these results show that the coefficient of friction increases with distance slid. The Oxley model (the model initially proposed for analysing the influence of asperity slope on the friction behaviour of exfoliated graphite) cannot model this increase in coefficient of friction with distance slid as it is a rigid plastic model. It can however be used to determine the initial intrinsic coefficient of friction of the interface of the wedge and the packing rings set once it has been modified to allow for elastic recovery of the exfoliated graphite packing rings. FE analysis of the wedge test rig is carried out to determine the stresses and strains in the packing ring set during a wedge test as they cannot be determined experimentally. These results are used to investigate the hypothesis that the increase in coefficient of friction occurs as a result of failure of the material under the wedge as it is slid back and forwards against the inner diameter of the packing ring set.

Chapter 7

Discussion

7.1 Introduction

The primary objective of this thesis was to further develop the scientific understanding of compression packing ring behaviour in order to bring about improvements in valve packing installation and operation. The necessity for this scientific study was brought about due to environmental concerns and legislative demands regarding fugitive emissions. The first objective of this thesis was the development of a non-linear elastoplastic FE material model of 1.5 g/cm^3 exfoliated graphite packing rings, which was brought about through an extensive programme of experimental testing. The experimental testing programme involved the testing of exfoliated graphite under confined compression and triaxial test conditions. The FE material model was validated by comparing experimental results from the confined compression test rig with FE results from a simulation of the same test rig.

The second objective of this thesis was to use the FE material model developed in the first part of this thesis to investigate the influence of loading, valve stem friction, valve stem wear, and valve stem cycling on the behaviour of a 1.5 g/cm^3 exfoliated graphite packing ring set. The third objective of this thesis was to determine the influence of valve stem surface texture on the friction and wear behaviour of exfoliated graphite packing rings. Practical

engineering experience shows us that surface roughness plays an important role in the forces that develop between two rubbing surface. An analytical model of a single hard asperity sliding over a softer plastically deforming material developed by Oxley et al. [20] was proposed as a possible model with which to predict the influence of asperity angle on the friction behaviour of exfoliated graphite.

Due to the lack of data available on the friction and wear behaviour of exfoliated graphite a tribotest was developed to investigate the influence of asperity slope and atmosphere on the friction and wear behaviour of exfoliated graphite packing rings. From experimental tests it was determined that the coefficient of friction of exfoliated graphite packing rings increases with stroke number. It was hypothesised that this increase in coefficient of friction was related to a failure of the surface layer of the packing ring set ID. A FE model of the wedge test rig was used to investigate this hypothesis as the stresses and strain in the packing ring set could not be determined experimentally.

This chapter discusses the limitations in the range of materials tested, the constitutive material model, the FE valve cycling model and the wedge test rig. The FE results for decay in radial stress against the stem and the valve stem cycling force are compared with previously developed analytical models to predict valve packing behaviour. The influence of asperity slope on the friction and wear of exfoliated graphite packing rings is discussed in light of experimental results and FE analysis. FE analysis of valve packing wear is used to determine the optimum radial sealing stress against the stem for maximum life of the packing rings set. Finally, the achievements of the thesis are detailed.

7.2 Limitations of the present study

7.2.1 Range of materials tested

There are a vast range of packing ring materials used in industrial valve sealing applications. This thesis solely investigates the behaviour of exfoliated graphite packing rings. Exfoliated graphite packing rings were chosen because their mechanical properties do not differ significantly from one manufacturer to another. They are also one of the more homogeneous packing ring types and represent a good starting point for developing experimental and mathematical methods to describe general compression packing behaviour. There is still however, a vast range of packing rings material types whose mechanical behaviour needs to be characterised through a programme of mechanical testing and FE analysis.

A wide variety of exfoliated graphite packing ring densities are use in practice varying from 1.1 g/cm^3 to 1.8 g/cm^3 . In this thesis complete mechanical testing was only carried out for one density of exfoliated graphite this being 1.5 g/cm^3 . This particular density of exfoliated graphite was chosen because it the most widely used density in practice.

FE analysis was carried out using a 1.5 g/cm^3 packing ring set which consisted of three 1.5 g/cm^3 exfoliated graphite packing rings. Exfoliated graphite packing rings are used on their own in a packing ring set when the media pressures are less than 100 bar and the valve clearances are less than 0.5 mm, but if the media pressure and the clearances are greater it is advisable to use braided carbon yarn end rings or other means to protect the graphite rings against extrusion. Further research is required to develop FE models of braided carbon yarn packing rings, so that packing ring sets of this type can be investigated using the techniques developed in this thesis.

7.2.2 Constitutive FE material model

The modified Mohr Coulomb material model in DIANA was initially chosen as the best available FE material model and package with which to model exfoliated graphite. DIANA has very advanced geotechnical material models implemented in its code. However, convergence problems occurred while trying to model contact friction in DIANA. Contact friction has a significant effect on the behaviour of a compression packing set in a valve. Contact friction cannot be omitted from any FE model which is trying to predict the behaviour of compression packings rings in a valve. The best available alternative had to be chosen, this was the modified Cam clay material model in ABAQUS/Standard. The modified Cam clay material model in ABAQUS/Standard is not as advanced as the modified Mohr Coulomb material model in DIANA, one particular shortfall of the modified Cam clay material model in ABAQUS/Standard is that it cannot support tensile stresses.

The modified Cam Clay material model in ABAQUS/Standard is used to simulate the wedge test rig. Convergence problems occurred when trying to model this test rig. Plastic collapse was found to occur on the free surface, which in this case is the top of the block (which represents the packing rings), unless a pressure was applied to this free surface. This occurred because the modified Cam clay material model in ABAQUS/Standard does not support tensile stresses. However, the tensile strength of graphite can be simulated in the model by applying an artificial hydrostatic pressure of approximately 3 times the uniaxial tensile strength to the top of the block, thus allowing the FE model of the wedge test rig to converge. A better option would be to develop a material model in ABAQUS/Standard using the umat option [62] which allows the programmer to develop their own user defined material model. A umat could be developed to allow for the inclusion of tensile strength in the modified Cam clay material model which would mean that an artificial tensile strength would not have to be given to the block through the application of an external stress. This however would take a considerable amount of time to complete. Time constraints meant that it could not be

considered in this project.

7.2.3 Valve cycling model

An FE model of three exfoliated graphite packing rings in a valve as described in Section 4.2.2 is implemented in ABAQUS/Standard to investigate the influence of loading, valve stem cycling, valve stem friction and wear on the behaviour of a 1.5 g/cm^3 exfoliated graphite packing ring set. The model however, does not account for effects of system pressure, temperature, and pressure cycles that would generally be experienced by a packing ring set in a valve. These variables are set by system design and they are known to have a significant influence on the behaviour of a packing ring set. These are variables which could be investigated in future research.

7.2.4 Wedge test

The wedge test rig described in Section 6.2 was used to investigate the influence of asperity angle and atmosphere on the friction and wear behaviour of compression packing rings. The friction behaviour of graphite is known to depend on the presence of oxygen in the atmosphere [51]. Tests were carried out in both air and argon (an inert gas) to investigate this phenomenon with regard to graphite packing rings. No actual measurements were taken of the oxygen levels within the test head. Therefore it is not possible to say with 100% accuracy that there is no oxygen in the test head during any particular test carried out in argon. High purity grade argon was used during testing to minimise the introduction of impurities from the test gas itself. High purity grade argon has a minimum purity of 99.998% (i.e. less than 20 ppm of O_2).

7.3 FE analysis of a valve packing set

The FE material model developed and validated in the first part of this thesis is used to model a packing ring set which consists of three 1.5 g/cm^3 exfoliated

graphite packing rings in a valve. The FE model is detailed in Section 4.2.2. The model is subjected to two separate loading conditions. The first loading condition mimics that of a standard bolted valve. This is the most common method of loading a valve packing set. Under displacement control conditions the top of the packing ring set is displaced by a fixed amount.

The second loading condition mimics that of a live loaded valve. A live loaded valve applies a near constant axial stress to the top of the packing ring set. The axial stress is applied through a set of Belleville washers as seen in Figure 2.2. The set of Belleville washers act as a spring applying a force to the top of the packing ring set. The spring force in a live loaded system does however, change due to volume loss in the packing ring set. When the packing ring set experiences volume loss the springs will elongate, thus causing a reduction in applied axial stress. This change is minimal and can be assumed to be constant over 5 stem cycles, the number of valve stem cycles implemented in the FE model. Packing manufactures recommend the use of live loaded valves in critical applications. Live-loading provides numerous benefits, especially in systems with frequent pressure or temperature changes or high-cycle applications. It compensates for pressure and temperature changes and wear.

FE analysis was used to investigate the influence of loading and valve stem friction on the behaviour of an exfoliated graphite packing ring set. During the FE analysis the following variables were investigated, applied axial stress, radial stress against the stem and force required to cycle the stem.

7.3.1 Applied axial stress

A complete set of results for applied axial stress depending on loading conditions and valve stem friction can be seen in Section 5.4.1. Figure 7.1 compares the applied axial stress at the top of seal 1 under load and displacement control conditions when the coefficient of friction between the packing ring set ID and the stem is $\mu_{stem} = 0.15$.

Under displacement control conditions the applied axial stress at the top

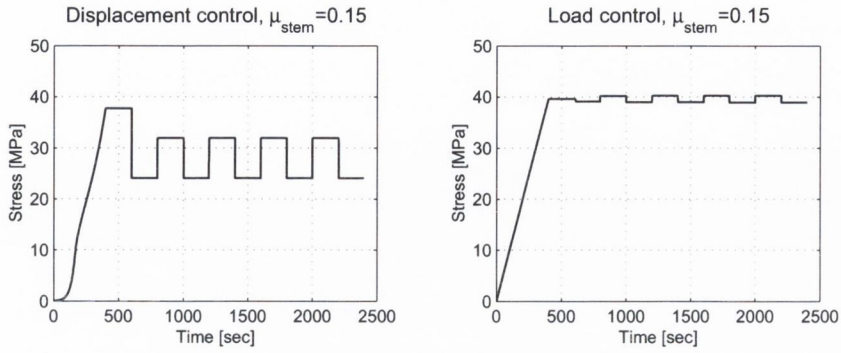


Figure 7.1: Stress at the top of seal 1 for $\mu_{stem} = 0.15$ under displacement load control conditions

of seal 1 is seen to decrease significantly after one valve stem cycle, the applied axial stress at the top of seal 1 is also seen to fluctuate significantly when the valve stem is cycled. These fluctuations are seen to increase as the coefficient of friction between the packing ring inner diameter and the stem is increased. This occurs due to a phenomenon called stress shakedown.

Under load control conditions the applied axial stress at the top of seal 1 is held relatively constant. The stress at the top of seal 1 is seen to fluctuate slightly as the valve stem is cycled. These fluctuations are more pronounced when the valve stem friction is increased.

7.3.2 Radial sealing stress

Contact friction at the packing ring set stuffing box interface resists the transfer of applied axial stress through a packing ring set. This results in a decay in radial sealing stress against the stem and housing along the length of the packing ring set. The decay in radial stress against the stem has a complicated interdependence on applied axial stress, axial deformation of the packing ring set and K_{rad} , the radial stress transfer coefficient. Through FE analysis it is possible to determine the decay in radial stress against the stem under a specific set of operating conditions.

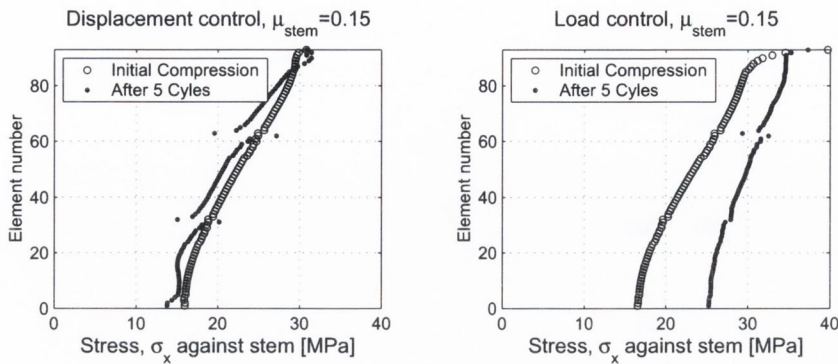


Figure 7.2: Comparison of radial stress against the stem on initial compression and after 5 stem strokes under conditions of displacement and load control

Figure 7.2 compares the radial stress against the stem under displacement and load control conditions where the coefficient of friction between the packing ring set ID and the stem is $\mu_{stem} = 0.15$. Under displacement control conditions the stress against the stem is seen to deteriorate after 5 valve stem cycles. Under load control conditions however, the radial stress distribution against the stem is seen to improve after 5 valve stem cycles giving better sealing and less leakage from the valve stem. This phenomenon is called stress shakedown, whereby the initial radial stress distribution against the stem develops into a new stress distribution after a series of valve stem cycles.

These results demonstrates the benefit of live loaded valves over standard bolted valves. A valve packing set under load control conditions has an improved distribution of radial sealing stress against the valve stem after it has been cycled, resulting in a lower leak rate from the valve. Under displacement control conditions the radial stress against the stem is seen to deteriorate after the valve stem is cycled increasing the risk of leakage and failure of the valve packing set. No experimental test has been developed to date to accurately determine the decay in radial stress against the stem

for a complete packing ring set. The FE method developed in this thesis represents a significant step forward in analysing valve packing behaviour.

7.3.3 Force to cycle stem

The primary function of a valve is to control the flow of a fluid in a system. In order to control the flow it is essential that the valve can be satisfactorily opened and closed when required. Valves can either be actuated mechanically or by hand. It is critical that the power required to operate a valve does not exceed the capabilities of the actuator or the operator in a particular application.

The force required to cycle the stem will vary depending on the radial stress against the stem and the coefficient of friction between the packing ring set inner diameter and the stem. A comparison between a valve under displacement control conditions and a valve under load control conditions, for a coefficient of friction of $\mu_{stem} = 0.15$, is shown in Figure 7.3. The radial stress against the stem under load control conditions is greater than the radial stress against the stem under displacement control conditions after the valve stem has been cycled, therefore it stands to reason that the force required to cycle the stem under load control conditions will be greater than that under displacement control conditions.

7.4 Comparison with analytical solutions

7.4.1 Decay in radial stress against the stem

The analytical models which describe the radial stress against the stem developed by Denny & Turnbull [9] and Salter [11] are compared with FE results for valve packing sets under the same operational conditions. The analytical models developed by Denny & Turnbull and Salter are detailed in Equations 2.1 and 2.2 respectively. The analytical models assume that packing ring behaviour is elastic over the loading range.

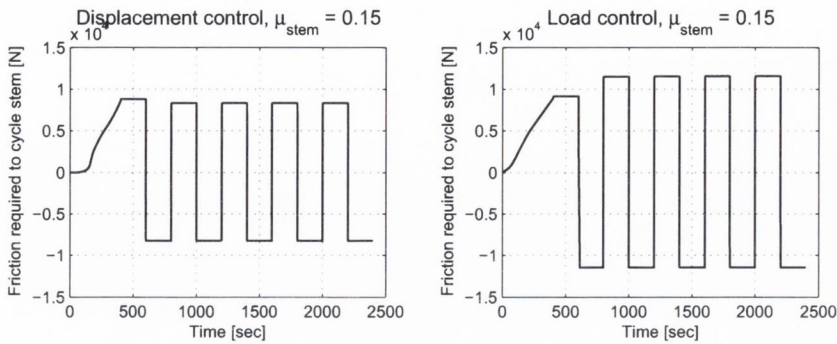


Figure 7.3: Comparison of the force required to cycle the stem under displacement and load control conditions

The analytical equations demand the input of an applied axial stress, under displacement control conditions the applied axial stress is seen to change after the valve stem is cycled. The applied axial stress also shows significant fluctuations as the valve stem is opened and closed, this behaviour can be seen in Figure 7.1. If the analytical models were to be compared with the case of the FE model under displacement control conditions the analytical solutions would have to be recalculated after the valve stem is initially cycled and for each case of opening and closing the valve stem. Therefore only the case of the FE model under load control conditions is compared with the analytical models to determine the decay in radial stress against the stem. On initial compression the FE results are compared with the two analytical models which aim to predict the radial stress against the stem, the result of this comparison can be seen in Figure 7.4. The FE model predicts 10-15% greater radial stresses against the stem than the analytical models.

After 5 cycles the FE data is again plotted against the results from the analytical models as seen in Figure 7.5. The FE results are seen to deviate significantly from the analytical solutions. This deviation occurs as a result of stress shakedown. The analytical models cannot model stress shakedown, thus the analytical models developed previously by Denny & Turnbull [9]

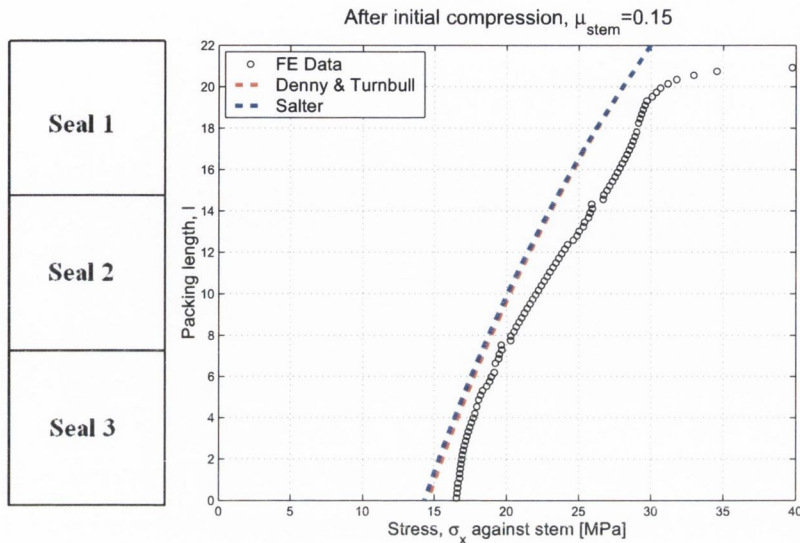


Figure 7.4: Stress against the stem on initial compression, comparing FE data with analytical models

and Salter [11] are not capable of modelling the radial stress behaviour of an exfoliated graphite packing ring set once the valve stem is cycled. This demonstrates the applicability and usefulness of FE analysis in analysing the stresses in a valve packing set, and the inadequacies of the analytical models.

7.4.2 Force required to cycle stem

The force required to cycle a valve stem was analysed by Thomson in 1958 [29]. Equation 2.3 was developed by Thomson by means of an integration of the axial force over the packing length resulting in an exponential decay in the axial stress from the gland follower to the stuffing box bottom due to friction. A second integration leads to the frictional stem force. In both assumptions it is assumed that the coefficient of friction does depend on axial stress. Klenk [12] proved experimentally that this is incorrect.

Klenk devised a new empirical formula, (Equation 2.5) to predict the frictional stem force and verified the formula by means of extensive experimental testing on a variety of packing ring material types of different lengths. The

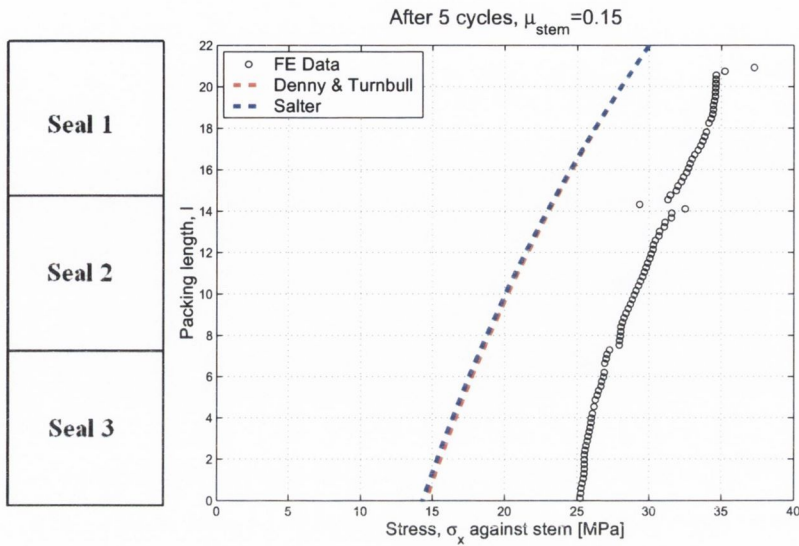


Figure 7.5: Stress against the stem after 5 cycles, comparing FE data with analytical models

formula developed by Klenk was compared with FE results using the model seen in Figure 4.8 with a coefficient of friction $\mu_{stem} = 0.15$. Results of this analysis can be seen in Figure 7.6. FE results are for the case of load control conditions because the stress at the top of seal 1, σ_B is not constant after the valve stem is cycled and it fluctuates when the valve stem is opened and closed.

The FE results are seen to match the empirical formula derived by Klenk for the force required to cycle the valve stem under a given set of operational conditions. The FE model predicts a 2.8 % lower force to move the stem than the empirical formula developed by Klenk, this difference is minimal. Klenk proved experimentally that this equation is valid for a wide range of materials of different lengths, thus validating the FE material model. The formula derived by Klenk is only true for valve packing sets under displacement control conditions if the applied axial stress σ_B is changed depending on whether or not the valve is being opened or closed.

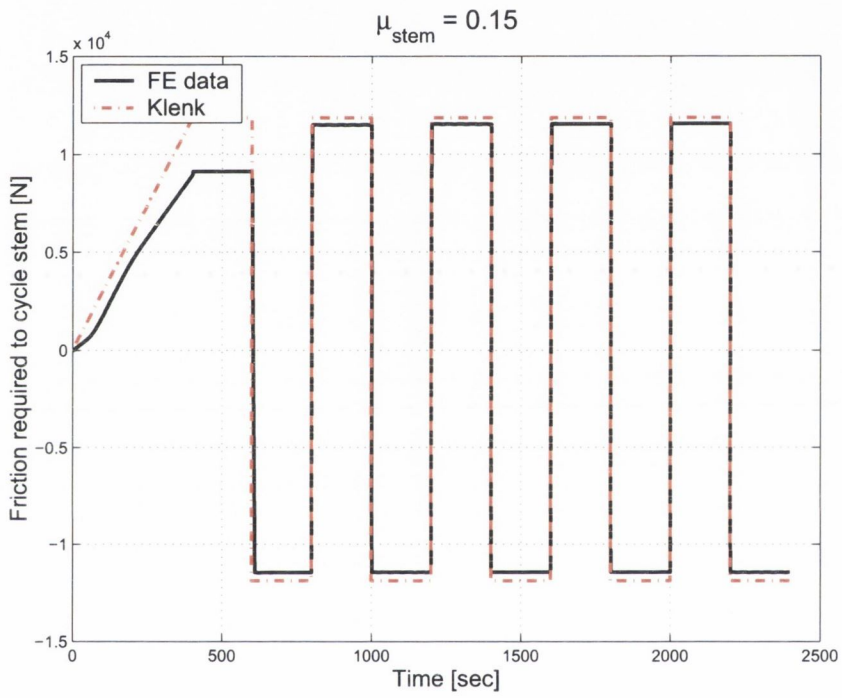


Figure 7.6: Comparison of FE data with the empirical formula for the force required to cycle the stem

7.5 Compression packing friction

A series of experiments were carried out to determine the influence of asperity surface slope and atmosphere on the friction and wear behaviour of compression packing rings. The test rig is described in Section 6.2. Four different wedge angles were used in the experimental program, these being 4° , 5.88° , 8.12° and 8.93° wedge angles. These represent the range of average asperity slope seen on standard valve stems. The average asperity slope of a particular valve stem depends on the manufacturing process used to prepare the valve (i.e. turning, grinding and/or polishing).

The experimental wedge test results for 1.5 g/cm^3 exfoliated graphite are shown in Figures 6.3 and 6.4 for air and argon respectively. From these figures it can be seen that an increase in coefficient of friction occurs with increasing stroke number. This increase in coefficient of friction with stroke number is significantly more pronounced in argon.

Initially it was hypothesised that the increases seen in coefficient of friction in exfoliated graphite packing rings seen in tests carried out in argon resulted from the presence of oxygen in the test head at the beginning of the test. It was hypothesised that there was still enough oxygen present in the test head to have a positive influence on the frictional behaviour at the wedge valve packing interface. As the test progresses and as argon is continuously fed through the system the level of oxygen within the test head decreases and the friction at the packing valve interface deteriorates. This however did not explain the fact that increases in coefficient of friction are seen in both air and argon. Though the increases in air are not as dramatic as those seen in argon. This hypothesis does not explain the fact that experimental test results show that increases in coefficient of friction are seen to depend on wedge angle.

Therefore a second hypothesis was made that states that the dramatic increases seen in the coefficient of friction of exfoliated graphite packing rings can be attributed to a failure of the surface layer of the compression packing rings. The more dramatic increases in coefficient of friction seen in argon

can be explained by the fact that the initial values of intrinsic coefficient of friction are greater in argon than in air. The greater the value of the initial intrinsic coefficient, the sooner failure of the surface will occur. A higher initial intrinsic coefficient of friction will lead to greater deviatoric stresses within the packing ring set and hence failure of the surface layer of the packing ring set ID will occur sooner as the wedge is stroked against the ID of the packing ring set.

An interesting result was observed in wedge tests carried out on a special 1.5 g/cm^3 exfoliated graphite packing ring. This special exfoliated graphite packing ring has a secondary substance included in the packing ring which can not be detailed in this thesis due to a company confidentiality agreement. Tests on this material gave much lower coefficient of friction values compared with standard 1.5 g/cm^3 exfoliated graphite packing rings. This means that the inclusion of an additive which aids lubrication at the packing ring inner diameter will result in reductions in the friction and wear behaviour of packing ring sets.

7.5.1 Intrinsic coefficient of friction

Initially it was proposed that a model developed by Oxley et al. [20] would be used to model the influence of asperity angle on the friction behaviour of exfoliated graphite packing rings. Experimental tests showed that the coefficient of friction of exfoliated graphite increases with stroke number. Equation 2.10 developed by Prof. Oxley et al. [20] does not allow for the prediction of this increase in coefficient of friction with stroke number. The equation does, however, allow for the prediction of the initial intrinsic coefficient of friction of the interface of the wedge and the exfoliated graphite packing ring set based on wedge angle and atmosphere. This equation decouples the effect of asperity slope from the intrinsic coefficient of friction of the interface. The original model described in Equation 2.10 was modified to allow for the elastic recovery of exfoliated graphite. The elastic recovery of exfoliated graphite causes a reduction in the actual wedge angle leading to a new effective wedge

angle, this analysis is detailed in Section 6.3.5. This modification of the Oxley model allows for increased accuracy in the calculated results of initial intrinsic coefficient of friction.

The values of the intrinsic coefficient of friction are calculated for the beginning of the test and can be seen in Table 6.1. The intrinsic coefficient of friction is calculated for each individual test material in both air and argon. Figure 6.12 illustrates that there is a good correlation between the experimental results for initial intrinsic coefficient of friction and the predicted intrinsic coefficient of friction values obtained from Equation 2.10.

7.5.2 FE analysis of wedge test

In investigating the increases seen in coefficient of friction in experimental tests on exfoliated graphite packing rings it was hypothesised that the dramatic increases in the coefficient of friction resulted from failure of the surface layer of the packing ring set. It is believed that the observed increases in coefficient of friction result from the stresses in the material under the wedge reaching the critical state, which is the failure criterion of the modified Cam clay material model. Critical state is reached when the critical state line defined by $\eta = \frac{q}{p}$ lies exactly on the top of the ellipse which defines the yield surface of the modified Cam clay material model. The critical state line in p-q space is the line that connects the tops of the ellipses of different sizes. The wedge test rig records the forces on the wedge and the displacement of the wedge into the packing rings during a test. This data is used to determine the coefficient of friction and wear coefficient of a particular packing material in a given environment.

However, the stresses and strains in the packing rings cannot be measured experimentally. Therefore this hypothesis could only be investigated using the FE method. FE analysis of the wedge test rig was carried out for all four wedge angles in argon. FE analysis of the wedge test was only carried out for the case of an exfoliated graphite packing ring set in argon due to time constraints, also the increases in coefficient of friction are more

pronounced in argon and therefore results from FE analysis should give significant differences between different wedge angles allowing for validation of this hypothesis. The trendlines for the evolution of η with stroke number are shown in Figure 6.31. As expected the slope of the stroke number versus η curve increases with wedge angle.

Experimental results for coefficient of friction of 1.5 g/cm^3 exfoliated graphite packing rings in argon show that after a specific number of strokes the coefficient of friction is seen to increase significantly. The point at which this significant increase occurs varies depending on the angle of the wedge as seen in Figure 7.7.

The value for η for each of the wedge angles at the corresponding stroke number is calculated from the data in Figure 6.31. It was found that the point at which the dramatic increases in coefficient of friction occurs for each of the wedge angles corresponds to a unique value of $\eta = 0.75$. This is the value of η inputted into the modified Cam clay material model to predict the failure of the material. $\eta = M$ in the in the modified Cam clay material model when the material has reached the critical state.

Table 7.1 details the wedge angle and corresponding stroke number at which a dramatic increase in coefficient of friction will be seen for tests carried out on 1.5 g/cm^3 exfoliated graphite in argon. The results seen in Table 7.1 show that an average asperity angle of 4° will lead to a significantly longer life for the packing ring set than an average asperity angle of 5.88° or higher. A 4° average asperity angle will allow for 43.3×10^6 times as many strokes of the valve stem than a 5.88° average asperity angled valve stem. This suggests that the surface finish of a valve stem may have a large effect on the life of a packing ring set. One fact that has not been considered in this analysis is what will occur at the interface of a real stem and packing ring set where the packing ring material will be in contact with the front and back faces of the asperities on the stem. Packing ring material in contact with the back face of the asperity will result in forces being applied to the back face of the asperity. This will result in variations in the measured forces on the asperity

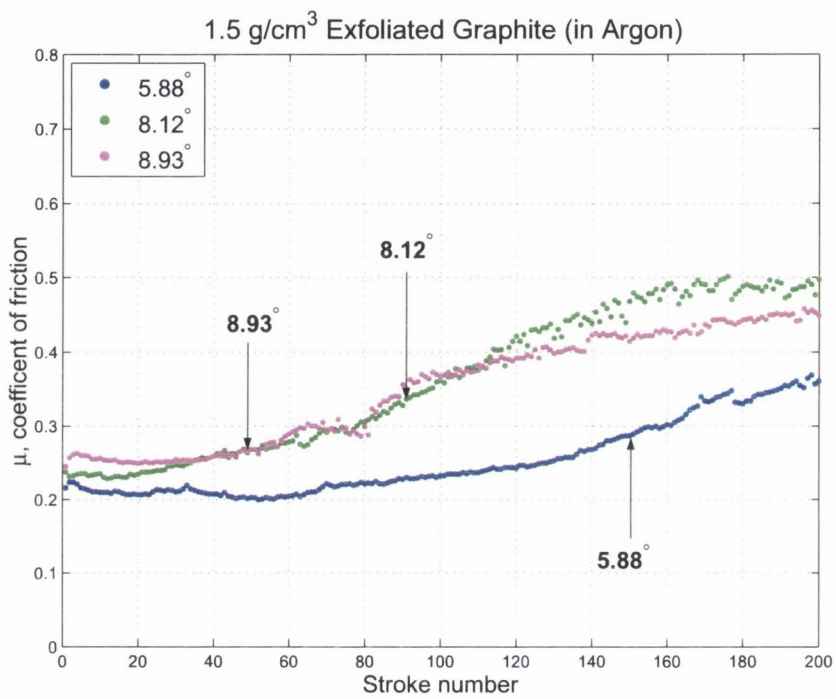


Figure 7.7: Stroke number at which dramatic increase in coefficient of friction for 1.5 g/cm³ exfoliated graphite is seen

Table 7.1: Strokes until η reaches 0.75 for 1.5 g/cm^3 exfoliated graphite with an intrinsic coefficient of friction of $\mu = 0.15$

Wedge angle	Stroke number	η
4.00	6500×10^6	0.75
5.88	150	0.75
8.12	90	0.75
8.93	50	0.75

and hence the coefficient of friction at the real stem packing set interface. It is not known how large these effects would be. This fact has not been considered in this thesis but is proposed as future work.

When determining the average asperity slope of an actual stem the bandwidth over which you measure the average slope has to be considered. The bandwidth is the distance along a length of a surface over which the surface chosen surface characteristic is investigated. The choice of bandwidth is known to effect the measured surface profile parameter. The surface parameter investigated in this thesis is the average surface slope. The influence of bandwidth on the average asperity slope of a valve stem was investigated using a computer software package called FAST [89]. FAST allows for the influence of bandwidth on the average asperity slope of a particular profile to be investigated.

The influence of bandwidth on the average asperity angle of a steel surface given 5 different surface preparations were investigated, these being;

- Roughly ground
- Ground and lightly polished
- Ground and highly polished
- Ground and diamond polished

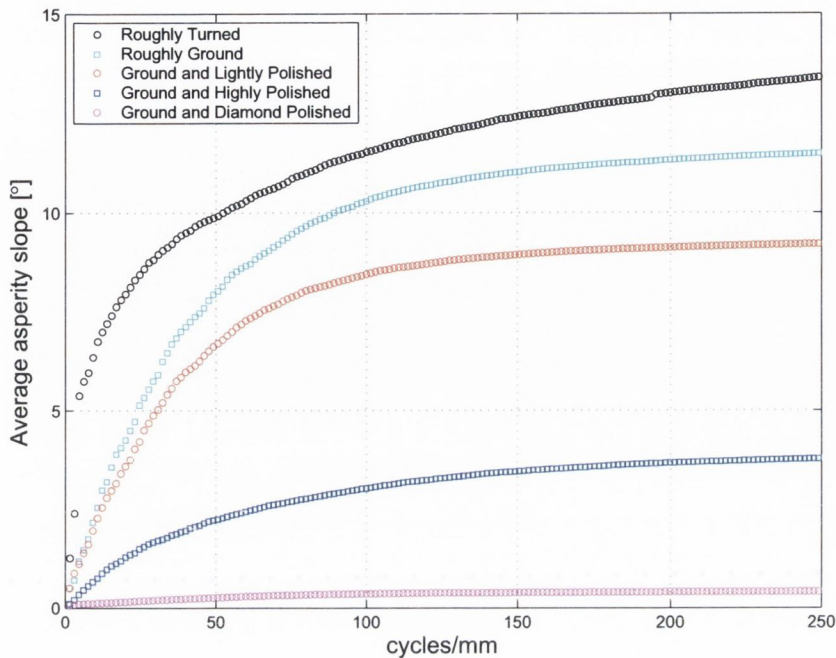


Figure 7.8: Change in average asperity slope with bandwidth

- Roughly Turned

The surface profiles used during this analysis were 10 cm in length. The actual length of a valve stem could be multiple times longer than this 10 cm profile tested. Figure ?? details the difference in average surface slope with bandwidth for all five surface profiles.

Even though the significant bandwidth for an entire valve stem has not been determined significant conclusions can be taken from these results. From Figure ?? it can be concluded that the average surface slope of a roughly turned has a greater average surface slope than a roughly ground surface. The average surface slope of a turned surface does not exceed 13.5° over the bandwidth tested where the average surface slope of a roughly ground surface does not exceed 11.5°. A ground and lightly polished surface has a lower average surface slope and a ground and highly polished surface has an

even lower average surface slope. In these specimens tested a ground and lightly polished surface has an average surface slope that does not exceed 9.5° whereas a ground and diamond polished surface has an average asperity slope which does not exceed 0.45° . Further tests should be carried out to find the significant bandwidth of an entire stem.

7.6 Packing ring wear

Wear analysis allows for the understanding and prediction of volume loss from a packing ring set. Wear of a packing ring set will cause a reduction in radial stress against the stuffing box and hence an increase in leakage from the valve. Wear is quantified by the wear coefficient, K which is calculated using Equation 6.15. results from experimental testing show that wear of exfoliated graphite packing rings is seen to increase significantly with wedge angle. Values for the wear coefficient are an order of magnitude greater for tests carried out in argon thus demonstrating the influence that atmosphere has on the wear of an exfoliated graphite packing ring set. The special 1.5 g/cm^3 exfoliated graphite packing ring shows significantly lower wear rates than standard exfoliated graphite packing rings. This demonstrates the ability of additives which aid lubrication at the packing stem interface to reduce wear of the packing ring set.

In a wedge test a process of compaction occurs under the wedge initially. After this process of compaction stabilises, a process of steady state wear can be assumed to be occurring under the wedge. This is why only the final third of the test data is used to calculate the wear coefficient.

It is intuitive that an increase in coefficient of friction should result in an increase in wear. The results for exfoliated graphite packing rings are investigated. The predicted average coefficient of friction μ , is plotted against the wear coefficient, K in air and in argon. The results of this analysis are shown in Figure 7.9.

From Figure 7.9 it can be seen that an increase in the friction coefficient

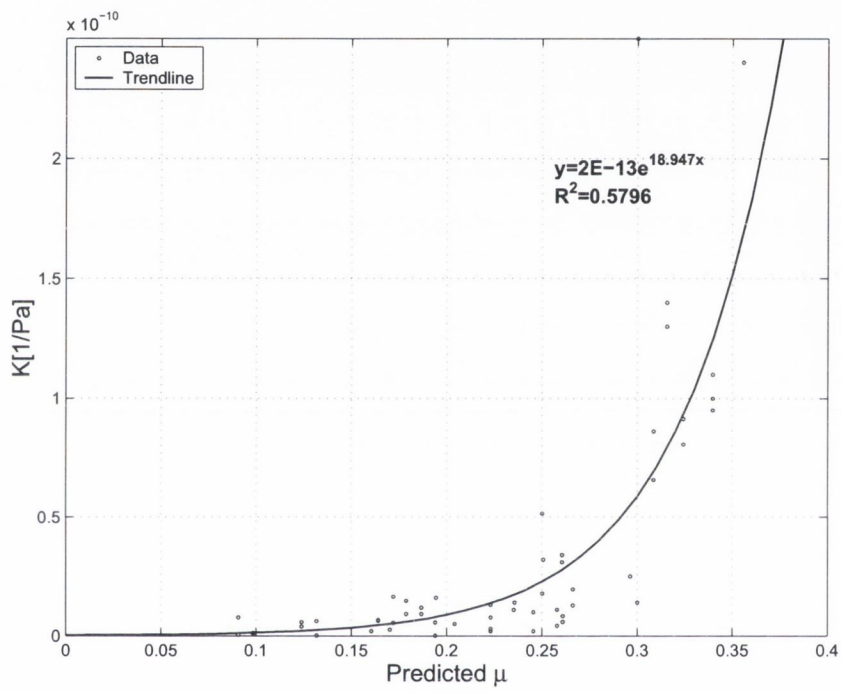


Figure 7.9: Correlation between predicted friction coefficient, μ and the wear coefficient, K

will cause an exponential increase in the wear coefficient of exfoliated graphite packing rings. This demonstrates the need to minimise the coefficient of friction so that excessive wear of a packing ring set does not occur.

The tribological analysis carried out for this thesis focused mainly on developing a better understanding of the friction behaviour of exfoliated graphite packing rings. More work needs to be carried out on the wear data to produce a proper predictive model of its behaviour. The wear that was measured in the wedge test is also only indicative of what would happen in a real valve. Wear is a complicated process, of which only wear loss was measured. In a real valve the wear particles will be trapped and the total wear of the system will depend on how they are trapped and on how they escape from the system.

7.7 Valve design rules

It is critically important that a packing ring set is clamped with the optimum applied axial stress for a given application. The optimum applied axial stress is a compromise between maximum allowable leakage, minimum wear of the packing ring set and optimum valve cycling force. If an excessive axial stress is applied to the packing ring set the force required to cycle the stem may exceed the power of the actuator and it will become impossible to cycle the valve stem. If the applied axial stress is too great excessive wear of the packing rings set will occur. On the other hand the greater the applied axial stress the lower the leakage from the valve. The most desirable situation is one where the applied axial stress is optimised in terms of leakage, wear and the force required to cycle the valve stem.

Wear of a packing ring set was simulated using FE analysis. A model of three 1.5 g/cm^3 exfoliated graphite packing rings in a stuffing box (as seen in Figure 4.8) was used to carry out wear analysis. A fixed displacement was applied to the top of seal 1 and the valve stem was cycled 5 times. The analysis was only carried out under displacement control conditions because if the

model was implemented under load control conditions it would compensate for the wear that was occurring at the packing ring set inner diameter and maintain a constant load on the packing ring set. This would result in no reduction of radial stress against the stem. Following this initial simulation the valve stem was moved away from the packing ring set stem interface to simulate wear of the packing ring set inner diameter. The radial stress against the stem was recorded as the stem was moved away from the packing ring set.

The decay in radial stress against the stem was plotted as a function of W_c and S_c , where

$$W_c = \frac{h}{t} \quad (7.1)$$

in which h is the wear depth and t is the packing ring thickness and

$$S_c = \frac{S_{i+1}}{S_i} \quad (7.2)$$

where S_{i+1} is the average radial stress against the stem along a packing ring set of length l and S_i is the average radial stress against the stem along a packing ring set of length l under conditions of no wear. The analysis generates a graph of W_c against S_c defined by Equation 7.3.

$$S_c = e^{-233.94W_c} \quad (7.3)$$

Equation 7.3 is modified to obtain Equation 7.4.

$$S_c = e^{-233.94\frac{h}{t}} \quad (7.4)$$

Assuming that Archard's equation applies, the wear depth, h after n cycles can be found as follows.

$$h_n = K S_n Z \quad (7.5)$$

where K is the wear coefficient, S_n is the stress after n cycles and Z is the distance slid.

All these variables can be included in Equation 7.3 to obtain a modified version of this equation which is dependent on the wear coefficient and distance slide. This result is seen in Equation 7.6.

$$S_{i+1} = S_i e^{-233.94 \frac{K S_{i+1} Z}{t}} \quad (7.6)$$

This formula can be used to determine what distance the valve stem would need to slide for the stress to fall to a critical value. Equation 7.4 can be generalised into a form seen in Equation 7.7.

$$S = S_0 e^{-B \frac{h}{t}} \quad (7.7)$$

$$\frac{dh}{dz} = KS = K S_0 e^{-B \frac{h}{t}} \quad (7.8)$$

If we allow the relative stress to fall to S_c , then

$$\ln(S_c) = -B \frac{h}{t} \quad (7.9)$$

and

$$h_c = -\frac{t}{B} \ln(S_c) \quad (7.10)$$

The sliding distance to achieve this result is given by

$$Z = \frac{1}{K S_0} \int_0^{h_c} e^{h \frac{B}{t}} dh = \frac{1}{K S_0} \frac{t}{B} (e^{h_c \frac{B}{t}} - 1) = \frac{1}{K S_0} \frac{t}{B} (e^{-\ln S_c} - 1) = \frac{1}{K S_0} \frac{t}{B} (S_c - 1) \quad (7.11)$$

Equation 7.11 can be used to determine the distance that the valve stem would have to travel in order for the stress against the stem to fall to a critical value at which the leak rate would exceed the maximum allowable value.

7.7.1 Optimum initial radial stress

To calculate the optimum initial average radial sealing stress to get maximum life from the packing ring set, we define the stroke length of the valve as L , and the radial stress against the stem required to prevent leakage as S_l . From Equation 7.11 the number of cycles until leakage will occur can be calculated.

$$N_l = \frac{Z}{L} = \frac{1}{KB} \frac{t}{L} \left(\frac{S_l}{S_0^2} - \frac{1}{S_0} \right) \quad (7.12)$$

Differentiating Equation 7.12 and setting it equal to zero gives the optimum initial pressure:

$$\frac{dN_l}{dS_0} = \frac{1}{KB} \frac{t}{L} \left(\frac{-2S_l}{S_0^3} - \frac{1}{S_0^2} \right) \quad (7.13)$$

$$S_l = 2S_0 \quad (7.14)$$

Equation 7.13 reduces to Equation 7.14. This equation states that the optimum initial average radial sealing stress should be twice the radial sealing stress which causes the maximum allowable leakage. EPRI [26] found that the optimum applied axial stress from experimental tests was found to be 1.75 x applied axial stress. From the analysis in this section to determine the optimum radial stress it is determined that the optimum applied axial stress is approximately 2.67 times the initial stress, which is significantly greater than that determined experimentally by EPRI. There is however no data available from the EPRI report on how many time they retightened the bolts during testing. The FE analysis carried out in this thesis did not consider the case where the bolts were retightened to overcome the reduction in applied axial stress that occurs after the valve stem is cycled when the packing ring set is under displacement control conditions.

7.8 Achievements of this study

This study is the first to develop a non-linear elastoplastic FE model of 1.5 g/cm^3 exfoliated graphite packing rings, which is implemented in a commercial FE package. This was realised through an extensive programme of experimental testing and FE model validation. Developing and validating this FE model took some time and is put forward as a major achievement of this research.

This FE material model was then used to investigate the influence of loading, valve stem cycling, valve stem friction and wear on the behaviour of an exfoliated graphite packing ring set. The benefits of live loaded valves over standard bolted valves was demonstrated using FE analysis. Previously developed analytical models used to predict the behaviour of compression packing rings in a valve were compared with FE analysis results. It was found that FE analysis is vastly superior to analytical analysis in predicting the behaviour of compression packing rings in a valve.

As part of this study a new novel test rig was developed which can be used to predict the influence of valve stem surface texture and atmosphere on the friction and wear behaviour of exfoliated graphite packing rings. The coefficient of friction at the stem packing interface was found to increase with stroke number even in an oxygen rich environment. It was only possible through the use of FE analysis to investigate the rise in coefficient of friction with increasing stroke number. The non-linear elastoplastic FE model developed in the first part of this thesis was used to investigate this phenomenon. It was found that FE analysis could be used to predict the increase in coefficient of friction with increasing stroke number seen in exfoliated graphite packing rings because it occurred as a result of failure of the surface layer of the packing ring set asperity interface. This tool is used to determine the optimum surface finish of the stem to give maximum life from the packing ring set.

Chapter 8

Conclusion

8.1 Main conclusions

A non-linear elastoplastic FE material model to predict the behaviour of exfoliated graphite was presented in this thesis. This material model was used to predict the response of exfoliated graphite packing rings to stress, friction and wear. The following points are the main conclusions of this study:

- Under displacement control conditions the radial sealing stress against the stem is seen to deteriorate after the valve stem is cycled. Under load control condition the opposite is seen to be true. Thus demonstrating the benefits of live loaded valves over standard bolted valves.
- Analytical models are not capable of modelling the phenomenon of stress shakedown that occurs in the valve packing set after the valve stem is cycled.
- FE analysis is able to determine the behaviour of exfoliated graphite packing rings in a valve much more accurately than analytical models.
- FE analysis is an important tool in analysing the behaviour of valve packing rings due to their non-linear elasto-plastic behaviour. FE

analysis allows for the accurate prediction of the packing ring set's response to applied axial stress, valve stem cycling and friction at the valve stuffing box packing ring set interface.

- Standard exfoliated graphite packing rings show an increase in coefficient of friction with wedge angle in air. The coefficient of friction is seen to increase gradually with stroke number.
- In argon the coefficient of friction for standard exfoliated graphite packing rings is seen to increase significantly with stroke number.
- A modified version of a model developed by Prof Oxley et al. [20] was used to predict the initial intrinsic coefficient of friction based on surface roughness.
- Standard exfoliated graphite packing rings exhibit an increase in coefficient of friction with time. This phenomenon cannot be predicted using this model.
- A FE model of the friction test rig was set up to investigate the stresses in the packing rings under the wedge.
- The increase in friction coefficient seen in standard exfoliated graphite packing rings with stroke number is a result of failure of the surface layer of the packing ring under the wedge.
- A valve stem with an average asperity slope of 4° will prolong the life of a valve packing set significantly compared with a 5.88° average asperity angled valve stem or higher.
- A ground and polished valve stem will give an average asperity angle on the valve stem of approximately 4° . This surface finish is recommended to allow for the optimum friction and wear response in the packing ring set from the valve.

- An increase in the coefficient of friction leads to an exponential increase in the wear coefficient.
- The optimum initial applied radial stress against the stem should be twice the radial stress that gives the maximum allowable leakage.

8.2 Future work

The following recommendations are made for future work on the subject of this thesis:

- System pressure, temperature and pressure cycle effects should be included in the FE valve cycling model.
- FE analysis should be used to determine the optimum applied axial stress in a given application.
- Detailed experimental testing should be carried out to characterise other packing material types. The experimental data should then be used to develop FE material models of these packing material types.
- FE analysis of the wedge test rig for 1.5 g/cm^3 exfoliated graphite in air should be carried out to determine the number of strokes until the surface layer of the packing rings fail.
- Experimental testing of the frictional properties of a complete stem given a set average asperity slope to determine how the theory in this thesis of a single asperity sliding against an exfoliated graphite packing ring set applies to a real valve and packing ring set.

Bibliography

- [1] European Environment Agency. <http://www.eea.eu.int/>.
- [2] Environmental Protection Agency. <http://www.epa.gov>.
- [3] European Sealing Association. <http://www.europeansealing.com>.
- [4] K.B. Schnelle and C.A. Brown. *Air Pollution Control Handbook*. CRC Press, 2001.
- [5] European Integrated Pollution Prevention and Control Bureau. <http://eippcb.jrc.es/pages/factivities.htm>.
- [6] Reyes R.J. and Riddington J.W. Valve failure problems on lwr power plant. *Nuclear Safety*, 22(2), March-April 1981.
- [7] Electrical Power Research Institute (EPRI). Effect of valve performance on boiling water reactor unit capacity. Technical Report NP 1473, Nuclear Services Corporation, Pennsylvania, USA, August 1980.
- [8] Fluid Sealing Association & European Sealing Association. Guidelines for the use of compressions packings, 1997.
- [9] Denny D.F. and Turnbull D.E. Sealing characteristics of stuffing-box seals for rotating shafts. *Proc Instn Mech Engrs*, 174(6):271-291, 1960.
- [10] Thomson K. A theory of sealing with particular reference to the packed stuffing box. In *British Hydromechanics Research Association, International Conference on Fluid Sealing*, page Paper B1, 1961.

- [11] Salter. Analytical assesment of the packed gland for recipocating valve stems. Technical Report C373/023, Central Electricity Generating Board, Southampton, 1989.
- [12] Klenk T. *Kennwerte Fur Stopbuchspackungen*. PhD thesis, University of Stuttgart, 1999.
- [13] R.T. Fenner. *Finite Element Methods For Engineers*. Imperial College Press, 1996.
- [14] O.C. Zienkiewicz and R.L. Taylor. *The Finite Element Method: Basics v.1*. Butterworth Heinemann, 2000.
- [15] Wood Muir David and Graham J. Aniotropic elasticity and yielding of a natural plastic clay. *International Journal of Plasticity*, 6:377–388, 1990.
- [16] Challen J.M. and Oxley P.L.B. An explanation of the different regimes of friction and wear usign asperity deformation models. *Wear*, 1979.
- [17] Challen J.M., McLean L.J., and Oxley P.L.B. Plastic deformation of a metal surface in sliding contact with a hard wedge. *Proc. Roy. Soc. Lond. Ser. A*, pages 161–181, 1984.
- [18] Challen J.M. and Oxley P.L.B. A slip line analysis of the transition from local asperity contact to full contact in metallic sliding friction. *Wear*, (100):171–193, 1984.
- [19] Komvopoulos K., Saka N.P., and Suh N.P. Plowing friction in dry and lubricated metal sliding. *ASME J. Tribol.*, (108):301–313, 1986.
- [20] Black A.J., Kopalinsky E.M., and Oxley P.L.B. Sliding metal friction with boundary lubrication: an investigation of a simplified friction theory and of the nature of boundary lubrication. *Wear*, (137):161–174, 1990.

- [21] Valve Manufactures Association (VMA). Valves for industry. 1050 17th Street, NW, Suite 701, Washington DC 20036-5503.
- [22] Valve Diagnostics. <http://www.valvediagnostics.com>.
- [23] *Seals and sealing handbook*. The trade & technical press limited, 1985.
- [24] Doubt G.L. Reference book for design of valve packings, sealing high temperature water. Technical Report No.5010, atomic Energy Of Canada Limited, January 1976.
- [25] Engineered Valves. <http://www.engvalves.com>. website.
- [26] EPRI Electrical Power Research Institute. Valve stem packing improvements, final report. Technical Report Research Project 2233-3, NP-5697, May 1988.
- [27] Turnbull D.E. The sealing action of a conventional stuffing-box. Technical Report RR592, British Hyromechanics Research Association (BHRA), 1958.
- [28] Harwanko E. Valves in power industry-gland sealing problems. 1981.
- [29] Thomson J.L. Packed glands for high pressures: An analysis of fundamentals. *Proc Instn Mech Engrs*, 172:471-486, 1958.
- [30] Denny et al. Contribution to discussion. *Proc Instn Mech Engrs*, 172:499-511, 1958.
- [31] Kwu-richtlinie zum rechnerischen festigkeitsnachweis im kraftflußliegenden bauteile von armaturen. Technical Report V 29/82/1029 b, KWU, 16.08.1983 1983.
- [32] Berechnung sicherheitstechnisch wichtiger schieber und ventile hinsichtlich funktion und auswirkungen von stellkräften. Technical report, TUV, August 1993.

- [33] B. Bhushan. Contact mechanics of rough surfaces in tribology: single asperity contact. *Applied Mechanics Reviews*, 49(5):275–298, May 1996.
- [34] Bowden G.L. and Tabor D. *The Friction and Lubrication of Solids*, volume I. Oxford, 1950.
- [35] Bowden G.L. and Tabor D. *The Friction and Lubrication of Solids*, volume II. Oxford, 1964.
- [36] B. Bhushan. *Introduction To Tribology*. John Wiley & Sons, New York, 2002.
- [37] ASME New York. Surface texture (surface roughness, waviness, and lay). (ANSI/ASME B46.1), 1985.
- [38] Kappor A. and Johnson K.L. Plastic ratchetting as a mechanism of metallic wear. *Proc. R. Soc. London*, (A 445):367–381, 1994.
- [39] B.J. Briscoe and M.J. Adams, editors. *Tribology In Particulate Technology*. Adam Hilger, 1987.
- [40] Kapoor A., Franklin F.J., Wong S.K., and M. Ishida. Surface roughness and plastic flow in rail wheel contact. *Wear*, (253):257–264, 2000.
- [41] Moalic H., Fitzpatrick J.A., and Torrance A.A. The correlation of the characteristics of rough surfaces with their friction coefficients. *Proc. I. Mech. Eng.*, (201):321–329, 1987.
- [42] Lacey P., Torrance A.A., and Fitzpatrick J.A. The relation between the friction of lubricated surfaces and apparent normal pressure. *ASME J. Tribol.*, (111):260–264, 1989.
- [43] Torrance A.A. and Parkinson A. Towards a better surface finish for bearing materials. In Godet M. Dowson, D., editor, *19th Leeds-Lyon Symposium*, pages 91–98, 1993.

- [44] Torrance A.A. Using profilometry for the quantitative assesment of tribological function: Pc based software for friction and wear. *Wear*, (181):397–404, 1995.
- [45] Briscoe B.L. and Evans D.C.B. The shear strength of thin lubricant films. *Proc. Roy. Soc. Lond. Ser. A333*, pages 99–114, 1973.
- [46] Hirst W. and Stafford A.E. Surface finish and damage sliding. *Proc. Roy. Soc. Lond. Ser. A 337*, pages 379–394, 1974.
- [47] Hirst W. and Stafford J.V. Transition temperatures in boundary lubrication. *Proc. I. Mech. Eng.*, (1986):172–192, 1972.
- [48] R.S. Sayles. basic principles of rough surface contact analysis using numerical techniques. *Tribology International*, 29(8):639–650, 1996.
- [49] J.A. Greenwood and J.B.P Williamson. Contact of nominally falt surfaces. *Proc. Roy. Soc.*, A295:300–319, 1966.
- [50] M.N. Webster and R.S. Sayles. A numerical model for the elastic frictionless contact of real rough surfaces. *Trans. ASME J. Triblo.*, 108(3):314–320, 1986.
- [51] Hutchings I.M. *Tribology: friction and wear of engineering materials*. Edward Arnold, London, 1992.
- [52] B. Bhushan, editor. *Modern Tribology Handbook Volume One*. CRC Press, 2000.
- [53] Archard J.F. Contact and rubbing of flat surfaces. *J. appl. Phys.*, 24(981), 1953.
- [54] Lee B.J. Characterisitcs of exfolaited graphite prepared by intercalation of gaseous so_3 into graphite. *Bull. Korean Chem. Soc.*, 23(12):1801–1805, 2002.
- [55] SGL Carbon. <http://www.sglcarbon.com>.

- [56] Crane Packing Company. Technical information, graphite ribbon, bulletin no. p-429-1.
- [57] Bouvard D., Lanier J., and Stutz P. Mechanical behaviour of graphite powder. *Powder Technology*, (54):175–181, 1988.
- [58] Potts D.M. and Zdravkovic L. *Finite element analysis in geotechnical analysis in geotechnical engineering, theory*. Thomas Telford Publishing, 1999.
- [59] Manoharan N. and Dasgupta S.P. Consolidation analysis of elasto-plastic soil. *Computers & Structures*, 54(6):1005–1021, 1995.
- [60] Ahadi A. and Krenk S. Implicit integration of plasticity models for granular materials. *Comput. Methods Appl. Mech. Engrg*, (192):3471–3488, 2003.
- [61] TNO DIANA BV. *DIANA 7.2 Help Manual*. Delft, The Netherlands.
- [62] ABAQUS Inc. *ABAQUS/Standard 6.4 Help Manual*. Rhode Island, New York, USA.
- [63] Viladkar M. N., Noorzaee J., and Godbole P.N. Convenient forms of yield criterion in elasto-plastic analysis of geological materials. *Computers & Structures*, 54(2):327–337, 1995.
- [64] Symon K.R. *Mechanics*. Addison-Wesley, 3rd, 1971.
- [65] Kleppner D. and Kolenkow R.J. *Introduction to Mechanics*. McGraw Hill, 1973.
- [66] Lemaitre J. and Chaboche J.L. *Mechanics of Solids Materials*. Cambridge University Press, 1990.
- [67] Hunter S.C. *Mechanics of Continuous Media*. Ellis Horwood LTD., 2nd edition, 1983.

- [68] Wood David Muir. *Soil Behaviour and critical state soil mechanics*. Cambridge University Press, 1990.
- [69] Groen A.E. Elastoplastic modelling of sand using a conventional model ii. parameter determination. Technical Report 03.21.0.31.35, Delft University, Nov 1995.
- [70] Terazaghi K. *Erdbaumechanik auf bodenphysikalischer Grundlage*. Franz Dueticke, Leipzig und Wien, 1925.
- [71] Coulomb de C.A. Essai sur une application de maximis & minimus a quelques problemes de statique, relatif a l'architecture. *Mem. Math. & Phys.*, 7(342-382), 1776.
- [72] Das M. D. *Advanced Soil Mechanics*. Taylor and Francis, Washington D.C., 2nd edition, 1997.
- [73] Roscoe K.H. and Schofield A.N. Mechanical behaviour of an idealized 'wet' clay. volume 1, pages 47-54. 2nd ECSMFE, Weisbaden, 1963.
- [74] Schofield A.P. and Wroth C.P. *Critical State Soil Mechanics*. McGraw Hill, London, 1968.
- [75] Roscoe K.H. and Burland J.B. On the generalized stress-strain behaviour of 'wet' clay. *Eng plasticity*, pages 553-609, 1968.
- [76] van Eekelen S.J.M. and van den Berg P. The delft egg model, a constitutive model for clay. *DIANA Computational mechanics '94*, pages 103-116, 1994.
- [77] Vermeer P.A. and de Borst R. Non-associated plasticity for soils, concrete and rock. *Heron*, 29(3), 1984.
- [78] Casagrande A. The determination of the preconsolidation load and its practical significance. In *Proc. 1st Int. Conf. Soil Mech. Cambridge, Mass.*, volume 3, 1936.

- [79] R.E. Goodman. *Introduction to Rock Mechanics*. Wiley, 1989.
- [80] Head K. H. *Manual of Soil Laboratory Testing*, volume 2. John Wiley & Sons, Inc. New York, 2nd edition, 1994.
- [81] Head K.H. *Soil Technicians' Handbook*. Pentech Press, London, 1989.
- [82] Vogler U.W. and Kovari K. Suggested methods for determining the strength of rock materials in triaxial compression, for isrm commission on standardization of laboratory and field testing. *Int. J. Rock Mech. Min. Sci.*, 15:47–52, 1978.
- [83] Bésuelle P. and Desrues J. Internal instrumentation for strain measurements on soft rocks tested in axisymmetric triaxial cell. *Geotechnical testing journal*, 24(2):193–199, 2001.
- [84] Scholey G.K., Frost J.D., Lo Presti D.F., and Jamiolkowski M. A review of instrumentation for measuring small strains during triaxial testing of soil specimens. *Geotechnical testing journal*, 18(2):137–156, 1995.
- [85] AMTEC. <http://www.amtec-services.de/english/ghome.htm>.
- [86] Atkinson J.H. *Foundation and Slopes an introduction to applications of critical state soil mechanics*. Mc Graw-Hill Book Company(UK) Limited, 1981.
- [87] K.L. Johnson. *Contact mechanics*. Cambridge University Press, 1985.
- [88] A.E. Groen, R. Borst de, and S.J.M. Eekelen van. An elastoplastic model for clay: Formulation adn algorithmic aspects. In G.N. Pande and S. Pietruszczak, editors, *Proceedings of the fifth international symposium on numerical models in geomechanics*, volume NUMOG V, pages 27–32. A.A. Balkema Rotterdam, 1995.
- [89] <http://www.mecheng.tcd.ie/~torrance/using-fast.pdf>.
- [90] Teadit. <http://www.teadit.com>.

Appendix A

Compression test results

A.1 1.3 g/cm^3 exfoliated graphite

The results that follows are for 1.3 g/cm^3 exfoliated graphite. The tests involved subjecting one 1.3 g/cm^3 exfoliated graphite packing ring to two loading cycles

The radial stress response described by $K[-]$ on initial compression is seen in Figure A.2. On reloading the radial stress response $K[-]$ can be seen in Figure A.3.

A.2 1.8 g/cm^3 exfoliated graphite

The results for 1.8 g/cm^3 exfoliated graphite are detailed below in Figures A.4, A.5 and A.6.

1.8 g/cm^3 exfoliated graphite compresses the least of all the exfoliated graphite ring types tested. This is to be expected as 1.8 g/cm^3 exfoliated graphite has the highest initial density of all the rings types tested. $K[-]$ is non-linear on initial compression and on second compression. 1.8 g/cm^3 exfoliated graphite is not as efficient at transferring axial stress into radial sealing stress as are 1.3 g/cm^3 and 1.5 g/cm^3 exfoliated graphite packing rings.

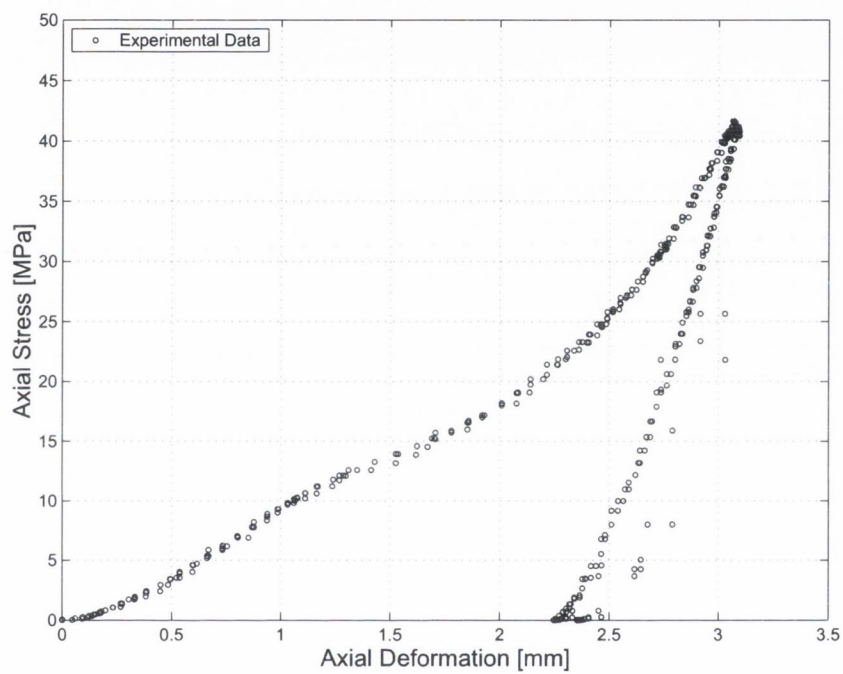


Figure A.1: Compression of one 1.3 g/cm^3 exfoliated graphite packing ring

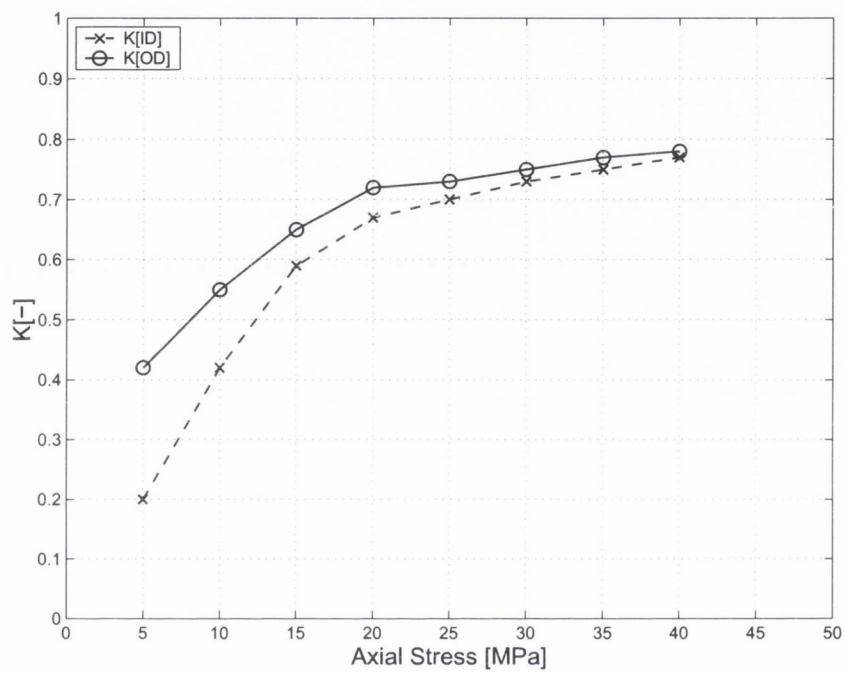


Figure A.2: $K[-]$ for the initial compression of one 1.3 g/cm^3 exfoliated graphite packing ring

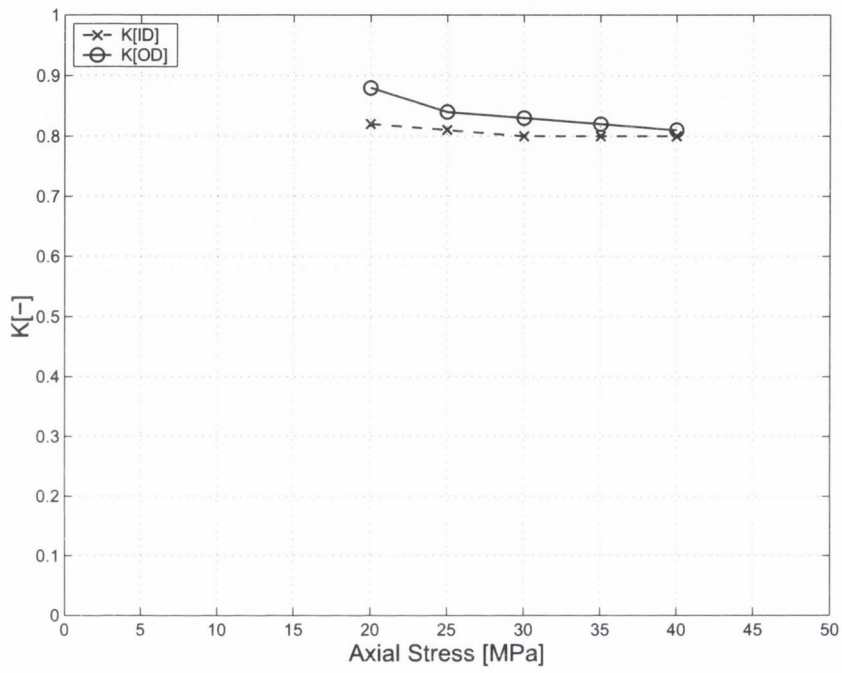


Figure A.3: $K[-]$ for the second loading cycle of one 1.3 g/cm^3 exfoliated graphite packing ring

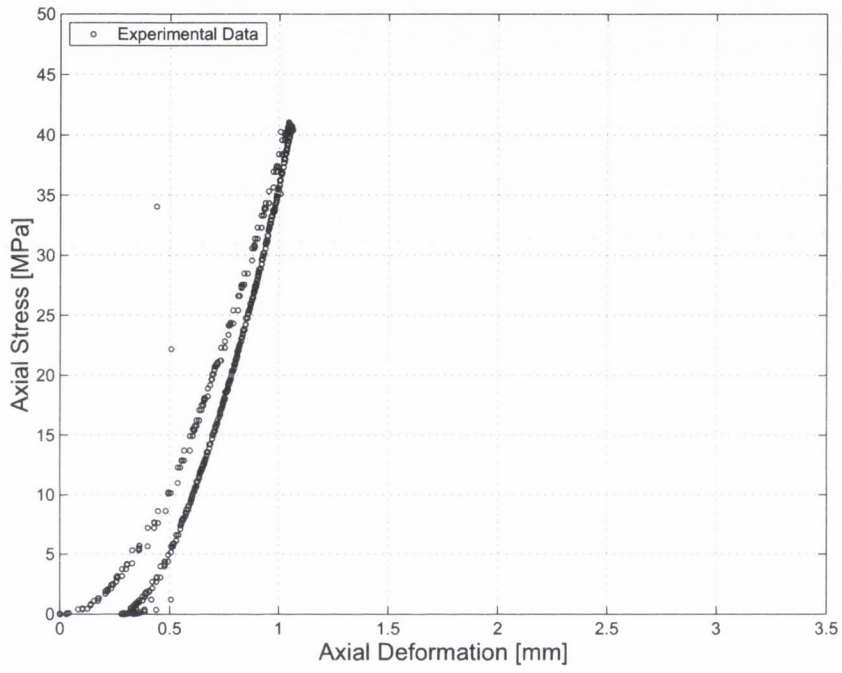


Figure A.4: Compression of one 1.8 g/cm^3 exfoliated graphite packing ring

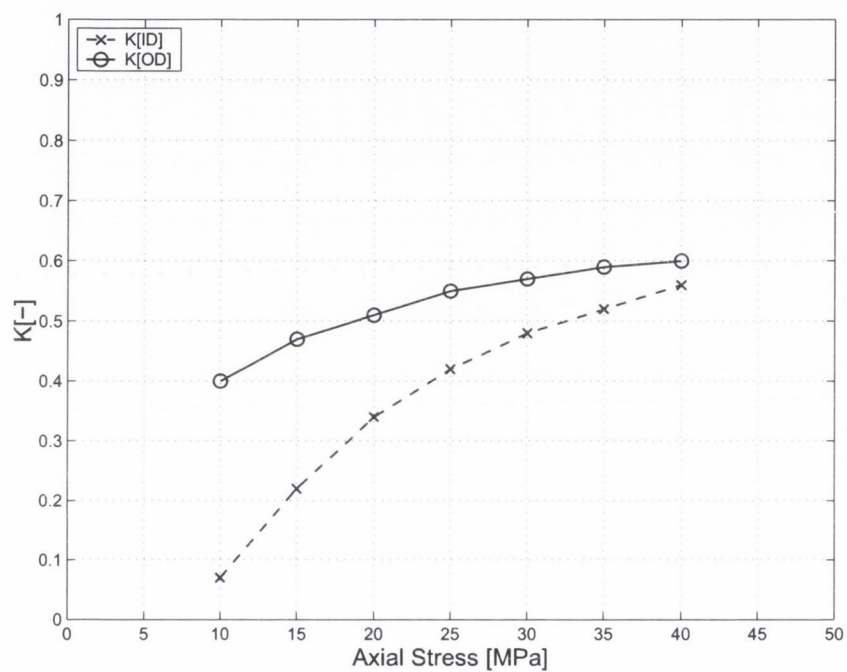


Figure A.5: $K[-]$ for the initial compression of one 1.8 g/cm^3 exfoliated graphite packing ring

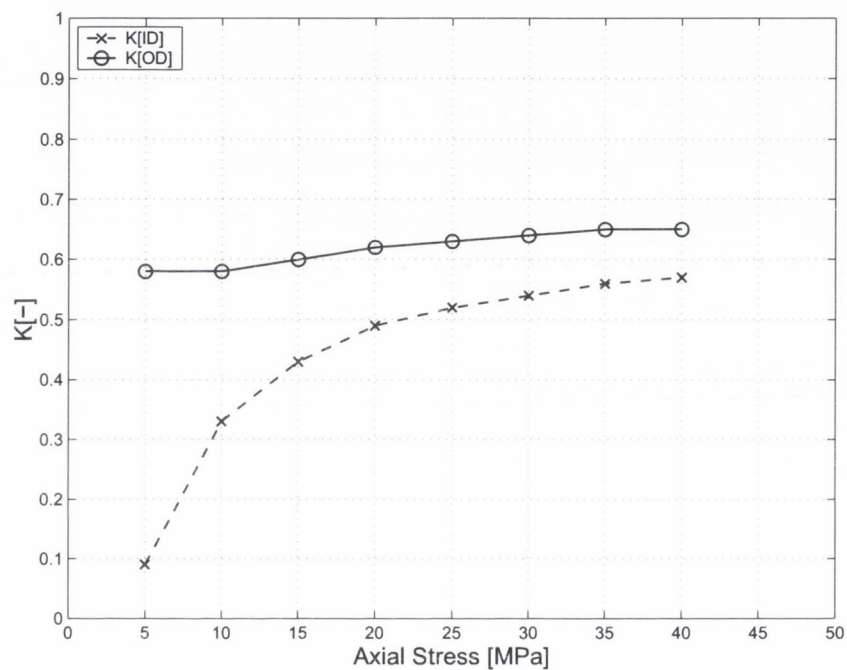


Figure A.6: $K[-]$ for the second loading cycle of one 1.8 g/cm^3 exfoliated graphite packing ring

Appendix B

Triaxial test results

This appendix details the raw data obtained from each of the 6 triaxial tests carried out for this thesis. Details of each of the test specimens and the test parameters are described in Table B. The second test is a multistage test. Multistage tests are used widely in rock testing. The test involves changing the plane of failure of the material by increasing the hydrostatic pressure when the peak stress has been reached.

Table B.1: Triaxial test initial parameters

Test No	Cell Pressure [MPa]	Density [g/cm^3]	Height [mm]	Diameter [mm]	Weight [g]
1	1	1.566	66.54	38.01	120.869
2	Multistage [1, 5, 10, 20, 30]	1.355	66.65	38.01	103.2334
3	5	1.59	66.55	38.01	119.8729
4	10	1.614	66.40	38.01	122.2529
5	20	1.628	67.50	38.01	125.1328
6	30	1.393	65.5	38.01	105.2037

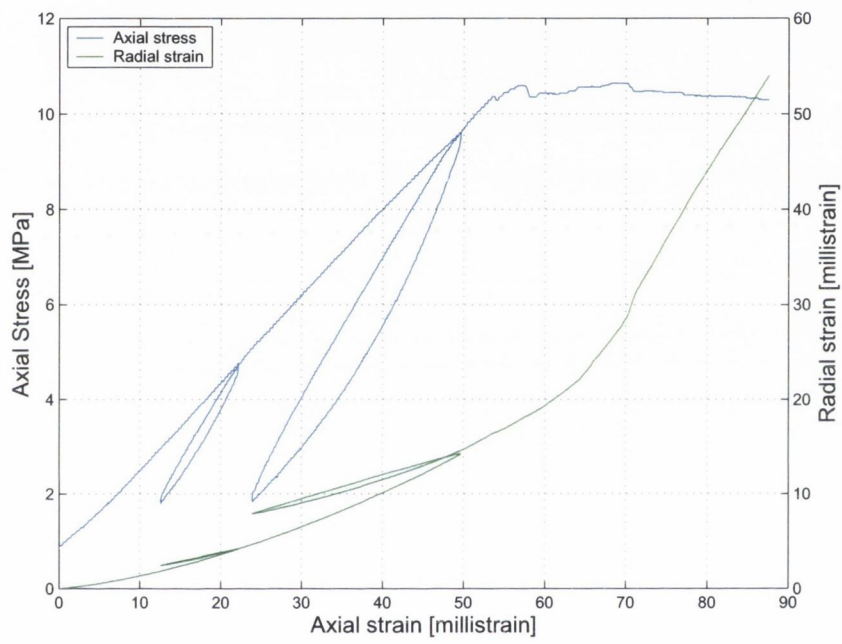


Figure B.1: Triaxial test results for triaxial test 1 (See Table B)

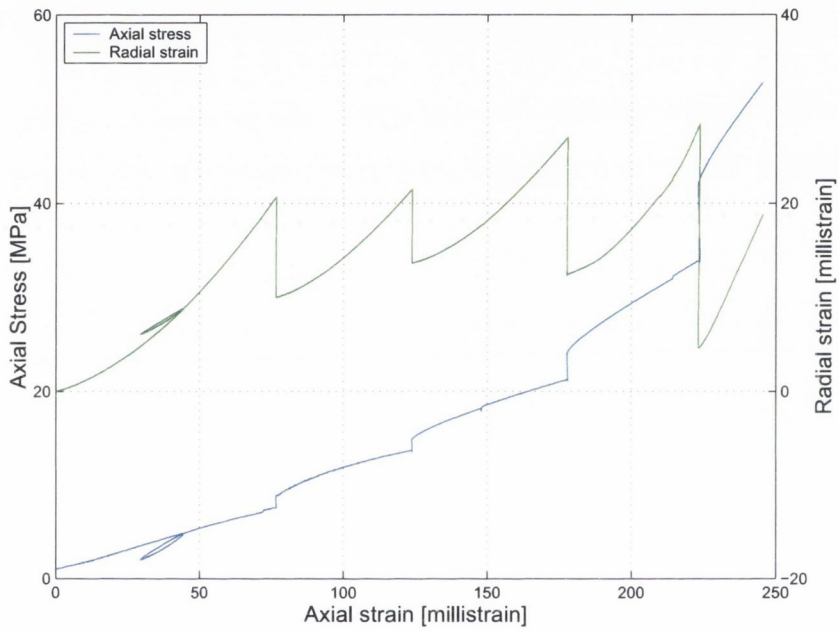


Figure B.2: Triaxial test results for triaxial test 2 (See Table B)

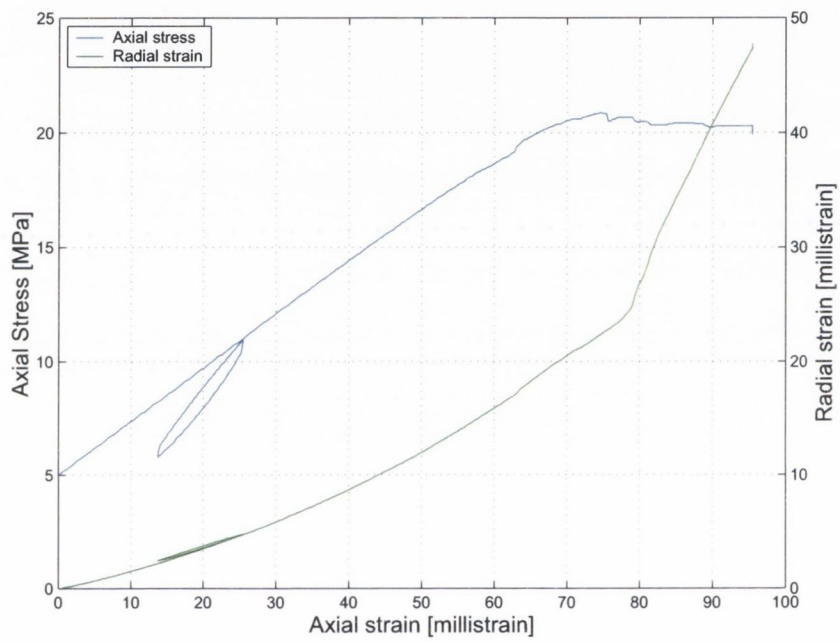


Figure B.3: Triaxial test results for triaxial test 3 (See Table B)

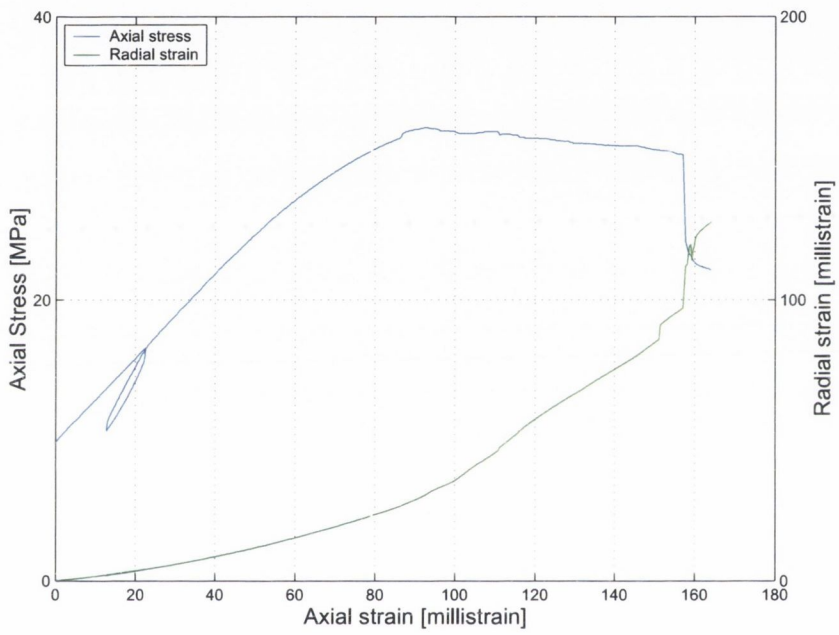


Figure B.4: Triaxial test results for triaxial test 4 (See Table B)

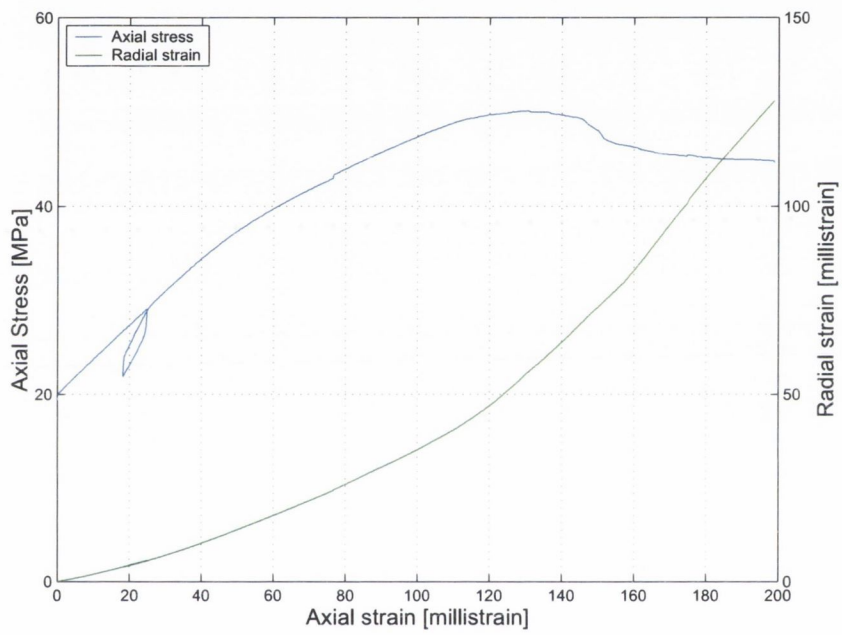


Figure B.5: Triaxial test results for triaxial test 5 (See Table B)

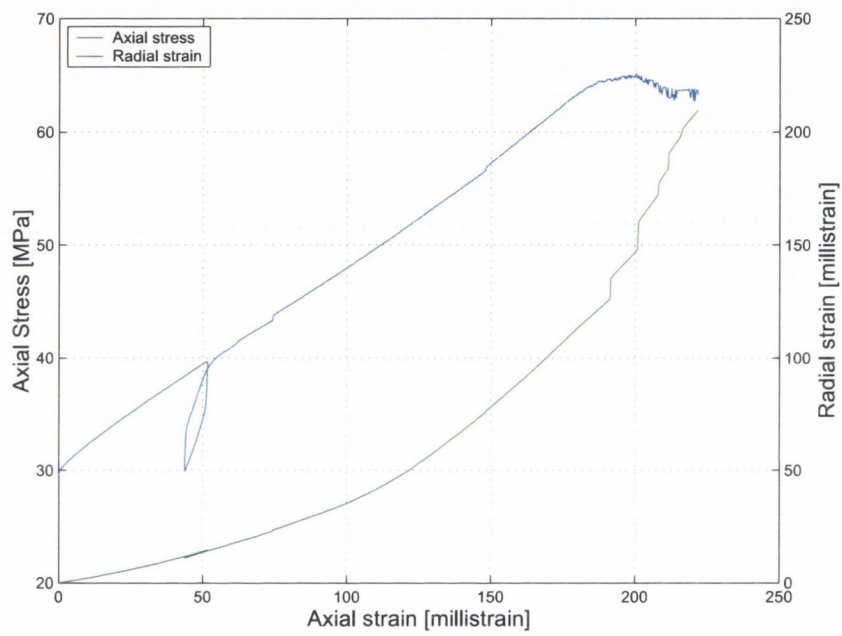


Figure B.6: Triaxial test results for triaxial test 6 (See Table B)

Appendix C

Exfoliated graphite friction and wear results

C.1 Friction results

C.1.1 1.4 g/cm^3 exfoliated graphite

Tests were carried out using all 4 wedge angles. Results for the coefficient of friction of 1.4 g/cm^3 exfoliated graphite in air and argon can be seen in Figures C.1 and C.2 respectively.

Figures C.1 and C.2 both demonstrate the dependence of the coefficient of friction on wedge angle. The coefficient of friction is seen to increase with increasing wedge angle. As expected the coefficient of friction for a 4° wedge has the lowest coefficient of friction and the highest coefficient of friction can be seen for the 8.93° wedge angle.

In air the coefficient of friction is seen to increase over the course of a test. In argon, the situation is significantly different. The results for a 4° wedge in argon show little variation over the course of the test. Whereas the results for 5.88° , 8.12° and 8.93° wedge angles in argon show a marked increase in coefficient of friction as the test progresses.

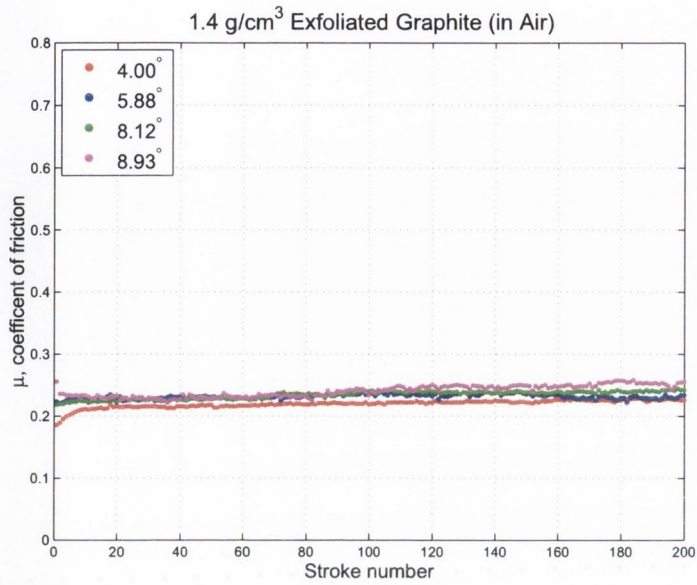


Figure C.1: Test data for 1.4 g/cm³ exfoliated graphite in air

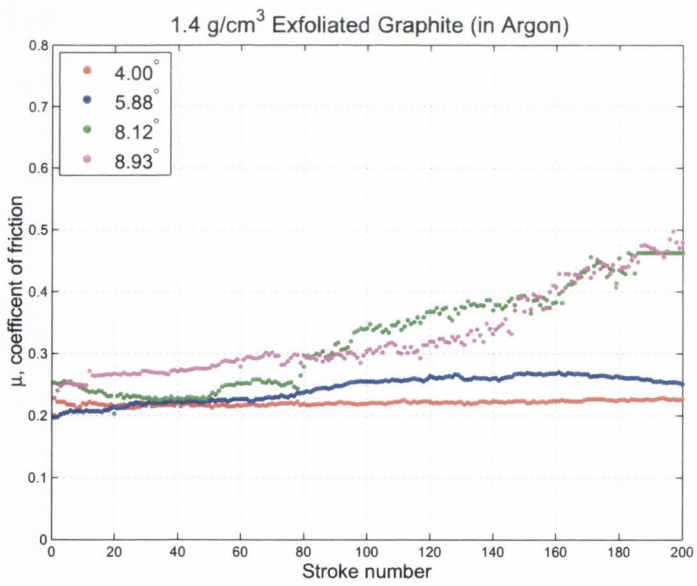


Figure C.2: Test data for 1.4 g/cm³ exfoliated graphite in argon

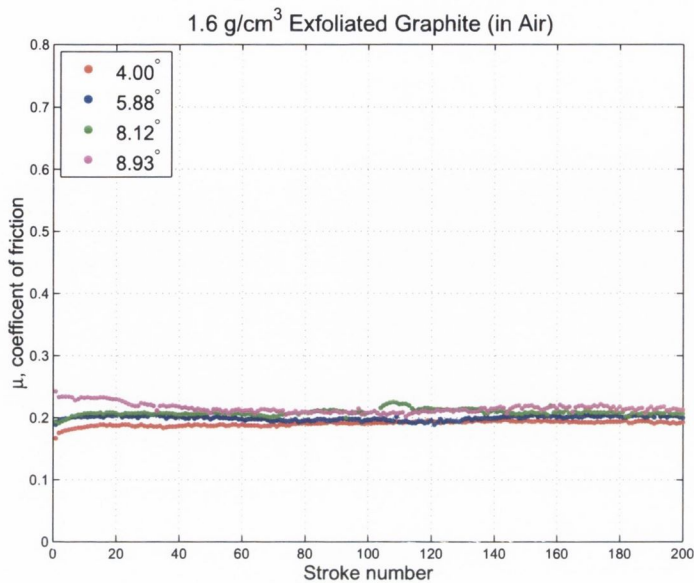


Figure C.3: Test data for 1.6 g/cm^3 exfoliated graphite in air

C.1.2 1.6 g/cm^3 exfoliated graphite

Test data for 1.6 g/cm^3 exfoliated graphite is shown in Figures C.3 and C.4.

The results for 1.6 g/cm^3 exfoliated graphite in air show a slight difference in coefficient of friction with wedge angle. The results for the tests carried out in argon show a marked increase with time and wedge angle.

C.2 Wear results

C.2.1 1.4 g/cm^3 exfoliated graphite

Wear results were obtained for all 4 wedge angles. A sample of the results can be seen in Figures C.5 and C.6, tests were carried out both air and argon respectively.

In Figure C.5 the wear data is shown for 1.4 g/cm^3 in air. The slope of the wear curve is seen to increase with wedge angle. The actual numerical

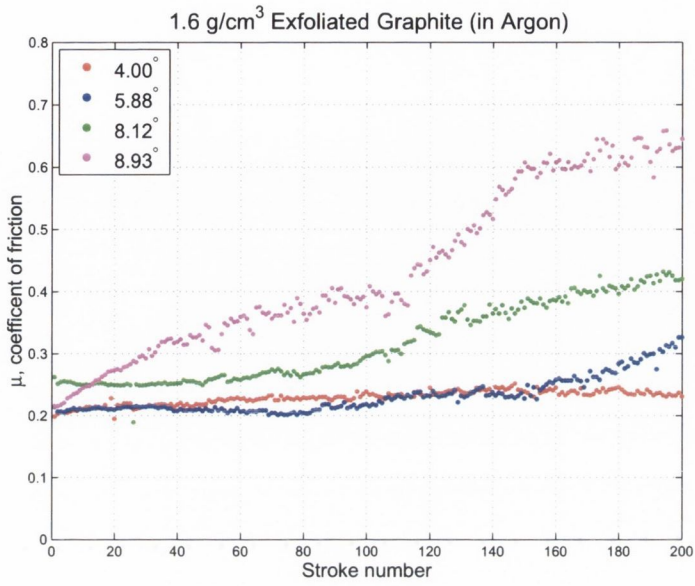


Figure C.4: Test data for 1.6 g/cm³ exfoliated graphite in argon

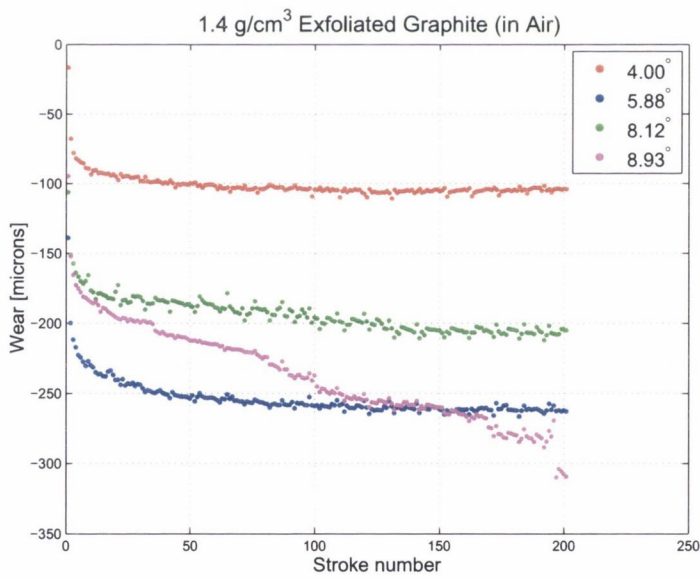


Figure C.5: Time versus wear for 1.4 g/cm³ exfoliated graphite in air

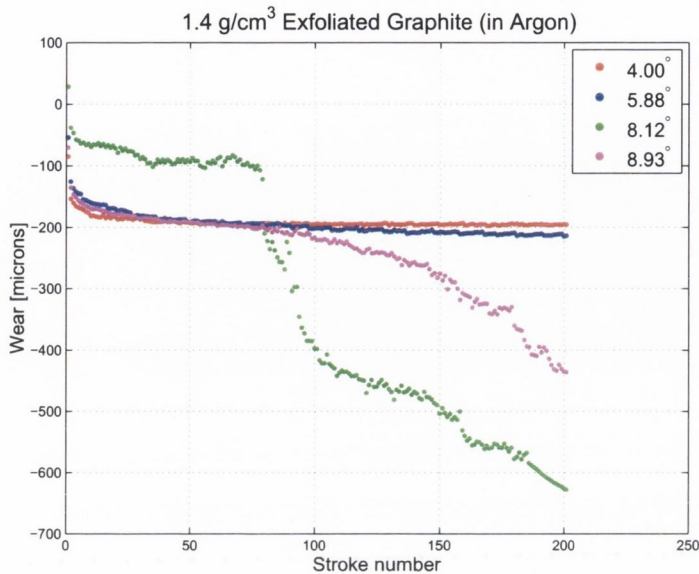


Figure C.6: Time versus wear for 1.4 g/cm^3 exfoliated graphite in argon

values of wear are not as important as the slope of the time vs. wear curve. The numerical values are simply dependent on whether or not the LVDT was zeroed prior to the start of the test.

In argon the wear results for 1.4 g/cm^3 are more pronounced than those carried out in air. The slopes for 4° and 5.88° wedge angle are not as extreme as those for 8.12° and 8.93° wedge angles.

C.2.2 1.6 g/cm^3 exfoliated graphite

Tests were carried out on all four wedge angles. Figures C.8 and C.8 and show results for 1.6 g/cm^3 exfoliated graphite in air and argon respectively.

The results for 1.6 g/cm^3 show the same trends for wear as 1.4 g/cm^3 and 1.5 g/cm^3 exfoliated graphite packing rings. There is a degree of scatter in the results for the higher degree angles. This could be due to the fact that a stronger material will be significantly harder to destruct by repeated disturbances of the frictional bonds as these frictional bonds are stronger in

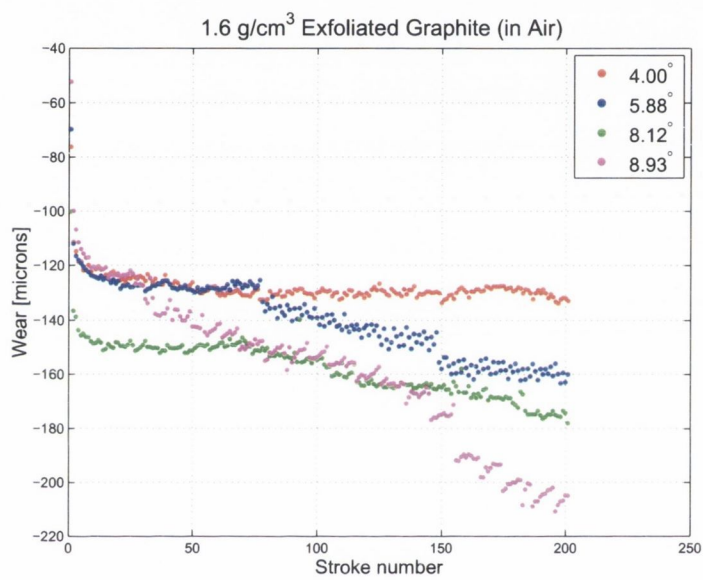


Figure C.7: Time versus wear for special 1.6 g/cm^3 exfoliated graphite in argon

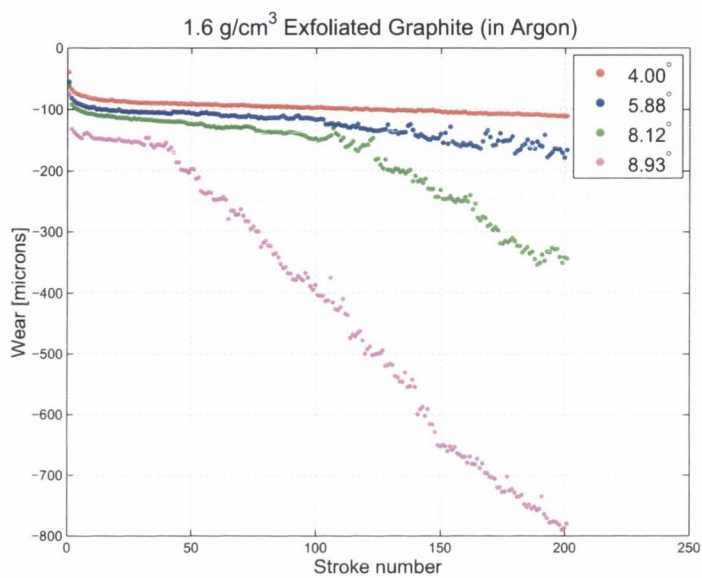


Figure C.8: Time versus wear for special 1.6 g/cm³ exfoliated graphite in argon

denser materials.

Appendix D

Teadit friction and wear results

Wedge tests were carried out on three different braided packing types,

- Teadit 2001
- Teadit 2200
- Teadit 2202

Teadit 2001 shown in Figure D.1a is a diagonally braided from pure graphite yarn with a minimum purity of 99%, treated with corrosion inhibitor and pure graphite powder.

Teadit 2200 shown in Figure D.1b is diagonally braided from high quality carbon fibre yarn and impregnated with a corrosion inhibitor.

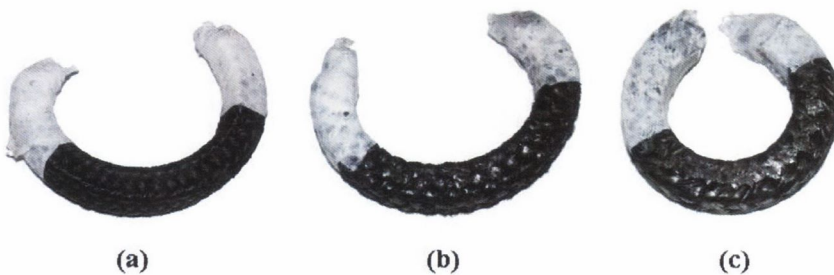


Figure D.1: (a) Teadit 2001 (b) Teadit 2200 (c) Teadit 2202

Teadit 2202 is a diagonally braided from pure expanded flexible graphite and reinforced at the corners with a high quality carbon yarn, shown in Figure D.1c

Teadit 2001, Teadit 2200 and Teadit 2202 are not endless rings. They are cut to length from lengths of the manufactured packing material. They have single cuts are made at 45° angles to the section. Teadit 2001, Teadit 2200 and Teadit 2202 have winds of PTFE tape wrapped around the end sections (joints) of each ring [90]. This feature can be seen in Figures D.1.

D.1 Friction data

D.1.1 Teadit 2001

Results for Teadit 2001 carried out on the PTFE sections of the packing rings in air and argon respectively are shown in Figures D.2 and D.3. Figures D.4 and D.5 detail the results of tests carried out on the non-PTFE section of Teadit 2001 packing rings in air and in argon.

Results for tests carried out on PTFE sections show a much lower coefficient of friction than those carried out on non-PTFE sections. The same trend as seen in exfoliated graphite can be seen in Teadit 2001 packings, that being there is a definite influence of wedge angle on the coefficient of friction recorded during the tests. The influence being that the coefficient of friction increases with wedge angle.

The lack of oxygen/presence of argon leads to increases in the coefficient of friction for tests carried out on both the PTFE and non PTFE sections. One significant difference seen between Teadit 2001 packings and exfoliated graphite packing is the absence of an increase in the coefficient of friction over time.

D.1.2 Teadit 2200

Figure D.6, D.7, D.8 and D.9 detail the results for Teadit 2200.

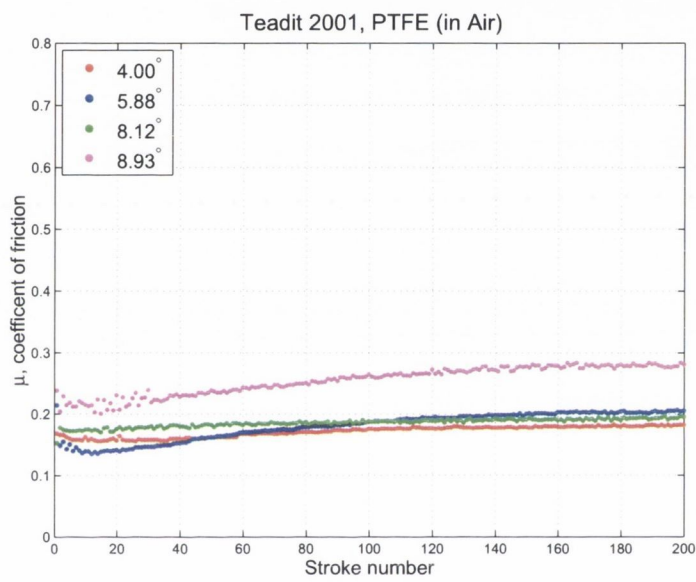


Figure D.2: Teadit 2001, wedge test results for tests carried out on PTFE sections of packing rings in air

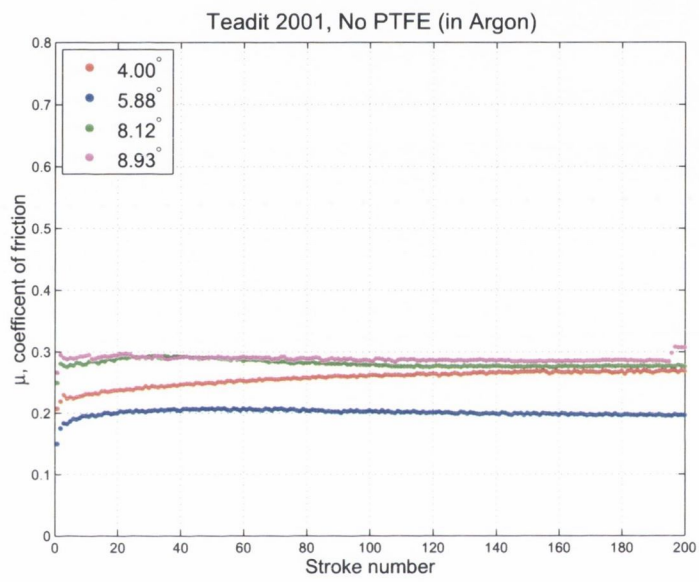


Figure D.3: Teadit 2001, wedge test results for tests carried out on PTFE sections of packing rings in argon

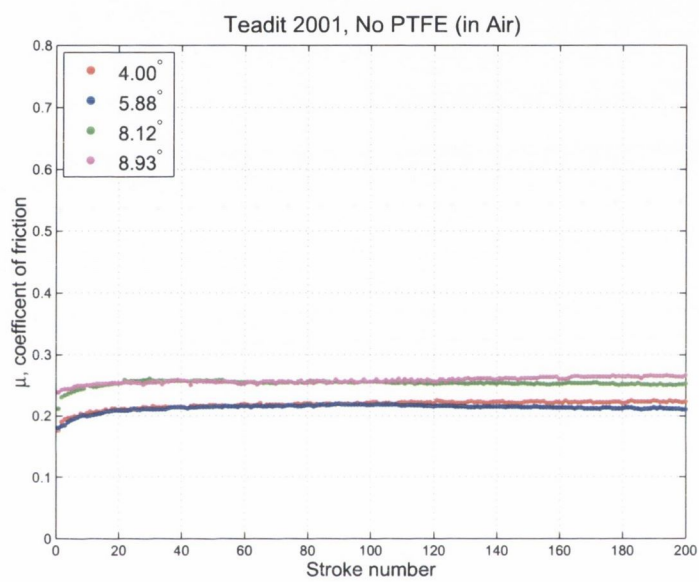


Figure D.4: Teadit 2001, wedge test results for tests carried out on non-PTFE sections of packing rings in air

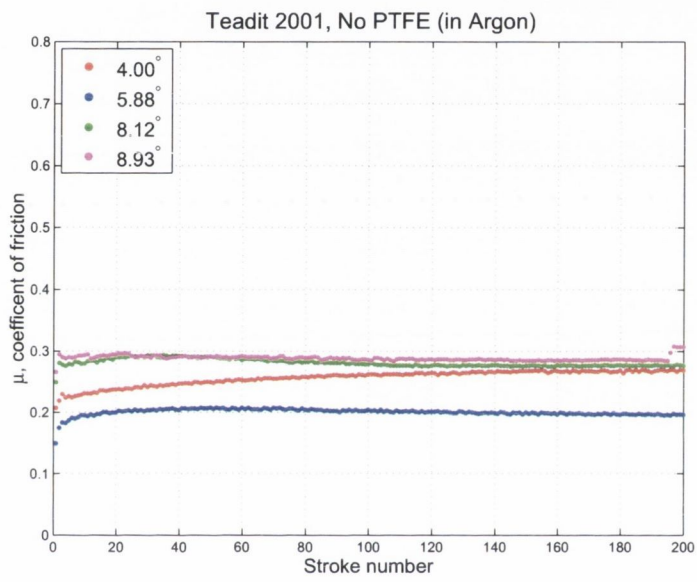


Figure D.5: Teadit 2001, wedge test results for tests carried out on non-PTFE sections of packing rings in argon

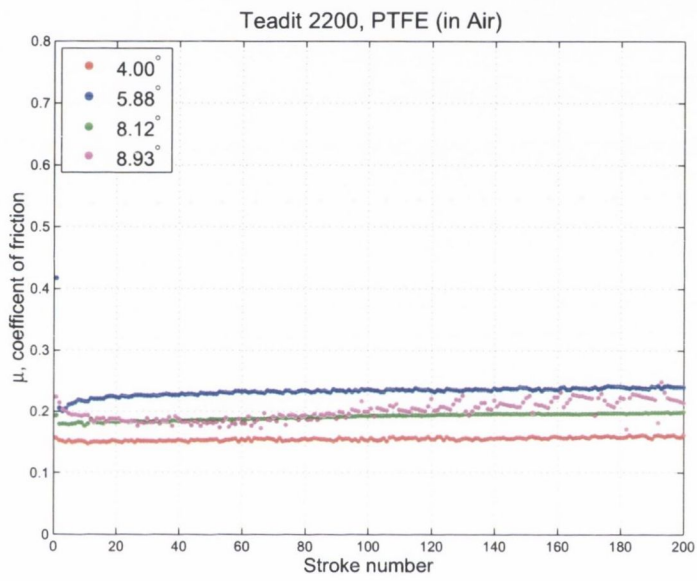


Figure D.6: Teadit 2200, wedge test results for tests carried out on PTFE sections of packing rings in air

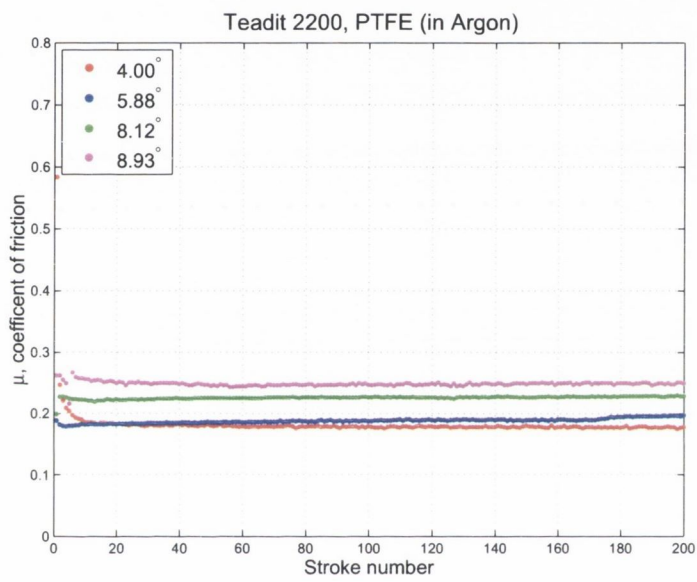


Figure D.7: Teadit 2200, wedge test results for tests carried out on PTFE sections of packing rings in argon

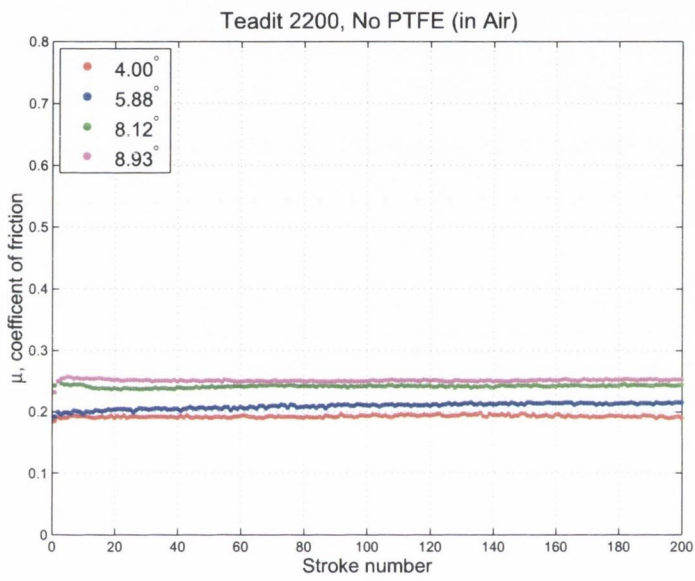


Figure D.8: Teadit 2200, wedge test results for tests carried out on Non-PTFE sections of packing rings in air

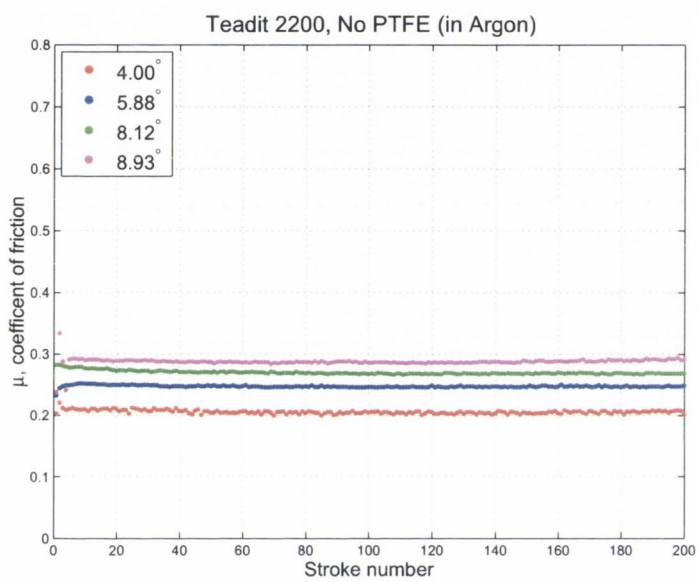


Figure D.9: Teadit 2200, wedge test results for tests carried out on Non-PTFE sections of packing rings in argon

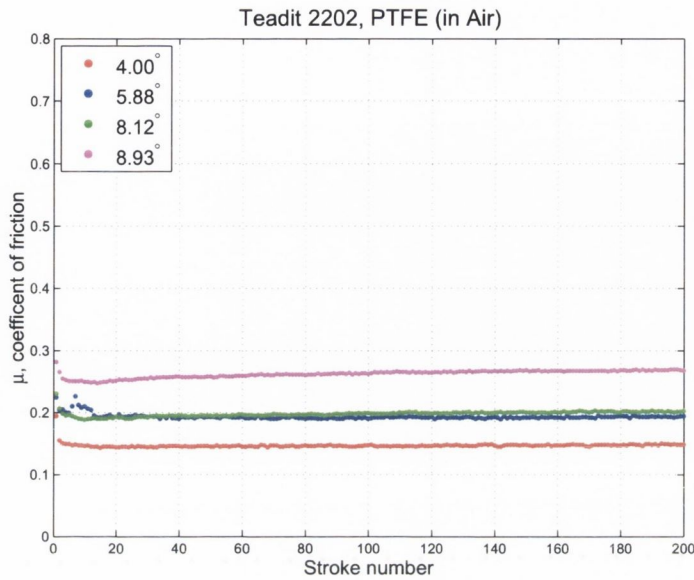


Figure D.10: Teadit 2202, wedge test results for tests carried out on PTFE sections of packing rings in air

The trends seen in Teadit 2001 are seen in Teadit 2200, the results for each of the wedge angles in both air and argon do not vary significantly. There is also no increase seen in the coefficient of friction, μ with time.

D.1.3 Teadit 2202

Test data for Teadit 2202 is shown in Figures D.10, D.11, D.12 and D.13.

The trends seen in Teadit 2001 and Teadit are seen in Teadit 2202, the results for each of the wedge angles in both air and argon do not vary significantly between packing types. There is also no increase seen in the coefficient of friction, μ with time. The values for the coefficient of friction across the whole series of variables, wedge angle, PTFE, lack of PTFE, normal atmosphere (test carried out in air) or an inert atmosphere are lowest for Teadit 2202.

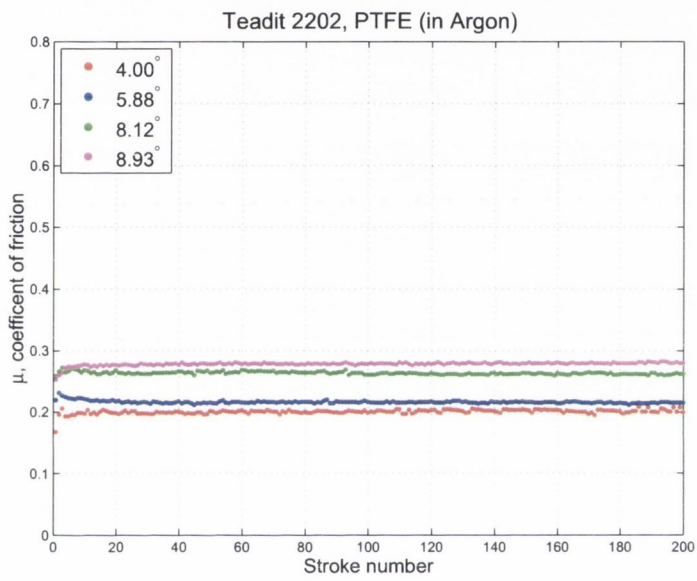


Figure D.11: Teadit 2202, wedge test results for tests carried out on PTFE sections of packing rings in argon

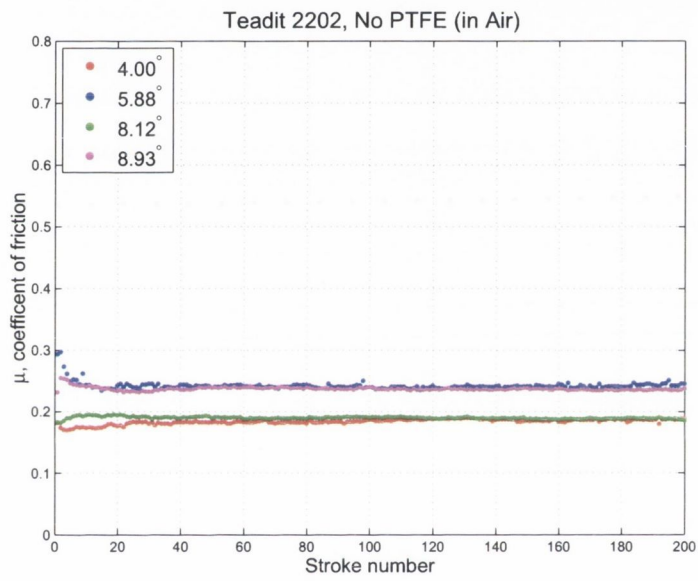


Figure D.12: Teadit 2202, wedge test results for tests carried out on Non-PTFE sections of packing rings

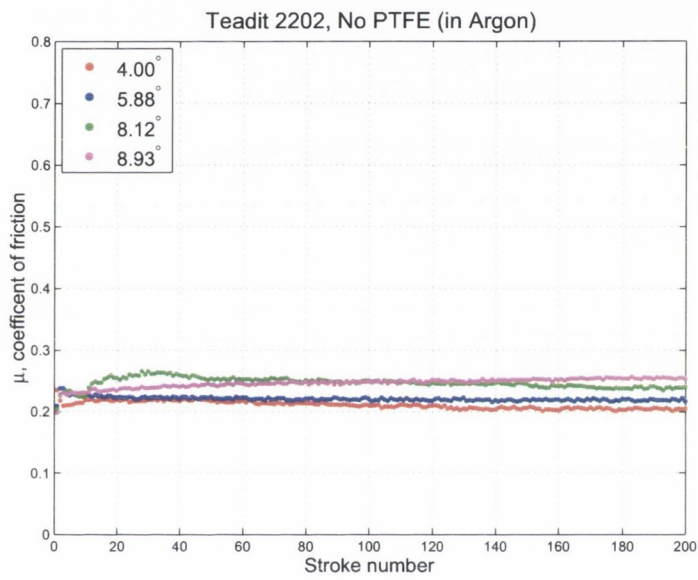


Figure D.13: Teadit 2202, wedge test results for tests carried out on Non-PTFE sections of packing rings

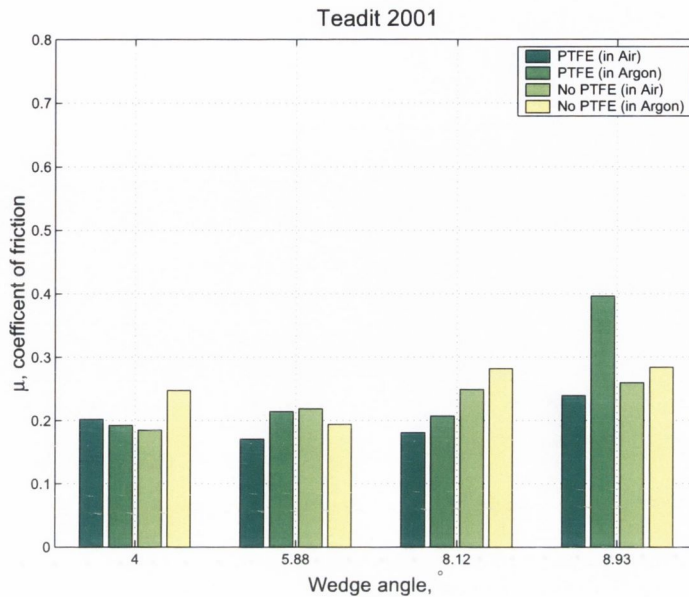


Figure D.14: Wedge angle vs. average coefficient of friction for Teadit 2001

D.1.4 Correlation data

Correlation data details the average coefficient of friction over the course of 201 strokes. This data is much more representative of the actual test data than the correlation data for exfoliated graphite packings as the coefficient of friction for braided TEADIT packings are not seen to increase significantly over the course of the test.

A general increase is seen with increasing wedge angle for all three braided graphite packings types. An inert atmosphere is also seen to cause an increase in the coefficient of friction with each wedge angle.

D.2 Wear data

Tests were carried out on 3 different types of braided graphite packing rings, all manufactured by Teadit Italia [90]. All 3 packing types have winds of PTFE tape around portions of the ring length. Wedge tests were carried out

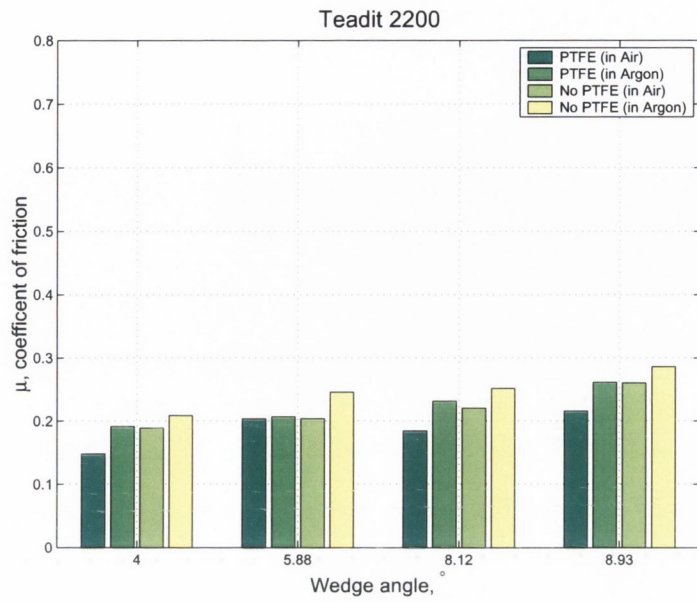


Figure D.15: Wedge angle vs. average coefficient of friction for Teadit 2200

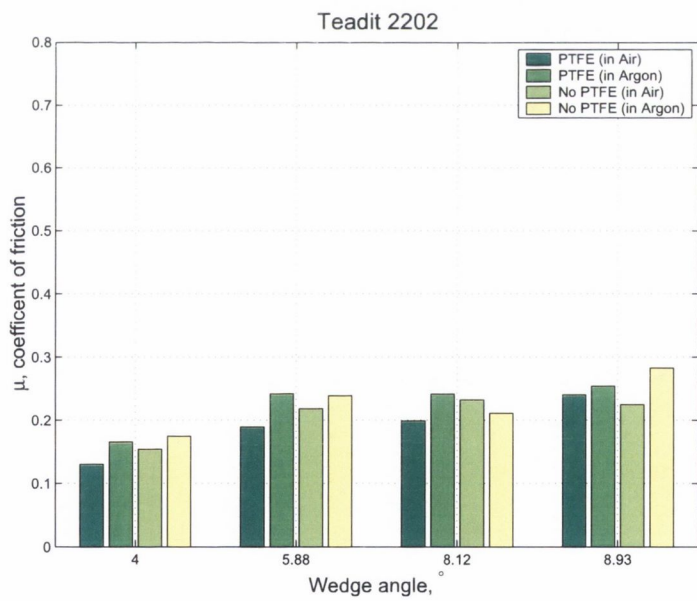


Figure D.16: Wedge angle vs. average coefficient of friction for Teadit 2202

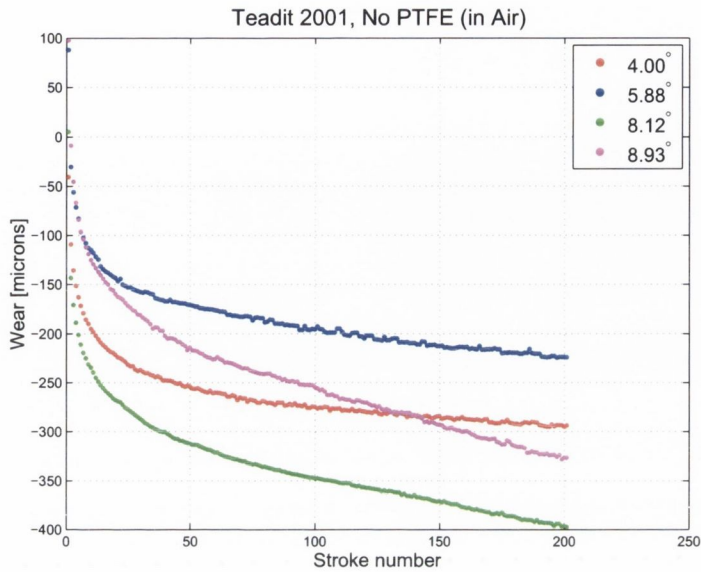


Figure D.17: Wear coefficient, K for Teadit 2001 on non PTFE sections: in air

on both the PTFE and non-PTFE section of each ring type in both air and argon.

D.2.1 Teadit 2001

Test were carried out using all four wedge angles. Tests results in air on both the PTFE and Non-PTFE section of the packing rings are shown in Figures D.19 and D.17. Figures D.20 and D.18 show results for tests carried out on the PTFE and Non-PTFE sections in argon.

Wear results for Teadit 2001 do not show as great a dependence on wedge angle as exfoliated graphite. The wear on the non-PTFE sections are not as great as that seen on the PTFE sections.

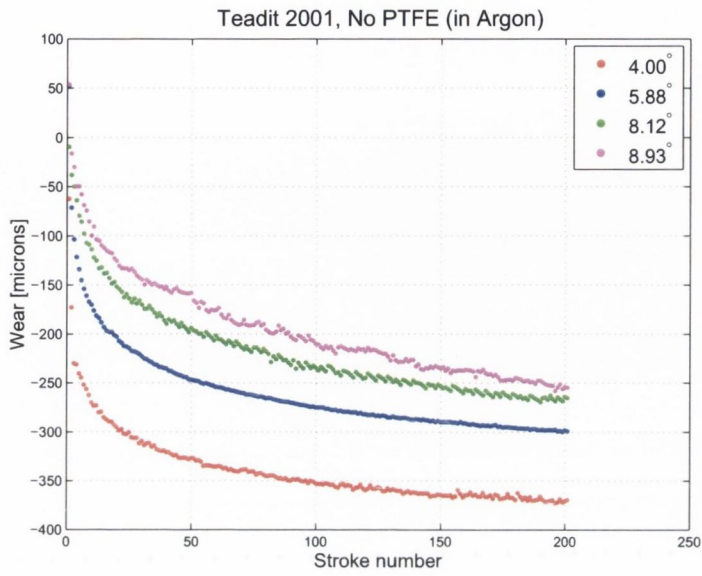


Figure D.18: Wear coefficient, K for Teadit 2001 on non PTFE sections: in argon

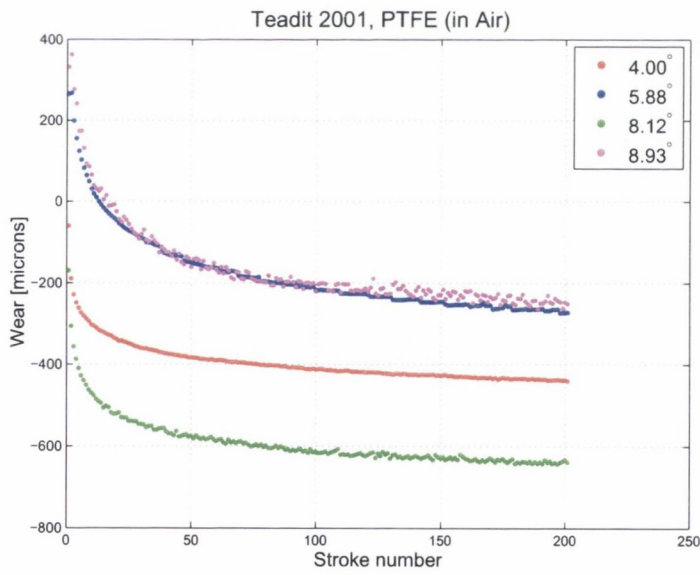


Figure D.19: Wear coefficient, K for Teadit 2001 on PTFE sections: in air

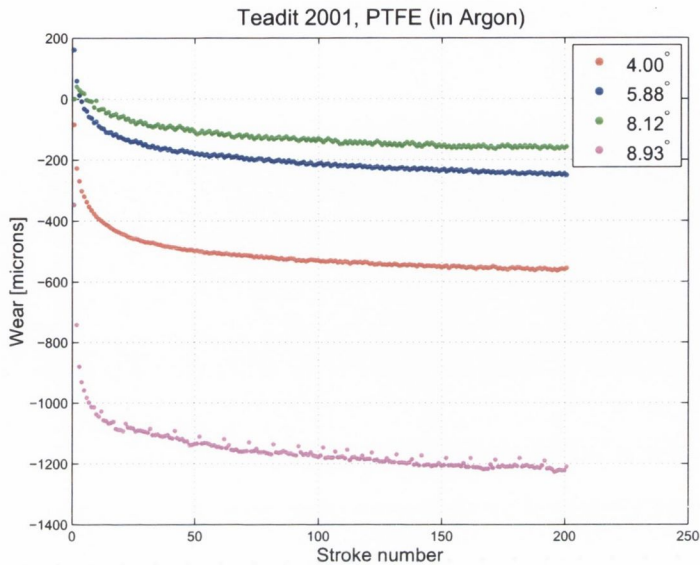


Figure D.20: Wear coefficient, K for Teadit 2001 on PTFE sections: in argon

D.2.2 Teadit 2200

As with Teadit 2001, wear results for Teadit 2200 were obtained for all four wedge angle on the PTFE and non-PTFE section of the packing rings in both air and argon. Results for Teadit 2200 in air can be seen in Figures D.21 and D.23. Results for tests carried out in argon can be seen in Figures D.22 and D.24.

The wear results show the same trends as seen with Teadit 2200.

D.2.3 Teadit 2202

Test data for Teadit 2202 in air is shown in Figures D.25 and D.27. Test data for Teadit 2202 in argon is shown in Figures D.26 and D.28. These tests were carried out on both the PTFE and non-PTFE section of the packing rings.

The wear results show the same trends as seen with Teadit 2200 and Teadit 2200.

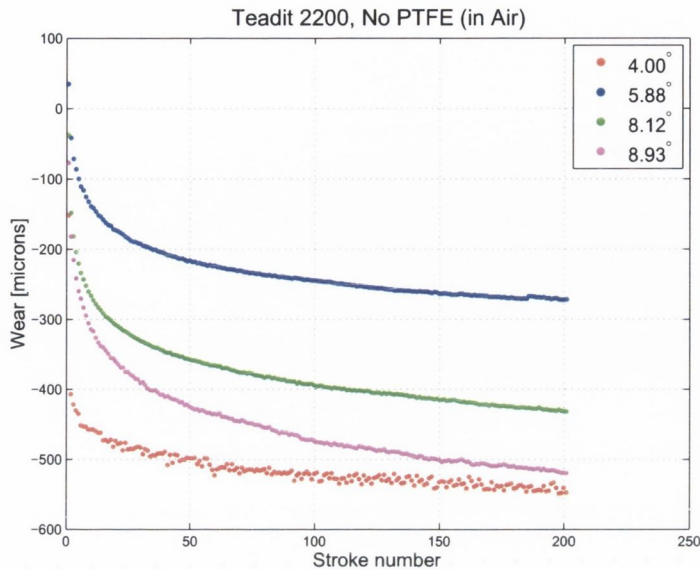


Figure D.21: Wear coefficient, K for Teadit 2200 on non PTFE sections: in air

D.2.4 Wear coefficient, K for braided graphite packing rings

Wear coefficient data for Teadit 2001, Teadit 2200 and Teadit 2202 can be seen in Figures D.29, D.30 and D.31.

The data for the wear coefficients for Teadit 2201, Teadit 2200 and Teadit 2202 show some experimental variation. There is no general trend that can be seen in the data. One reason as to why the results show no correlation or trend is that the braided nature of the packing rings will cause the wedge to ride up and down across the ridges and grooves of the braids thus giving fluctuations in the wear depth depending on where on the inner diameter on the individual packing rings the wedge slid.

More investigation needs to be carried out into the wear behaviour of Teadit 2001, Teadit 2200 and Teadit 2202 packing rings to understand the wear mechanisms that occur in these packing rings. The wedge test method may

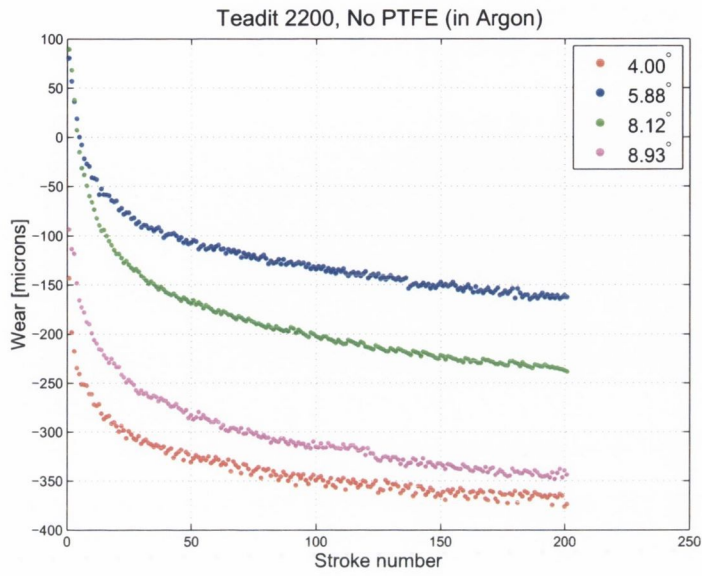


Figure D.22: Wear coefficient, K for Teadit 2200 on non PTFE sections: in argon

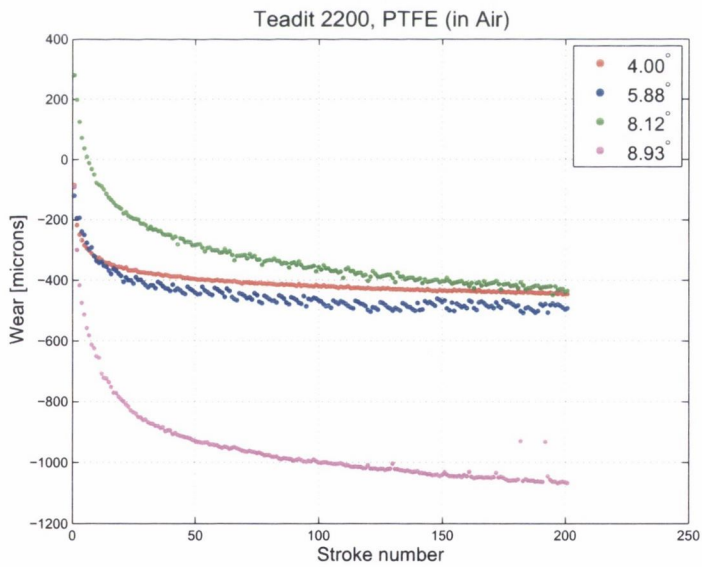


Figure D.23: Wear coefficient, K for Teadit 2200 on PTFE sections: in air

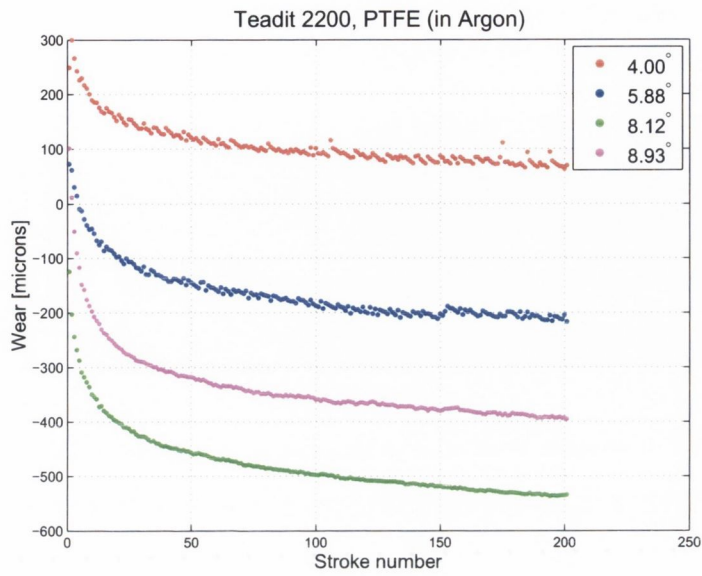


Figure D.24: Wear coefficient, K for Teadit 2200 on PTFE sections: in argon

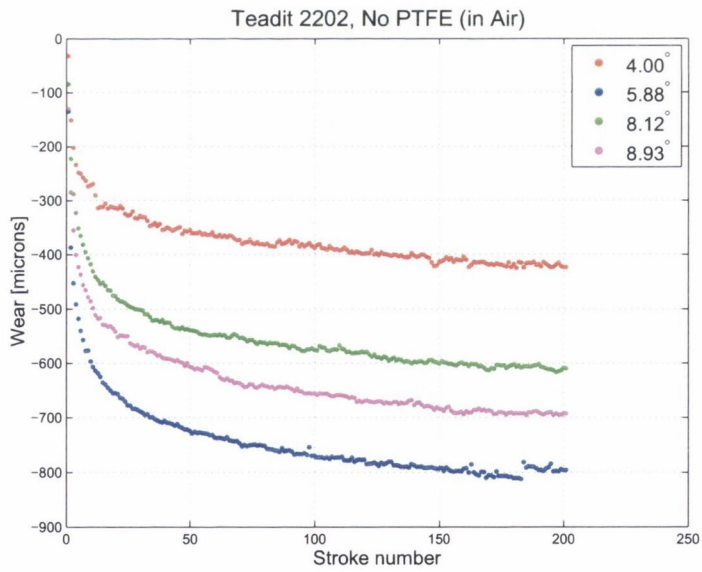


Figure D.25: Wear coefficient, K for Teadit 2202 on non PTFE sections: in air

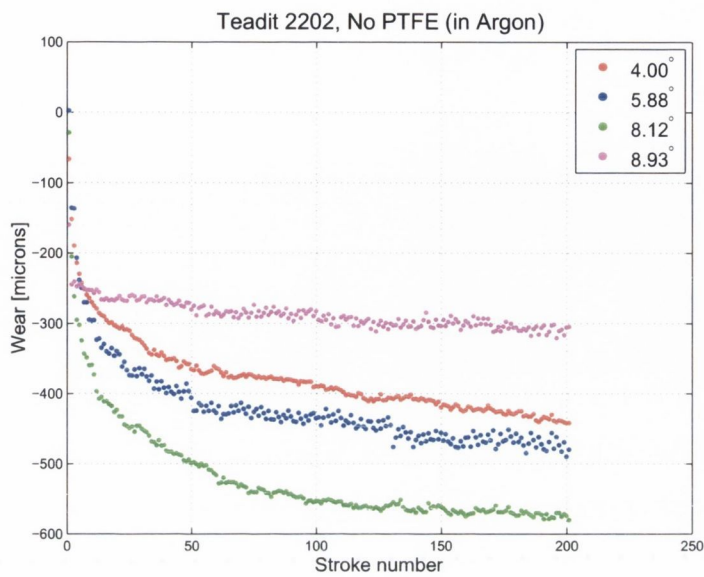


Figure D.26: Wear coefficient, K for Teadit 2202 on non PTFE sections: in argon

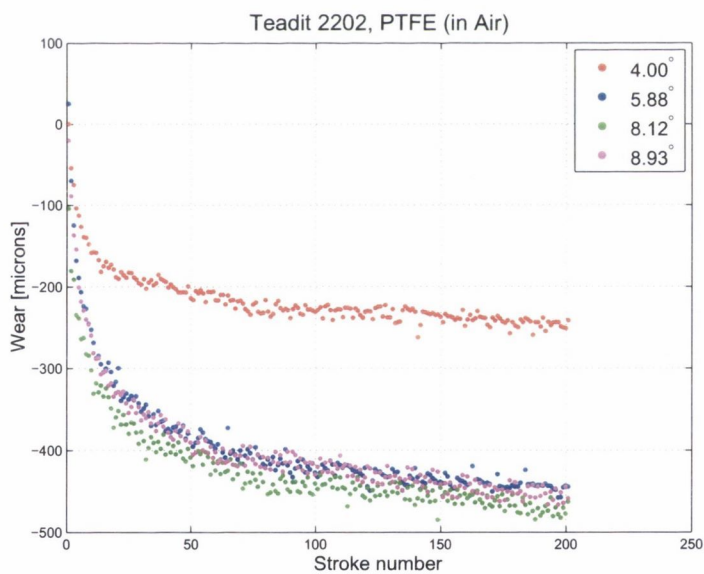


Figure D.27: Wear coefficient, K for Teadit 2202 on PTFE sections: in air

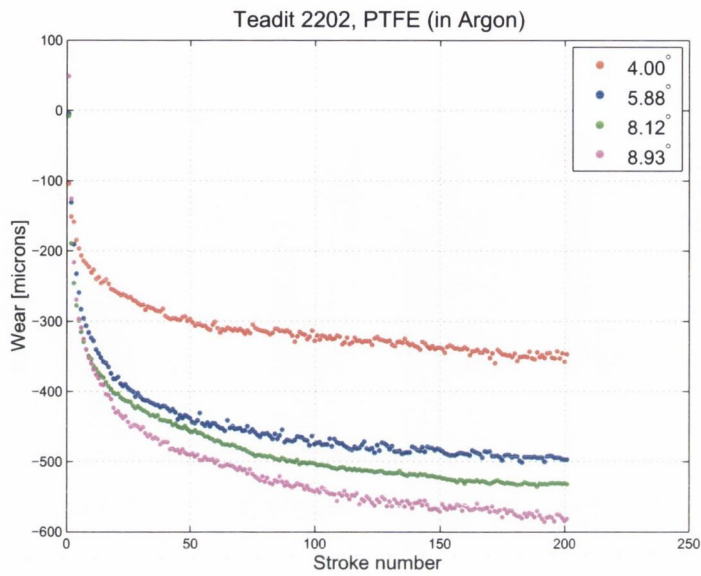


Figure D.28: Wear coefficient, K for Teadit 2202 on PTFE sections: in argon

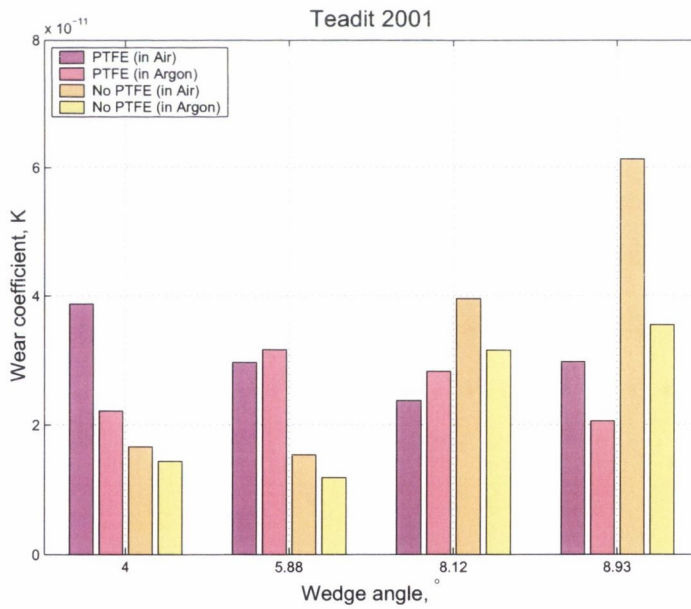


Figure D.29: Wear coefficient, K for Teadit 2001

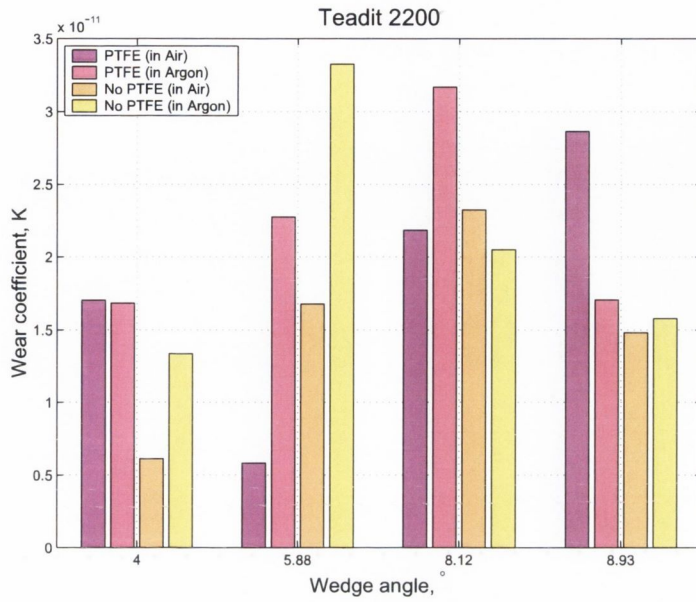


Figure D.30: Wear coefficient, K for Tedit 2200

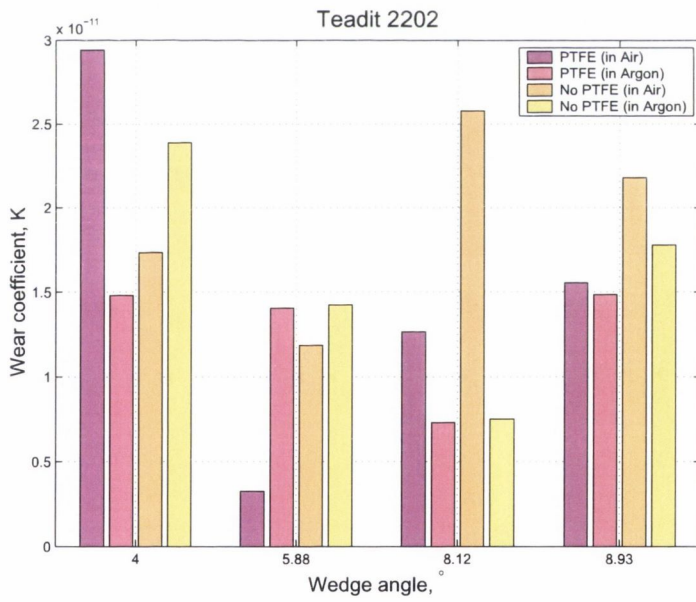


Figure D.31: Wear coefficient, K for Tedit 2202

be too sensitive to fluctuations in the braided packings to accurately measure the wear coefficient K .